3D Printing Microfluidics for Modeling Cerebral Small Vessel Pathology

Master Thesis

N.V. de Haan

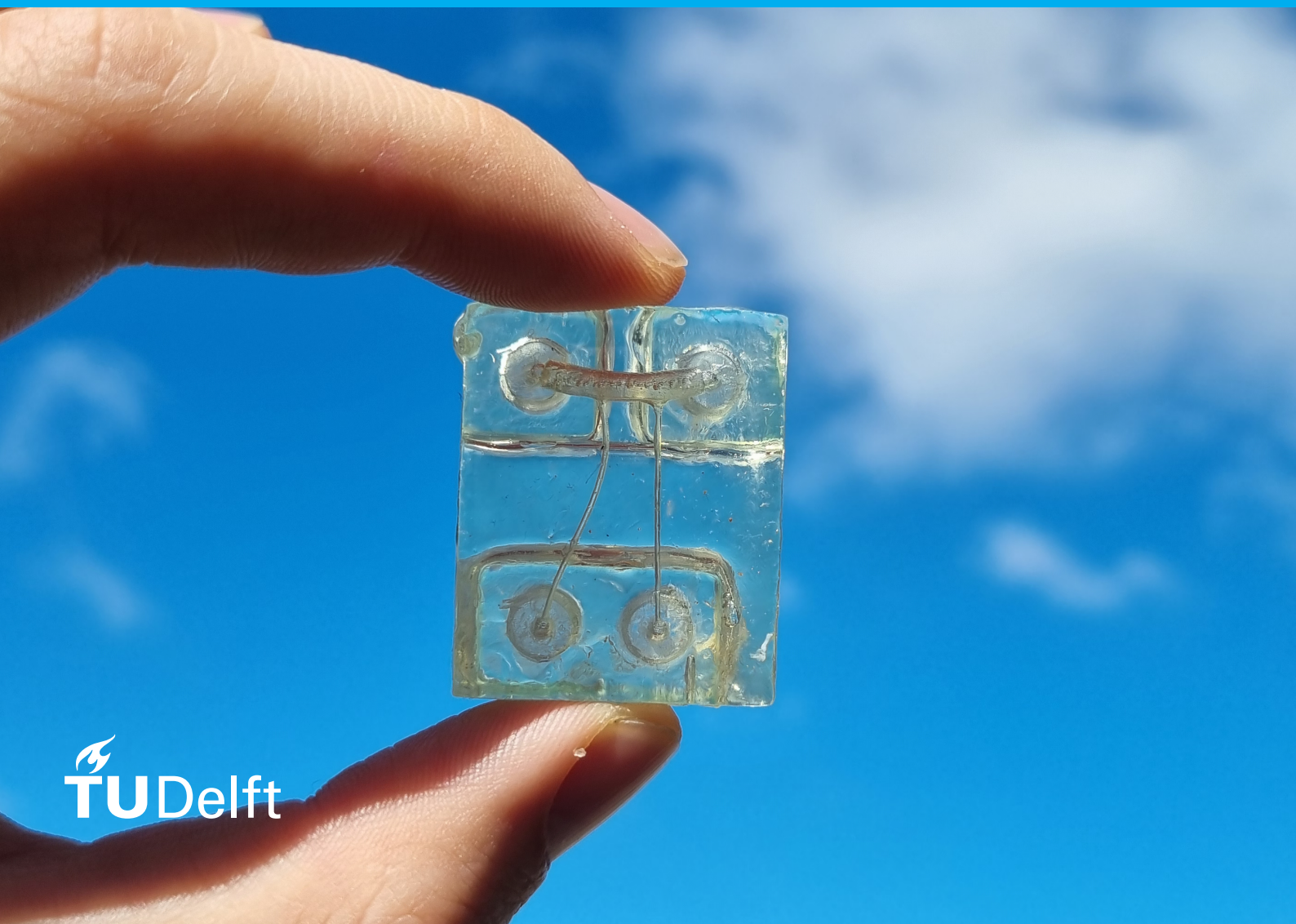

TU Delft

3D Printing Microfluidics for Modeling Cerebral Small Vessel Pathology

Master Thesis

by

N.V. de Haan

in partial fulfilment of the requirements of Master of Science in
Biomedical Engineering, track Medical Devices
at the Delft University of Technology,
to be defended publicly on Wednesday April 16, 2025 at 8:30 AM.

Student number:	4492706	
Project duration:	March, 2024 – March, 2025	
Thesis Committee:	Chair: Dr. S. Pirola,	TU Delft, BME, Supervisor
	Dr. I. Apachitei,	TU Delft, BME
	Dr. P. Fanzio,	TU Delft, PME, Supervisor
	Dr. M. K. Ghatkesar,	TU Delft, PME
Daily Supervisor:	Dr. A. Sharaf,	TU Delft, PME

An electronic version of this thesis is available at http://repository.tudelft.nl/.

TU Delft

Preface

This multifaceted project brought together a wide range of disciplines; from 3D printing and computational fluid dynamics to microfluidics, data science, statistics, and a whole suite of software tools. I am grateful for the opportunity to work on a true experimental engineering project, one that has culminated in a tangible device I can now hold in my hands. Along the way, I discovered an unexpected love for 3D printing. Even after countless hours spent troubleshooting and iterating, my excitement for the technology never waned.

This preface marks the end of a challenging, yet rewarding, journey. Like rowing, life is a team sport. I want to acknowledge people in my team to whom I owe a great deal of gratitude and who supported me throughout this process. I would like to thank my supervisors, Paola and Selene, for their continuous guidance and kindness. Their teams have been welcoming and inclusive, and I've made many new friends as a result in an environment open to learning. A special thanks to Ahmed for being a generous sparring partner. I appreciated his collaboration on the poster presentation. For their invaluable support during the project, I would like to thank the lab assistants.

I am also thankful to my family and friends. To my sister Ava: thank you for being consistently unavailable during my time in Delft, wisely relocating to Australia and taking on a full-time job before returning to university just as I leave. Fortunately, my friends Monica, and Rens were always there to fill the gap, providing both coffee and distraction. My parents will always have my thanks for their limitless and unwavering support throughout my entire academic journey. A special thanks would go out to Azza, who had traded Italy for the PME department alongside me. However, she did not want to be mentioned. And to Merlijn, thank you for sitting beside me through the highs and lows in our personal TPM office eating junk food.

To paraphrase Rens Ursem *et al.* [1], a thesis on 3D-printed microfluidics for biomedical applications is indeed "worth your sweat." His device might have helped me monitor my stress levels through cortisol, perhaps mine might one day explain his stress headaches through increased blood pressure.

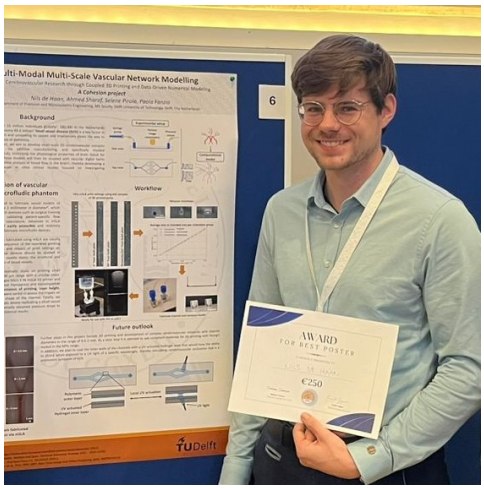

N.V. de Haan
Delft, March 2025

Contents

Nomenclature

Abbreviations

Abbreviation	Definition
2PP	Two-photon polymerization
ACA	Anterior cerebral artery
ACha	Anterior choroidal artery
AComm	Anterior communicating artery
AICA	Anterior inferior cerebellar artery
BJ	Binder jetting
2PP	Two photon polymerization
CAD	Computer assisted design
CAL	Computed axial lithography
CFD	Computational fluid dynamics
CLIP	Continuous liquid interface production
CoW	Circle of Willis
CSVD	Cerebral small vessel disease
DED	Directed energy deposition
DLP	Directed light processing
FEP	Fluorinated ethylene propylene
FDM	Fused deposition modelling
ICA	Internal carotid artery
LCD	Liquid crystal display
LSA	Lenticulostriate arteries
MCA	Medial cerebral artery
ME	Material extrusion
MJ	Material jetting
MRI, MRA	Magnetic resonance imaging, angiography
MSLA	Masked stereolithography
NAE	Normalized error of the area
OCT	Optical coherence tomography
OphA	Ophthalmic artery
PDMS	Polydimethylsiloxane
PBF	Powder bed fusion
PCA	Posterior cerebral artery
PComm	Posterior communicating artery
PICA	Posterior inferior cerebellar artery
PIV	Particle imaging velocimetry
SCA	Superior cerebellar artery
SLA	Stereolithography
SLS	Selective laser sintering
VA	Vertebral artery
VPP	Vat photopolymerization

1

Abstract

Cerebral small vessel disease (CSVD) is a leading cause of stroke and dementia, making the study of small vessel hemodynamics vital for advancing diagnostic and therapeutic strategies. This research focuses on fabricating microfluidic devices that replicate the lateral lenticulostriate arteries (LSA) to validate computational flow models of small cerebral vessels. A key challenge in studying CSVD is the lack of experimental validation for computational fluid dynamics (CFD) models, which are widely used to simulate hemodynamics. To address this, additive masked Stereolithography (mSLA) was employed to fabricate a microfluidic model of the LSAs.

The study explored the impact of orientation, exposure time, and layer height on the roundness and error of the intended area of printed micro-pores, to optimize the manufacturing of a microfluidic device. The smallest printed pore measured 270 µm in diameter. Pores printed at a larger angle as assessed from the build plate were more likely to remain open, but exhibited a larger decrease in area compared to smaller angles. A lower exposure time exhibited a larger pore area, whereas a larger layer height showed a decrease in area from intended. The layer height and angle did not influence the roundness, whereas an increase in exposure time decreased the roundness of the pores. Additionally, flow experiments were conducted using a 3D printed microfluidic device to compare empirical data with CFD and analytical simulations. The encountered resistance was larger for the experimental results (3.19 $\cdot 10^{11}$ Pa·s/m^3) compared to the analytical result (1.96 $\cdot 10^{11}$ Pa·s/m^3) and the computational result (1.90 $\cdot 10^{11}$ Pa·s/m^3), likely due to deviation from the intended size. Finally, arterial microfluidic devices were printed and flow was induced to showcase their functionality. Achieving precise channel dimensions remains the primary challenge in mSLA printing due to cumulative dosage effects.

This research bridges the gap between computational modeling and experimental validation, providing a platform for studying cerebral microcirculation. The findings demonstrate the feasibility of using commercially available 3D-printed microfluidic devices to replicate small cerebral vessels. The outcomes of this study contribute to the advancement of vascular biomodeling, with implications for future clinical applications in stroke and neurovascular research.

2

Introduction

This chapter provides an overview of the process for fabricating microfluidic devices intended to validate computational flow models of small cerebral vessels. It begins with a discussion of cerebral arteries and cerebral small vessel disease, focusing on the lateral lenticulostriate arteries (LSA), which play a significant role in this study. These arteries were replicated using additive manufacturing, a method selected after reviewing various microfluidic fabrication techniques. The chapter then details the additive manufacturing process, with an emphasis on the DLP (Digital light processing)/mSLA (masked stereolithography) printing technique used to produce micro-channels. Finally, the research question pertaining to the mechanics of 3D printing is introduced.

2.1. Cerebral Arteries

The anatomy of the brain vasculature must be understood if the goal is to imitate it for flow modelling. Already over 2000 years ago, Herophilus of Chalcedon described the vascular structure at the base of the brain as *"rete mirabile"*, or wonderful net [2]. This structure is a circle of arteries that are interconnected, combining the input of the two internal carotid arteries and the basilar arteries. The anastomotic structure understood today as the "circle of Willis" (CoW) can be identified in other animals and is thought to serve as a compensatory system for occlusion [3]. However, as described by Vrselja *et al.* [3], from an evolutionary perspective it is unlikely that pathologic conditions mainly prevalent in older individuals would drive evolution, and it is more likely that the circle of Willis serves as an energy dissipating system.

Most of the arteries supplying the brain originate from the circle of Willis. A schematic overview of the Circle of Willis is provided in Figure 2.1. The circle of Willis itself consists of six main arteries: the *arteria cerebri anterior dextra* and *sinistra* (together, the anterior cerebral arteries or arteriae cerebri anteriores, ACA), the *arteria cerebri media dextra* and *sinistra* (together, the middle cerebral arteries or arteriae cerebri mediae, MCA), which originate from the internal carotid artery, and the *arteria cerebri posterior dextra* and *sinistra* (together, the posterior cerebral arteries or arteriae cerebri posteriores, PCA) from the basilar artery.

The arteriae cerebri anteriores are connected via the single *arteria communicans anterior*, while the arteriae cerebri mediae and arteriae cerebri posteriores are connected via the *arteria communicans posterior* on either side. The cerebral small vessel arteries originate from the subarachnoidal and perforating arteries, generally stemming from the Circle of Willis, and are usually found in the basal ganglia, thalamus, pons, and white matter tracts in the subcortical region. This is specifically situated in the area where the lenticulostriate branches originate from the anterior and middle cerebral arteries, as well as the paramedian branches stemming from the basilar artery [5]. The small cerebral vessels have little overlap in their respective regions of perfusion [6].

The deep cerebral perforators stemming from the Circle of Willis vary in size, number, origin, and vascular territory [7]. These perforators generally have diameters in the micrometer range and mark

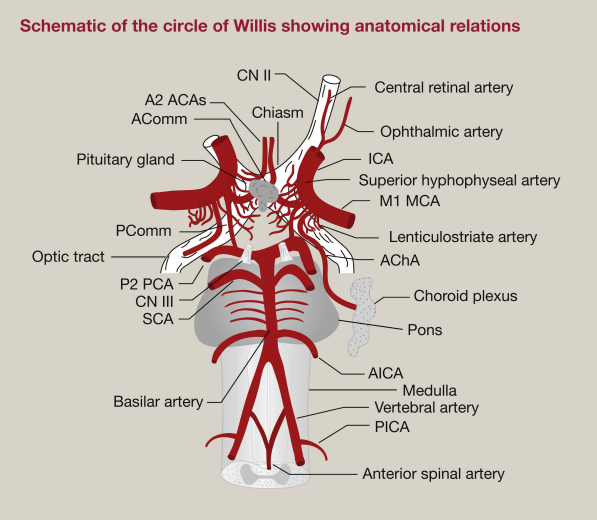

Figure 2.1: A schematic overview of the Circle of Willis sourced from Shah *et al.* [4]. As described in the Figure and quoted from Shah *et al.* [4]: *ACA, anterior cerebral artery; AChA, anterior choroidal artery; AComm, anterior communicating artery; AICA, anterior inferior cerebellar artery; CNII, optic nerve; CN III, oculomotor nerve; ICA, internal carotid artery; M1 MCA, middle cerebral artery; OphA, ophthalmic artery; PCA, posterior cerebral artery; PComm, posterior communicating artery; PICA, posterior inferior cerebellar artery; SCA, superior cerebellar artery.*

the beginning of the microcirculation. Vogels *et al.* [7] describe the anatomical variation in perforating arteries. Diseased perforating arteries can cause cerebral small vessel disease (CSVD) [8].

One example of small vessels are the lateral lenticulostriate arteries. The lateral lenticulostriate arteries branch off the proximal middle cerebral artery to supply the subcortical areas (the caudate nucleus, globus pallidus, putamen, and part of the posterior limb of the internal capsule) and infarction can cause a motor syndrome with hemiplegia [7, 9]. They are known as important small vessels and are more likely to be present in smaller numbers in the presence of small vessel disease [10]. The mean outer diameter of these perforating branches of the MCA is 0.39 mm (range 0.1-1.1 mm) and the number of these arteries branching off varies between 1-17 [11, 7]. The mean outer diameter of the lateral lenticulostriate arteries is approximately 0.47 mm with a length of 16.67 mm [11]. The tortuosity of these vessels is 1.2 [12]. The M1 segment of the middle cerebral artery, of which these arteries originate, has a diameter of 2.66 mm and is about 20 mm in length [13].

2.2. Small Vessel Disease

Small vessel disease is a broad umbrella term with various definitions in different contexts [14, 15]. It is a systemic disease of small vessels that can be further specified to organs such as the brain, then called cerebral small vessel disease, but can in principle affect various other organs in the body without necessarily involving the brain [14]. Small vessel disease can pertain to pathology of small arteries, arterioles, capillaries, venules, and small veins. The diameter of the affected vessels in small vessel disease ranges from 50 to 400 µm [16]. The microvascular system can be said to start at the level of arterioles, or approximately 100 µm, meaning that small vessels outside of the microvasculature are already involved [17].

CSVD is linked to stroke, dementia, and motor impairment [14]. It can occur acutely, as in a stroke or brain bleed, or develop gradually over time, leading to cognitive decline [18, 19]. CSVD is responsible for approximately 25% of ischemic strokes in Europe and contributes to nearly 45% of dementia cases [20, 16]. Although scientists recognize the effects of CSVD, the exact causes are still not fully understood [16, 5]. It was once believed that high blood pressure was the main cause, but recent research suggests that damage to the blood-brain barrier, the protective layer that controls what enters and exits the brain, may play a larger role than previously thought [5]. Some studies indicate that white matter damage in the brain may come before reduced blood flow, potentially leading to stroke-like symptoms [21].

CSVD can likely develop in different ways. One common explanation is that tiny arteries deep in the brain become stiff and narrow over time, reducing blood flow and leading to blockages [5]. In some cases, the disease starts from larger blood vessels that supply these small arteries. Other forms of CSVD are linked to conditions such as cerebral amyloid angiopathy (where proteins build up in blood vessels), immune system disorders, and genetic factors [16, 5]. As blood vessels stiffen and their ability to regulate blood flow changes, the brain may not receive the oxygen and nutrients it needs. Understanding how blood moves through these tiny vessels (hemodynamics) is crucial for uncovering the causes of CSVD and developing better treatments [22].

2.2.1. Hemodynamics in CSVD

Flow analysis in CSVD plays a crucial role in understanding disease mechanisms and treatment development. There are three main approaches to studying hemodynamics: *in vitro* (laboratory-based), *in vivo* (live subjects), and *in silico* (computer simulations). *In vitro* and *in silico* studies offer a key advantage over *in vivo* research in its ability to precisely control experimental conditions. However, to ensure accuracy and generalizability, computational models require validation using real-world data from *in vivo* or *in vitro* studies [23, 13].

One of the main challenges in cerebrovascular flow modeling is the limited validation of computational models. Unlike cardiac hemodynamic studies, where intracranial pressure measurements are more common, intracranial validation is often lacking [24]. Another gap in the research is the lack of data on the effects of small downstream vessels in simulations of cerebral circulation [13]. Addressing this could significantly improve model accuracy. A promising approach is the combination of *in vitro* and *in silico* validation techniques, particularly for studying small vessel pathology [25]. Rigorous validation enhances the predictive capability of fluid flow models, making them more reliable for clinical and research applications. However, several challenges remain, including ethical concerns in *in vivo* experiments, computational complexity, and anatomical variability. Successful experimental validation of computational CSVD models requires a multidisciplinary approach, incorporating:

- Device manufacturing that mimics cerebral vessel anatomy and biomechanics.
- Accurate fluid properties to replicate blood rheology.
- Measurement techniques for precise flow assessment.
- Computational models that integrate small vessel dynamics.

Addressing these challenges will improve our ability to model CSVD accurately, leading the way for better diagnosis and treatment strategies. The LSA are involved in small vessel disease, responsible for infarcts, and fabrication of flow validation devices of the LSA can aid in understanding focal cerebral pathology [11]. The diameter of these vessels places them at the larger end of microfluidic devices.

2.3. Traditional Microfluidics for Manufacturing Small Channels

Fabrication of devices for validation of flow models of the LSA can be done using existing microfluidic production techniques. An example of such microfluidic devices is seen in Figure 2.2. *In vitro* models of blood vessels larger than the small vessel range, and guides on manufacturing them, already exist [27, 28, 29, 30, 31]. Flow phantoms have been developed to validate imaging techniques and investigate flow, and have existed for decades at least [32, 33]. Microfluidics can aid in the development of flow phantoms for small vessels and the microvasculature [17]. One approach to fabricating devices for *in vitro* flow validation of small vessels and the microvasculature is using existing subtractive or additive microfluidic manufacturing techniques [34]. Manufacturing microfluidic devices can be done directly, using mechanical (e.g. micro-milling) or energy assisted methods (e.g. laser ablation or electron beam machining), or it can be done using a master mould for replication techniques [35]. A mould can be manufactured to more cheaply fabricate multiple replications of a single initial design. Manufacturing a device to validate flow for a specific geometry is a form of low volume prototyping. As a result, the most suitable ”traditional” methods for fabrication of microfluidic devices for validating flow models are casting, laminate manufacturing, laser fabrication, and additive manufacturing [35].

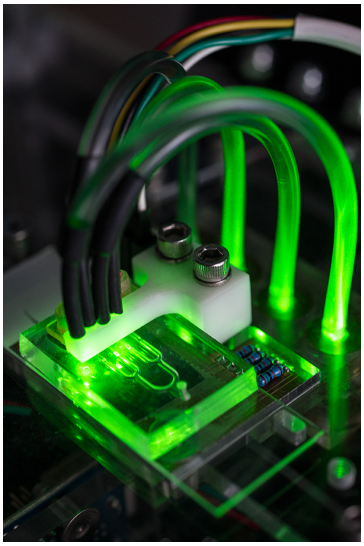

Figure 2.2: An example of a microfluidic device mimicking blood vessels as sourced from Georgia Institute of Technology [26]

- Casting, or soft lithography, is a process in which a soft material, usually polydimethylsiloxane (PDMS), is cast onto a patterned master mold. It has advantages in that it can produce three dimensional patterns at low cost [36]. Multiple forms of soft lithography exist, such as microcontact printing, replica moulding, micromoulding in capillaries, microtransfer moulding, etc. [35, 36, 37]. Replica moulding can be used in conjuction with high resolution additive manufacturing to recreate vascular geometry and advance beyond the more general rectangular cross section [38, 39]. Similarly, a hydrogel can be cast around a steel cylindrical needle to recreate a cylindrical cross section [40]. This technique is limited to straight channels, however, since the needle must be removed after casting. Lastly, the geometry of the veins of the Hedera Elix leaf was obtained in PDMS using casting as a soft lithography technique [41].
- Laminate manufacturing is the process of bonding a stack of individual layers with cutouts to create a microfluidic device [35]. Laminated layers can be bonded in different ways allowing for the use of many different materials. This technique was used to manufacture a microfluidic device with a straight channel to research shear stress on endothelial cells [42]. Laminated microfluidic devices can be manufactured for more complex three dimensional designs, but such a layered approach is generally not viewed as a suitable approach for the recreation of vasculature [43, 44].
- Laser micromachining is a fabrication technique that uses focused laser beams to precisely cut, engrave, or ablate materials at a microscale level. Laser micromachining for microfluidic prototyping is a relatively cheap alternative to mechanical micromachining, and is capable of engineering complex 3D structures [45, 46]. Two main types can be identified, namely scribing (serial mode) and using a mask-imaging technique (parallel mode) [45]. Scribing is preferred for prototyping, since no mask is required.
- Finally, there is 3D printed microfluidics, which consists of a variety of printing techniques [47]. 3D printing techniques can be classified in several ways, for instance by the technology used, or the raw material that is supplied [48]. Seven categories of 3D printing can be observed using the separation of technologies by system architecture and physics of material transformation as proposed by Gibson *et al.* [48]. These processes are: vat photopolymerization (VPP), Powder bed fusion (PBF), material extrusion (ME), material jetting (MJ), binder jetting (BJ), sheet lamination (SL), and directed energy deposition (DED). A last form of printing, bioprinting, makes use of several of these printing techniques, facilitating interplay between the disciplines of in vitro flow modelling and tissue engineering [49].

If the intention is to replicate patient- or otherwise derived complex three dimensional vascular anatomy, standard two dimensional manufacturing techniques may fail to sufficiently imitate complex shapes.

Collingwood *et al.* [50] provide a review on 3D printed microfluidics. One of the mentioned benefits of 3D printing microfluidic devices is the improvement in accessibility to fabricating three-dimensional shapes. One advantage of 3D printing over other manufacturing techniques is the predictability of the performance of the device as a result of digital inspection of the CAD model based on segmented images of real anatomy [51]. Similarly, the required patient specific anatomy can be recreated and evaluated for the production of personalized stents, visualization for the surgeon prior to the surgery, or analysis of pathologies involving flow such as aneurysms or infarctions [44]. 3D printing is already used for biomedical applications, and some of its inherent advantages may be specifically well suited for in vitro flow modelling of (micro)vasculature [52]. Lastly, circular cross sectional shape microfluidic devices are ”nearly impossible to find” on the market according to Akeredolu [53]. Again, additive manufacturing may provide a simple and accessible alternative.

2.4. 3D Printed Microfluidics

The applications of 3D printing for biomedical and healthcare utilization are well established [48, 54, 47, 52, 55]. Additive manufacturing is employed by hospitals for education, visualization, surgical planning, validation of new technology, and personalized medical device design [56, 57]. Larger arteries, such as the circle of Willis, were already able to be visualized using MRI [58]. The perforating arteries can now be visualized and segmented using 7T MRI [59, 60, 61, 62]. This makes the direct printing of patient-derived anatomical models of small vessels possible. For printing small vessels, the focus should be on printing complex tortuous structures accurately. These can be hollow or solid, depending on whether an indirect printing approach is utilized. A secondary focus is on the available material selection for imitating mechanical properties of biological tissue. Newer 3D printing machines keep appearing with improved resolution, such as the FormLabs 3 [63], with new materials for biomedical applications such as the BioMed Flex 80A Resin and BioMed Elastic 50A Resin [64]. These facilitate improved and more accessible anatomical modeling over previous studies.

Of the 3D printing techniques, Material extrusion, material jetting, and vat photopolymerization were mainly used in the resulting studies from a systematic review on 3D printed flow studies as seen in Appendix A. Direct energy deposition and sheet lamination are not considered suitable approaches towards printing vascular geometry [44]. Similarly, powder based approaches such as PBF and BJ may not be suitable due to the resulting surface roughness, complicated post-processing, and lack of improvement in accuracy or precision to justify the investment or effort. These considerations are reflected in the absence of the printing approaches observed in the literature for manufacturing *in vitro* vascular models.

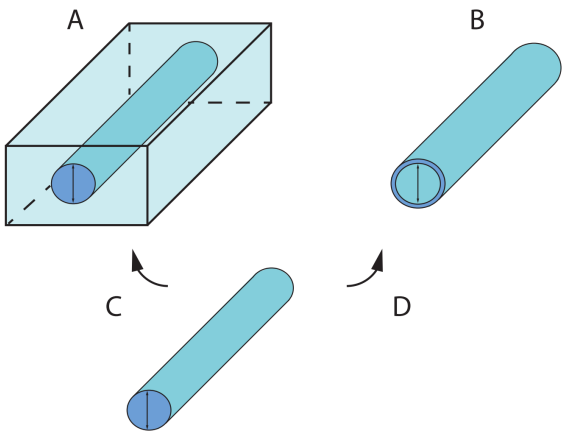

Figure 2.3: A schematic illustration of the main identified fabrication processes. A: Direct printing of a wall-less phantom. B: Direct printing of a vascular construct. C: Indirect printing of a sacrificial mold for the fabrication of a wall-less phantom by casting. D: Indirect printing of a sacrificial mold for the fabrication of a vascular construct by coating.

For 3D printing vessels, 4 main strategies were observed in the systematic review in Appendix A. Figure 2.3 illustrates the processes used for fabricating vessels using 3D printing. They consisted of a categorization into a direct and indirect approach. In direct printing cylindrical vessels, post-processing is limited to improving the optical transparency, biocompatibility, surface roughness, and clearing the channels of residual material. The printed arteries can be wall-less phantom with internal hollow geometry replicating the vascular anatomy, or they can be true thin-walled cylinders. The indirect printing approach relates to printing of a sacrificial mold that represents the lumen. After the lumen is printed, it can be coated or cast using various materials after which it is dissolved. Printing vessels directly is desirable, since patient specific geometry could be directly manufactured for research purposes. The systematic review illustrated that VPP processes were mostly used for printing devices, and that the indirect approach was mostly used. Wall-less devices were mainly fabricated using an indirect printing approach with exceptions being Reddy *et al.* [65] and Carlsohn *et al.* [66]. Approximately 11 studies used SLA printing for their manufacturing process, and 7 studies used a form of inkjet printing (see Table A.1). FDM printers were exclusively used for indirect 3D printing, except in the case of Anderson *et al.* [67]. Several studies managed to manufacture at or below 1 mm diameter resolution [68, 69, 66]. One study used SLA with a rigid photopolymer to manufacture the phantoms, whereas the other two studies were based on inkjet printing and a prototype machine that is not expanded upon.

The review in Appendix A illustrates that cerebral arteries as small as 1 mm in diameter have been fabricated, which is not yet in the range of small vessels. The smallest channel achieved for VPP, fused deposition modeling (FDM, a subtype of ME), and MJ are reported by Gonzalez *et al.* [70] to be 18, 54, and 40 micrometers respectively [71, 72, 73]. It seems therefore possible to recreate smaller channel sizes for the purpose of creating small vessel phantoms. The advantages and disadvantages of 3D printing subtypes for different intended purposes have been extensively discussed [74, 44, 75, 70, 47, 76, 52, 55, 54, 77, 78, 79, 80]. It must be mentioned that resolution is dependent on the printer and material for every printing technique. One technique may on average reach higher resolution as a result of its working principle, but the expected resolution reached is variable and must be adjusted to the machine and materials at hand.

Inkjet (a type of MJ), FDM, and stereolithography (SLA, a subtype of VPP) are the most used additive manufacturing techniques for microfluidic applications, which bears resemblance to the main used additive manufacturing techniques observed for intracranial vasculature [81]. FDM is not ideally suited for direct printing of microfluidic applications due to leakage between layer deposits, limitations in resolution, and surface roughness [51]. It has been used for direct printing of channels with dimensions under 100 micrometer by optimizing the nozzle and printing parameters [81]. Inkjetting and FDM do not require post processing of powders or resins to the extent that SLA and selective laser sintering (SLS, a subtype of PBF) do. Laminated object manufacturing requires relatively more post-processing than SLA or SLS [51]. SLA and PolyJet (a subtype of MJ) have the best resolution of the 3D printing techniques [51, 47].

SLA is a relatively popular choice for 3D printing of microfluidics due to it being low cost and easy to use [82]. Polyjet, DLP (another subtype of VPP), and FDM have been directly compared in the context of creating a laminar flow microfluidic device [83]. Macdonald *et al.* [83] concluded that the smallest channels with the smoothest surfaces were produced by the DLP machine and is well suited for microfluidics. The study done by Lee *et al.* [84] similarly conclude that PolyJet is superior in terms of resolution, surface roughness, and dimensional accuracy for microfluidic applications with regards to FDM, but they did not compare against VPP processes. Collingwood *et al.* [50] indicate that DLP processes are superior to MJ or FDM for complex geometry microfluidic devices, and that bottom-up DLP is the most suitable for microfluidic device fabrication. Bottom-up DLP refers to light source being underneath the vat containing the photopolymer, in contrast to top-down where the light source is situated above the vat. Bottom-up devices performed better than top-down devices in obtaining consistent and controllable layer-thickness.

As a result of the aforementioned comparison studies showcasing comparably superior surface roughness of VPP processes, in particular DLP printing, and the ability to make comparatively small channels

using DLP and SLA this study intends to use a VPP process for fabricating a microfluidic device [51, 47, 83, 50, 82]. VPP processes have already been used in studies for the purpose of recreating microfluidic channels of dimensions similar to that of the lateral lenticulostriate arteries‘[85, 86].

2.5. Vat Photopolymerization for Microfluidics

VPP Mostly uses UV or visible light to cure photosensitive polymers, and in rare situations gamma rays, X-rays, or electron beams [48]. Thermoplastic polymers used in injection molding have a linear or branched molecular structure suited to repeated melting and solidification. Photosensitive polymers used for VPP, however, are cross-linked and do not melt. These resins consist of monomers, oligomers/binders, photoinitiators, reactive diluents, fexibilizers, and stabilizers [48, 87]. To simplify, UV radiation interacts with photoinitiators in the resin, which in turn reacts with the monomer to form a chain and to solidify the material [48]. Two main types of photosensitive polymers are prevalent; Free-radical photopolymerization using acrylates, or cationic photopolymerization using epoxy and vinyl ethers [48]. An extensive list of materials used in VPP and their applications is provided by Al Rashid *et al.* [87] and Pagac *et al.* [88].

VPP can be further classified into more specific techniques such as stereolithography (SLA), digital light processing (DLP), continuous liquid interface production (CLIP), two-photon polymerization (2PP), and computed axial lithography (CAL) [87, 70]. DLP and CLIP are mask projections and have decreased surface smoothness due to ”stair stepping” caused by rectangular voxels [89]. One subtype of VPP similar to DLP is masked stereolithography (mSLA, sometimes referred to as LCD printing), which uses a LCD instead of a projector. SLA uses a laser for polymerization of the photopolymer. The width and profile of the cured line is generally dependent on material and laser characteristics, and scan speed. 2PP has the best resolution of all printing techniques, but is limited by printing speed and dimensions [48]. A comparison of the main VPP additive manufacturing processes in provided in Figure 2.4. In this graph a visualization of the minimum feature size and maximum build area is provided. 2PP performs best in terms of minimum feature size, but is limited in the build area. Overall, DLP processes seem to be most optimal for combining small feature sizes with structure dimensions in the cm^2 range. A cm^2 range is indicated for microfluidic devices of the LSA which measure on average to be approximately 2 cm in length. A 5 cm^2 range is required for the circle of Willis to fit with space for small branches [90]. MSLA has shown to be cheaper to DLP for comparable results in printing open microfluidic channels as shown by Leong *et al.* [85] and is therefore preferable.

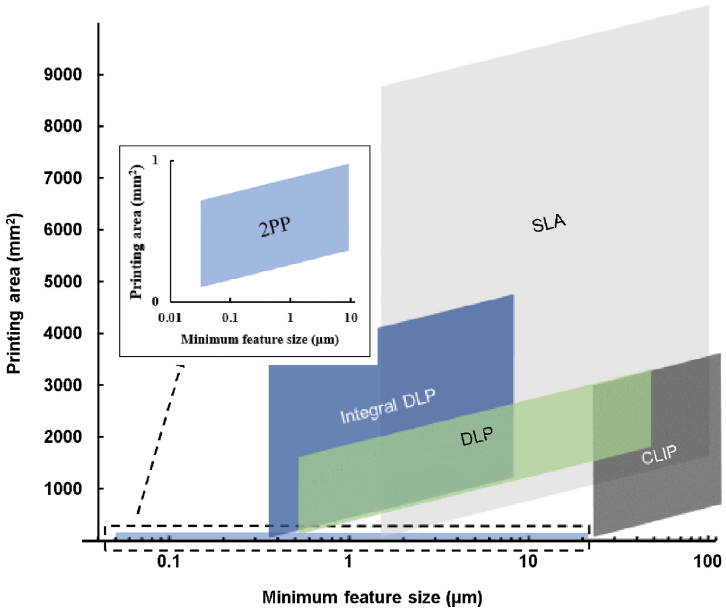

Figure 2.4: A comparison of different printing VPP additive manufacturing methods as sourced from Amini *et al.* [91].

2.6. Mechanics of MSLA for Microfluidics

DLP and mSLA printing polymerize layers of the photopolymer using a light projector or light emitted by a LCD. After printing the prints are post-cured to obtain desirable mechanical properties. To ensure the layer polymerizes and sticks to previously printed layers, the backside of every layer must be subjected to a critical dose of UV-light. A mathematical relation between the photopolymer and light for DLP printing is provided by Gong *et al.* [86]. This approach should be transferrable to mSLA printing. The process for fabricating a microfluidic channel is schematically illustrated in Figure 2.5 as adapted from Gong *et al.* [86]. In this image a bottom-up process is shown, in which the build table (or build plate as it will be referred to in this study) moves down into the photopolymer resin to be polymerized by the emitted light. This build plate will move up to allow consequent layers to be printed. Part A of the Figure shows three printed layers sticking together. Part B shows 5 printed layers with a small channel representing pixels that did not polymerize. Part C shows a closed channel filled with photopolymer resin, and Part D shows the result when removed from the build plate and when the resin inside the channel is removed. In this process light is partly transmitted through consequently printed layers,

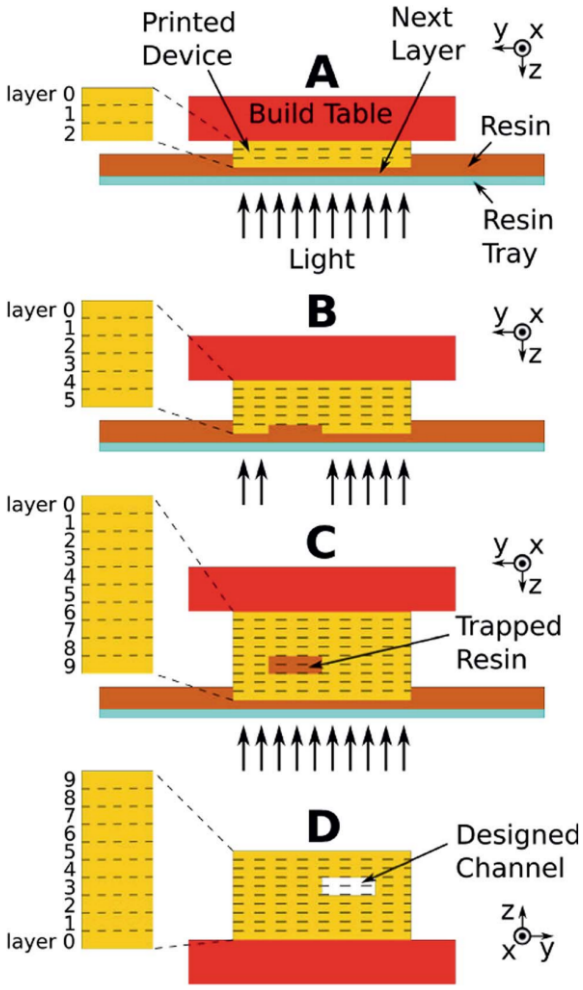

Figure 2.5: The layer-wise production process of a microfluidic device sourced from Gong *et al.* [86]. in A 3 solid layers are printed and attached to the build plate. In B a small channel is produced at layer 5 by masking the area from UV light. In C The 2 layers deep channel is closed by 3 additional layers. In D the buildpate is turned and the channel is empty to show the final solidified block containing the designed channel.

increasing the dosage that every layer receives. This is problematic, since the trapped photopolymer resin in the channel will also receive this extra dosage. If the cumulative dosage from consequent layers exceeds a critical dose threshold, the photopolymer resin in the channel will solidify and close. The effect of the relationship between the photopolymer resin and the DLP/mSLA machine on the curing

depth can be described as seen in Equation 2.1 as explained by Schittecatte *et al.* [92] and is based on Lambert-Beer's law [93]. The Curing depth is dependent on the energy provided by the machine and the penetration depth in the resin itself.

$$C_d = D_p \ln\left(\frac{E}{E_c}\right) \tag{2.1}$$

This relationship describes how C_d, or Curing depth in µm, is affected by the light penetration depth D_p in µm (similar value to h_a as described by Gong *et al.* [86]), Exposure dose E in mJ cm^{-2}, and critical exposure dose to start curing (E_c) in mJ cm^{-2}. The value of E for SLA processes is calculated by the the laser power divided by the product of the hatching distance and laser speed. For mSLA and DLP processes, E is obtained by multiplying the light power with the exposure time. The values of D_p and E_c are material dependent and must be obtained experimentally.

In addition to the curing depth, the critical dose as described by Gong *et al.* [86] tells the dose required for polymerization and solidification. The dose for a given layer varies at the front and the back. The normalized dose of a printed layer received at the back is described by equation 2.2.

$$\Omega_{\text{back}} = \tau_l e^{-\zeta_l} \tag{2.2}$$

Ω_{back} is the normalized dose received at the back of the layer, τ_l is a normalized metric for the relation between the layer height and penetration depth: $\frac{z_l}{h_a}$ which stands for the layer height z_l and the penetration depth h_a. A normalized metric for the exposure time and the critical exposure time is ζ_l as expressed by $\frac{t}{T_c}$: with the exposure time being t and the critical exposure time being T_c (which is the same ratio as $\frac{E}{E_c}$). This dose only affects the current layer and previous layers, not subsequently printed layers. The normalized value received by the layer at the back should be larger or equal to one for the layer to print successfully.

The cumulative normalized dose is important for the uncured resin inside the channel, as they might still be exposed due to light bleeding through subsequently printed layers. Gong *et al.* [86] describe a mathematical model for the cumulative total dose caused by multiple exposure effects on the fabrication of an embedded channel. This equation is given in equation 2.3.

$$\Omega(\gamma, \tau_l) = \sum_{n=0}^{N-1} \tau_l e^{-(n+1-\gamma)\zeta_l}, \quad \text{for } \gamma \leq N \tag{2.3}$$

This is a summation of N number of normalized doses. In this equation, γ stands for $\frac{z}{z_l}$ or the depth measured from the build plate (= 0) over the layer height. An example of the variation of dosage expressed as the normalized cumulative dosage in four printed layers is provided in Figure 2.6 as adapted from Gong *et al.* [86]. In this figure the values are provided to be: ζ_l is 0.69 (unitless), τ_l is 2.0 (unitless), and h_a is 72.5 µm. The back of layer four is the intersection with the critical normalized dose for polymerization (the critical normalized dose is always one). Layers 0-3 were printed with similar settings, but the normalized cumulative dose increases due to added doses of subsequent layers as visualized in the figure by an increasing total exposure. Gong *et al.* [86] also note dose inhomogeneity within every layer possibly causing internal stress of cured devices.

The modeled channel described with the equation by Gong *et al.* [86] was only printed at one orientation (parallel to the build plate). This is relevant, since channels printed vertically or orthogonal to the build plate would not be similarly subjected to the depth decreasing effect of overcuring the channel internals. Angled channels are still susceptible to light bleeding into the internal channel, but the orientation may be less prone to the error caused by an increased cumulative dose inside the channel, since the cross section increases in height when angled. This is especially pronounced in channels orthogonal to the build plate. Furthermore, printing at an angle is done by hobbyists for flat surfaces to evenly distribute layer steps. This is visualized in Figure 2.7. The angle chosen is based on the arc tangent of the layer height and pixel width as described in Equation 2.4.

$$\arctan\left(\frac{\text{layer height}}{\text{pixel width}}\right) \tag{2.4}$$

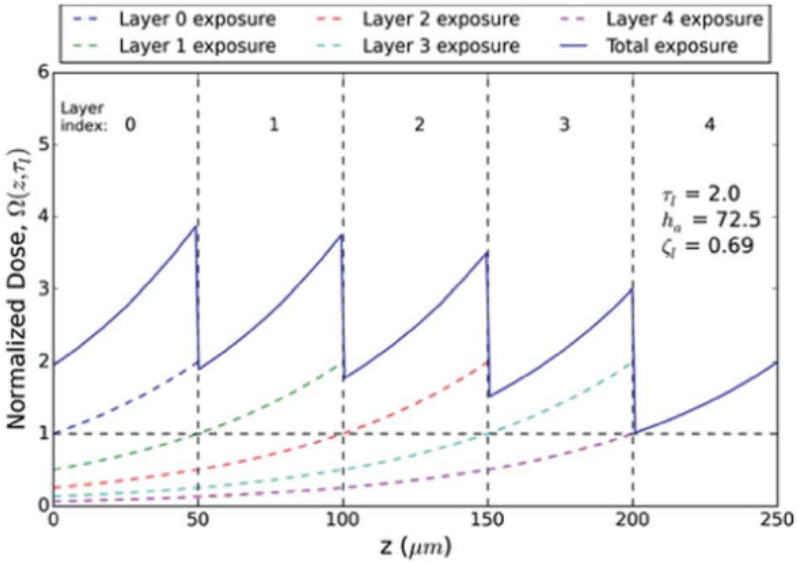

Figure 2.6: An illustration of the effect of dosage building up after the light emitted of consequent printed layers. Every layer receives a normalized dose of 1 at the back, meaning the dose is sufficient for the entire layer to polymerize and attach to the previous layer. The light penetrates deeper than the back of the layer and adds to the cumulative dose of previous printed layers. Sourced from Gong *et al.* [86].

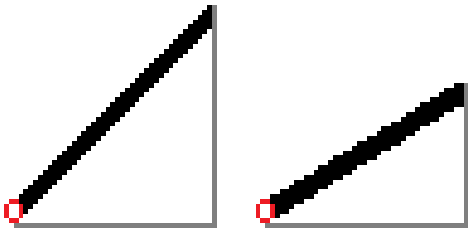

Figure 2.7: Visualization of the effect of the arc tangent angle orientation. On the left is a stylized sample oriented using the arc tangent rule, on the right at a smaller angle.

Heidt *et al.* [94] illustrate the influence of the print orientation on printing open channels, instead of closed channels, and found that increased angling (ranging from 0° to 90°, 90° being orthogonal to the build plate) is more likely to remain open at smaller intended channel size. Cotabarren *et al.* [95] mention 0° angles relative to the build plate performed worse for manufacturing open cylindrical channels, and similarly present that smaller pixel size and layer height were the decisive factors in printing smaller diameter cylinders consistently. Lastly, research has indicated that the printing angle may affect the printing accuracy and translucency [96, 97]. As a result the angle of planar devices might be impactful on the resulting channel dimensions.

Varying printer settings and known influential parameters on the dimensional accuracy may help in optimizing vessel and cross sectional shape replication and to establish an optimal workflow for direct printing of small vessel geometry. Accessible desktop SLA 3D printers (mainly consisting of DLP and mSLA) are generally not optimized for printing embedded channels [98]. Ahmed *et al.* [98] mention that deeper embedded channels are more likely to be closed due to residual curing of these channels due to exposure of subsequent layers. It can be theorized using the aforementioned equations that lowering the exposure settings may facilitate deeper embedded channels to remain open. This is important, since studies using mSLA/DLP for microfluidic device fabrication are often still limited in their

resolution. mSLA/DLP achieved the best surface roughness and feature replication compared to FDM and PolyJet printing, but was noted to be limited to producing closed channels of 500 µm in width. By optimizing the printer settings, such as demonstrated by Gong *et al.* [86], reaching smaller features seems possible. Using commercial resins they managed to create rectangular channels measuring approximately 350 µm by 350 µm. A specialized custom resin managed to decrease this number to a width and height of 250 µm. DLP based VPP processes have been used by Xu *et al.* [99] to create embedded channels as small as 10 micrometers in height using an additional build plate. Reaching diameters capable of replicating small vessels therefore seems likely.

Additionally, orientation, layer height, and exposure settings could influence the cross-sectional shape. Cumulative dosage can build up in side channels altering the cross-sectional shape. Similarly, increased layer height can alter the roundness due to increased pixelation of the cross-section when printed at an angle. Finally, the orientation could impact the replication of circular cross-sectional channels, and an interplay with the layer height and exposure time with the orientation may exist. The effect of increased cumulative normalized dose, layer height, and print orientation on the roundness of the cross-section can be studied.

2.7. Research Question

A lack of 3D printed phantoms of smaller cerebral arteries is observed according to the results of the systematic search in Appendix A. 3D printed models of the circle of Willis have been observed, such as the device fabricated by Ariana *et al.* [100], but exclude smaller branches that are more downstream. The smallest arteries in diameter modeled are the optic artery and the anterior and posterior communicating arteries and were specified to be between 0.8-1 mm in diameter. Among the 3D printing approaches, VPP processes (with DLP/mSLA printing in particular) seem to be most optimally suited for the purpose of recreating small cerebral vessels.

In order to fabricate a microfluidic phantom of small vessels additional considerations must be taken into account. Materials must be selected for the intended purpose and be compatible with the printer. Biocompatible and soft materials are preferred due to the possibility of cell-seeding, and a variety of commercially available options exist (tested based on the ISO 10993 standards for biological evaluation of medical devices) [101]. Some concerns exist regarding reaching optimal accuracy using flexible, biocompatible materials [102]. Measuring flow in microfluidic applications can be done a multitude of ways, however, and for various types of fluids, flow conditions, and at different temperatures [103]. The intended flow measurement technique must be accounted for when fabricating this device in order for it to be usable. PIV seems preferable over MRI for in vitro intracranial flow estimations according to Roloff *et al.* [104]. For an accurate quantification of the magnitude of the velocity field, micro PIV is indicated according to Cavaniol *et al.* [103]. Standard measurement methods such as PIV require transparent materials. The phantom will take a wall-less shape due to stability concerns with thin walled designs [105].

The resulting research question for further investigation of these arteries based on the identified gap is formulated as:

> ”How to use mSLA 3D printing for direct printing of a phantom of the lateral lenticulostriate perforating arteries branching off of the circle of Willis?”

This phantom can consequently be used to inform flow models, for the development of artery-on-a-chip, and the development and testing of medical devices and therapeutics. Multiple sub-objectives can be answered to achieve this goal:

- To investigate the effects of the printer settings (exposure time and layer height) and orientation on the printed roundness, error, and area.
- To compare the results of a printed microfluidic device to a computational model.
- To recreate (part of) the circle of Willis with the lenticulostriate arteries.
- To measure the flow in these arteries.

The scope of this research is purposefully limited to flow modeling, since requirements for printing vascular grafts or surgical phantoms may differ or be conflicting. An example is vascular phantoms for the purpose of echo validation, these are more concerned with acoustic impedance of the material than transparency. The sub questions should facilitate the fabrication of circular cross section microfluidic devices resembling small vessels for validating computational flow analysis.

3

Methods

In this chapter a comprehensive overview of the workflow and methodologies used in this study is provided. It starts by discussing the material selection process and the methodology used to optimize the printer settings. This is followed by the CAD designs of the samples containing pores for the optimization tests, the microfluidic devices, and the physiological devices, and an explanation of the slicer settings used to export the CAD into the printer. Next, a description of the experimental setup and experimental flow tests is given. The chapter also covers the data analysis procedures for both the optimization and experimental tests. Finally, we present the analytical and numerical models to compare to the experimental results.

3.1. Materials Selection

A large number of materials and a select number of resin printers were considered for this study and are provided in Appendix B. The material and printer selection is based on the desired goal and is accompanied by considerable interplay. As a result the decision must be made in tandem. For the current study, 3 types of VPP printing were considered. These include LFS (Low Force Stereolithography, a novel form of traditional SLA), mSLA, and DLP printing. 2PP was excluded due to limitations in the print size as a result of the small build plate. Additionally, this type of printing is expensive, which is counter to rapid prototyping and accessibility. Commercially available materials were evaluated on four parameters in the following order of importance; Transparency, Cost, Biocompatibility, and Flexibility. Commercially available printers available within Delft University of Technology were evaluated based in order of importance on the parameters; Pixel size/ Resolution, build plate size, and the wavelength of the emitted light. Material compatibility with the printer must be taken into account and is defined by the wavelength used by the printer and the light intensity (if reported), and the compatibility of the photopolymer for this wavelength and intensity. The penetration depth and critical energy for polymerization of the photopolymer resin were not taken into consideration due to a lack of reporting by most commercial agents.

The results of the printer and material selection are provided in Appendix C. A mSLA machine, the **Elegoo Mars 4 9k**, was selected based on having the smallest pixel size with a sufficiently large build plate. The selected material was the **Liqcreate Bio-Med clear** acrylate based photopolymer resin. The light power of this printer was reported by Elegoo to be approximately 4.0 mW/cm^2 as measured without the vat installed, and similar in UV intensity to the DLP Mars 4 version. The resolution and the build plate size of the printer are provided in Table 3.1. Additionally, the material properties and composition of the Liqcreate Bio-Med clear resin are described in Table 3.1. These were obtained from the material data and safety sheets as provided by Liqcreate [106].

Equipment	Parameters
Elegoo Mars 4 9k (mSLA) [107] 	**X/Y resolution:** 18 µm, **Layer height:** 10 – 200 µm, **UV wavelength:** 405 nm, **Build Platform Size:** 153.36 x 77.76 x 175 mm
Liqcreate Bio-Med clear [108] 	**Density:** 1.18 g/cm^3, **Viscosity:** 475 cps at 25°C, **Critical energy (Ec):** 6.10 mJ/cm^2, **Penetration depth (Dp):** 0.12 mm, **Composition:** *Esterification products of 4,4'-isopropylidenediphenol, ethoxylated and 2-methylprop-2-enoic acid* 85-<100%, *pentaerythritol tetraacrylate* 3-<9%, *Diphenyl(2,4,6-trimethylbenzoyl) phosphine oxide* 0.5-<2%, *cyclohexane* 0.01-<0.1%, *Toluene* 0.01-<0.1%

Table 3.1: Specifications of the Used 3D Printer and Material. The Critical energy (Ec) is the energy required for the photopolymer to solidify. The Penetration depth (Dp) is the depth of penetration of the UV light.

3.2. Printing Process

3.2.1. Settings for the Optimization of Printing Pores

CAD designs containing pores were made to test the influence of the exposure time, orientation, and layer height on the roundness and area. These designs are described in Section 3.3. The orientation, exposure time, and layer heights were varied to find the optimal settings for accurate and replicable prints and to investigate the effect of over- or underexposure in circular cross-sectional channels .

Optimization Tests

Three tests were devised to investigate the influence of the printer settings on the area and roundness. Firstly, prints were conducted to evaluate the effect of the exposure time. The effect of exposure times was evaluated at constant layer height (10 µm) by decreasing the time in steps of 0.5 seconds from a 5 seconds exposure time, which is recommended at 50 µm layer height by the photopolymer manufacturer, until failure to print. The second test intended to evaluate the effect of layer height on the area and roundness. Layer heights of 10 µm, 20 µm, 50 µm, and 100 µm were printed with differing exposure time settings advised by Liqcreate. The exposure time should not be kept constant. It is important to ensure minimal effect of exposure time (to match the dosage for every layer height) for consistent between-group comparison of the layer height samples. Both tests for investigating the layer height and the exposure time include pores printed at varying orientations. These samples containing pores were printed at an angle to the build plate, orthogonal to the build plate, and parallel to the build plate. The last test was done to investigate the effect of orientation on the area and roundness. These samples were printed at constant exposure time (5 seconds) and layer height (50 µm) specifically to test the impact of the angle using the following angles as evaluated from the build plate: 0°, 19.79°. 22.5°, 45°, 67.5°, 70.20°, 90°. These tests are illustrated in Table 3.2. Prints were intended to be replicated at similar exposure times and layer heights 3 times, at an angle, horizontal, and vertical. The orientations of the pores are consequently angled, orthogonal to the build plate, and parallel to the build plate, respec-

Table 3.2: Variables used for investigating the effect of printer settings on the roundness and area of the pores.

Variables for Printing	
Variable	**Value**
Test 1: Orientation	0°, 19.79°, 22.5°, 45°, 67.5°, 70.20°, 90°
Test 2: Exposure time	{5, 4.5, 4, …, 'Failed print'} (s)
Test 3: Layer height	10, 20, 50, 100 (µm)
Orientation of the pores relative to the build plate in test 2 & 3	Parallel, Orthogonal, $\arctan\left(\frac{dy}{dx}\right)$, $90° - \arctan\left(\frac{dy}{dx}\right)$

tively. An additional angle was added to investigate whether the optimal angle for the pore, or the flat surface of the device was more impactful on the pores. The angle was evaluated from the norm of the build plate by the slicer software, instead of from the build plate itself. This study consistently mentions angles as measured from the build plate. Therefore, it must be noted that the optimal channel/pore angle is 90° - arctan($\frac{dy}{dx}$) for channels/pores orthogonal to the largest flat surface, with arctan($\frac{dy}{dx}$) being the optimal print angle for the flat surface of the sample. This is due to the channels being orthogonal to the largest flat surface.

Additional Fixed Parameters

Parameters that were not changed during the printing process are described in Table 3.3. The effects of these printing parameters on print quality or dimensional accuracy have not been extensively researched [92]. As a result these values were kept constant as not to interfere with the variable parameters. The bottom layers and exposure time ensure the print stick to the build plate. Transition layers make a transition from the bottom layers to the print settings in order for the print to stick to the bottom layers and not detach from the build plate due to peeling forces of the printer FEP film. Lift speed and retract speed indicate the movement of speed of the build plate in the printing process and consist of 2 values. Lift speed 1 is the lift speed as the print is still attached to the film. Lift speed 2 is the lift speed as the build plate moves up through the resin. Retract speed 1 is the retract speed as the build plate moves down. Retract speed 2 is the retract speed as the part nears the FEP film. Usually lift and retract distance also consist of two values. Lift 1 distance should be the distance until the print detaches from the FEP film. Lift 2 distance should provide sufficient space for the resin to fill the void. The retract distance should match the lift distances. The effects of these settings are most pronounced in larger prints, where increased peel force and resin displacement may cause the print to detach or surfaces to print with a grainy texture due to fluid movement. In this study, the standard values as provided by the manufacturer were selected and kept constant for the prints as to not confound the results.

Table 3.3: Constants for testing the influence of varying the exposure time, layer height, and orientation on the area and roundness of the pores.

Constants for Printing	
Printer Settings	**Value**
Bottom layers	2
Bottom layer exposure time	50 (s)
Transition Layers	9
Lift speed	90/90 mm/min
Lift distance	6 mm
Retract speed	150/150 mm/min
Retract distance	6 mm
Wait times	0/2/1 (s)

3.3. CAD Designs

All CAD files were prepared using SolidWorks 2023 [109]. Designs were made for for the device containing pores to test printer settings, for a simple microfluidic channel, and for physiological devices.

3.3.1. Pore Design For Process Optimization

Test objects were 5x50x2 millimeter and contained two lines containing 20 cillindrical pores both ranging in intended diameter from 1 to 50 µm, with 50 µm intervals. The diameters of the pores in the CAD design are illustrated in Figure 3.1. Printing pores of similar dimensions twice facilitated investigating within print variations of similar intended diameter holes.

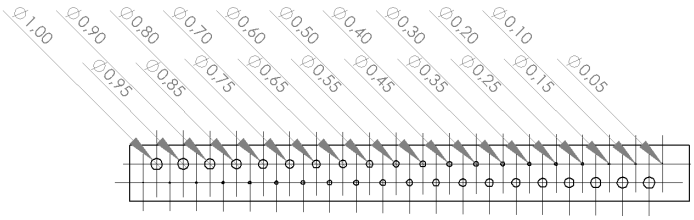

Figure 3.1: A SolidWorks drawing illustrating the CAD design of the test object and the internal channels in millimeters

3.3.2. Channel Design for Flow Test

Several devices were manufactured for performing the flow tests, with settings based on the outcomes of the previous section testing printer optimization. A small device as described in Appendix D was created to test the connectors for the Fluigent tubing and connectors. The dimensions of this small device and the printed connectors are provided in the Appendix. These channels were increased in length to result in 3 microfluidic devices measuring 5 cm in channel length as seen in Figure 3.2. These simple channels varied in intended diameter between 400 µm, 450 µm, and 500 µm. Their length would increase their contribution to the total resistance of the setup when tubing was added, similarly increasing their contribution to measured pressure drops.

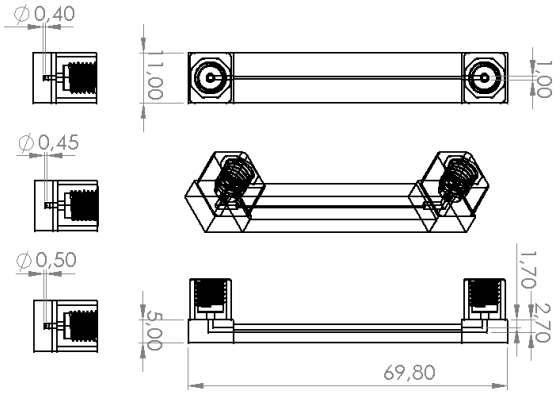

Figure 3.2: Dimensions of the singular channel printed microfluidic devices. The channel with an intended diameter of 450 µm was used for the flow test.

3.3.3. Physiological Devices for Flow Measurement

Two devices mimicking arteries were finally manufactured. The first device, dubbed the **"abstract"** artery did not attempt to mimic existing arteries with a bifurcation. It was printed to see if a bifurcation would cause additional problems. The device and the internal channels are visualized in Figure 3.3. A second and final physiological device was fabricated with the explicit intention of mimicking the lenticulostriate arteries. This device was named the **"physiological device"** and will henceforth be referred to as such. It includes fillets at the interface between the lenticulostriate branches and the M1 segment of the medial cerebral artery to ease the transition and better imitate real arteries. The diameter of the M1 segment was set to be 2.66 mm and the diameter of the two lateral lenticulostriate branches were 0.5 mm. Their respective lengths are 13.88 mm for the M1 segment, 20.4 mm for the straight artery as measured from the center-line of the M1 segment, and 21.34 mm for the curved artery as measured from the center-line of the M1 segment. The dimensions of the device and arterial structure are provided in Figure 3.4.

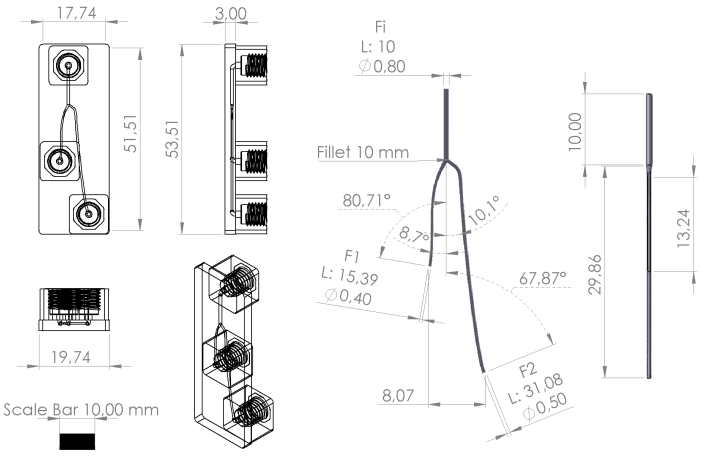

Figure 3.3: Dimensions of the device containing the channels and the geometry of the internal channels of the abstract device. The inlet is labeled as Fi, with the outlets labeled as F1 and F2. The length L of the outlets are given. The fillet used for the bifurcation is similarly provided. Detailed data on the splines used is provided in Appendix D.1.

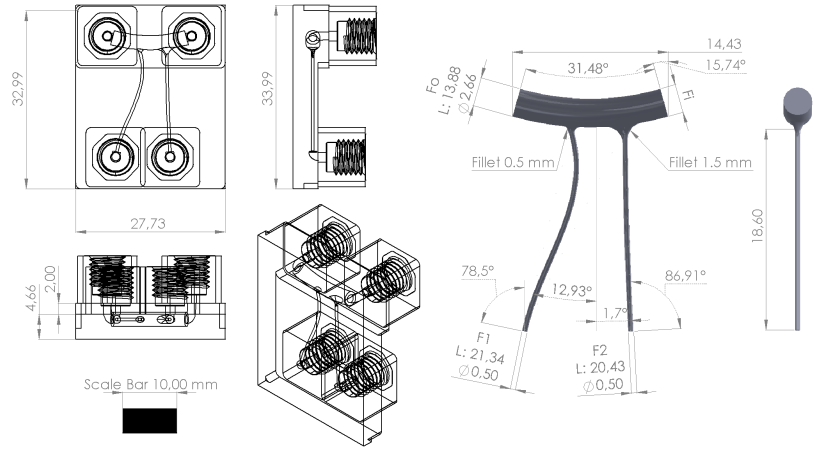

Figure 3.4: Dimensions of the device containing the channels and the geometry of the internal channels of the physiological device. The inlet is labeled as Fi, with the outlets labeled as Fo, F1, and F2. The length L of the outlets are given. The fillet used for the bifurcations are similarly provided. Detailed data on the splines used is provided in Appendix D.2.

3.4. Slicer Input

The export of the CAD design to the printer was done using LycheeSlicer 6 (6.0.200) [110]. The orientations, layer height, exposure times, lift and retract speeds, and fixed additional parameters were manually entered. The orientation of the channels are visualized in Figures 3.5, 3.6, and 3.7. Figure

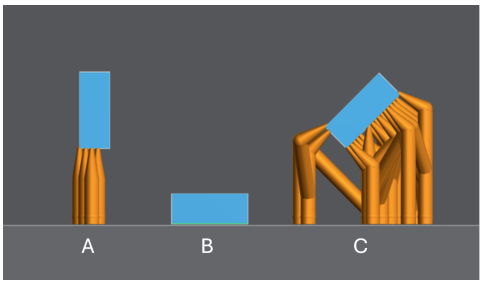

Figure 3.5: The side view of the orientation of the plates with pores in the Lychee slicer. The plates are indicated as the blue structures, and the supports in orange. The supports attach the plates containing the pores to the build plate. A; Pores are parallel to the buildplate. B; Pores are oriented orthogonally to the build plate, and C; pores are angled relative to the buildplate.

3.5 shows the orientation of the test objects containing the pores as printed in different orientations. The orthogonal pores (as seen at B) were printed flat on the build plate without supports, this prevented the buildup of resin on a supported flat surface and increases the likelihood of the print to succeed and to be dimensionally accurate. Both other orientations were printed using supports, colored in orange in the illustration. Figure 3.6 shows the orientation and positioning on the build plate of the samples

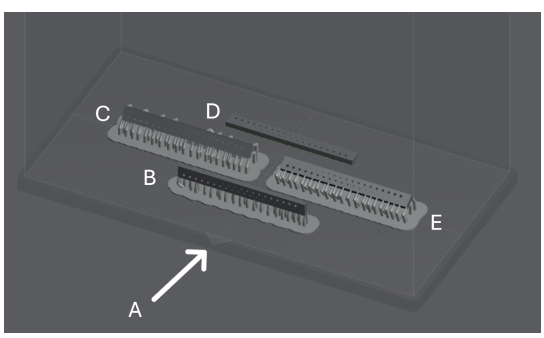

(a)

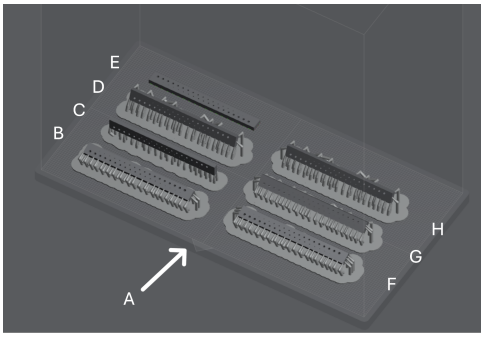

(b)

Figure 3.6: The orientations of the different groups of printed samples for testing the printer settings. (a) The samples as printed for Tests 1 and 2. A; is the build plate, B; consists of pores parallel to the build plate, C; is pores oriented angled (according to the arctan rule) to the build plate, D; are pores orthogonal to the build plate, and E; are pores angled at 90 - arctan. (b) The samples as printed for Test 3. A; is the build plate, B; are pores angled at 90 - arctan, C; consists of pores parallel to the build plate, D; is pores oriented angled (according to the arctan rule) to the build plate, E; are pores orthogonal to the build plate, F; are pores angled at 67.5 degrees, G; are pores angled at 45 degrees, are pores angled at 22.5 degrees.

containing the pores. Part (a) shows the orientation for tests 1 and 2 for the exposure time and the layer height, whereas part (b) shows the orientations of the samples for test 3 to investigate the effect of angling the samples. Figure 3.7 shows the orientations and positioning of the microfluidic and physiological devices. When printing the physiological devices, the optimal angles of the channels no longer conflict with the optimal angle of the surface of the device containing the channels.

3.5. Post-Processing

The prints were sprayed using Isopropyl alcohol after being removed from the build plate and consequently washed using an ultrasound cleaner in Isopropyl alcohol two times for three minutes as recommended for the Bio-Med material by Liqcreate. Pressurized air was applied between the two washes using a Hyundai Super Silent compressor of 30 Liters and 8 bar. After the washes, supports were removed using a scalpel, metal saw, and cutting pliers. A luerlock syringe was applied to a designed connector (as visualized in Appendix D) made from the same Liqcreate material to be able to clean longer channels with screw connectors by applying manually pressurized isopropyl alcohol, water, and

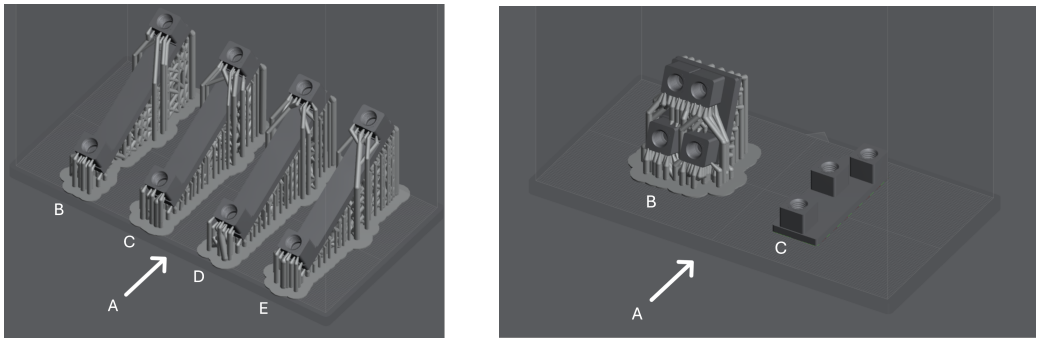

(a) (b)

Figure 3.7: The orientation of the printed channels. (a) The microfluidic channels. A; Is the build plate, B; the microfluidic channel with 350 µm internal diameter, C; the microfluidic channel with 400 µm internal diameter, D; the microfluidic channel with 450 µm internal diameter, E; the microfluidic channel with 500 µm internal diameter. (b) The physiological and abstract microfluidic devices. A; is the build plate, B; is the physiological device, C; is the abstract device.

air. Curing of the prints was done using a FormLabs Form cure for 30 minutes at 60 °C. In order to decrease the diffuse reflection caused by surface irregularities and to test the material suitability for µOCT, a varnish coating was applied after sanding using p600 and p320 sandpaper, and a cork sanding block. A detailed description of the printing and post-processing protocol is provided in Appendix E.

3.6. Imaging

Images of the channels were made using a Keyence Digital Microscope VHX-6000, and VHX-6000 communication software [111], and were measured using Fiji (ImageJ) [112].

3.6.1. Imaging of the Pores

Every Image was taken using a standard 20x-200x zoom lens at 150x magnification and full ring lighting to facilitate detailed depth-composite images of the pores using 2 separate image captures per sample. This resulted in single images of half a test sample measuring approximately 4000x17000 pixels, which translates to every full test sample having been imaged at 4000x34000 pixels or 1.25-1.47 µm pixel size.

3.6.2. Imaging of the Channels

The channels and microfluidic devices were visualized both completely using stitched images and inspected for artifacts. Measurements of channel diameter was done by utilizing the parallel lines function in the VHX-6000 communication software for straight channels, and 2-point distance measurement for curved channels. Every Image was taken using a standard 20x-200x zoom lens at varying magnification levels.

3.7. Flow Testing of the Channels

3.7.1. Experimental Setup

A Fluigent microfluidic setup was used for experimental flow testing, consisting of a microfluidic low pressure generator (FLPG plus SMF), LineUP FlowEZ microfluidic flow controller (2 bar unit), LineUP LINK to connect to the OXYGEN software, 4 FLow Unit L+, 1 PRESSURE UNIT Inline pressure sensor (1000 mbar), and CTQ-KIT-HQ+ tubing [113]. All tests were done with water. Connectors were printed to fit the connectors of the Fluigent CTQ-KIT-HQ+ tubes and fittings. These consist of HQ Flow Unit Connectors (1/4-28 Flat-Bottom for 1/16 inch outer diameter tubing), Ferrules for the HQ Flow Unit Connectors, and (Fluorinated Ethylene Propylene) FEP tubing measuring 1/16 inch in outer diameter, and 254µm in internal radius. The experimental setup was used to measure flow and/or pressure in the printed microfluidic devices and is broadly visualized in Figure 3.8. The FlowEZ microfluidic flow controller (B in Figure 3.8) was connected to the microfluidic low pressure generator, the LineUP link to connect to the computer, the reservoir, and to the flow sensor to obtain feedback. The microfluidic

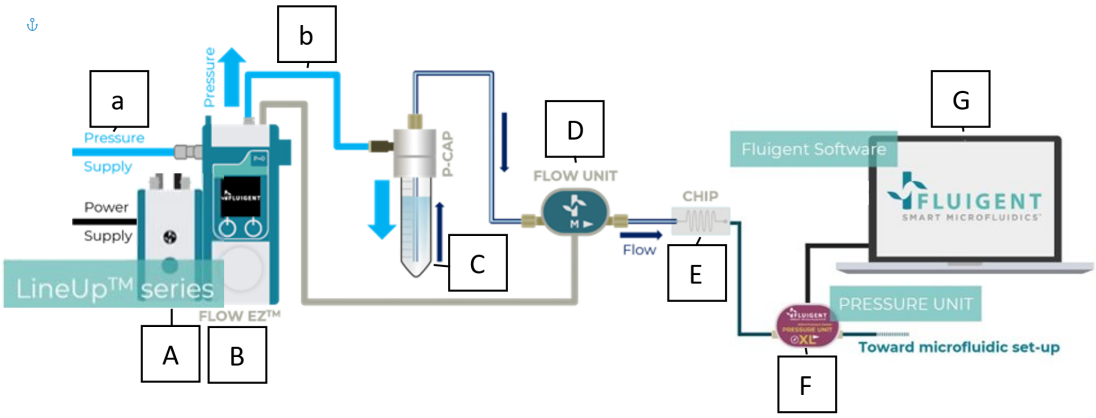

Figure 3.8: A schematic representation of the pressure driven microfluidic setup with the included materials for testing a simple microfluidic device. [a] A 6 mm outer diameter, 4 mm inner diameter hard polyurethane cable connecting the pressure source to the FLOW EZ component [b] A 4 mm outer diameter, 2.5 mm inner diameter polyurethane pneumatic tube. [A] Microfluidic software control [B] Microfluidic flow controller [C] P-CAP microfluidic reservoir [D] Inline Flow unit (1400 µm internal diameter) [E] Microfluidic device [F] Inline pressure unit (500 µm internal diameter) [G] OXYGEN software connected to the LineUp series and inline pressure unit.

devices were connected to the fluigent setup using printed connectors as described in Appendix D.

In total 4 tests were done. One control test to investigate the agreement between the analytical, computational, and experimental approaches. A second test to investigate the agreement between the printed microfluidic channel and the analytical and computational results of the intended channel dimensions. Lastly, two flow tests were conducted to showcase the ability to print microfluidic channels resembling small vessels.

3.7.2. Measurement Approach

Control Test

Firstly, a control test was performed to investigate the hydraulic resistance of a tube of known length and diameter. The tube was 508 µm in diameter and measured 20.5 cm in length. The setup as seen in Figure 3.8 was used excluding the microfluidic device between the pressure and flow sensors. The setup is schematically illustrated in Figure 3.9. The measurements of the individual parts is provided in Table 3.4. A constant pressure was applied using the LineUP FlowEZ microfluidic flow controller and the flow rate and pressures were consequently measured. The pressure and flow sensors were swapped to keep the total resistance constant and to be able to measure the pressure before and after the tube to calculate the hydraulic resistance at a constant flow rate. The pressure at the inlet was varied. For the testing the experimental setup the pressure at the inlet varied between, 100 mbar, 300 mbar, 500 mbar, 1000 mbar as applied at the LineUP FlowEZ microfluidic flow controller.

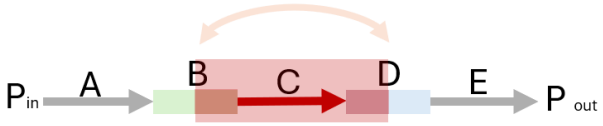

Figure 3.9: The experimental setup of the control test.P_{in}; The pressure coming from the pressurized vial. P_{out}; The vial collecting the water at atmospheric pressure. A; Tube to flow sensor, B; Flow sensor, C; Tube to pressure sensor for hydraulic resistance measurement, D; Pressure sensor, E; Tube to outlet. The shaded area in red is the section over which the pressure drop is measured.

Table 3.4: System parts and dimensions

Part	Name	⌀ (µm)	L (cm)
A	Tube	508	49.5
B	Flow Sensor	1400	5
C	Tube	508	20.5
D	Pressure sensor	500	5
E	Tube	508	10
F	Tube	508	20
G	Microfluidic channel	450	5
H	Abstract device	Fig 3.3	Fig 3.3
I	Physiological device	Fig 3.4	Fig 3.4

Microfluidic Channel

In the second test, the microfluidic channel of 450 µm in diameter measuring 5 cm in length was added to the setup so it perfectly resembled Figure 3.8. The setup is schematically illustrated in Figure 3.10 with the dimensions presented in Table 3.4. Again, a constant pressure was applied using the LineUP FlowEZ microfluidic flow controller and the flow rate and pressure at the pressure sensor were consequently measured. The pressure sensor and flow sensor were swapped to obtain the pressure before and after the microfluidic device. In this way, the hydraulic resistance could be measured over the device, the tubes connecting the device to the flow and pressure sensors, and half of the sensors themselves. The microfluidic device was tested using 50 mbar, 100 mbar, 300 mbar, 500 mbar, 1000 mbar pressures as applied by the LineUP FlowEZ.

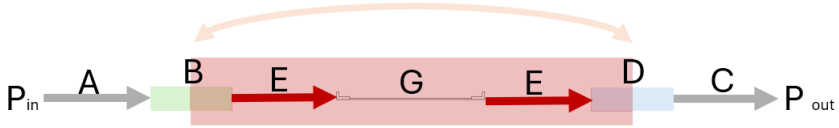

Figure 3.10: The experimental setup of the control test. P_{in}; The pressure coming from the pressurized vial. P_{out}; The vial collecting the water at atmospheric pressure. A; Tube to flow sensor, B; Flow sensor, C; Tube to outlet, D; Pressure sensor, E; Tubes to and from the device, G; The microfluidic device. The shaded area in red is the section over which the pressure drop is measured.

Physiological and Abstract Devices

The last two tests pertained to flow tests performed on both microfluidic devices representing physiological channels. Schematic representations are provided in Figures 3.11 and 3.12, with the dimensions presented in Table 3.4. The flow was measured only using 300 mbar inlet pressure as applied by the microfluidic flow control unit. The pressure value at the inlet was not selected to imitate the pressure found in small arteries, but instead to increase differences in flow between the outlets to find discrepancies. This is likely to increase the difference in flow between outlets to be larger than the limit in sensitivity of the flow measurement device for water (50 µl/min for flow smaller than 1 ml/min). The "abstract" device had 1 inlet and 2 outlets. The "Physiological" device contained one inlet and 3 outlets.

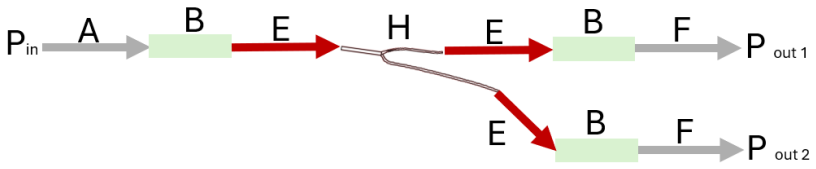

Figure 3.11: P_{in}; The pressure (300 mbar) coming from the pressurized vial.$P_{out\ 1}$; The vial collecting the water at atmospheric pressure at outlet 1. $P_{out\ 2}$; The vial collecting the water at atmospheric pressure at outlet 2. A; Tube from inlet to flow sensor, B; Flow sensors, E; Tubes connecting flow sensors to the abstract device, F; Tubes from flow sensors to the outlet, H; Abstract device.

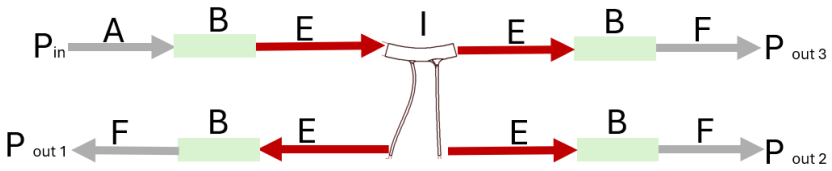

Figure 3.12: P_{in}; The pressure (300 mbar) coming from the pressurized vial. $P_{out\,1}$; The vial collecting the water at atmospheric pressure at outlet 1. $P_{out\,2}$; The vial collecting the water at atmospheric pressure at outlet 2. $P_{out\,3}$; The vial collecting the water at atmospheric pressure at outlet 3. A; Tube from inlet to flow sensor, B; Flow sensors, E; Tubes connecting flow sensors to the physiological device, F; Tubes from flow sensors to the outlets, I; Physiological device.

3.8. Data Analysis

3.8.1. Area and Roundness of the Pores

Ovals were fitted to the pores in ImageJ (Fiji) [114]. Ovals were selected over ellipses, since ovals do not have the restriction to be symmetrical in all axes. The measurements of the captured image and the pixels were obtained from the high resolution 2D images and extracted to compute a pixel to mm conversion factor for every image separately. The perimeter, area, major and minor diameter of the fitted ovals are extracted using ImageJ. ImageJ uses Ramanujans approximation to obtain the perimeter from the fitted ovals. The pixel values of the extracted values were then converted to millimeters.

The unitless parameter resembling roundness was calculated using the perimeter and Equation 3.1. The roundness is different from the circularity, in that it quantifies the overlap with a circle, instead of giving an indication about the smoothness of the surface. This is desirable since the fitted ovals have smooth edges. As a result, investigating the circularity is not informative.It is known that arterial cross-sections are not perfectly round [115]. Studies on the cross-sectional roundness are scarce and the target roundness is therefore determined to be a roundness of one. This is a perfect circle. The Normalized Error of the area to the intended area was calculated using 3.2. In this equation A stands for the area.

$$\text{Roundness} = \frac{\text{Perimeter}^2}{4\pi \cdot \text{Area}} \tag{3.1}$$

$$\text{Normalized Error Area} = \frac{A - A_{\text{Intended}}}{A_{\text{Intended}}} \tag{3.2}$$

Exposure Time, Layer Height, and Orientation Graphs

Data on the roundness and normalized error of the area were pooled for pores of samples printed with similar settings (exposure time, layer height and orientation). The assumption is that the roundness and the normalized error of the area do not depend on the size (defined as the area) of the channel. The truthfulness of this assumption was investigated by grouping all the areas with the same intended area together, and by performing a Kruskal-Wallis test meant to assess the difference in roundness and area for intended pore sizes (this statistical test was chosen based on the results of a Shapiro-Wilks testing for their normality). The values for the roundness and the mean normalized error of the area were then plotted for the three tests using the matplot library in Python [116, 117].

3.8.2. Error Estimation

Several types of error are present in doing these measurements. Measurement error is introduced by obtaining the area and perimeter using pixelated ovals in Fiji (ImageJ). Additionally, three types of error can be expected in this analysis. These are variations within the expected dimensions due to printer inaccuracy or precision, Intra-operator error, and inter-operator error. Samples at every orientation will be measured twice by two independent researchers, and the error will be quantified as the absolute normalized relative difference and the non-absolute normalized relative difference. By measuring each channel twice, the within print variability is kept constant. For the area and the roundness, the values of the intra-operator error are defined as the absolute normalized relative difference are calculated as seen in Equation 3.3 since no directionality in bias is expected. In this equation X_n is the measured value, X_{mean} is the mean of the measured values, and ΔX_{rel} normalized relative difference between the measured values. The absolute normalized relative difference is used in order to be able to compare

differences in channels of varying diameter. The error is then the averaged value of all the calculated relative difference values of the intra-, and inter-operator error.

$$|\Delta X_{\text{rel}}| = \frac{|X_1 - X_2|}{X_{\text{mean}}} \tag{3.3}$$

Both researchers measured the same channel twice to research the intra-operator error. The inter-operator difference is computed by using the means of the found values of the two channel measurements by both researchers as illustrated by Equation 3.4 and Equation 3.5. Equation 3.5 shows two methods for calculating the normalized relative error. Since operators may have a systemic bias, both approaches will be computed for the inter-operator error. The normalized inter-operator difference was computed using the intended are as seen in Equation 3.6. No absolute values were used, since directionality and consistent errors may be observed. Bland-Altman plots are provided of all three errors to facilitate qualitative assessment of bias. For the inter-operator error both the absolute value and non-absolute value of the normalized relative difference are investigated.

$$X_{\text{Mean}} = \frac{X_1 + X_2}{2} \tag{3.4}$$

$$|\Delta X_{\text{Interoperator Difference}}| = |X_{\text{Mean 1}} - X_{\text{Mean 2}}| \quad \text{or} \quad \Delta X_{\text{Interoperator Difference}} = X_{\text{Mean 1}} - X_{\text{Mean 2}} \tag{3.5}$$

$$\text{Normalized Difference} = \frac{\Delta X_{\text{Interoperator Difference}}}{\frac{X_{\text{Mean 1}} + X_{\text{Mean 2}}}{2}} \tag{3.6}$$

3.8.3. Analysis of Experimental Flow and Pressure Data

The pressure drops for their respective flows measured in the experimental test, analytical calculations, and numerical model for the test of the experimental setup and the microfluidic device are compared for the control test and the microfluidic channel. The flows as measured in the experimental tests have been averaged over time and used as input for the analytical and numerical models. Flow measurements are provided for the physiological devices to showcase the functionality.

3.9. Analytical and Computational Analyses

Results of the experimental setup were compared to computational and analytical simulations. Analytical calculations were used in combination with computational methods to compare the resistance in the control test, and for the resistance of the straight microfluidic channel. This culminated in analytical results being employed twice for comparison between methods. The segments over which the resistance was calculated are schematically illustrated in Figure 3.13. In A the control test is schematically visualized, whereas in B the channel calculations is shown. These areas correspond to the areas over which the resistance was measured experimentally in Figures 3.9 and 3.10 respectively.

3.9.1. Analytical Approach

Hagen-Poisseuille for Hydraulic Resistance

Analytical calculations were done as described by [118] using the Hagen–Poiseuille equation. An electronic-hydraulic analogy was used for resistances lined up in series, where their resistances were combined for the total resistance of the channel. The flow measurements were used in combination with the calculated resistance of the channel to determine the expected pressure drop. The experimentally measured flow rates were used with ta calculated resistance to obtain the pressure drop. The resistance was calculated as seen in Equation 3.7. In this equation η is the viscosity of water (0.001 Pa·s), L the channel length, and r the radius in meters. The pressure drop was calculated by multiplying the flow rate with the calculated resistance. The flow rates used for the equivalent applied pressures in the experimental test are provided in Table 3.5.

$$R = \frac{8\eta L}{\pi r^4} \tag{3.7}$$

To make sure the flow was laminar, the Reynolds number was calculated for every segment in the system using Equation 3.8. In this equation ρ is the density of water (1000 kg/m³), and u the speed in

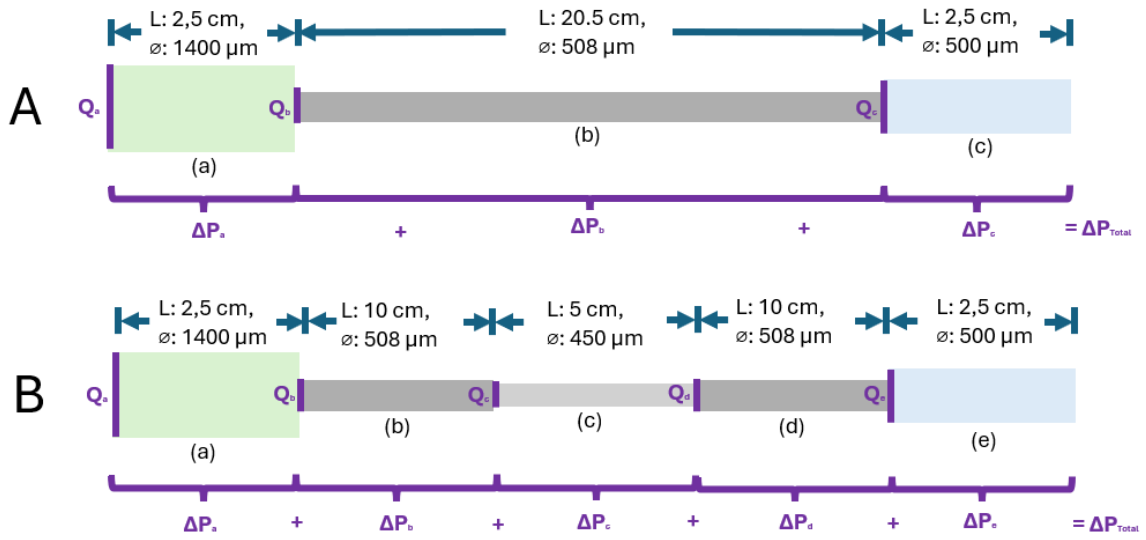

Figure 3.13: A: The control test model. The segments consisted of: (a) The flow measurement device. (b) The tubing. (c) The pressure measurement device. B: The channel test model. The segments consisted of: (a) The flow measurement device. (b) The tubing. (c) The microfluidc device. (d) The tubing. (e) The pressure measurement device. Q_n represents the applied flow rate at every segment, ΔP_n represents the calculated pressure drop. ΔP_{Total} is the total pressure drop after adding the calculated pressure drop for every segment.

Table 3.5: Flow rates used for both the control test and the channel test to calculate the pressure drop matched for the equivalent pressure applied in the experimental test.

Pi Experimental test (mbar)	A: Q Control test (ml/min)	B: Q Channel test (ml/min)
50	–	0.35
100	1.21	0.79
300	3.59	2.47
500	5.72	4.08
1000	10.41	7.66

m/s of the fluid. This did not capture the effects caused by curvature of the tubes as the Deans number would.

$$Re = \frac{\rho u L}{\eta} \tag{3.8}$$

This was done both for the control test, including half of the resistance of the inline flow and pressure sensors and the tube itself, and for the simple microfluidic channel.

Assumptions

The flow was assumed to be laminar and steady, and the fluid was assumed to be incompressible and Newtonian in a uniform circular cross-sectional channel. In addition, there was assumed to be single phase fully developed flow, no wall-slip, and negligible effect of gravity or body forces.

3.9.2. Computational Analysis

Two axisymmetric two-dimensional computational models were constructed in COMSOL® (version 6.2) [119]. The first imitated the control test and was compared to the experimental and analytical results. The second model was used to compare to the experimental and analytical results of the microfluidic device flow test.

Physics and Solver Setup

The COMSOL® model wizard was used to create two two-dimensional axisymmetric single-phase laminar fluid flow models. Navier-Stokes momentum and continuity equations for steady-state incompressible flow were used in these models to solve for velocity u, v, and w, and pressure p. The P1-P1 velocity-preserving scheme was used, where both velocity and pressure fields were discretized using first-order Lagrange elements. This is suitable for capturing the main flow components while limiting computational complexity. A direct stationary solver (PARDISO) was automatically applied for all models and the relative tolerance was automatically set to 0.001.

Geometry

The geometry replicated in the computational models, as constructed in COMSOL®, are schematically visualized in Figure 3.14. A is the geometry used as used in the computational model of the control test, and B is the geometry used in the computational model of the channel test. The axis of symmetry, or the centerline of the channels, is illustrated in line z. These models matched the analytical model in geometry, and the region of pressure drop measurement in the experimental setup. The lengths, diameters and radii are provided in the figures.

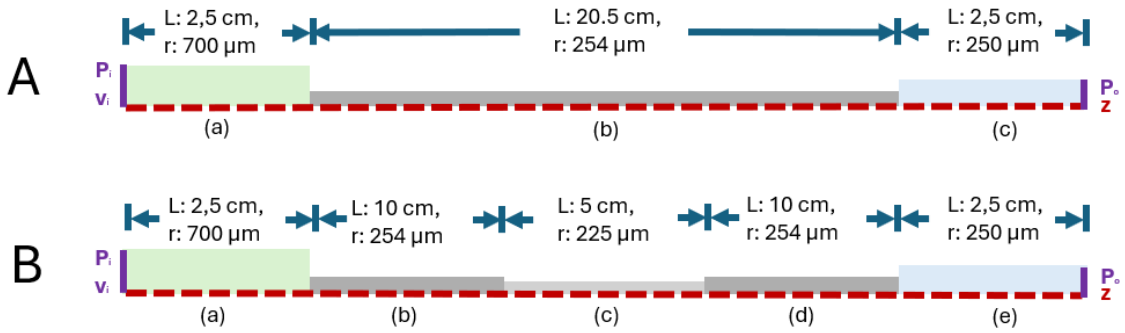

Figure 3.14: The axis of symmetry "z" is provided, with r being the radius of the segments. P_i represents the boundary probe for the pressure measurement inlet. v_i is the applied velocity. P_o represents the boundary probe for the pressure measurement at the outlet. A: The control test model. The segments consisted of: (a) The flow measurement device. (b) The tubing. (c) The pressure measurement device. B: The channel test model. The segments consisted of: (a) The flow measurement device. (b) The tubing. (c) The microfluidic device as seen in Section 3.3.2. (d) The tubing. (e) The pressure measurement device.

Mesh

A free triangular mesh was constructed for both tests. A mesh sensitivity analysis was performed by increasing the number of elements and recording changes in the pressure drop. A mesh was selected once the change in pressure drop relative to the previous iteration was < 1%. The results of the mesh sensitivity analysis are provided in Appendix F. The final meshes are described in Table 3.6.

Table 3.6: Mesh description for both the control test and the channel test.

Mesh Description	A: Control Test	B: Channel Test
Status	Complete mesh	Complete mesh
Mesh vertices	89,679	26,199
Triangles	164,261	44,267
Number of elements	164,261	44,267
Minimum element quality	0.5501	0.5514
Average element quality	0.937	0.8994
Element area ratio	0.0057043	0.0014608
Mesh area	7.582 $\times 10^{-5}$ m²	8.58 $\times 10^{-5}$ m²

Boundary Conditions & Initial values

The initial velocity field and pressure were set to zero. The observed flow in the experimental test was applied in both tests at the inlet as fully developed. The measured flow rate was converted to a velocity using the reported dimensions of the flow measurement device and applied. COMSOL® automatically sets the reference pressure to 1 atmosphere, so the pressure at the outlet was set to zero gauge pressure to effectively obtain atmospheric pressure.The density and dynamic viscosity of water were manually entered as 1000 kg/m^3, and 0.001 Pa·s respectively. The temperature was set to be 293.15 Kelvin, matching room temperature. A no-slip condition was applied at the walls. The velocities of the fluid applied at the inlet boundary are supplied in Table 3.7. The pressure drop was consequently measured using a boundary probe at the inlet and the outlet for the pressures.

Table 3.7: Velocity data used for both the control test and the channel test to calculate the pressure drop matched for the equivalent pressure applied in the experimental test.

P_i Experimental test (mbar)	A: v Control test (m/s)	B: v Channel test (m/s)
50	–	0.004
100	0.01	0.01
300	0.04	0.03
500	0.06	0.04
1000	0.11	0.08

Assumptions

The assumptions of this COMSOL® model are similar to those of the analytical calculations. Radial and axial differences along the model can be captured unlike in the analytical model. This model can in principle also account for developing flow and entrance effects, time-dependent behavior, and inertial terms for turbulent flows. However, the setup used in this study remained limited to fully developed steady-state and laminar flow.

4

Results and Discussion

In this chapter the smallest printed pore, the results of the optimization test, the observed errors in the printing process, the printed microfluidic devices, and the results of the experimental flow tests compared to the analytical and computational solutions are provided and discussed.

4.1. Printer and material assessment

4.1.1. Photopolymer light interaction

Using the provided information on the UV intensity and penetration depth of the printer and resin as provided in Section 3.1 respectively it is possible to model the curing depth and expected normalized cumulative dose for channels printed parallel to the build plate or at an angle using Equations 2.2 and 2.3 from Section 2.6. This can inform on the minimum expected channel size that will remain open after printing and possible alterations to the cross sectional shape due to overcuring. Earlier research indicates that the minimum flow channel height for a particular resin is typically between 3.5–5.5 times the penetration depth and 4 pixels in the width plane [86]. Using the penetration depth of 0.12 mm as provided by Liqcreate and the 18 µm pixel width, the expected minimum channel height would range between 420 and 660 µm and the minimum channel width would be 72 µm. The minimum channel width was not tested in this study. The depth was just above the required minimum channel diameter of 400 µm. However, experimental results with different resins by the same authors has shown the channel height can be as low as 2.3 times the penetration depth, which would be sufficiently low to recreate small vessels with the equipment used in this study [120]. Additionally, curing resin using cumulative dosing inside the channel could decrease the channel height in a controlled matter, potentially at the cost of roundness. This means modeling a larger channel and decreasing its internal diameter through the cumulative dosing effect.

The cumulative dose has been simulated for the Liqcreate Bio-Med clear material and Elegoo mars 4 9k printer with variations in the exposure time and layer height as explained in Section 3.2.1 in Figure 4.1. This simulation shows that a 500 µm diameter channel in a 5 mm thick device starting at 3 mm as measured with the build plate being the start (0 mm) will always have an area under the polymerization threshold. Therefore, the hypothesis is that the channels should stay open and that if resin is trapped in the channel, it will not all solidify and block the channel. In (a) the cumulative normalized dose of different layer heights with varying exposure times are compared. While the advised exposure times were used, it can be seen that the cumulative dose does not stay uniform and that the larger layer heights receive comparatively less dosage. Figure 4.1 (b) shows the printed exposure times for the constant layer height samples. As expected the cumulative normalized dose increases for longer exposure times. It is noteworthy that the shortest exposure time still reaches a cumulative dose 15 times larger than required for polymerization. This is the result of the smaller layer heights requiring more frequent exposure to the UV light for every new layer to cure, increasing the cumulative dose due to the penetration depth being larger than one single layer height. Furthermore, the cumulative dose of higher exposure times passes the polymerization threshold at a lower depth. This shows that increased exposure times should produce smaller channels, at least in the direction orthogonal to the LCD pro-

jecting the UV light. The Curing depth for the exposure times used in this study is visualized in Figure

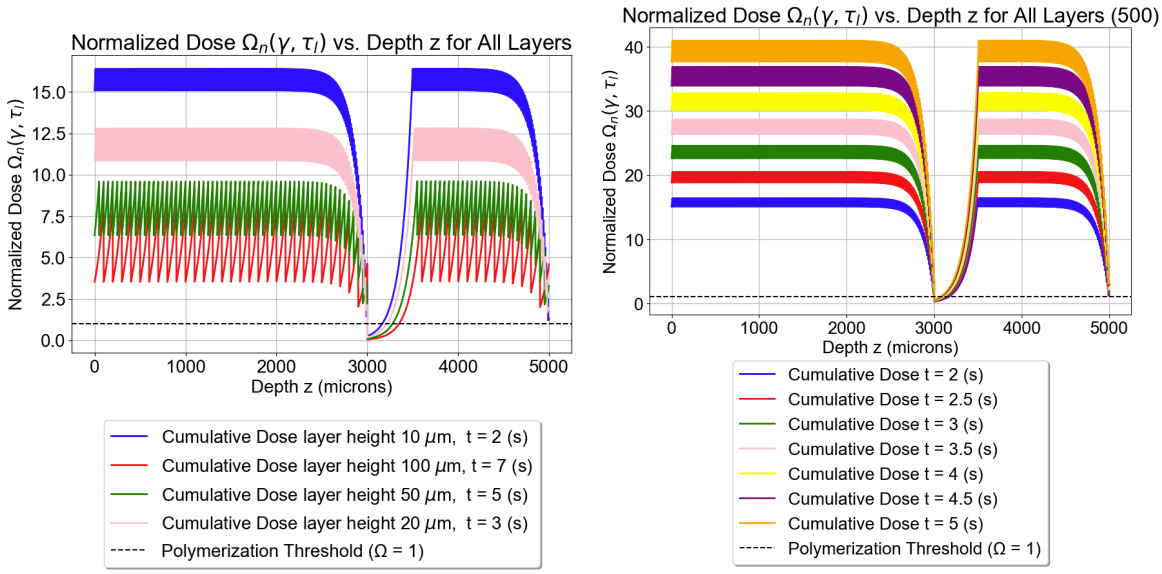

(a) (b)

Figure 4.1: (a) The cumulative dose of a simulated 500 µm channel embedded at 3 mm in a 5 mm sample with varying layer height and exposure times as recommended by the resin manufacturer. It can be observed that the cumulative dose for increasing layer heights decreases, this is in accordance with the proportion of the curing depth to the layer height. (b) The cumulative dose of a simulated 500 µm channel embedded at 3 mm in a 5 mm sample with varying exposure time and constant layer height (10 µm).

4.2. The curing depth is illustrative of the layer depth that will polymerize using this exposure time. Figure 4.2 shows that exposure times below 1.525 seconds will not cure any amount of photopolymer using this 3D printing machine and photopolymer. Using 2 seconds of exposure time is capable of solidifying a layer of approximately 33 µm. The values of the curing depth for the exposure time do not change with increasing layer height, but rather is indicative of the maximum printable layer height using that exposure time. Figure 4.2 is related to Figure 4.1 in that curing depth and layer height both contribute to the cumulative normalized dose. Increasing curing depth by lengthening the exposure time can still be related to lower cumulative normalized dose at higher layer height as a result of less frequent illumination of the photopolymer.

Finally, the orientation may increase the channel depth relative to the LCD. Figure 4.3 (a) shows a parallel channel of 500 µm diameter. The increase in depth relative to the LCD amounts to approximately 1461.90 µm when angling this channel at 70 degrees (as visualized in (b). Since the cumulative dose will be the same for both channels (curing the resin to a similar depth), the relative error is likely

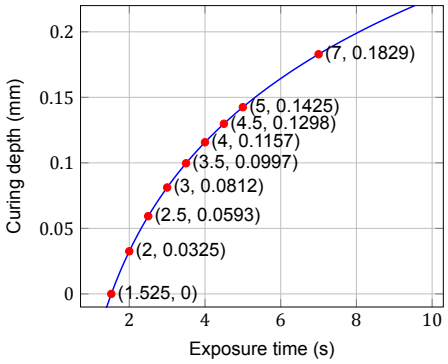

Figure 4.2: Graph representing the curing depth versus the exposure time for all exposure times used in the pore tests performed in this study.

smaller in the angled channel. In Figures 4.4 (a) and (b) the approximation of the cross-section for such a parallel and angled channel are illustrated at 100 µm layer height using the pixel width of the Elegoo Mars 4 9k. A channel orthogonal to the LCD will have the largest depth and is least affected by cumulative dosage curing resin in the channel lumen. The effect of pixelation using large layer height is simultaneously illustrated in Figure 4.4. Using the angle and the normalized cumulative dose we can predict the shape and size of the channel. Figure 4.5 shows in red the approximate area that would polymerize in the channel due to the cumulative dosage inside the channel altering the final cross-sectional shape in green. Printing at a large angle additionally reduces the negative effect of a large layer height on the cross-sectional roundness of the channel. This is best observed when looking at Figures 4.4 (a) and 4.5 (b). Both channels use the same settings, but the channel in Figure 4.5 (b) was modeled at 70 degrees. Figure 4.6 shows in (a) the channel size printed at an angle versus (b) horizontally. The angle is therefore theorized to impact both the channel size and cross-sectional shape.

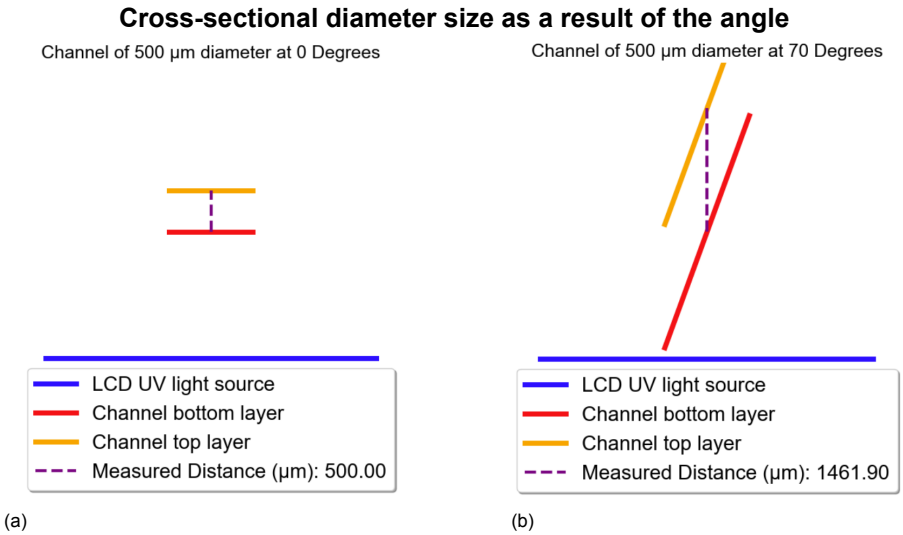

Figure 4.3: A visualization of the increase in depth of the channel as seen from the LCD oriented (a) parallel to the build plate, and (b) angled to the build plate. The depth increases at larger angles and channels oriented orthogonally to the build plate (90 degree angle) will have the largest distance.

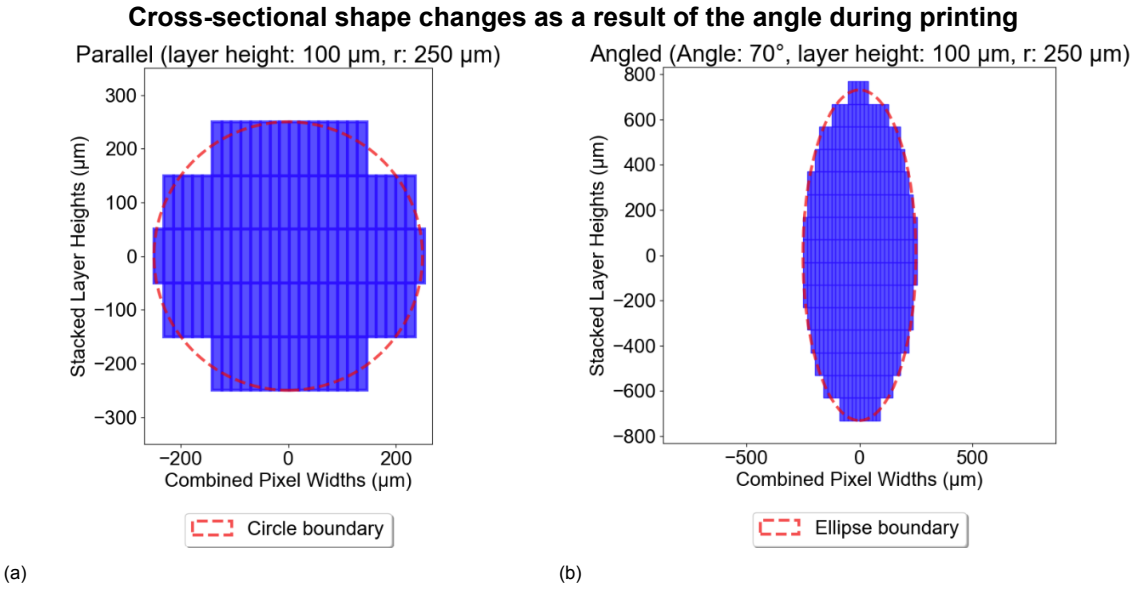

Figure 4.4: A visualization of the cross-sectional changes of the channel of 500 µm diameter when oriented (a) parallel to the build plate, and (b) angled to the build plate. The layer height in this example is 100 µm with a pixel width of 18 µm. These images are related to Figure 4.3

Figure 4.5: A visualization of the cross-sectional changes of the channel of 500 µm diameter due to overcuring at (a) a 70 degree angled orientation, and (b) when observed as the final printed channel placed at 0 degrees. The layer height in this example is 100 µm with a pixel width of 18 µm and an exposure time of 7 seconds.

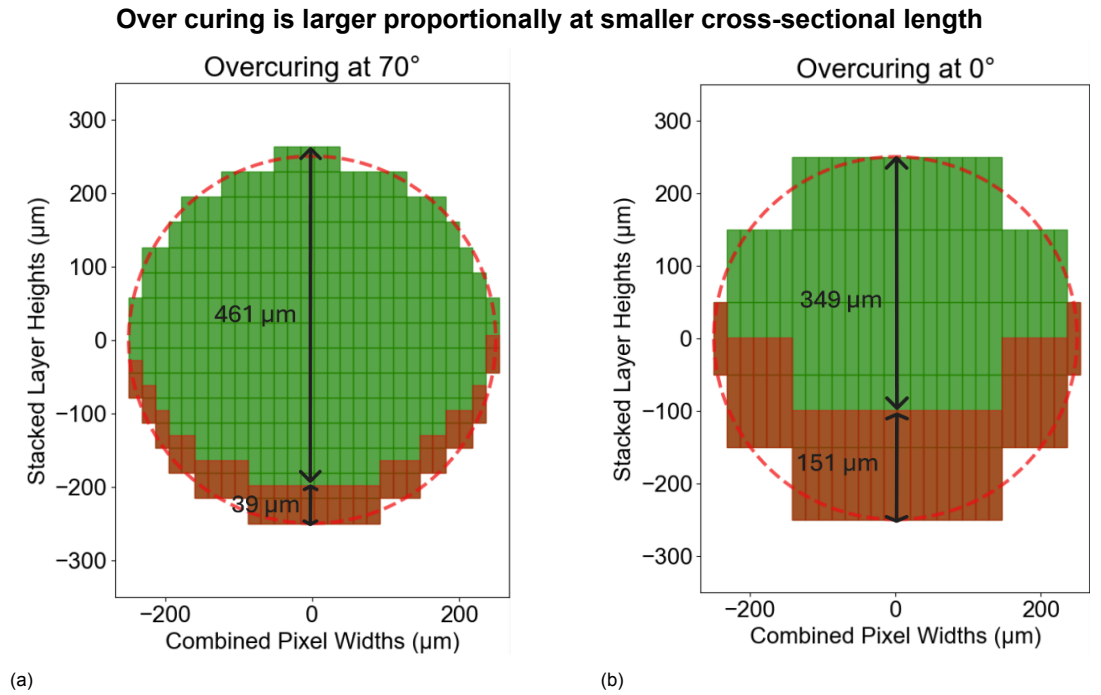

Figure 4.6: A visualization of the cross-sectional changes of the channel due to overcuring at (a) a 70 degree angled orientation, and (b) compared to a channel printed parallel to the LCD at the same settings. The layer height in this example is 100 µm with a pixel width of 18 µm and an exposure time of 7 seconds.

Limitations to the choice of photopolymer and 3D printer affect the ability to replicate small vessels. One such limitation in this study is the use of a rigid material. However, the compliance of small vessels is likely to be small (about 2% of vessel radius) and rigid materials may better capture diseased vessel behaviour [121, 122]. Liqcreate Bio-med clear has a relatively low penetration depth which is good for microfluidics, and has recently been used in microfluidic applications [123]. However, microfluidics specific materials are sold that may have improved performance and materials can be developed if the goal is to create small channels [86].

The machine as presented has been used previously for manufacturing microfluidic devices [124, 123], however lower wavelength mSLA printers may be preferred in order to decrease the penetration depth of the UV light. A yellowish discoloration is caused by using a longer (405 nm) wavelength [125]. Using a shorter wavelength is therefore beneficial to the penetration depth and discoloration. It follows that DLP based printers for microfluidic specific applications exist, however these do not seem to have large advantages to more accessible machines apart from a 385 nm wavelength [126]. Finally, the curing station illuminated the object from the outside, meaning that the inside may not experience the same level of illumination. This can cause stress [127]. Larger layer heights are more prone to shape distortion due to such stresses, and attention must be paid to curing the inside of the channel to ensure biocompatibility of photopolymer resins when applicable.

This study used a simple commercial printer and photopolymer resin, strategies in the literature are described to improve the printing of microfluidics using mSLA. Recently, a study was published by Zhang *et al.* [123] who have developed a platform for compensating the effects of overcuring to fabricate the desired channel. It is noteworthy that this study used both the same printer and material as used in this study, ensuring that the implementation is likely feasible and reinforcing the suitability of the material and printer selection for the intended purpose of microfluidic device design using mSLA. Their approach mostly targets printing rectangular cross-sectional devices. For direct printing of circular channels not all strategies to reduce the cumulative dose are effective. One such example is given by Xu *et al.* [99], who use a second build plate to stop incoming dose into the channel. For circular cross-sections, dosage would accumulate as the channel closes since closure happens per pixel instead of in one layer. Machine learning was applied for increasing accuracy for microfluidic applications by Wang *et al.* [128], They achieved 20 µm feature sizes using this approach. This may be a useful addition to general compensation for fabricating fully three-dimensional structures that adhere as optimally as possible to the intended feature size. A dosing and zoning strategy for improved accuracy was developed by Luo *et al.* [129], which builds upon the mathematical model used in this study. They achieved 20 µm channels using a commercial printer with 10 µm pixel size. They used a material with a penetration depth of 30 µm, which is a fourth of the penetration depth of the material used in this study

4.1.2. Slicer Output

In the printing process process of the pores and channels, the Solidworks channels were converted into pixelated projections on the LCD as seen in Figures 4.7 and 4.8. This pixelation process alters the cross-sectional shape and area as viewed projected on the LCD, since the channel and pore shapes at different orientations are approximated using the LCD pixel size. Additionally, the target diameter must be reached using pixels of a set size and layer heights of variable size, making it impossible to perfectly replicate the intended channel diameter at sizes smaller than the pixel size (or a multitude thereof). Figure 4.7 showcases the effect of the orientation on the UV light mask projection. This projection is in the plane of the LCD and therefore different from the cross-sectional shape as seen in Figure 4.7, since it does not include the layer height. The projection on the LCD is always limited to the pixel size. Part (a) of Figure 4.7 shows a pore orthogonal, (b) angled, and (c) parallel to the build plate. These areas are the non-illuminated areas on the LCD screen. In part (a), the cross-sectional roundness of the resulting channel is fully determined by the LCD screen pixel size. In (b) and (c) the roundness of the printed pore is determined both by the pixel size and the layer height.

Figure 4.7: The orientations are pixelated in different ways. (a) The pores printed orthogonally to the buildplate remain constant but may vary in size and roundness from the intended channel size at smaller intended diameters. (b) The pores printed at an angle to the buildplate remain constant and are slightly elongated, increasing their dim area on the LCD. (c) The pores printed parallel to the buildplate appear as lines and vary over time as they appear only shortly when printing, due to them being open only for several layers.

Figure 4.8 showcases how pixelation affects the roundness of the pores orthogonal to the build plate. At smaller intended diameters, the pixelation alters the intended dimensions. The smallest channel was intended to be a round cross-sectional channel of 50 µm in diameter. The slicer alters this channel to be a collection of six pixels, measuring 54 µm at its largest extent. The area of this collection of pixels deviated slightly from the intended circular channel (1944 μm^2 for the pixelated sliced channel versus 1963.5 μm^2 for the round intended channel). In this study errors were calculated compared to the round intended channels before slicing. Pixelation in the slicing process will therefore have caused slight errors from the intended round pores and channels, in addition to changes in settings, errors caused by measurement, or errors caused by the printing process. Dimensional errors may therefore be the result of the slicing process in addition to the printing process itself. Having control of how, especially smaller circular channels, are sliced and exported to the printer may aid in approximating the correct cross-sectional dimensions (especially in the LCD plane).

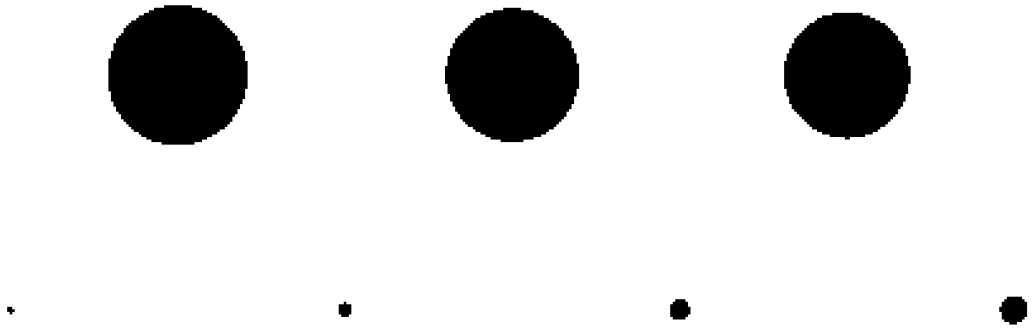

Figure 4.8: The pores orthogonal to the build plate after slicing. On top larger pores of 1 mm, 0.95 mm, and 0.9 mm from left to right are depicted. On the bottom channels from 50 µm, 100 µm, 150 µm, and 200 µm are illustrated. The pixelation is clearly visible, and smaller channels are not round. Instead it consists of six pixels, a cross shape and the upper left corner. Since the pixel size of the printer is 18 µm, the intended dimensions after slicing are 54 µm maximum in width and height, which remains close to the modelled dimension of 50 µm.

4.2. Characterization of the Pores

4.2.1. Printed Pores

In total 38 samples were printed for the optimization of the cross-sectional parameters. The number of open pores for every line of channels in every sample was counted in order to make an initial assessment on the minimum reached diameter. The 10 samples with channels printed parallel to the build plate were deemed insufficiently developed for inclusion in the analysis as seen in Figure 4.9 (b). This is illustrated in the number of open pores, which was smaller than in the angled and orthogonally printed samples as seen in Figure 4.9 (a) and (c) (and as provided in the tables included in Appendix G). It can be concluded that channels parallel to the build plate are most likely to fail, indicating that printer settings should primarily be optimized towards segments of 3D designs printed at this orientation. This is the consequence of the cross sectional diameter as seen from the build plate is minimized at this orientation as mentioned in Section 4.1.1. Ovals were fitted to the angled and orthogonal pores. The printed samples with pores and fitted ovals can be inspected in Appendix H. The included samples are provided with their print settings in Appendix I. The pores oriented orthogonal to the build plate exhibited a tapered decrease in pore depth as visualized in Figures 4.10a and 4.10b. These pores were closed at the backside, since they were printed on the build plate directly as illustrated earlier in Figure 3.5. To determine whether a pore was open, an arbitrary threshold of 10% decrease in depth as observed using the digital microscope was assumed to be closed. These pores may have been open, however, and the resin could simply have been difficult to remove due to the closed backside. Curing of closed pores with unremoved resin may have closed them to a larger degree. 28 samples were included for the analysis, resulting in 56 lines of varying pore diameters. 22 of these samples where included for the general tests, whereas 6 samples were part of a separate test intended to investigate the influence of the angle on the roundness (exposure time 5 s, layer height 50 µm). Printing these together made sure the prints were subject to the same context apart from location on the build plate. In total 1120 printed pores were potentially included for analysis, of which 609 were found to be open as illustrated in Table 4.1. To these pores ovals were manually fitted. The intended area falls within the 95% confidence interval for all mean values of the measured printed areas. As can be seen, diameters down to 800 µm were printed in all cases regardless of orientation, (over) exposure, or layer height. Pores down to an intended diameter of 350 µm were printed.

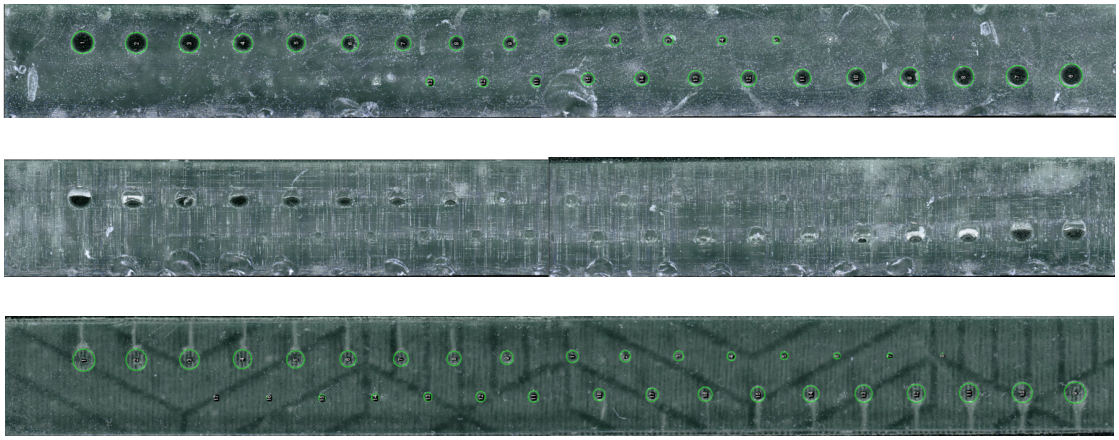

(a)

(b)

(c)

Figure 4.9: Examples of samples printed at 10 µm layer height and 2.5 s exposure time with fitted ovals. The dimensions are 50x5x2 mm (a) Sample printed at an angle to the build plate, (b) Sample printed perpendicular to the build plate with pores parallel to it, (c) Sample printed horizontal to the build plate with pores orthogonal to it.

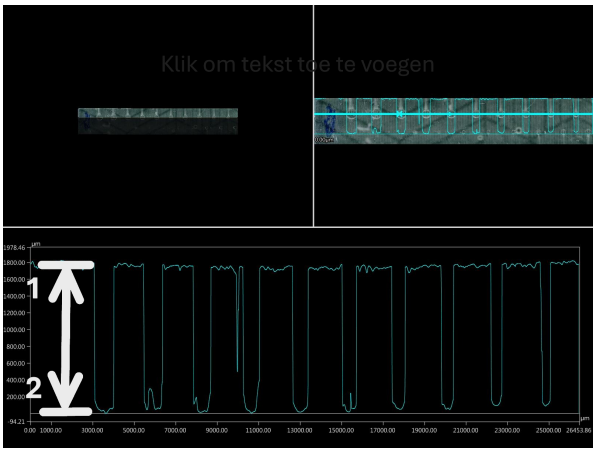

(a) Image of side A of horizontal line 1 (exposure time: 2 s)

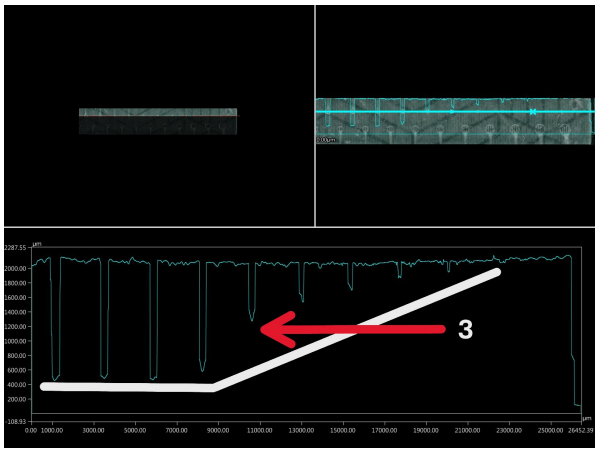

(b) Image of side B of horizontal line 1 (exposure: 2s)

Figure 4.10: An illustration of the use of the Keyence depth up images for the recognition of depth tapering and to identify open pores. The measurement is taken from above, orthogonal to the face of the sample. In the images the pore depth is visualized relative to the top surface. A decrease in this depth translates to an increase in the minimal measured depth for that pore. (a) Side of the sample starting from the larger pores with all being open, 1. stands for the surface of the sample and 2 for the bottom of the pore. (b) Side of the sample from 500-50 µm with pronounced depth tapering leading to the smallest pores being indiscernible. Number 3. shows where the channel is clearly more than 10 percent smaller than the preceding pore.

4.2.2. Smallest Fabricated Pore

The 3 smallest pores found were all in angled samples as illustrated in Table 4.2 and Figure 4.11. The two smallest pores (printed at a diameter of approximately 270 µm) were printed using the largest layer height and longest exposure time (exposure time 7 s, layer height 100 µm). They were intended to print at a diameter of 400 µm. This can be explained by the computed normalized cumulative dose being comparatively smaller to pores using smaller layer heights and shorter exposure times, as seen in Figure 4.1. As described by [86], larger layer heights are able to decrease the normalized cumulative dose at a cost of increased within layer stress and problems with layer-to-layer adhesion.

This achieved pore size is smaller than described as the limit for this resin by Gong *et al.* [86], who describe a limit of 3.5 times the penetration depth for resins with a penetration depth over 50 µm. The photopolymer resin used in this study has a penetration depth of 120 µm, translating to a channel/pore size 2.25 times the penetration depth at suboptimal normalized cumulative dosage dosage conditions as illustrated in Figure 4.1 (b). This may be the result of printing at an angle, which was not done by Gong *et al.* [86]. The normalized cumulative dosage remains about 5 times larger than required, and

Table 4.1: Count of open pores with measured average area (mm^2) including the confidence interval and the intended area.

Count (n)	Mean Area with CI (mm^2)	Intended Area (mm^2)
56	0.786 ± 0.016	0.785
56	0.702 ± 0.016	0.709
56	0.625 ± 0.015	0.636
56	0.555 ± 0.015	0.567
56	0.490 ± 0.014	0.503
55	0.425 ± 0.013	0.442
51	0.370 ± 0.013	0.385
47	0.322 ± 0.012	0.332
43	0.273 ± 0.012	0.283
40	0.227 ± 0.012	0.238
39	0.187 ± 0.011	0.196
33	0.149 ± 0.011	0.159
17	0.120 ± 0.016	0.126
4	0.105 ± 0.025	0.096

further lowering the cumulative dose may facilitate the printing of smaller pores. This is indicative of the variability caused by the printer and resin. The same authors remarked that commercial resins were successful in fabricating channels of 350 by 350 µm [86]. The smallest pore size achieved in this study shows that smaller channels can be manufactured using commercial resins. Using a custom resin this size was reduced to 60 µm by 108 µm at 10 µm layer height by the same authors. Using both a custom DLP printer and custom resin channels as small as 20 by 18 µm can be manufactured [120].

Table 4.2: Smallest area and roundness values. LH: Layer Height, O: Orientation, E: Exposure Time, Line, Line 1 or 2 of the pores on the same sample.

ID: LH, O, E, Line	Area (mm^2)	Intended Area (mm^2)	Roundness	Error of Area (%)
100 µm, 79.8 °, 7 s, line 1	0.057048	0.125664	1.000391	-54.6
100 µm, 79.8 °, 7 s, line 2	0.058076	0.125664	1.000266	-53.8
10 µm, 61.0 °, 2.5 s, line 1	0.088483	0.096211	1.000115	-8.03

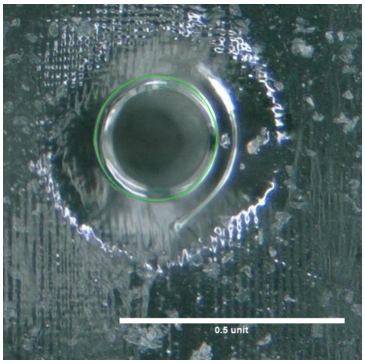

(a) Pore printed using the settings; Layer Height: 100 µm, Orientation: angled, Exposure Time: 7 s, line 1, the scale bar represents 0.5 mm.

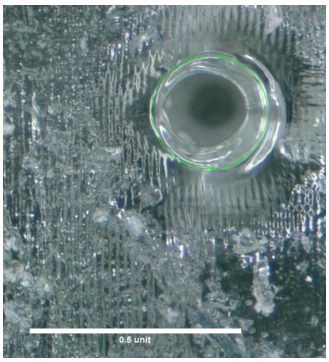

(b) Pore printed using the settings; Layer Height: 100 µm, Orientation: angled, Exposure Time: 7 s, line 2, the scale bar represents 0.5 mm.

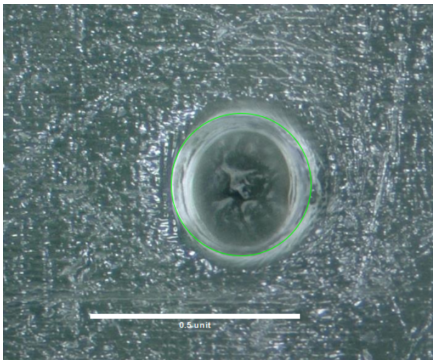

(c) Pore printed using the settings; Layer Height: 10 µm, Orientation: angled, Exposure Time: 2.5 s, line 1, the scale bar represents 0.5 mm.

Figure 4.11: The three smallest diameter pores with 0.5 mm scale bars.

4.2.3. Estimation of the Error

Ovals were fitted to the pores to investigate the roundness and area. Manual fitting of ovals to the pores required error quantification. For this purpose 2 independent researchers have fitted ovals to a complete angled and horizontal sample twice. The sample was printed at 10 µm layer height and 2.5

(s) exposure time. In total 116 ovals were fitted per researcher, totaling 232 ovals. The ovals were fitted to both open and closed pores. Both angled and orthogonally oriented pores were researched due to differences in appearance of the samples.

The results of the estimation of the measurement errors are provided in detail in Appendix J. Pores were printed twice per sample, and the measurements of equivalent pores were compared in Table K.2. The difference in the absolute normalized relative error of the area between pores of the same intended size on the same sample (printed under the same circumstances) was **4.8% (4.3%, 5.3%)**. The absolute normalized relative error of the roundness for these pores was determined to be **0.115% (0.094%, 0.136%)**. These measurements were subject to measurement error introduced by the manually fitted ovals. The overall absolute intra-operator error of the normalized relative area is provided in Table K.3 and was **2% (95% CI: 1.6% - 2.3%)**. The overall absolute intra-operator error relative to their own measurements for the roundness was **0.030% (0.024%, 0.037%)**. The overall absolute inter-operator difference for the area amounted to **3% (95% CI: 2.3% - 3.8%)** as can be seen in Table K.6. The overall absolute relative difference for the roundness was **0.028% (0.017%, 0.039%)** . A difference between the operators was observed for the normalized error of the area, where one operator consistently measured pores to be by about **-1.82% (-2.82%, -0.82%)** smaller compared to the other. The inter-operator difference was larger due to a likely consistent measurement error using the manual oval placement, which invalidates the exact resulting values for the roundness and the normalized error of the area in the optimization test. While a larger size than intended is found in the next chapters for the pores, this may be attributed to inter-operator error. However, Leong *et al.* [85] do report channels that are larger than intended for open microfluidic channels. This outcome is unlikely according to the curing model, which states that light intensity is either sufficient or not sufficient to cure the photopolymer. The found error may also be caused by error approximating the channel size using the pixel size in the slicer, or by unevenly distributed light intensity across the pixel. The approximately 2% intra-operator error is smaller and allows for cross-group comparison of measurements done by a single operator. Additionally, the measurements of equivalent pores exhibited a larger difference than the measured intra-operator error. A true printing error for prints of similar intended dimensions may therefore exist.

Literature on within single print errors, and errors within separate prints using separate settings, are seemingly scarce. Qualitative studies on the impact of parameter changes or print outcomes exist [130]. Differences in same-sample pore sizes may be attributed to pores higher on the sample receiving a larger cumulative normalized dose resulting from the increased number of layers printed after the channel. However, the effect of the location of the channnel in the sample is not researched in this study. Other potential causes for within-print differences include local dimming of pixels in the LCD, slight damage or changes to the transparency of the FEP, movement of the printer or resin during printing, or photo-polymer resin that was not mixed well. Further research is indicated to better assess within-print dimensional variability.

4.2.4. Setting Optimization

Several tests were done to investigate the impact pf parameter changes. The samples included in every test are listed in Appendix L. As reported in Section 3.8, data on the roundness and normalized error of the area were pooled for pores of same intended size of samples printed with different settings (exposure time, layer height and orientation). The assumption was that the average roundness and the average normalized error of the area do not depend on the pore size (defined as the intended area) and that the error and roundness can be pooled to investigate parameter changes between samples printed with different settings. The validity of this assumption was investigated by grouping all the areas with the same intended area together, and by consequently doing a Kruskal-Wallis test meant to assess the difference in roundness and normalized error of the area for the intended pore sizes (this statistical test was chosen based on the results of a Shapiro-Wilks testing for their normality). The results are provided in Appendix M. As a result of the underlying printing mechanism and the Kruskal-Wallis test of the roundness, it cannot be ruled out that smaller diameter channels are comparatively less round and may still exhibit increased deviation from the intended area.

Orientation
Firstly the angled samples were compared to the orthogonal samples for their roundness and mean normalized error of the area. This is provided in Appendix N and O. The angled and orthogonal pore groups differed significantly from each other in roundness and mean normalized error of the area according to the Mann-Whitney U tests. The mean normalized error of angled samples did not significantly differ from 0, meaning that angled pores might have printed accurately on average. However, the roundness value is smaller, and therefore closer to being circular, for the orthogonal pores. This is expected, as orthogonally printed pores are not impacted by overcuring of resin in the channels. Additionally, the impact of angling itself was researched. This has been done in two ways. Firstly, the hypothesized optimal angle adhering to the arctan rule for the channels was compared to 90° - arctan rule (which is theorized to be optimal for printing the flat surface samples) to investigate the influence on the mean normalized error of the area and the roundness. Furthermore, an angle test was done to compare the effects of multiple angles. The results for the effect of the arctan rule are provided in Appendix N. A Mann-Whitney U test shows a significant difference in the roundness and normalized error of the area between the two groups. Table N.2 shows that channels adhering to the arctan rule are both more round and larger relative to the intended area compared to other angles.

The angle test consisted of samples printed at intervals at constant layer height and exposure time (0.05 mm, 5 s). The angles of the pores as measured from the buildplate included; 0°, 19.79°. 22.5°, 45°, 67.5°, 70.21°, 90°. As previously mentioned, the channel parallel to the build plate is not included in the analysis (0°). The means and 95% CI of the roundness and normalized error of the area for the groups of pores are displayed in Table 4.3. The values are displayed in Figure 4.12. The roundness values in Figure 4.12 (a) are consistent, with the 45° sample being a clear outlier. Looking at the fitting of the ovals in Appendix H, it may be that human error manually fitting these ovals caused this difference.

Table 4.3: Summary of Roundness and Normalized Error Area by angle of samples printed at 0.05 mm layer height and 5 s exposure time.

Angle	Roundness (Mean and 95% CI)	Normalized Error Area (Mean and 95% CI)
70.21	1.00066 (1.00023, 1.0011)	-0.09672 (-0.13629, -0.05716)
19.79	1.00035 (1.00012, 1.00059)	0.04167 (0.02878, 0.05456)
90.00	1.00026 (1.00002, 1.00051)	-0.17394 (-0.21607, -0.13182)
45.00	1.0028 (1.00122, 1.00438)	-0.05892 (-0.09184, -0.02599)
67.50	1.00049 (1.00012, 1.00087)	-0.15168 (-0.19666, -0.10669)
22.50	1.00047 (1.00011, 1.00082)	-0.0321 (-0.05371, -0.01049)

The angle based on the arctan rule for pores at this layer height was calculated to be 70.21 degrees. Pores printed at the 19.79 orientation were the only ones with a calculated mean positive error to the intended area as illustrated in Figure 4.12 (b). This is likely a sample-specific measurement error, as enlargement of the pores is theoretically implausible. However, Leong *et al.* [85] observe a 10 % increase in channel width of open microfluidic channels. While the inter-operator error may cause measurements to be slightly larger than the pores are in reality, it cannot be ruled out that the channels are slightly larger than intended due to the slicing process. The graph does suggest that larger angles may increase the error. Both of the smallest printed pores as expanded upon in Section 4.2.2 were at relatively steep angles, however. This result is in contrast with the findings of Heidt *et al.* [94], who note a decrease in error for larger angles using SLA printing. They note the optimal angle to be the 90 degree, or orthogonal, angle. The difference may be due to the use of a form 2 printer, which uses a laser instead of a LCD.

Grymak *et al.* [131] note that the optimal angle for dental casts using mSLA is 45 degrees. The error found in this study for the different orientations was at constant layer height and exposure time. It was expected error the decrease with increasing height as a result of a decease in the effect of overcuring on the pore size. Angled pores had a larger number of open pores at smaller diameter and smaller diameter pores might still introduce a larger error. It may therefore be true that the results are impacted by samples containing pores at larger angles also containing an increased number of smaller pores with a larger error from the intended area. This theory is supported by the fact that the smallest

diameter pores were printed at comparatively larger angles of 61° and 78°. Other studies of angle placement were not seen to relate the error found to the printing mechanism and did not research the arctan rule.

The decrease in area from the intended area of orthogonally printed poresis unlikely to be caused by measurement error, since the inter-operator error for the measurement of orthogonal pores was approximately 2%. A cause could be the optical proximity effect being particularly pressing in this orientation. Where the pore height is smallest for parallel pores as seen from the LCD, the cross-sectional area is smallest for orthogonally printed pores. The cumulative normalized dose is smallest for the orthogonal pores compared to parallel pores, but the reduction of the dimensions due to ”bleeding” of the light at the edges into the pore may start influencing the pores to a larger degree due to repeated exposure to UV light at a constant location. This issue may be present at larger angles as well, where steps increasingly stack orthogonal to the LCD. The presence of this phenomenon at perpendicular angles to the build plate was mentioned already by Yu *et al.* [132], who propose a solution in the form of a greyscale optimization at the edges. This is different from anti-aliasing in that it is not intended to smooth edges but to preserve dimensional accuracy. As explained in Section 4.2.1, depth-tapering was observed for orthogonally printed pores and was likely caused by trapped resin due to unilateral obstruction caused by the burn-in layers. It is therefore not clear what size diameter would have been the minimum feature size to print successfully. Printing samples containing pores detached from the build plate (using supports) would not have been a solution to this problem. The issue of printing thin layers would likely cause bends and dimensional inaccuracy due to the movement in the resin. Furthermore, resin could get trapped on top of the layer and cure due to the cumulative normalized dose. Printing at an angle minimizes these issues due to the angle decreasing the printed cross-section and an angle facilitating downward flow of resin.

The benefit of the printing using the arctangent rule as used by hobbyists for flat surfaces seems to be minimal for the pores, although a significant difference was found with pores printed at different angles. However, if the pores printed at this theorized ”ideal” angle where more likely to be angled higher relative to the build plate, this could impact the result and decrease the error. To conclude, while a statistical difference was observed it cannot be conclusively ruled out that this difference was due to the benefit of increasing the angle instead of the rule itself. A benefit of the arctangent rule is that larger layer heights increases the arctangent angle relative to the build plate. This would have the added benefit of improving the resolution of the cross-sectional shape due to the round shape being impacted disproportionally by the pixelation of the projection on the LCD of the printer. This pixel width is smaller than a large layer height.

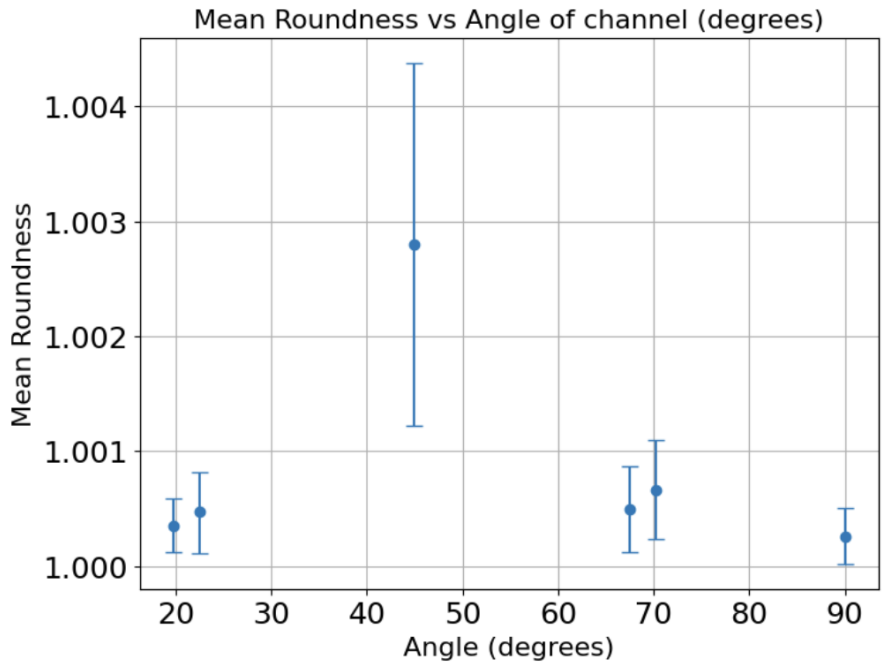

(a)

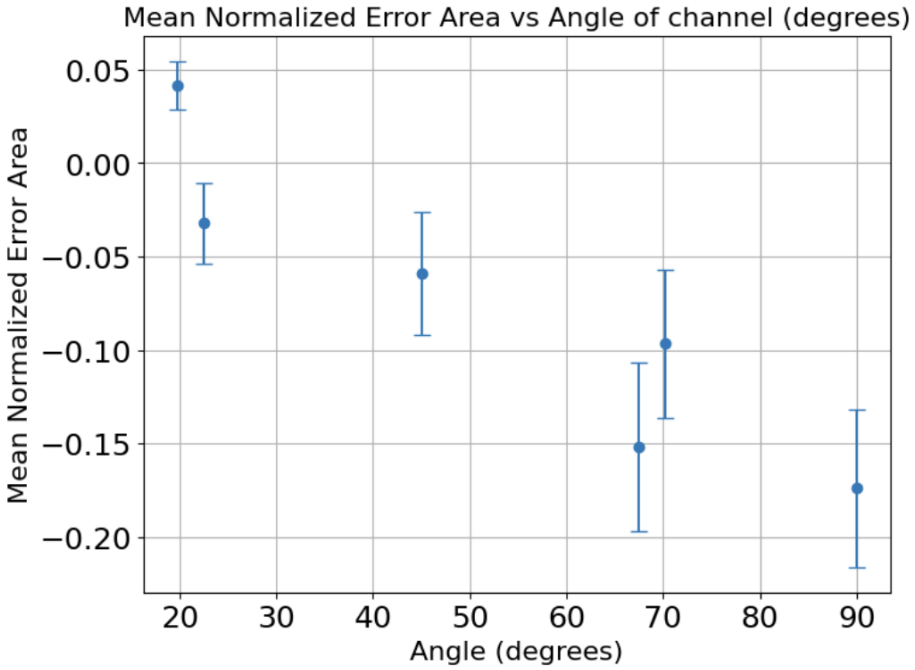

(b)

Figure 4.12: Graphs showcasing differences between angles of the pores as determined from the build plate. (a) The mean Roundness for the samples included for the analysis including the 95% confidence interval of the mean. The 45° sample is a clear outlier. (b) The mean normalized error to the intended area per angled sample including the 95% confidence interval of the mean.

Exposure Time
The exposure time was varied at constant layer height (10 µm) from 5 seconds downward until the print failed. This occurred at 1.5 seconds of exposure time. This result was expected based on the curing depth for the exposure time as illustrated in Figure 4.2. The curing depth would not reach the layer height at this exposure time. Increasing exposure times leads to increasing cumulative doses as is seen in Figure 4.1. The cumulative dose of the smallest exposure time used at the smallest layer height is approximately fifteen times the required dose. Due to light impedance of the film, and aging or damaging of the LCD printing at the exact limit is not advisable. As a result of increasing cumulative dosage the roundness of the pores diverges from 1, the perfect circle, as seen in Figure 4.13 (a). The mean normalized error of the area as seen in 4.13 (b) is not closest to zero at the smallest exposure time. Pores seem to be larger than intended at small exposure times (and relatively low cumulative dose). The means of the roundness and normalized error to the intended area are represented in Table 4.4. An exposure time closer to the critical dose required for polymerization is therefore more optimal to maintain he roundness for microfluidic channels with an intended circular cross section. An exposure time of 2.5-3.5 seemed to minimize the mean normalized error of the area using the photopolymer and mSLA machine used in this study at 10 µm layer height.

For planar devices it may make sense to print as few as possible layers on top of the intended channel to reduce dose build-up allowing for higher exposure times. While this may come with added fragility of the top layer, microfluidic device strength can be increased as part of the post-processing step by applying additional resin and curing once the channels are empty, or by applying an acrylic top coating. This has the added advantage of improving the transparency for channels printed orthogonal to the build plate or at an angle, where the layers cause diffraction of light and reduce transparency.

Table 4.4: Means and Confidence Intervals for Roundness and NEA of different exposure time groups.

Exposure Time (s)	Roundness (Mean and 95% CI)	Normalized Error Area (Mean and 95% CI)
2	1.00026 (1.00014, 1.00039)	0.23769 (0.22303, 0.25235)
2.5	1.00186 (1.0013, 1.00243)	0.03728 (0.02626, 0.0483)
3	1.00347 (1.00288, 1.00406)	-0.04948 (-0.06383, -0.03513)
3.5	1.00183 (1.00132, 1.00234)	-0.03111 (-0.04525, -0.01696)
4	1.00725 (1.00631, 1.00819)	-0.11196 (-0.12905, -0.09487)
4.5	1.00254 (1.00168, 1.0034)	0.05659 (0.01326, 0.09993)
5	1.01404 (1.01095, 1.01712)	-0.18112 (-0.20874, -0.15351)

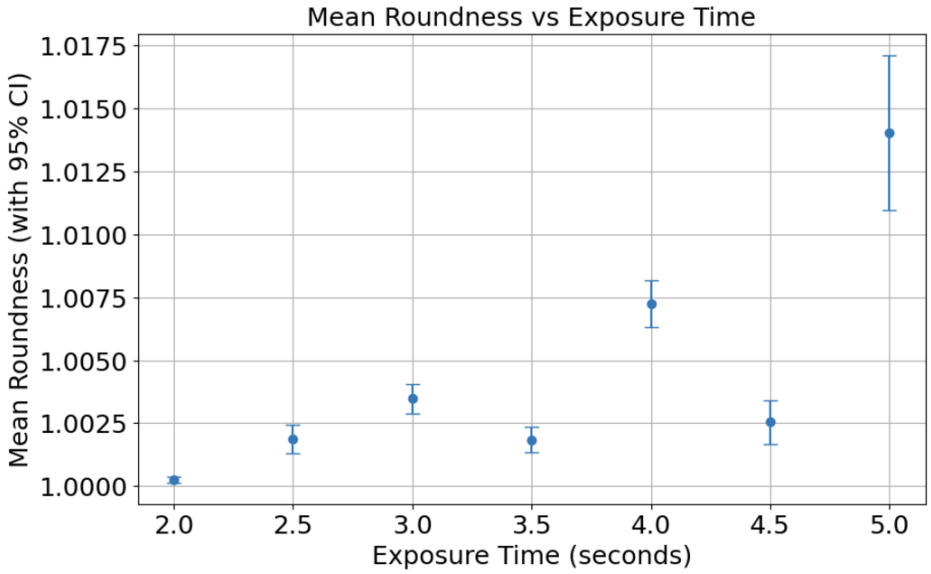

(a)

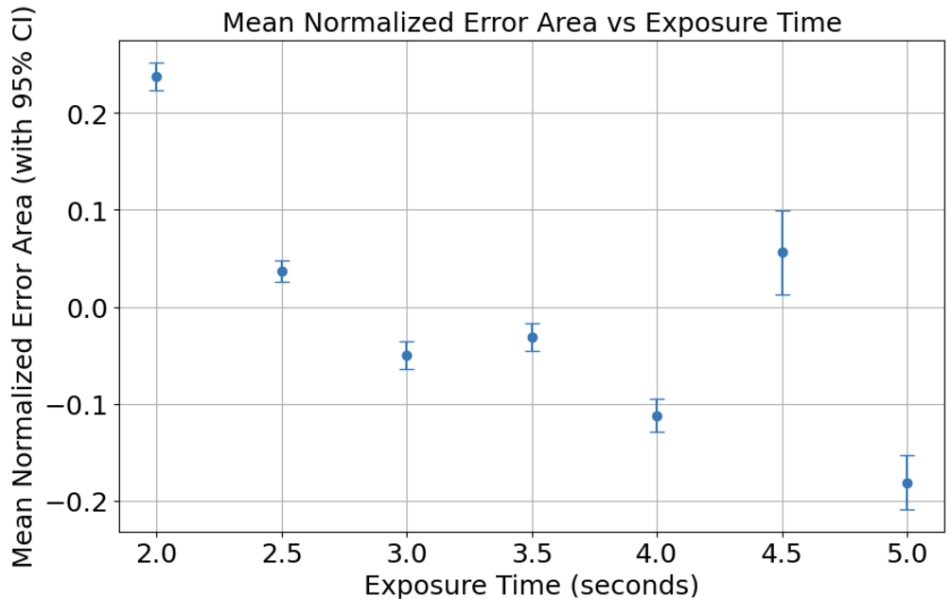

(b)

Figure 4.13: Graphs showcasing differences between exposure times of angled pores for the same 0.01 mm layer height. (a) The mean Roundness for the samples included for the analysis including the 95% confidence interval of the mean.(b) The mean normalized error to the intended area per exposure time including the 95% confidence interval of the mean.

Layer Height
The layer height was varied between 0.01, 0.02, 0.05, and 0.1 mm in samples oriented at an angle. The exposure time was not kept constant since this would influence the dosing and the results, but varied between 2, 3, 5, and 7 seconds respectively to the layer heights. These were the dosages as advised by the manufacturer. Upon closer examination these values did not keep the normalized cumulative dosage constant as intended, which is the main limitation of this test on the effect of the layer height on error from the intended area and the roundness. However, there are some benefits to this approach. In reality it is unlikely that perfect settings will be used when 3D printing small vessels. This would require a highly controlled environment with constant temperature, new films for the VAT after every use, and a LCD that does not degrade over time. As such, the tests done in this study better represent normal printer use by researchers not closely familiar with mSLA printing.

An inverse relation between the layer height and the normalized cumulative dosage for the printer, resin, and settings used in this test was observed. This means that at lower layer height the cumulative dose was higher. The roundness does not seem to vary significantly between different layer heights as seen in Figure R.1b (a), which is in contrast with the previous results illustrating that increased dosage decreases the roundness. This could be the result of a negative effect on the roundness by the layer height being offset by a lower cumulative dose being used. The normalized error seems to be minimized for a layer height of 50 µm as illustrated in Figure R.1b (b). The smallest layer height had the highest dose, but was measured to be larger than intended. This is similarly contrasting with the results of the exposure test, where the settings inducing the smallest dose showed the an increase in the area from intended. In contrast, decreased cumulative dosage showed smaller channels with increasing layer height. Increased layer height may therefore decrease the pore size.

Gong *et al.* [86] describe that the build thickness or layer height should be between 0.3-1h_a to reduce internal dose variation internal of individual layers and to reduce overexposing the channel (which occurs at smaller layer height due to frequent illumination). In this test only the 0.05 mm and 0.1 mm layer height samples satisfied this criterion. With this in mind, the optimal layer height occurred at a layer height of 50 µm for reducing the error as seen in Figure 4.14. Larger layer heights are accompanied with larger angles adhering to the arc tangent rule which was shown to be beneficial for reducing the error as well. It could therefore be advisable to print at larger layer height to reduce the cumulative dose, and increase the angle while using the arc tan rule. Dhanunjayarao *et al.* [133] mention layer height to be the largest influence on three dimensional accuracy for mSLA. This is in contrast to Borra *et al.* [134], who claim exposure time to be most influential. Both claims are likely to be equally valid, as they interact for the final result. If layer height is more influential than exposure time, it may explain why decreased dosage was still related to a decrease in pore size at larger layer heights.

Table 4.5: Summary of Mean Roundness and Normalized Error Area by Layer Height

Layer Height (mm)	Roundness (Mean and 95% CI)	Normalized Error Area (Mean and 95% CI)
0.01	1.00144 (1.00098, 1.00191)	0.01925 (0.00732, 0.03117)
0.1	1.00042 (1.00025, 1.00059)	-0.18600 (-0.21930, -0.15270)
0.02	1.00033 (1.00022, 1.00044)	0.08736 (0.07257, 0.10214)
0.05	1.00042 (1.00025, 1.00059)	-0.07721 (-0.10653, -0.04789)

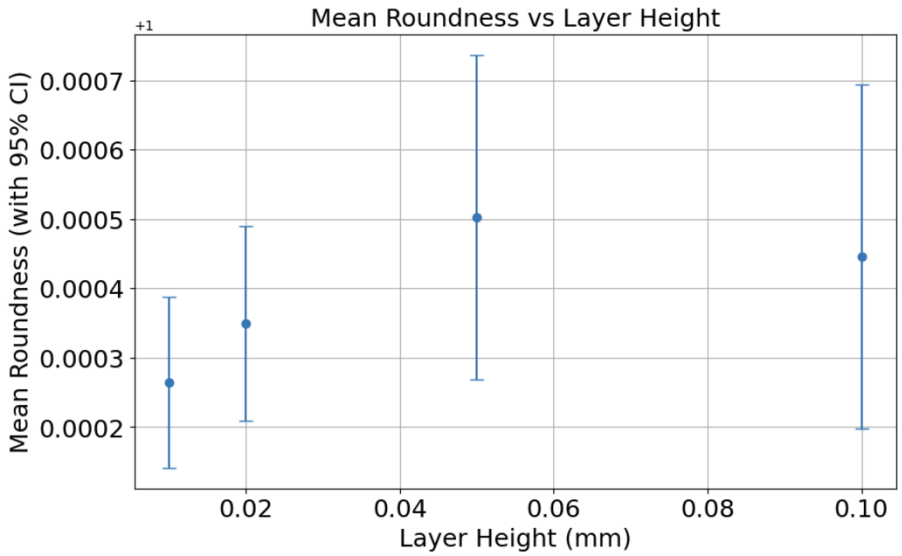

(a)

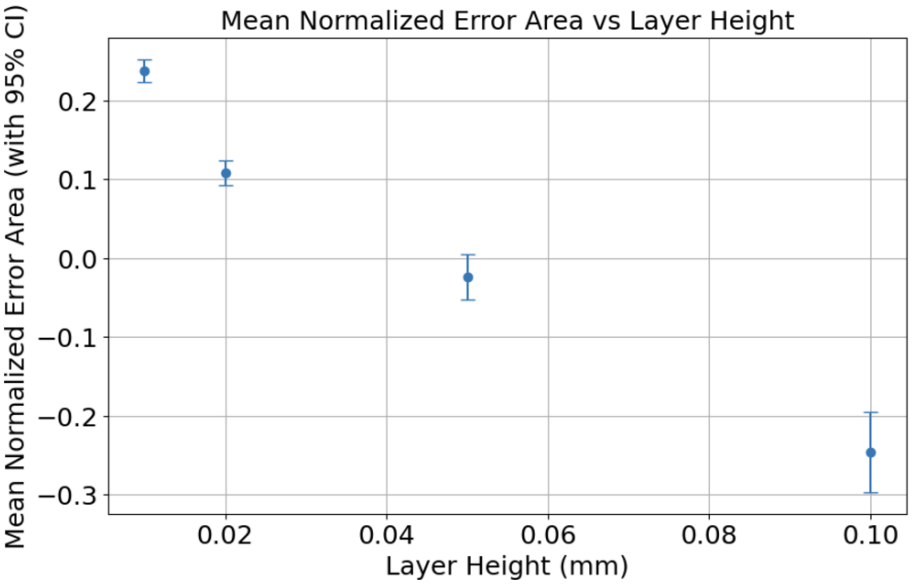

(b)

Figure 4.14: Graphs showcasing differences between layer heights of angled pores for exposure times as advised by the manufacturer. (a) The mean Roundness for the samples included for the analysis including the 95% confidence interval of the mean. (b) The mean normalized error to the intended area per exposure time including the 95% confidence interval of the mean.

4.3. Characterization of the Microfluidic Channels

The intention was to print 4 circular cross-sectional microfluidic devices to test if lengthening the channel size introduced obstruction and to do a flow test. These devices were printed at an angle of 61° from the build plate, 10 µm layer height, and 2.5 s exposure time. These were the settings used to manufacture the smallest pores without increasing the error of the area to 50%. The intended pore size varied in diameter and were 350 µm, 400 µm, 450 µm, and 500 µm large. The 350 µm diameter device did not print successfully, whereas the other microfluidic devices did print. The device used for flow testing is visualized in Figure 4.15.

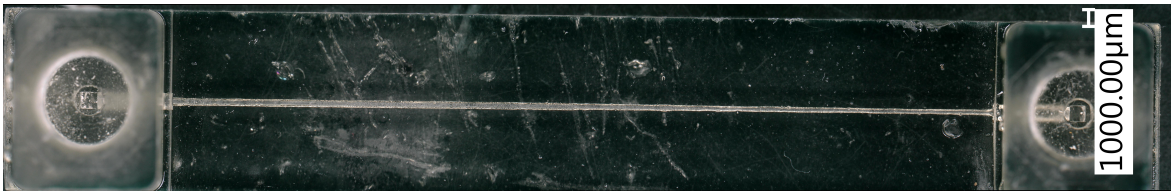

(a)

Figure 4.15: Device printed at 10 µm layer height and 2.5 s exposure time intended to be 450 µm in diameter.

4.3.1. Channel Printing Complications

Several issued were encountered during the printing of the channels and physiological devices intended fo flow testing. These issues are visualized in Figure 4.16. Narrowing of the channels was observed in some instances for unknown reasons, possibly slight movements during the printing as illustrated in Figures 4.16 (a) and 4.16 (b). Furthermore, the connectors had to be pushed all the way down in the connector fittings to prevent leakage as seen in Figure 4.16 (c). Overcuring due to higher exposure times during printing may complicate the fit due to slightly altered dimensions (decreasing the screw fitting port diameter). This problem can be improved by printing slightly larger diameter fittings and using teflon tape, or by adjusting the exposure time downwards.

Larger prints were more likely to detach from the build plate due to the larger cross-sectional area applying a stronger adhesion to the FEP film of the resin container. The retract speed can be lowered to reduce these forces. Thin walled connector fittings were likely to break, and were thickened as a result. Additionally, small bubbles entered the walls of these thicker fittings and create low resistance pathways for pressurized water to leak through during testing as seen in Figure 4.16 (d). Delamination occurred, especially when devices were printed at larger layer hight and parallel to the build plate (no angle) as seen in Figure 4.16 (e). The use of (prolonged exposure to) isopropyl alcohol may influence the appearance and material properties, as well as cause delamination [135], but this study adhered to the manufacturers guidelines. Such short exposure to isopropyl alcohol is unlikely to cause delamination. Figure 4.16 (f) shows protrusions connected to the channel that might be caused by delamination, but did not cause issues. For delamination, resin was applied at the location of delamination and consequently cured to close the device again. It must be taken into account that the resin may enter the channel during curing due to capillary flow. To overcome this a high viscosity acrylic nail polish was applied before adding additional resin to cure. Lowering the layer height should also be able to reduce the internal layer stresses.

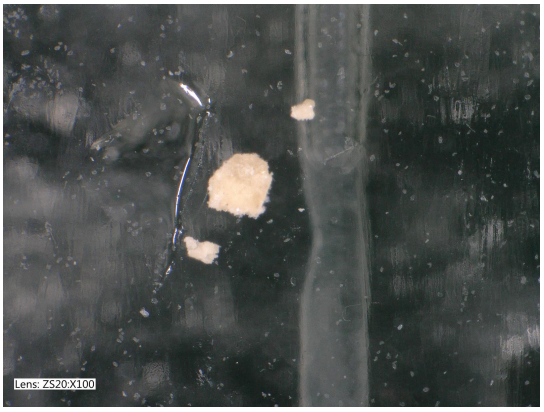

(a)

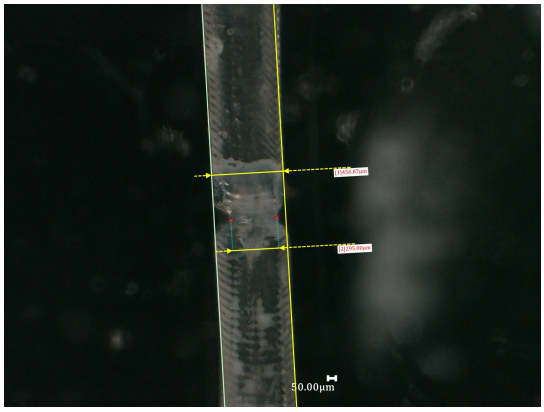

(b)

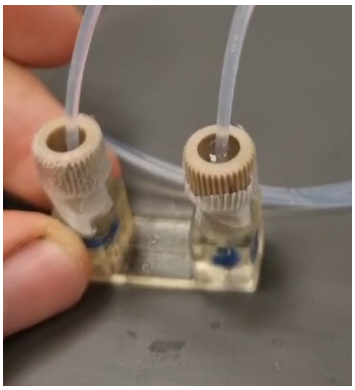

(c)

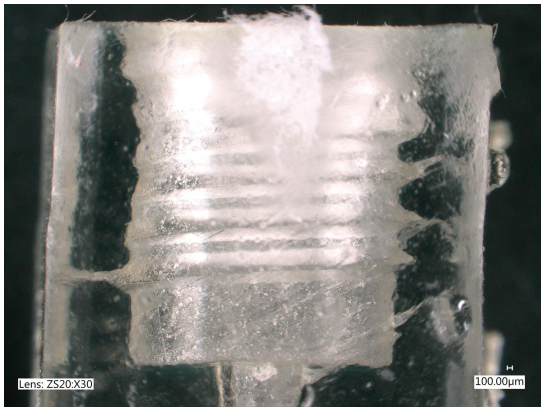

(d)

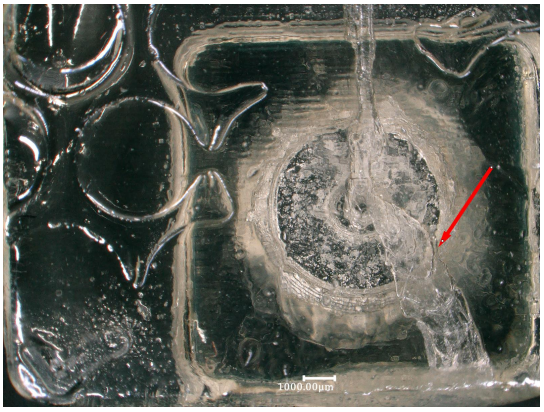

(e)

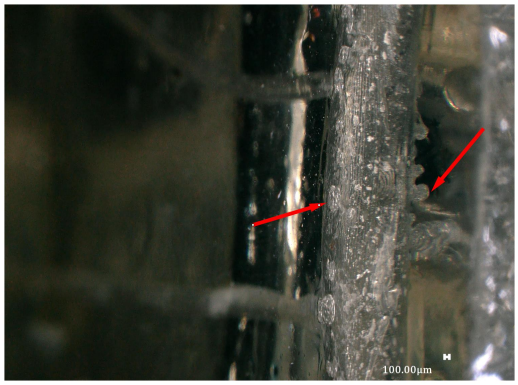

(f)

Figure 4.16: (a) An issue is inconsistent channel lumen. In this image a small decrease in the diameter can be seen. (b) Another occlusion as observed in the physiological device in the direction of outlet F2. (c) Leakage in the connector internal due to not sufficiently being able to be screwed in. (d) Channels emerging from the connector lead to leakage. (e) Delamination in the abstract device. It occurs at the bend, where the layers are delaminated due to insufficient adhesion. (f) Bubbles or artifacts formed at the M1 segment in the physiological device.

4.3.2. Optical Characterization

The channels in these 3 straight microfluidic devices were assessed using the digital microscope for their dimensional accuracy. As seen in Section 4.3.1, the channel diameter is not perfectly uniform across the length. This complicates the acquisition of the complete dimensions of the channel. Two

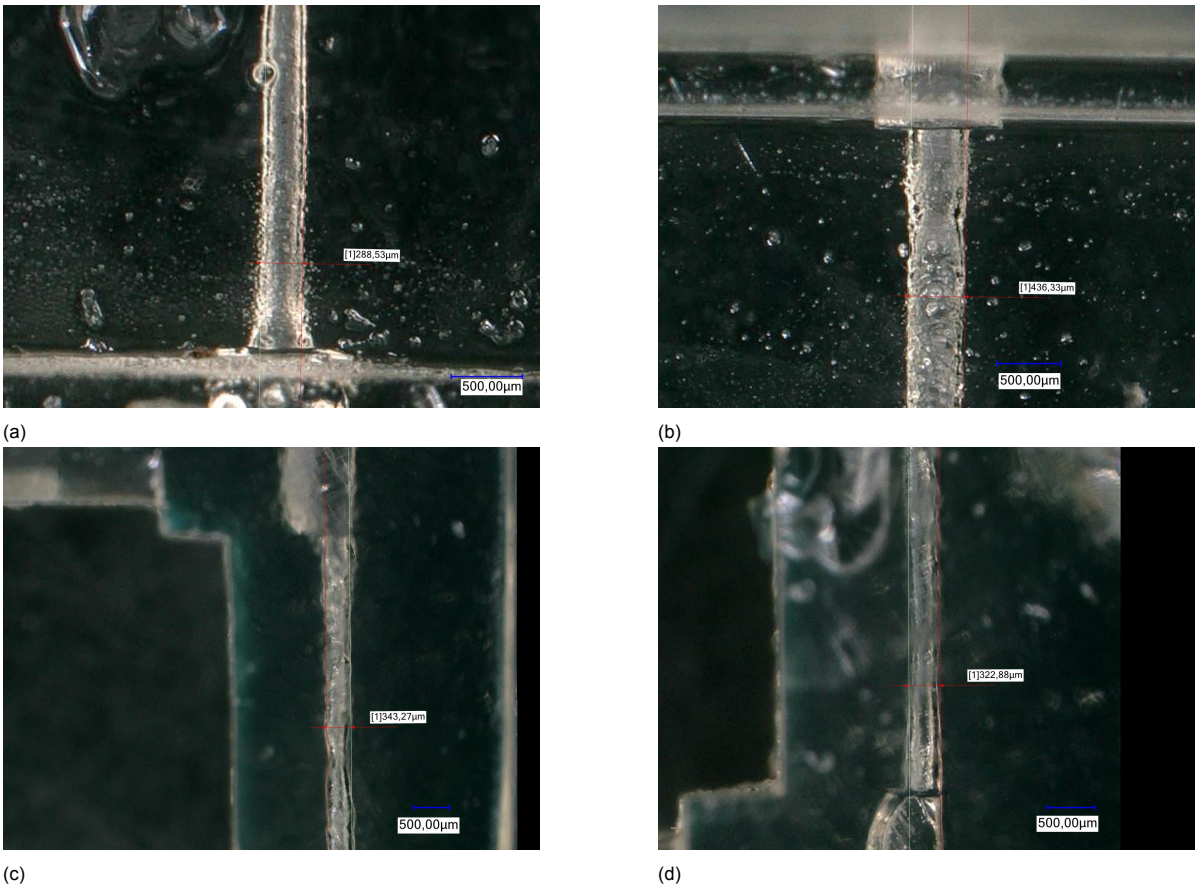

Figure 4.17: A visualization of the differences encountered in diameters at different sections of the channel intended to be 450 µm. (a) Top view of side 1 measuring 288.53 µm in diameter. (b) Top view of side 2 measuring 436.33 µm in diameter. (c) Side view of side 1 measuring 343.27 µm in diameter. (d) Side view of side 2 measuring 322.88 µm in diameter.

measurements at different locations may yield different diameters as illustrated in Figure 4.17. The measured diameter varies between (a) 288.53 µm and (b) 436.33 µm depending on the location of measurement and the view. From the side, the diameter was evaluated to be between (c) 343.27 µm and (d) 322.88 µm. To mitigate this issue, the diameter was determined using parallel lines along the channel sides over the entire channel using high resolution stitched imaging as seen in Appendix P Figures P.4, P.5, and P.6. The channels all were observed to be smaller than intended, by about 20 µm in in width as seen from the top, and up to 70 µm as seen from the side for the 400 µm diameter microfluidic device. The device used in the experimental test was measured to be 433 µm in diameter from the top view and 377 µm from the side view using this approach as seen in Figure P.5. The difference between the top view and side view can be attributed to the orientation on the build plate and the slight overexposure using 2.5 seconds exposure time leading to a larger cumulative dose inside the channel from the bottom (narrowing the channel as seen from the side). When curing a circular shape using an LCD-based process, fewer pixels define the sides compared to the middle. If overexposure occurs, these fewer pixels may all solidify completely, causing the shape to shrink from the sides. This results in a narrower cross-section than intended in addition to the excess curing at the bottom of the channel. Cumulative dosage acquired by the extra layers printed on the sides exacerbates this effect. Using the theory as provided in Section 4.1.1, an elliptical channel of 414 µm in width and approximately 280 µm in height was expected due to overcuring as explained in Appendix R.

4.3.3. Flow Characterization

Experimental Flow Test Results

In the experimental flow test, the flow rate and pressure drops were measured of the control test and microfluidic channel test. These experimental values for the control test and channel test respectively were compared to their analytical and computational solutions provided later in this section. The flow of the control test and the microfluidic device of 450 µm intended diameter was measured after applying a pressure using the pressure generator. For the control test, the pressure at the inlet was varied 4 times, between 100, 300, 500, and 1000 mbar. The flow rate and pressure drop for the microfluidic channel test were measured 5 times for pressures at the inlet of 50, 100, 300, 500, and 1000 mbar. The setup for these tests are visualized in Figure 4.18. The pressure drops resulting from the measured flow values (as provided in Section 3.9.1) are provided in Tables 4.6 and 4.7. The experimentally measured hydraulic resistance for the control test was $1.42 \cdot 10^{11}$ Pa·s/m^3. The hydraulic resistance for the microfluidic channel was $3.19 \cdot 10^{11}$ Pa·s/m^3. We can see the difference in the hydraulic resistance in the reduced measured flow rate and increased measured pressure drop in the microfluidic channel test when compared with the control test. This is the result of adding the microfluidic device to the system, consequently increasing the resistance.

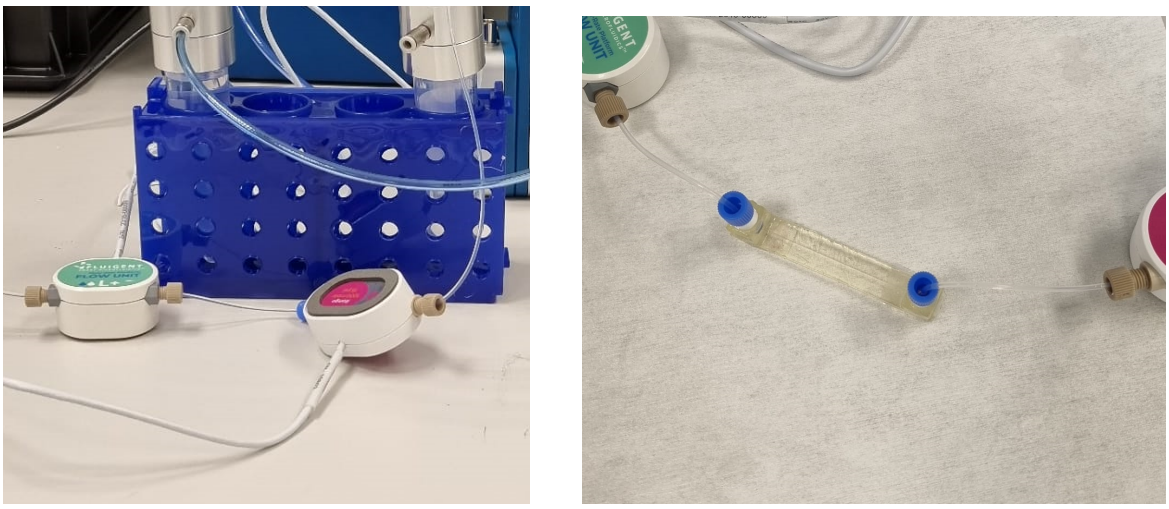

(a) The control test

(b) The microfluidic channel test

Figure 4.18: A visualization of the experimental setup containing microfluidic devices and tubing. (a) A test setup using a microfluidic tube connected to measurement devices using 10 cm 0.508 mm internal diameter tubes. (b) A simple microfluidic device connected to measurement devices using 10 cm 0.508 mm internal diameter tubes.

Table 4.6: Experimental pressure drop results over the measured microfluidic tube. Pi is the pressure provided at the inlet of the system and identifies the various tests. ΔP is the measured pressure drop. The Flow rate and ΔP were measured and compared in Section 4.3.3 to the analytical and computational values provided in Tables 4.8 and 4.10.

Experimental Control Test results		
Pi (mbar)	**Flow Rate (µl/min)**	**ΔP (mbar)**
100	1211.70	30.34
300	3594.28	78.31
500	5787.78	129.75
1000	10412.27	263.14

Table 4.7: Experimental pressure drop results over the measured region, including the microfluidic channel and microfluidic tubing. Pi is the pressure provided at the inlet of the system and identifies the various tests. ΔP is the measured pressure drop. The Flow rate and ΔP were measured and compared in Section 4.3.3 to the analytical and computational values provided in Tables 4.9 and 4.11.

Experimental Microfluidic Channel results		
Pi (mbar)	**Flow Rate (µl/min)**	**ΔP (mbar)**
50	354.94	21.68
100	787.92	41.60
300	2474.14	120.28
500	4084.51	200.74
1000	7659.30	412.57

Analytical Flow Test Results

The pressure drops as calculated using the analytical approach resulting from the measured flow values (as provided in Section 3.9.1) for the control test and microfluidic test are provided in Tables 4.8 and 4.9. The hydraulic resistance for every pressure input iteration was calculated and averaged. The experimentally measured hydraulic resistance for the control test was $1.49 \cdot 10^{11}$ Pa·s/m^3. The hydraulic resistance for the microfluidic channel was $1.96 \cdot 10^{11}$ Pa·s/m^3.

Table 4.8: Analytical pressure drop results over the measured microfluidic tube. The flow rate as measured in the experimental test as provided in Table 4.6 was used to calculate the pressure drop. ΔP is the resulting pressure drop. The flow rate and ΔP were compared to the experimental and computational values provided in Section 4.3.3.

Analytical Control Test results	
Flow Rate (µl/min)	**ΔP (mbar)**
1211.70	30.17
3594.28	89.46
5787.78	142.31
10412.27	259.17

Table 4.9: Analytical pressure drop results over the measured microfluidic device and tubes. The flow rate as measured in the experimental test as provided in Table 4.7 was used to calculate the pressure drop. ΔP is the resulting pressure drop. The flow rate and ΔP were compared to the experimental and computational values provided in Section 4.3.3.

Analytical Microfluidic Channel results	
Flow Rate (µl/min)	**ΔP (mbar)**
354.94	11.63
787.92	25.820
2474.14	81.08
4084.51	133.85
7659.30	251.00

Computational Flow Test Results

The pressure drops as calculated using the computational approach resulting from the measured flow values (as provided in Section 3.9.2) for the conrol test and microfluidic test are provided in Tables 4.10 and 4.11. The experimentally measured hydraulic resistance for the control test was $1.44 \cdot 10^{11}$ Pa·s/m^3. The hydraulic resistance for the microfluidic channel was $1.90 \cdot 10^{11}$ Pa·s/m^3.

Table 4.10: Computational pressure drop results over the measured microfluidic tube. ΔP is the resulting pressure drop. The flow rate and ΔP were compared to the experimental and analytical values provided in Section 4.3.3.

Computational Control Test results	
Flow Rate (µl/min)	**ΔP (mbar)**
1199.05	28.40
3560.86	85.13
5727.79	138.07
10419.45	255.58

Table 4.11: Computational pressure drop results over the measured microfluidic device and tubes. ΔP is the resulting pressure drop. The flow rate and ΔP were compared to the experimental and analytical values provided in Section 4.3.3.

Computational Microfluidic Channel results	
Flow Rate (µl/min)	**ΔP (mbar)**
354.86	11.08
787.69	24.68
2472.65	78.35
4081.33	130.43
7652.08	248.55

Comparing the Results

Figure 4.19 illustrates the observed pressure difference in the control test. The values used are provided in Tables 4.6, 4.8, and 4.10, and provided in one Table in Appendix Q. A small difference between the computational and analytical model is observed. This could be the result of residual computational errors in tolerances, pressure-velocity coupling, or the treatment of the axisymmetric boundary in the computational model. Since the pressure difference in the computational model resulted in being lower than in the analytical model for a geometry that is based on similar measurements, the error is unlikely to be caused by how the curved walls are approximated using the mesh. An insufficiently refined mesh would be more likely to increase the observed pressure drop in the computational model relative to the analytical model, which is the opposite from the observed result. Therefore it is unlikely to cause this discrepancy and the mesh sensitivity analysis has mitigated the impact of the mesh on the pressure drop. The experimental model exhibited a slightly lower resistance, which may be caused by measurement error of the pressure and flow sensors or deviations of the reported internal diameter of the tube.

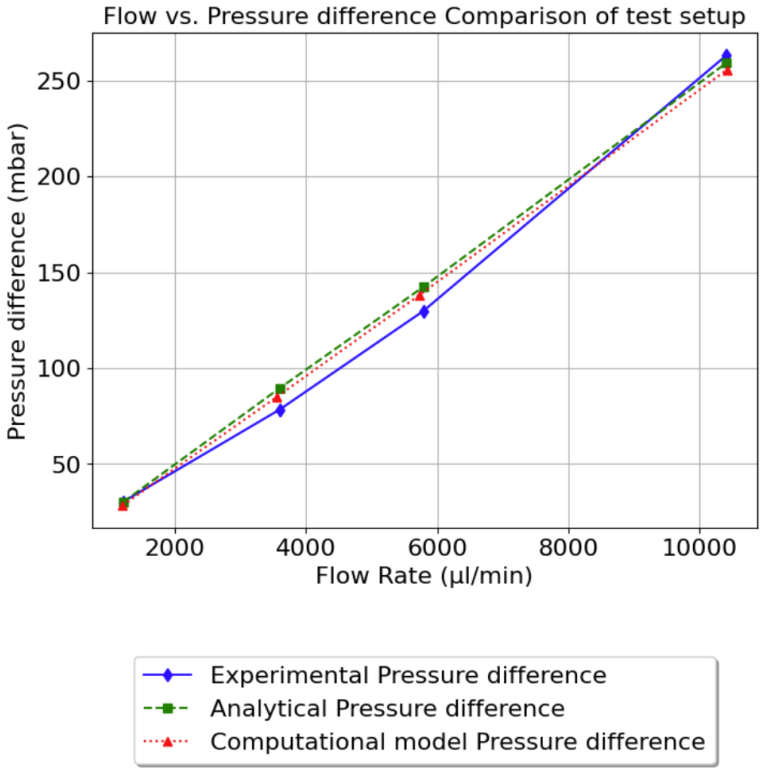

Figure 4.19: The pressure differences for the measured flow rates per model type for the control test.

The same was done for the microfluidic device setup using the 450 µm in diameter channel which was used to represent 0.47 µm outer diameter lateral lenticulostriate arteries. The pressure differences found are visualized with their respective flow rates in Figure 4.20. The data was mentioned in Tables 4.7, 4.9, and 4.11, and is provided in one Table in Appendix Q. The resistance found in the microfluidic channel differs significantly from both the analytical and computational model. The difference was expected; the channel was highly over exposed (a cumulative normalized dose of approximately 20 times more than necessary) when printed, as can be seen in Figure 4.1, and the analytical and computational model are using the intended size. Overexposure using this layer height cannot be prevented, as the minimum required exposure time for layers to attach will result in such overexposure. In reality, the microfluidic channel is smaller than modeled. This has been measured, was confirmed in the previous section, and is visualized in Figure P.5. The expected channel size for the observed resistance is provided in Appendix R and dependent on whether a circular or elliptical cross-section is assumed. If the channel remained cylindrical, the expected diameter would be approximately 330

µm, a 120 µm diameter decrease from intended. While the used settings predicted an 8% difference from the intended area in the pore, as seen in Table 4.2, using the same settings for a longer channel seems to have introduced a larger error. Calculations using the cumulative dose as provided in Figure 4.1 would theorize the channel to be approximately 329 µm in depth and 468 µm in width due to over-curing. The resistance measured included resistance caused by the microfluidic tubing. By increasing the diameter of the microfluidic tubing the resistance added by the tubing will be negligible and the model can be limited to the device. For now, the tubes are a necessary addition to the analytical and computational model to be able to validate the results as a result of the proximity of the diameter of the tubes to the diameter of the channels.

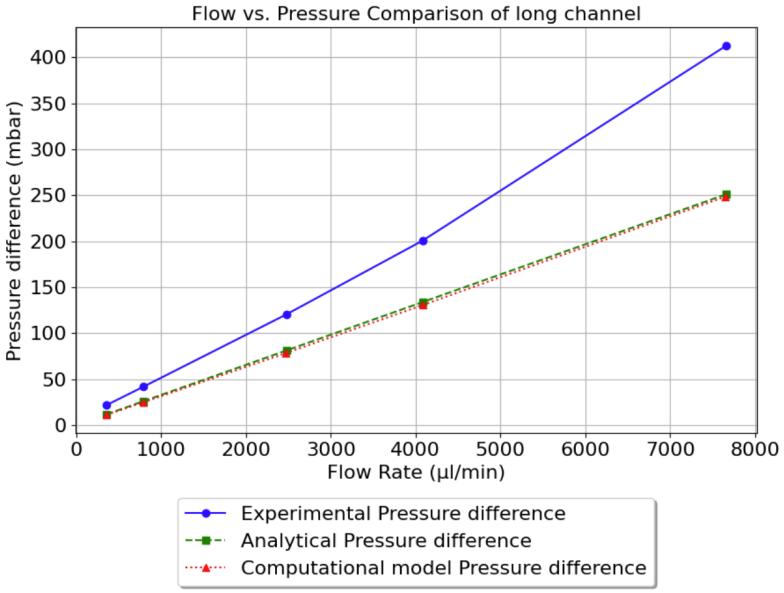

Figure 4.20: The pressure differences for the measured flow rates per model type for testing the resistance of the microfluidic device with an intended diameter of approximately 450 µm.

Apart from Gao *et al.* [136], dimensional inaccuracy is rarely mentioned or explicitly studied when 3D printing flow phantoms for modelling vascular anatomy. The model is highly sensitive to changes in the radius, however, as the output scales with the fourth power of the parameter as seen in Equation 3.7. Gao *et al.* [136] found a good agreement between the PC-MRI and CFD results (mean R^2 = 0.986), but claim that printing resolution and error sufficiently altered the surface texture to explain some of the differences. As Kaneko *et al.* [137] note that the flow volume is reduced, especially in the smaller printed vessels, compared to CFD. It was theorized that reduced diameter due to printing error may play a part. The impact of this diameter is seen in the Hagen-Poisseuile equation, where the radius is to the power of four. Based on the results in this study it is therefore important for flow analysis of small vessels to account for possible geometrical inaccuracies. Other flow studies of 3D printed small vasculature similarly report differences in observed outcomes with computational results. Paccione *et al.* [138] found a discrepancy between the observed pressures in computational and experimental results, reportedly due to the use of compliant material for the in vitro experiment and the assumption of rigid walls in the computational approach. Similarly discrepancies were found by Yu *et al.* [68]. Kaufmann *et al.* [139] report a 10% difference in average flow and velocities between the PIV and CFD results. Kaneko *et al.* [137] note that they observed reduced flow volume in the 4D MRI observations, especially in the small vessels, compared to the CFD. This was theorized to be the result of the phase-contrast acquisition's in-plane resolution. Some studies, such as that of Paccione *et al.* [138], used 3D printing methods other than mSLA. This study underscores the importance of parameter optimization and post printing dimension characterization of microfluidic devices manufactured using mSLA.

4.4. Physiological Devices

The devices mimicking arteries were printed using different settings from the microfluidic channel based on the preceding optimization test. The abstract device was printed at 2.5 seconds exposure time at 50 µm layer height with channels parallel to the build plate. The physiological device was printed using 2.5 seconds exposure time at 50 µm layer height at a 70.21° angle as assessed from the build plate. The exposure time used for printing was close to the calculated minimum of approximately 2.32 seconds required for polymerization (2.5 s) at this layer height to minimize the cumulative dose. This was deemed to be optimal based on the previous optimization results, the angle, layer height, and reduced exposure time were supposed to minimize the error of the area. Both physiological devices required additional resin to be applied due to delamination and consequently leakage occurring. This delamination is likely caused by a decrease in dosage due to the lowered exposure time.

(a) (b)

Figure 4.21: The printed abstract and physiological devices as seen from the back. The pattern visible on the Abstract device is the consequence of supplemental application of resin to close openings cause by delamination. This resin cured and formed to the shape of the curing station floor pattern.

4.4.1. Optical Characterization

Optical measurement is more complicated for more complex geometries due to the introduction of curves and the possibility of overlapping channels. Curves complicate the approach of fitting parallel lines across the total channel length. As a result the decision was made to measure the distance between points from the perspective orthogonal to the printed plane only. The device measurements are depicted in Figures 4.21 and 4.23. The measurements differed slightly compared to the intended channel size. The physiological device approximated the intended channel size, with measurements being 2628 µm, 480 µm, and 476 µm compared to the intended channel sizes of 2660 µm, 500 µm, and 500 µm, respectively. A slightly larger variation was observed in the abstract device, with measurements being 380 µm, 519 µm, and 783 µm for intended channel diameters of 400 µm, 500 µm, and 800 µm, respectively. The parallel printing orientation and observed delamination may have influenced the resulting dimensions and influenced the measurements. The effect of over curing on channel depth was not properly assessed.

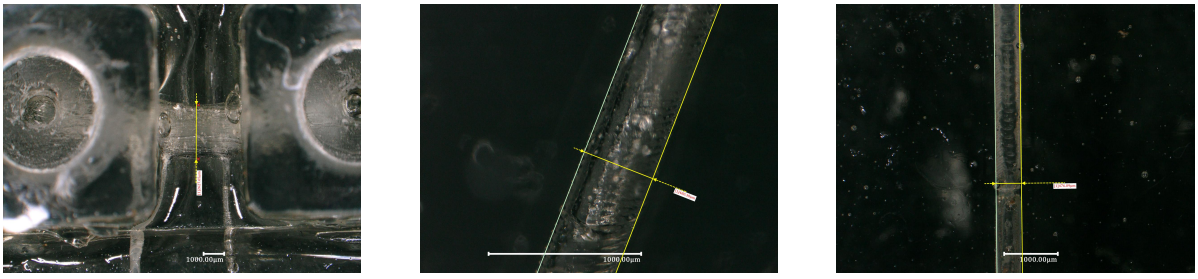

(a) (b) (c)

Figure 4.22: Meaurements of the physiological device. (a) Measurement of the replicated M1 segment of the MCA 2628 µm. (b) Measurement of the curved channel 480 µm. (c) Measurement of the straight channel 476 µm.

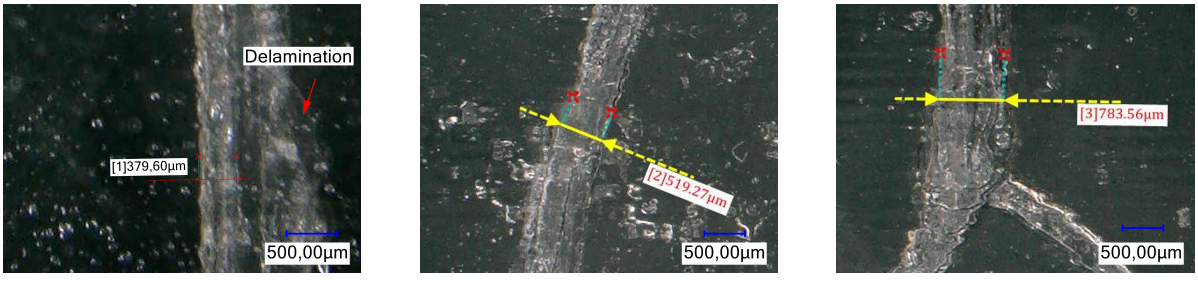

(a) (b) (c)

Figure 4.23: Measurements of the abstract device. (a) [1] 380 µm with visible delamination complicating the measurement of the dimensions, (b)[2] 519 µm, and (c) [3] 784 µm. The measurement was difficult due to delamination obscuring the channel walls in some areas.

4.4.2. Experimental Flow Test Results

A flow test was conducted to showcase the functionality of the manufactured channels. In addition, since the pressure sensors had a different internal diameter from the flow sensor, placement of a single pressure sensor would alter the distal resistance and flow per channel reducing the informational value of the measurement. As such the main information of value is the distribution of flow between the different vessels. The microfluidic devices in the experimental setup as explained in Section 3.7.2 are visualized in Figure 4.24. The measured flow rate at the inlet of both models was obtained by applying a 300 mbar pressure in the experimental setup. The measured flow rates are provided in Tables 4.12 and 4.13 and were averaged over time. The labels at the outlets in Figure 4.24 relate to the inlet and outlet ports as described in Tables 4.12 and 4.13. For the abstract device, a faster flow rate was

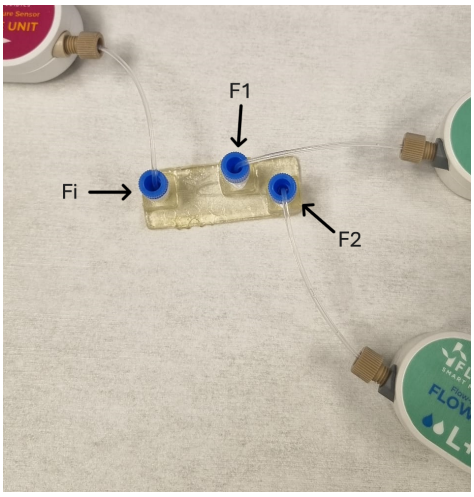

(a) The abstract device.

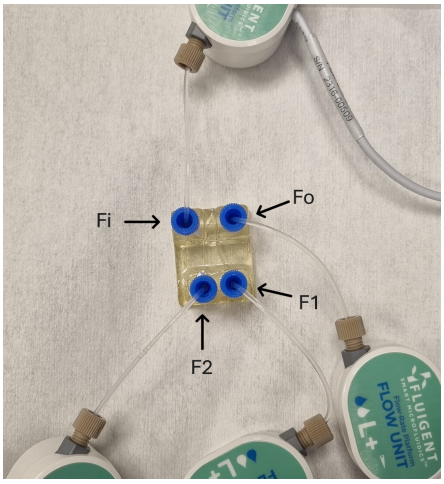

(b) The physiological device.

Figure 4.24: A visualization of the experimental setup containing microfluidic devices and tubing. (a) The abstract arterial device connected to measurement devices using 10 cm 0.508 mm internal diameter tubes. (b) The physiological device connected to measurement devices using 10 cm 0.508 mm internal diameter tubes. Flow was induced in both cases at Fi. The ports correspond to the ports as presented in Figures 3.3 and 3.4.

observed at the smaller diameter channel at port F1 compared to port F2. The resistance of port 2 may be higher due to the increased channel length. Additionally, the tapering due to the fillet at the bifurcation reduces the length of the channel directed towards port F1 at the smallest diameter of 400 µm. Finally, the delamination at this channel may increase its cross-sectional area and decrease its resistance. The physiological device exhibited similar volumetric flow rates at ports F1 and F2. The outlet at Fo was observed to have the highest flow rate, which was expected due to its relatively low resistance resulting from a larger diameter and shorter distance from the inlet at port Fi. F2 has a slightly shorter path to the port, but the resistance may be increased due to a narrowing of the channel as observed in Figure 4.16, mimicking a small arterial occlusion.

Table 4.12: Flow data for the abstract device.

Port	Measured Flow (µl/min)
Fi	3718.6
F1	2193.0
F2	1573.6

Table 4.13: Flow data for the physiological device.

Port	Measured Flow (µl/min)
Fi	4132.4
Fo	1701.0
F1	1246.1
F2	1252.3

Planar microfluidic devices replicating physiological small vessels have been successfully fabricated using mSLA. This study did not yet print three dimensional patient-specific geometry such as published by Li *et al.* [62]. Their recently published open source data and segmenting approach can be used to print patient-specific lateral lenticulostriate arteries.

5

Conclusions and Future outlook

5.1. Conclusions

The main goal of this study was to investigate mSLA for developing microfluidic devices of small vessels, in particular the lateral lenticulostriate arteries branching from the medial cerebral artery. These planar microfluidic devices were successfully printed using a commercially available photopolymer and mSLA printer, and flow was induced in the channels using water. Pores down to 270 µm in diameter were fabricated using suboptimal settings, and smaller channels can likely be fabricated using exposure times calculated to minimize the cumulative dose inside the channel for this photopolymer and UV wavelength and light intensity.

Furthermore, the impact of the exposure time, the layer height, and the orientation on the roundness and area of circular cross-sectional pores have been evaluated and related to the printing mechanics. This information contributes to 3D-printing microfluidics using mSLA in general, and is not limited to arterial phantoms. Layer height did not affect the roundness of the pores printed at an angle, whereas exposure time did. Again, this can likely be attributed to the cumulative normalized dose and the method of measurement. The overexposure of resin at the bottom of the channel may cause polymerization, and as a result change the cross-sectional shape to an ellipse. Examples of this were particularly visible in the overexposed parallel printed channels. Pores printed orthogonal to the build plate are uniformly impacted by the optical proximity effect, meaning a loss in dimensional accuracy but not necessarily in roundness. Angled channels were more accurate in replicating the intended area, but were less round compared to orthogonally printed pores. Increasing the angle is likely to decrease the effect of slight overexposure on the roundness and area. While pores angled according to the arctan rule proved to be significantly different from pores printed at different angles, this study cannot definitively claim this orientation to be optimal or superior to other angles. While this study did not investigate complete three-dimensional geometry, the information provided by researching the different orientations is informative for more complex shapes. Fitting ovals to the pores did not capture roughness along the edge, which was a major limitation in evaluating the roundness of channels with large layer height. The lack of studies on the *in vivo* cross-sectional roundness of small vessels complicates the comparison to physiological vessels.

Finally, This work has shown it is possible to print planar microfluidic devices replicating small cerebral vessels using mSLA, and to differentiate between channels. The introduction of bifurcations did not complicate the printing process. Deviations from the intended dimensions may still have altered the expected flow behavior. Several key challenges in the printing process and validating printed microfluidic devices have been identified. The main problem is overexposure causing a decrease in the cross-sectional area. The radius is influential for the resistance, causing discrepancies when attempting to validate computational models. Additionally, issues such as delamination, leakage, and print failures may complicate the fabrication of a microfluidic device using mSLA 3D printing. Overall, this study serves as a valuable source of practical information on the fabrication of microfluidic devices intended to imitate small vessels.

5.2. Future outlook

5.2.1. Photopolymer and 3D printing

To further improve the fabricated phantoms, a flexible photopolymer resin can be developed to better mimic the stiffness of small cerebral vessels. This material should ideally have a low curing depth to enable precise printing of small channels. However, the effect of material flexibility on channel integrity should be evaluated, as excessive flex may cause misalignment or deformation of embedded microchannels during printing.

For enhanced resolution, an mSLA or DLP printer with a 385 nm or lower wavelength could be used. While a smaller pixel width improves the resolution of orthogonal channels, a lower wavelength may also allow for better fabrication of parallel-aligned channels. One of the main current limitations is the occlusion of small, parallel channels due to overcuring. Alternative 3D-printing methods could be compared for the fabrication of microfluidic devices to assess their ability to reduce these effects.

Additionally, a blood analog should be developed to replace water as the working fluid. The ideal blood analog should replicate key rheological properties, including viscosity, non-Newtonian behavior, and surface tension, to improve physiological relevance in flow studies.

5.2.2. Optimization of Printing Parameters

Several printing parameters remain unexplored, such as anti-aliasing, lift speeds, and post-processing variations. Anti-aliasing may be particularly useful in reducing surface roughness caused by the staircase effect in angled channels. Additionally, optimizing curing time and replacing VAT film at regular intervals or prior to important prints may improve reproducibility and accuracy, particularly for high-precision applications. The effect of the orientation should be adjusted for the increased error of the area and roundness of smaller channels, and the increased number of smaller channels for larger angles. The impact of the layer height should be re-evaluated at constant cumulative dose and angle. Software could be developed that adjusts imported CAD dimensions to use the overcuring for that specific light and photopolymer interaction to reach the desired geometry.

The internal dimensional accuracy of printed channels should also be assessed more objectively. In this study, manual fitting of ovals to measure small pores may not fully capture the true channel geometry. More robust measurement techniques, such as micro-CT scanning, profilometry, or high-resolution optical coherence tomography, could provide a more precise evaluation of print consistency. Testing the reproducibility of channels printed under identical conditions will help quantify variability and reliability.

5.2.3. Patient-Specific Applications and Computational Model Validation

Future studies could explore patient-specific vascular models, where printed structures are directly compared to segmented anatomical data from imaging sources such as MRI or CT angiography. By quantifying the error between printed structures and computational models, it will be possible to separate fabrication-related errors from computational modeling errors. This step is beneficial to improving the reliability of *in silico* predictions for vascular disease modeling, surgical planning, and flow simulations. Finally, accurate small vessel models could be used for flow studies of patient-specific diseased vessels to validate computational models.

A

3D Printed Cerebral Arteries

Methods
A literature search was conducted in February 2024 in SCOPUS and PubMed according to the PRISMA checklist to qualitatively assess the current standing in the literature of 3D printing in vitro models of cerebral vasculature [140]. The following search queries were formulated to be similar and used to search the titles and abstracts in the databases:
For PubMed:

> (”additive manufactur*” [tiab] OR ”3d print*” [tiab] OR “Rapid Prototyping” [tiab]) AND (brain [tiab] or cerebr* [tiab] or neuro* [tiab] or ”circle of willis” [tiab]) and (vascul* [tiab] or arter* [tiab] OR vessel [tiab] OR microvascul* [tiab]) AND (”fluid dynamics” [tiab] OR ”hemodynamics” [tiab] OR ”blood flow”[tiab] OR “flow rate” [tiab])

and for SCOPUS:

> TITLE-ABS ((”additive manufactur*” OR ”3d print*” OR ”Rapid Prototyping”) AND (brain OR cerebr* OR neuro* OR ”circle of willis”) AND (vascul* OR arter* OR vessel OR microvascul*) AND (”fluid dynamics” OR ”hemodynamics” OR ”blood flow” OR ”flow rate”))

The search queries are constructed to involve keywords for four aspects. These are the use of (1) additive manufacturing for (2) vasculature of (3) the brain with (imitation of) (4) blood flow. Eligible studies were included by one independent researcher for qualitative analysis if they pertained to 3D printed vessels of hollow (proximal branches of) intracranial arteries, and perfused with a fluid. Reviews were excluded, since relevant articles should already be obtained using this search. Consequently, which vessels were recreated, the smallest achieved diameter, the printer or printing technique used, the materials used, whether flow simulations were performed, the fluid used, whether pathology was researched, and the method of flow visualisation were identified and extracted from the included reports.

A.1. Results

The search yielded 69 reports (45 from SCOPUS and 24 from PubMed), of which 19 were duplicates. Data was extracted from the 34 resulting reports. The main reason for exclusion was the printing of alternative structures such as stents. The studies and their extracted data are provided in table A.1 and table A.2.

Table A.1: Articles on 3D printing cerebral vasculature including fluid flow: Printing technique

Article	Arteries	Min d (mm)	Indirect 3D printing	Printer	Material
1. Paccione *et al.* [138]	CoW, ICA	3	no	PolyJet, Stratasys Eden 260V, Creality Ender 5	Tango +, PLA for aorta
2. Yu *et al.* [68]	ICA, VA, CoW, ACA, MCA, PCA	0.8	no	prototype machine	silicone
3. Pravdivtseva *et al.* [141]	CoW, BA, ICA	6	no	SLA (Form 2, Formlabs)	methacrylic acid esters and a photoinitiator (Clear Photoreactive Resin, Formlabs)
4. Tian *et al.* [142]	-	2	yes	SLA (Form 2, Formlabs)	PDMS, epoxy-based resin (epoxies, acrylate, oxetane, and photo initiators)
5. Kim *et al.* [143]	BA	-	yes	FDM, Fortus 400mc, Stratasys	ABD, PDMS
6. Reddy *et al.* [65]	ICA, MCA	-	no	SLA (Form 2, Formlabs)	Clear Resin (Formlabs)
7. Falk *et al.* [144]	ACA1, MCA1, ICA	3.54	no	SLA (Form 2, Formlabs)	Rigid polymer
8. Shaughnessy *et al.* [145]	MCA, ICA	4	-	-	Silicone
9. Sommer *et al.* [146]	CoW, MCA1, ACA1, PCA1	2	no	PolyJet, Stratasys Object 500	Tango+
10. Joseph *et al.* [69]	CoW and branches	1	no	PolyJet, Stratasys Object 500	A27 Shore hardness photopolymer
11. Levitt *et al.* [147]	-	-	yes	SLA (Form 2, Formlabs)	photoreactive resins, PDMS
12. Chivukula *et al.* [148]	Para-ophtalmic, mid-BA	-	yes	FDM, Flash Forge Creator Pro	PLA, silicone
13. Li *et al.* [149]	CCA, ICA, ECA	-	yes	FDM	ABS
14. Ho *et al.* [150]	ICA, MCA, PCA	1.3	yes	FDM (Model DX; CreatBot 3D Printer)	PLA, HIPS
15. Seong *et al.* [151]	CCA, ICA, ECA	-	yes	FDM (Dimension Elite)	ABS, silicone
16. Kaufmann *et al.* [139]	Aorta, Subclavia, CCA, VA	-	yes	PolyJet, Stratasys Object 500	silicone
17. Sherman *et al.* [152]	BA, PCA	1.95	yes	SLA	Accura 25, Elastomer 184 silicone
18. Souza *et al.* [153]	-	-	yes	SLA, ProJet 1200	Visijet FTX Green resin, PDMS
19. Yi *et al.* [154]	ICA	6.4	no	prototype machine	WaterShed XC 11122 materials
20. Deene *et al.* [155]	CoW, BA, PCA, ACA, MCA, VA, CA	-	yes	FDM, Dreamer Flashforge	PLA, hydrogel, silicone
21. Nagesh *et al.* [156]	ICA	-	no	-	-
22. Encarnacion Ramirez [157]	ICA, ACA, MCA	2.68	yes	-	PLA, silicone
23. Sommer *et al.* [158]	CoW , ICA	-	no	PolyJet, Stratasys Eden 260V	Tango+
24. Jang *et al.* [159]	BA	1.8	no	Ultimus V dispenser Nordson EFD	Silicone, fugitive ink, matrix
25. Kaneko *et al.* [137]	-	-	yes	FDM, Mojo 3D printer	a copolymer of acrylonitrile, butadiene, and styrene, silicone
26. Gao *et al.* [136]	-	2	no	SLA, home-built 3D printer	photosensitive epoxy-based resin
27. Ariana *et al.* [100]	CoW, ICA		no	PolyJet, Stratasys Eden 260V	Tango+
28. Lauren *et al.* [160]	CoW, ICA		no	PolyJet, Stratasys Eden 260V	Tango+
29. Liu *et al.* [161]	-	3	yes	FDM, D-Force 400	PLA, PVA, silicone
30. Anderson *et al.* [67]	-	3-4	no	FDM, MakerBot Replicator 2 3D printer	PLA, Makerbot Flexible Filament
31. Carlsohn *et al.* [66]	BA	< 1	no	SLA	transparent resin
32. Clark *et al.* [162]	Aorta, CCA, VA	4	no	SLA, RP printing	Accura 60 polymer
33. Zhu *et al.* [163]	VA, BA	10	yes	SLA, SCPS350	Resin, silicon
34. Kamoda *et al.* [164]	ICA	6	yes	SLA	Resin, silicon

Table A.2: Articles on 3D printing cerebral vasculature including fluid flow: Flow measurement technique

Article	Comp. model	pulsatility	fluid used	patient-specific	pathology	Measurement/ visualization
1. Paccione *et al.* [138]	CFD	yes	W/G:60/40	yes	Stenosis	Ultrasound and pressure sensors
2. Yu *et al.* [68]	1D	yes	W/G:75/25 by weight (RI: 1.41, μ: 0.0026 Pa·s, ρ: 1050 kg/m^3)	yes	Healthy	Ultrasound flow meter and pressure sensors
3. Pravdivtseva *et al.* [141]	-	no	W/G:60/40 by volume (μ: 0.00372 Pa·s)	yes	Aneurysm	3D RA and 3T MRI
4. Tian *et al.* [142]	CFD	yes	W/G:40.6/59.4 by weight (μ: 0.0048 Pa·s, ρ: 1080 kg/m^3)	yes	Aneurysm	3T MRI
5. Kim *et al.* [143]	-	-	W/G:60/40 by weight (RI: 1.413, kinematic μ: $8.7{\cdot}10^{-6}$ m^2/s.)	yes	Paramedian pontine infarction (PPI)	PIV
6. Reddy *et al.* [65]	-	yes	saline solution	yes	Stroke	Camera, RA
7. Falk *et al.* [144]	-	yes	W/G:60/40 (μ: 0.00379 Pa·s, ρ: 1111 kg/m^3)	yes	Healthy	3D DSA
8. Shaughnessy *et al.* [145]	-	yes	-	yes	Aneurysm	3D DSA, ultrasound flow meter
9. Sommer *et al.* [146]	-	yes	water	yes	Embolus	DSA
10. Joseph *et al.* [69]	-	yes	ICG dye (VERDYE 5 mg/ml)	yes	Aneurysm	Microscope
11. Levitt *et al.* [147]	CFD	yes	endothelial cell growth medium and 3.5% dextran	yes	Aneurysm	Microscope
12. Chivukula *et al.* [148]	-	-	-	yes	Aneurysm	parallel and monochromatic X-ray beam
13. Li *et al.* [149]	FEM	no	water	yes	Healthy	Thermocouples
14. Ho *et al.* [150]	-	yes	BMF with water, dextran, surfactant, glycerol, and nylon particles	yes	Aneurysm	Plane wave imaging
15. Seong *et al.* [151]	-	yes	W/G:60/40 by volume (μ: 0.0036 Pa·s, ρ: 1098 kg/m^3)	Idealized	Healthy	7T MRI
16. Kaufmann *et al.* [139]	CFD	no	PIV newtonian test fluid (μ: 0.007 Pa·s)	yes	Healthy	PIV
17. Sherman *et al.* [152]	-	yes	W/G:75/25 (μ: 0.00245 Pa·s, ρ: 1059 kg/m^3)	yes	Aneurysm	Camera
18. Souza *et al.* [153]	-	no	W/G:39/61 by weight (RI: 1.412)	yes	Aneurysm	PIV
19. Yi *et al.* [154]	CFD	yes	water	yes	Aneurysm	PIV
20. Deene *et al.* [155]	COMSOL	yes	deionized water doped with Nickel sulphate	yes	Healthy	Pressure sensors
21. Nagesh *et al.* [156]	-	yes	W/G:60/40	yes	Aneurysm	HSAngio
22. Encarnacion Ramirez [157]	-	yes	Liquid with paprika oleoresin (E160c) dye	yes	Aneurysm	-
23. Sommer *et al.* [158]	-	yes	-	yes	Thrombus	CTA
24. Jang *et al.* [159]	CFD	no	media	Idealized	Aneurysm	PIV
25. Kaneko *et al.* [137]	CFD	yes	W/G	yes	aterovenous malformation	3T MRI
26. Gao *et al.* [136]	CFD	yes	W/G:40.6/59.4	yes	Aneurysm	3T MRI
27. Ariana *et al.* [100]	-	yes	W/G:60/40 (μ: 0.00421 Pa·s)	yes	Healthy, stenosis, anatomical variation	DSA, Pressure sensor
28. Lauren *et al.* [160]	-	yes	W/G:60/40 (μ: 0.0037 Pa·s)	yes		Pressure sensor
29. Liu *et al.* [161]	-	yes	dye solutions	yes	Aneurysm	-
30. Anderson *et al.* [67]	-	no	water containing 0.2 mM gadopentetate dimeglumine	yes	Aneurysm	3T MRI
31. Carlsohn *et al.* [66]	-	yes	W/G	yes	Aneurysm	PIV
32. Clark *et al.* [162]	CFD	no	W/G:60/40 by volume (μ: 0.003801 Pa·s, ρ: 1104 kg/m^3)	Idealized	Embolism	PIV
33. Zhu *et al.* [163]	-	no	W/G (μ: 0.0106 Pa·s, ρ: 1157 kg/m^3)	yes	Healthy	PIV
34. Kamoda *et al.* [164]	-	yes	W/G:54/46 (μ: 0.00407 Pa·s, ρ: 1100 kg/m^3)	yes	Aneurysm	PIV

B

List of 3D printers and Photopolymers Considered

B.1. 3D printing Machines

Table B.1: Specifications of 3D printers in different labs. The sources of the images are provided.

Printer (type)	Resolution	Build Platform Size
Envisiontec Micro HiRes Plus (DLP) [165] 	X/Y 30 micron, resolution in Z 25–75 µm, UV wavelength 385 nm	45 x 28 x 100 mm
Prusa SL1 (LCD) [166] 	X/Y 100 micron, layer height: 25-100 µm, UV wavelength 405 nm	120 x 68 x 150 mm
FormLabs 3+ (LFS) [167] 	X/Y 25 micron, Layer height : 25-300 µm, Laser wavelength 405 nm	145 × 145 × 193 mm
Anycubic Photon M3 Premium (LCD) [168] 	X/Y 28.5 micron, layer height 10 – 100 µm, UV wavelength 405 nm	218.88 x 123.12 x 250 mm
Elegoo Mars 4 9k (LCD) [107] 	X/Y 18 micron, Layer height 10 – 200 µm, UV wavelength 405 nm	153.36 x 77.76 x 175 mm

B.2. Photopolymers

Table B.2: The materials assessed for their suitability with sources for the pricing. Prices were assessed at April 12th 2024. A preliminary selection was obtained from Guttridge *et al.* [101].

Material	**Intended Printing Technique**	**Wavelength or Energy**	**Properties**	**Price**	**biocomp. Cert.**
FormLabs BioMed Clear [169]	SLA	-	Limited to Formlabs, expensive	-	-
FormLabs Dental Clear [170]	SLA	-	Limited to Formlabs, expensive	-	-
Liqcreate Bio-Med Clear [106]	MSLA, SLA, DLP	385 – 420 nm	biocompatible, transparent	€90.90 per kg	Iso 10993-5
Loctite MED 413 [171]	DLP	4 mW/cm² to 8 mW/cm²	biocompatible, transparent	Approximately €516.00 per liter	Iso 10993-5, 10, 23
Accura ClearVue [172]	SLA (not compatible with 405 nm)	-	biocompatible, transparent	Not specified	Iso 10993-5
3Dresyn Biotough D70 MF Monomer Free or Based [173]	SLA, LCD, DLP	405 nm, not limited to	Options for color, monomer based or free, printer type	€242.00 per 500 grams	Iso 10993-5
3Dresyn BioTough D80 MF Monomer Free or Based [173]	SLA, LCD, DLP	405 nm, not limited to	Options for color, monomer based or free, printer type	€242.00 per 500 grams	Iso 10993-5
3Dresyn Biotough D90 MF Monomer Free or Based [173]	SLA, LCD, DLP	405 nm, not limited to	Options for color, monomer based or free, printer type	€242.00 per 500 grams	Iso 10993-5
Microfluidic 3Dresyn MF RLV1 Clear Rigid [174]	SLA, LCD, DLP	405 nm	Transparent, rigid, and biocompatibleatible	€605.00 for 500 grams	Iso 10993-5
B9Creations BIORES RED [175]	DLP	385 – 405 nm	Reddish hue, biocompatible	$315.00 per kg	“ISO 10993”
NextDent Ortho flexible [176]	DLP, mSLA (LCD)	108 Watt UV-A (315–400 nm), 108 Watt UV-Blue (400–550 nm)	Clear, biocompatible, flexible	€249.00 for 1.2 liters	Class 2a
NextDent Ortho Clear [177]	DLP, mSLA (LCD)	108 Watt UV-A (315–400 nm), 108 Watt UV-Blue (400–550 nm)	Clear, biocompatible	€249.00 for 1.2 liters	Class 2a

Table B.2: The materials assessed for their suitability with sources for the pricing. Prices were assessed at April 12th 2024. A preliminary selection was obtained from Guttridge *et al.* [101].

Material	**Intended Printing Technique**	**Wavelength or Energy**	**Properties**	**Price**	**biocomp. Cert.**
printodent® GR-18.2 IB [178]	DLP	385 nm UV	Transparent, flexible, biocompatible	-	Iso 10993-5
SprintRay EU Surgical Guide 3 Clear Resin [179]	DLP	≤ 405 nm	biocompatible , transparent	£246.90 for 1 kg	Not specified
Pro3dure GR-10 Guide [180]	DLP	385, 405 nm	biocompatible, translucent or transparent	€280.00 for 1 kg	Iso 10993-5
LOCTITE 3D IND405 [181]	DLP	3 mW/cm² to 7 mW/cm²	biocompatible, slightly flexibleible	€215 for 1 kg	Iso 10993-5
SprintRay IDB2 [179]	DLP	Not specified	biocompatible and transparent	$299.00 for 1 kg	Not specified
Harzlabs Dental Clear PRO [182]	DLP, LCD	Not specified	biocompatible, clear	€199.00 for 1 kg	Iso 10993-5
DSI 3D Clear Tray Resin [183]	mSLA	Not specified	biocompatible and clear	Quote	Not specified
DETAX – Medicalprint® Clear [184]	mSLA, DLP	378–388 nm	Class 2a biocompatible, clear	€324.00	Class 2a
Nexa3D NXE KeyGuide Resin [185]	DLP	385 – 405 nm	Class 1 biocompatible, clear	$1,250.00 for 5 kg, $275.00 for 1 kg	Class 1
Nexa3D NXE xMed 412 Resin [186]	Not specified	Not specified	biocompatible, clear	$1,925.00 for 5 kg	Iso 10993-5
Detax Freeprint® Mould 3D [187]	mSLA, DLP	UV 405 nm	Class 2a biocompatible, clear	€179 for 500 grams	Class 2a
Detax Freeprint® Ortho [188]	mSLA, DLP	385, 405 nm	Class 2a biocompatible, clear	€389.50 for 1 kg	Class 2a
FREEPRINT® Splint [189]	mSLA, DLP	385, 405 nm	Class 2a biocompatible, clear	€321 for 1 kg	Class 2a
MED-AMB 10 [190]	DLP	-	biocompatible, amber hue, translucent	€225.00	Iso-5
flexible 63A Resin Clear [191]	mSLA (LCD)	385 – 405 nm	Very flexible, extremely transparent, not biocompatible	€79.99 for 500 grams	-
Accura Phoenix [192]	405 nm DLP	405 nm	Not biocompatible, clear after post-processing	-	-
Design Concept Series: MSLA Modeling Clear [193]	mSLA	-	Not biocompatible	-	-

Table B.2: The materials assessed for their suitability with sources for the pricing. Prices were assessed at April 12th 2024. A preliminary selection was obtained from Guttridge *et al.* [101].

Material	**Intended Printing Technique**	**Wavelength or Energy**	**Properties**	**Price**	**biocomp. Cert.**
Liqcreate Clear Impact [194]	mSLA	-	Not biocompatible	-	-
eSUN Transparent High Precision PLA [195]	-	-	Not biocompatible, clear	-	-
Resione G217 Clear Non-yellowing Tough ABS Like 3D Printer Resin [196]	mSLA	-	Not biocompatible, clear	-	-
Nova3D Ultraclear [197]	mSLA, DLP	395-410	Not biocompatible	€34 for 500 grams	-
SIRAYA TECH CRAFT - 1 KG - HIGH CLEAR [198]	mSLA, DLP	405	Not biocompatible	€56 for 1000 grams	-
Piocreat High Transparency Clear Resin [199]	mSLA, DLP	-	Not biocompatible	-	-
Formfutura Engineering LCD Resin – flexible 82A [200]	mSLA, SLA, DLP	385 – 420 nm	flexible, translucent, not biocompatible	-	-
Accura SL 5530 [201]	-	-	Not biocompatible	-	-
Accura CastPro [202]	-	-	Not biocompatible	-	-
Accura 60 [203]	-	-	Not biocompatible	-	-
Accura ClearVue Free (SL 7870) [204]	-	-	Not biocompatible	-	-

C

Printer and Material Selection

C.1. Printer Selection

The selected printer is the **Elegoo Mars 4 9k**. Five available printers at the MNE department at the Technical University of Delft were compared and are listed in Appendix B. The one-time cost of acquiring the machine was not considered. The printer was first selected after which a suitable material was picked. Of the available printers, the FormLabs is limited to materials as provided by the company itself. It is the only LFS machine on the list. All machines except for the Envisiontec MicroHiRes Plus operated at 405 nm wavelength. The Envisiontec Micro HiRes Plus is the only DLP machine, has a UV wavelength of 385 nm, and has the smallest build plate size. The smallest pixel size is the Elegoo mars 4 9k. The largest build plate size was seen in the Anycubic Photon M3 Premium. A Harris profile was constructed to visualize the decision making progress in Figure C.1. If a machine was the best, they would score the highest (++). If they would perform worst, they would score the lowest (- -). One exception is for the criterium of wavelength, where all machines operating at the higher wavelength were given the same score since no machine performed significantly worse than another (-). Build plate sizes that facilitated prints of 5x5x5 cm and pixel sized below 50 µm were considered good and given a (+). The build plate size was selected so that the circle of Willis would be certain to fit with space for small branches [90]. The optimal machine was the Elegoo Mars 4 9k, since smaller pixel size was prioritized over build plate size.

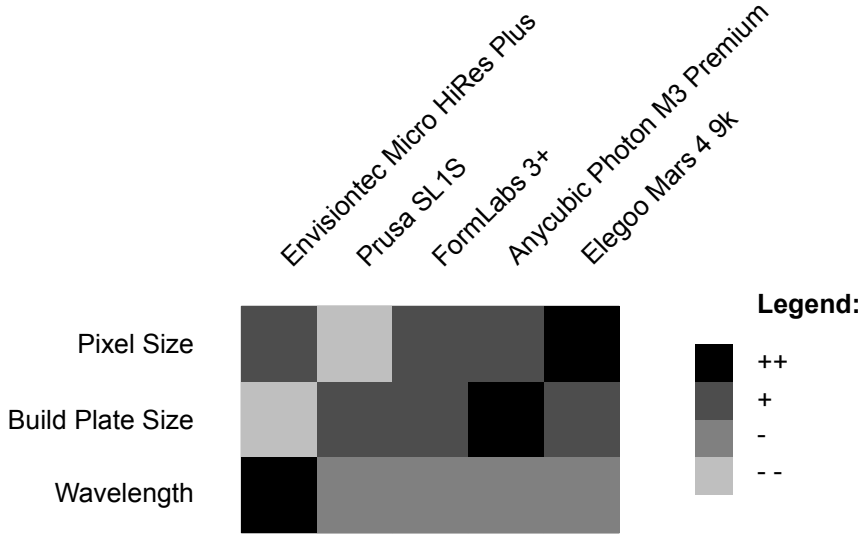

Figure C.1: A Harris Profile for comparing the available 3D printers.

C.2. Photopolymer Selection

The material selected was the **Liqcreate Bio-Med clear**. The material selection was done using a compiled list of commercially available transparent or translucent materials as provided in B based in part on materials as listed by Guttridge *et al.* [101] with additional research. This list is by no means complete and materials leave and enter the market continuously. The materials suitable for the Elegoo Mars 4 9k were compared based on the mentioned level of transparency (if elaborated on), the price, the biocompatibility, and the flexibility in this respective order of priority. Transparency is important for measurement of the internal channels and for further analysis. Price per kg is important as a result of the limited budget for this project. Biocompatibility and flexibility were no priorities. Biocompatibility is usually well defined based on ISO 10993 standards or class 1/2 biocompatibility as used for CE marking. Class 1 and 2 devices both adhere to ISO 10993-5, referring to in vitro cytotoxicity. Flexibility is mostly provided in the form of a Young's modulus. Flexible materials are rarely used for microfluidic devices and the advised range in layer height is usually higher compared to more rigid materials. Materials optimized for microfluidic applications, such as Microfluidic 3Dresyn MF RLV1 Clear Rigid resin, exist but are comparatively expensive. Materials with a suitable wavelength, known price after requesting a quote if a reply to the request was made, and that were known to be transparent were compared. If flexibility or biocompatibility were not mentioned, the materials were assumed to be rigid and non-biocompatible. Biocompatibility adhering to ISO-10993-5 was preferred, Class 1 and 2 materials were assumed to comply with ISO-10993-5. The Harris Profile for the materials is provided in Figure C.2. Materials with a cost below 150 euros per kg were considered optimal (++). If half a kg was available for under 150 euros, the material was denoted as good (+). Materials that had data of the transparency denoted as clear, or had images provide of the clarity were considered optimal (++). They were good if they were mentioned to be clear without supporting data or images. If the material was mentioned to be translucent or had a colored hue the material would be subpar (-). As mentioned, biocompatibility tested as cytotoxicity according to the ISO-10993-5 were considered optimal (++). Materials without mention of biocompatibility were assumed not to be biocompatible (- -). Finally, flexibility was cosnidered optimal if data on the material flexibility was available in the form of a Young's modulus. The optimal material resulting from this analysis was Liqcreate Bio-Med clear.

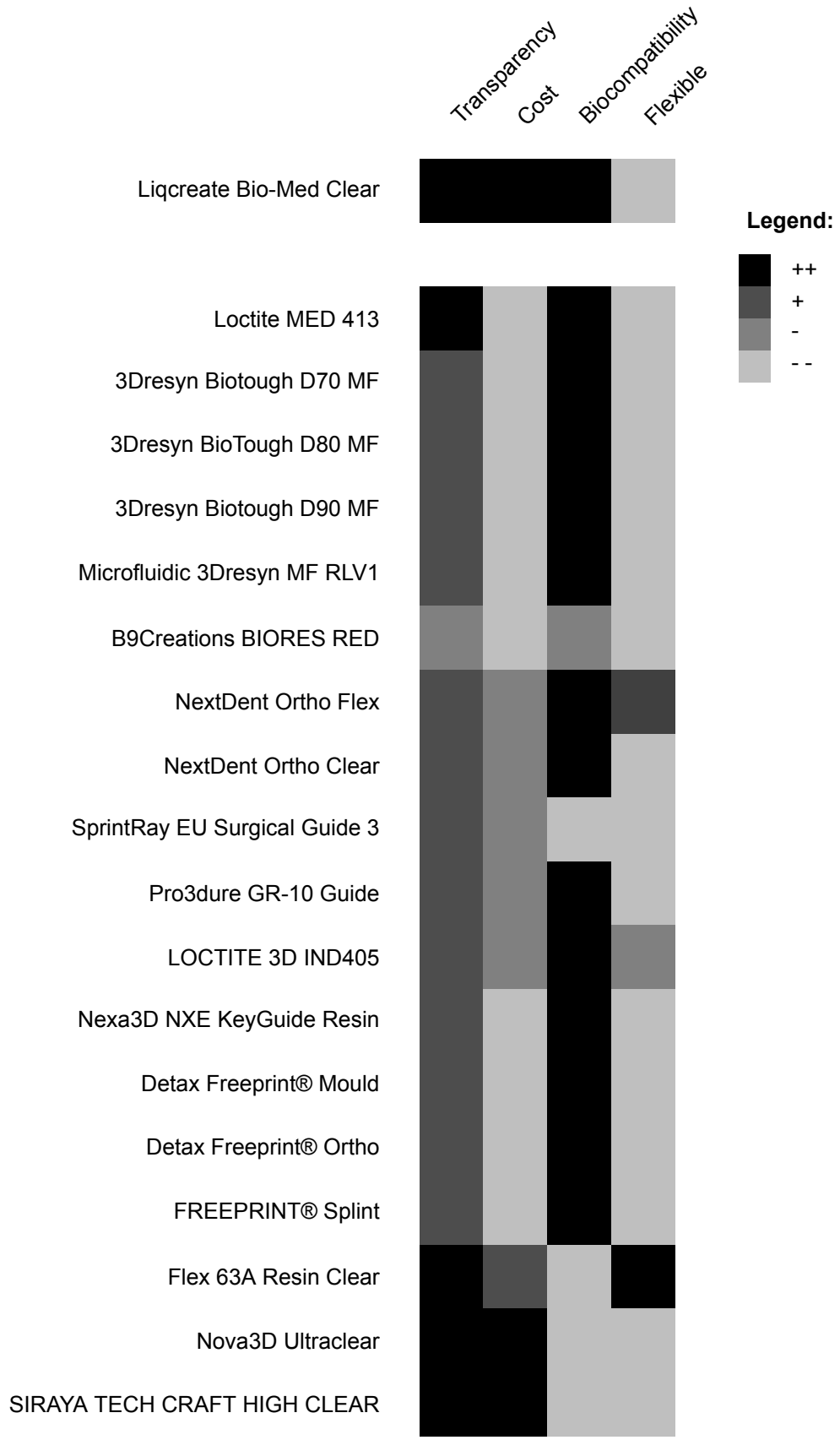

Figure C.2: A Harris Profile for comparing materials based on transparency, cost, biocompatibility, and flexibility, prioritized in this order.

D

CAD Designs Dimensions

D.1. Test Device Containing Pores

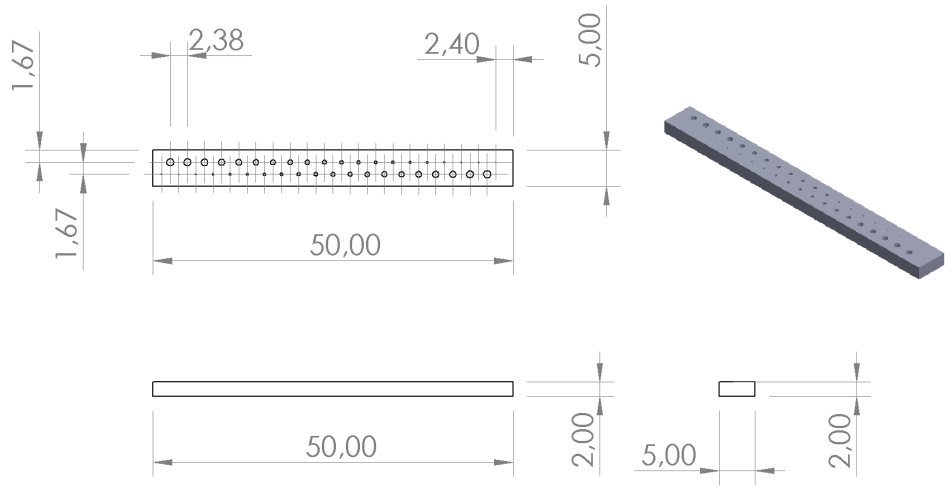

Figure D.1: A SolidWorks drawing illustrating the measurements of the CAD design of the test object in millimeters.

D.2. Test Device for connectors and microfluidic setup

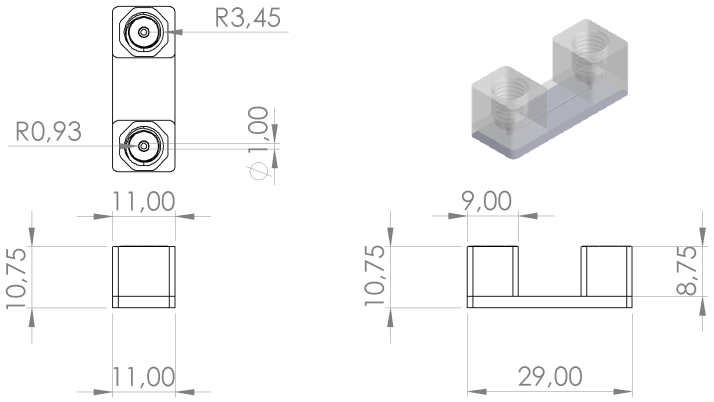

Figure D.2: The dimensions of the test device used for testing the connectors and to test imaging.

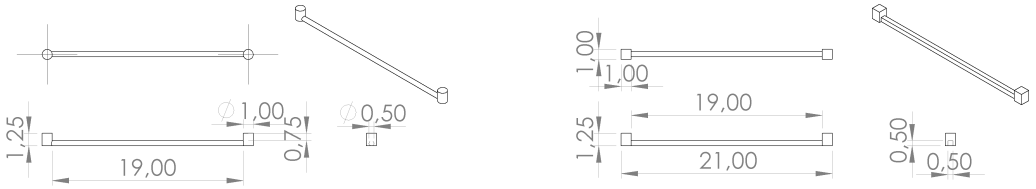

(a) (b)

Figure D.3: The channels as used in the object shown in Figure D.2. (a) shows the round channel and (b) illustrates the square channel.

D.3. Connectors

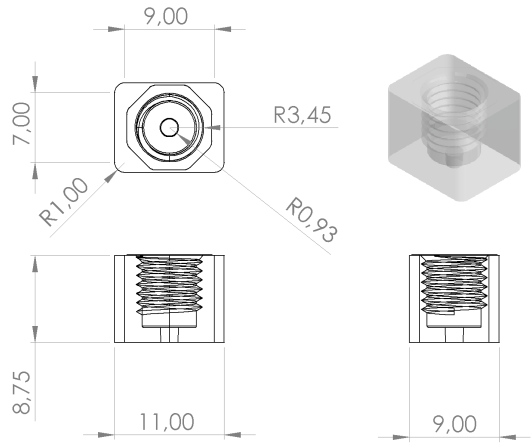

Figure D.4: Fitting for the fluigent screw connectors, adapted from Parallel Fluidics, Inc. [205].

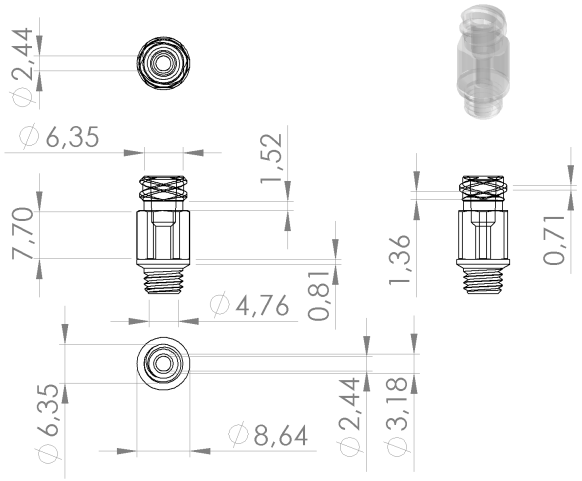

Figure D.5: Luer to screw connector for cleaning and post-processing the channel, adapted from Dassault Systèmes [206] and Dassault Systèmes [207].

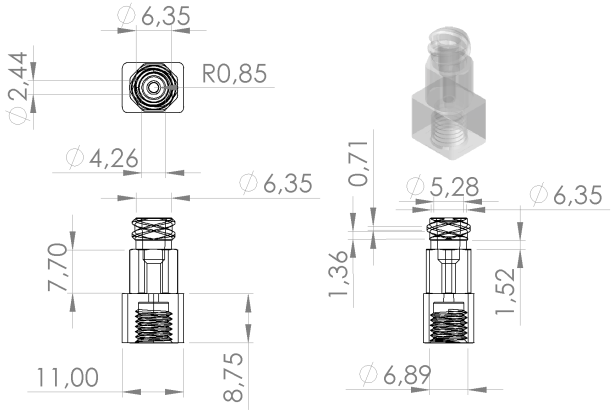

Figure D.6: Luer to ftting connector for cleaning the tubes of fluid, adapted from Dassault Systèmes [206] and Parallel Fluidics, Inc. [205].

D.4. Abstract and Physiological device spline data

The coordinates and tangent and magnitude of the vector spline handles is provided in Tables D.1 and D.2. The sketches and CAD can be reconstructed using this information.

Table D.1: Abstract device data. M1 and M2 represent the magnitude of the spline handles in opposing directions along the tangent. M1 is the magnitude of the incoming tangent vector at the node as perceived from starting node 1, whereas M2 is the magnitude of the outgoing tangent vector.

Node	X	Y	Tangent (°)	M1 (mm)	M2 (mm)	Type	Ø (mm)
Component Fi							
1	0	0, -10	-	-	-	Line	0.8
Component F1							
1	0	-10	-55.87	0	5.102	B-spline	0.4
2	1.723	-14.457	-80.274	4.716	6.515	B-spline	0.4
3	2.026	-21.051	-89.418	6.655	3.992	B-spline	0.4
4	2.306	-25	-80.64	3.935	0	B-spline	0.4
Component F2							
1	0	-10	-146.036	0	1.883	B-spline	0.5
2	-1.187	-10.862	-138.843	1.129	3.8	B-spline	0.5
3	-2.184	-15.696	-93.641	10.028	18.718	B-spline	0.5
4	-5.334	-40	-112.068	8.231	0	B-spline	0.5

Table D.2: Physiological device spline data. M1 and M2 represent the magnitude of the spline handles in opposing directions along the tangent. M1 is the magnitude of the incoming tangent vector at the node as perceived from starting node 1, whereas M2 is the magnitude of the outgoing tangent vector.

Node	X	Y	Tangent (°)	M1 (mm)	M2 (mm)	Type	Ø (mm)
Component Fi - Fo							
1	0	0	-15.741	0	7.094	B-spline	2.66
2	6.828	-0.965	-0.05	6.828	-0.965	B-spline	2.66
3	13.704	0	15.737	7.144	0	B-spline	2.66
Component F2							
1	3.621	-0.751	-89.926	0	10.649	B-spline	0.5
2	3.482	-11.396	-91.574	10.645	9.779	B-spline	0.5
3	3.084	-21.168	-93.088	9.783	0	B-spline	0.5
Component F1							
1	9.347	-0.837	-115.769	0	11.366	B-spline	0.5
2	8.874	-10.229	-72.679	9.226	7.537	B-spline	0.5
3	11.754	-17.351	-68.472	7.729	4.021	B-spline	0.5
4	12.938	-21.168	-78.504	3.994	0	B-spline	0.5

E

Printing Protocol

Start of Print:

1. Make sure the build plate is level according to the machine manufacturer instructions. Similarly, check for a working LCD and if the FEP film is tightly attached to the tray.
2. First tissues are placed on the table to provide a suitable surface to place the resin tray on.
3. The screws on either side of the tray are removed.
4. The resin tray is then removed from the printer and placed on the tissue.
5. The resin is poured into the tray, and the tray is placed back into the printer.
6. The screws are reinserted, the cover is placed on the printer, and the printer is turned on.
    (a) The settings screen is only handled without (dirty) gloves.

End of Print:

1. When the print is finished, tissues are placed on the table, and the cover is removed.
2. First, the printing platform is released using the screw on top and held at an angle to allow excess resin to drip into the tray.
3. The platform is then placed on one of the tissues.
4. The printer cover is placed back on the printer to prevent dust from falling into the resin tray.
5. Using the scraper (the beveled side to prevent damaging the build platform), the prints are removed and placed on a tissue in a transporting box.
6. The prints are sprayed with isopropanol, and the build platform is cleaned with isopropanol and tissues.
7. Once the build platform is clean, it is reinstalled in the machine after removing the cover.
8. The tray is then removed and placed on a new, clean tissue by first removing the screws.
9. The cover is reinstalled to prevent the LCD screen from being contaminated by resin or dust.
    (a) Inspect the LCD screen for resin leakage or visible damage resulting from the printing process.
10. Open the resin waste bottle and place it underneath the yellow funnel.
11. Place a filter in the yellow funnel.

12. Find the corner in the tray with the path for resin removal and angle it above the filter so the resin falls into it and drains into the bottle.
    (a) More viscous resin, such as the Bio-Med clear, tends to pull itself cleanly off the FEP foil in the resin tray. By being patient and letting the resin drip out, it will reduce the steps required for cleaning.
13. Once most resin is emptied into the filter, place the tray back on the clean tissue.
    (a) Make sure the excess resin on the leaking corner is cleaned before placing it back, as this can drip on the bottom side of the foil.
14. Clean the resin in the edges and corners of the tray by placing a tissue on it and gently sliding a playing card across the edges until it no longer leaves contaminated stripes on the tissue.
15. Clean the tray casing using tissues with isopropanol.
16. Remove the cover, reinstall the tray with the screws, and reinstall the cover.
17. Throw away the filter from the funnel by covering it with the waste tissues from the table and disposing of it in the correct trash can. Close the recycled resin bottle.
18. Use one last tissue with isopropanol to clean the table and printer cover.

Post-processing of the prints:

1. The prints are removed from the build plate and sprayed with isopropanol.
2. The prints are transported to the Multiscale Lab.
3. The prints are placed in an ultrasonic bath for 3 minutes.
4. They are then cleaned using pressurized air, for the samples focus is on targeting the channels.
5. If channels are printed, use a syringe to apply pressure using air or isopropanol to empty the channels.
6. Repeat the ultrasonic bath for 3 minutes.
7. Repeat the cleaning using pressurized air and a syringe.
8. Cure in the curing station according to the post-processing guidelines provided by the manufacturer for the specific material.
9. The transparency of the channels can be improved using acrylic varnish, an acrylic top coating for nail polish, etc.

Notes:

Resin can be left in the tray if another print is immediately started afterward. In that case, make sure to clean the build plate as described in steps 6-12 before turning on the machine again. Also, check the print for failure and inspect the resin tray for particles that may interfere with the following print. If the print has failed, first clean the resin tray and refill it with filtered resin before starting a new print. A failed print may leave partially cured objects sticking to the foil, which are difficult to see without emptying the resin tray first.

If the failed print sticks to the foil, do not use sharp objects, force, or your nails to pry it off! This may weaken the foil, leading to punctures and tears that could cause leakage on the LCD while printing. Remove the resin and gently press on the bottom of the foil where the failure is sticking with your finger, while softly scraping the top surface using a playing card. The bulge caused by pressure underneath will help the failed cured print detach more easily from the foil. If this is not working, you could loosen the foil on the back to increase the bulge caused by applying a gentle pressure.

F

Mesh for Computational Models

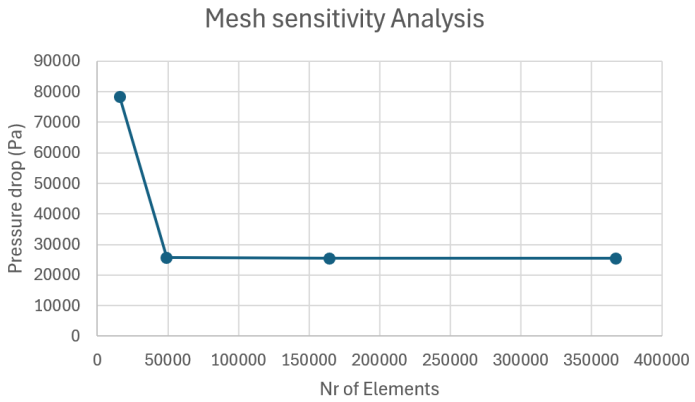

Figure F.1: Control test mesh sensitivity analysis. Convergence was obtained in the mesh sensitivity analysis once further refinement by increasing the number of elements led to changes smaller than 1% in the solution defined as the pressure drop.

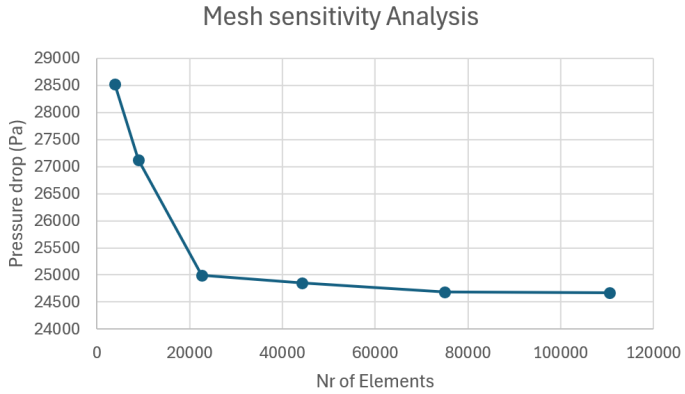

Figure F.2: Channel test mesh sensitivity analysis. Convergence was obtained in the mesh sensitivity analysis once further refinement by increasing the number of elements led to changes smaller than 1% in the solution defined as the pressure drop.

G

Number of Open Pores per Sample

Table G.1: Number of open pores for samples oriented orthogonally to the build plate.

Name	Line 1	Line 2
LH_0.01_ex2_OH	13	12
LH_0.01_ex2.5_OH	8	9
LH_0.01_ex3_OH	7	7
LH_0.01_ex3.5_OH	6	7
LH_0.01_ex4_OH	6	6
LH_0.01_ex4.5_OH	6	5
LH_0.01_ex5_OH	3	4
LH_0.1_ex7_OH	13	12
LH_0.02_ex3_OH	10	9
LH_0.05_ex5_OH	12	11

Table G.2: Number of open pores for samples oriented parallel to the build plate.

Name	Line 1	Line 2
LH_0.01_ex2_OV	5	4
LH_0.01_ex2.5_OV	8	4
LH_0.01_ex3_OV	1	0
LH_0.01_ex3.5_OV	2	0
LH_0.01_ex4_OV	2	2
LH_0.01_ex4.5_OV	4	0
LH_0.01_ex5_OV	0	6
LH_0.1_ex7_OV	9	5
LH_0.02_ex3_OV	5	4
LH_0.05_ex5_OV	7	7

Table G.3: Number of open pores for samples oriented angled to the build plate.

Name	Line 1	Line 2
LH_0.01_ex2_OA	14	13
LH_0.01_ex2.5_OA29	14	13
LH_0.01_ex2.5_OA61	12	14
LH_0.01_ex3_OA	13	12
LH_0.01_ex3.5_OA29	13	13
LH_0.01_ex3.5_OA61	12	13
LH_0.01_ex4_OA	12	13
LH_0.01_ex4.5_OA29	12	12
LH_0.01_ex4.5_OA61	13	12
LH_0.01_ex5_OA	12	12
LH_0.1_ex7_OA	13	12
LH_0.02_ex3_OA42	14	12
LH_0.02_ex3_OA48	12	13
LH_0.05_ex5_OA19.79	8	12
LH_0.05_ex5_OA22.5	7	8
LH_0.05_ex5_OA45	11	11
LH_0.05_ex5_OA67.5	12	11
LH_0.05_ex5_OA70.2	12	11

H

Test Samples Images and Fitted Oval

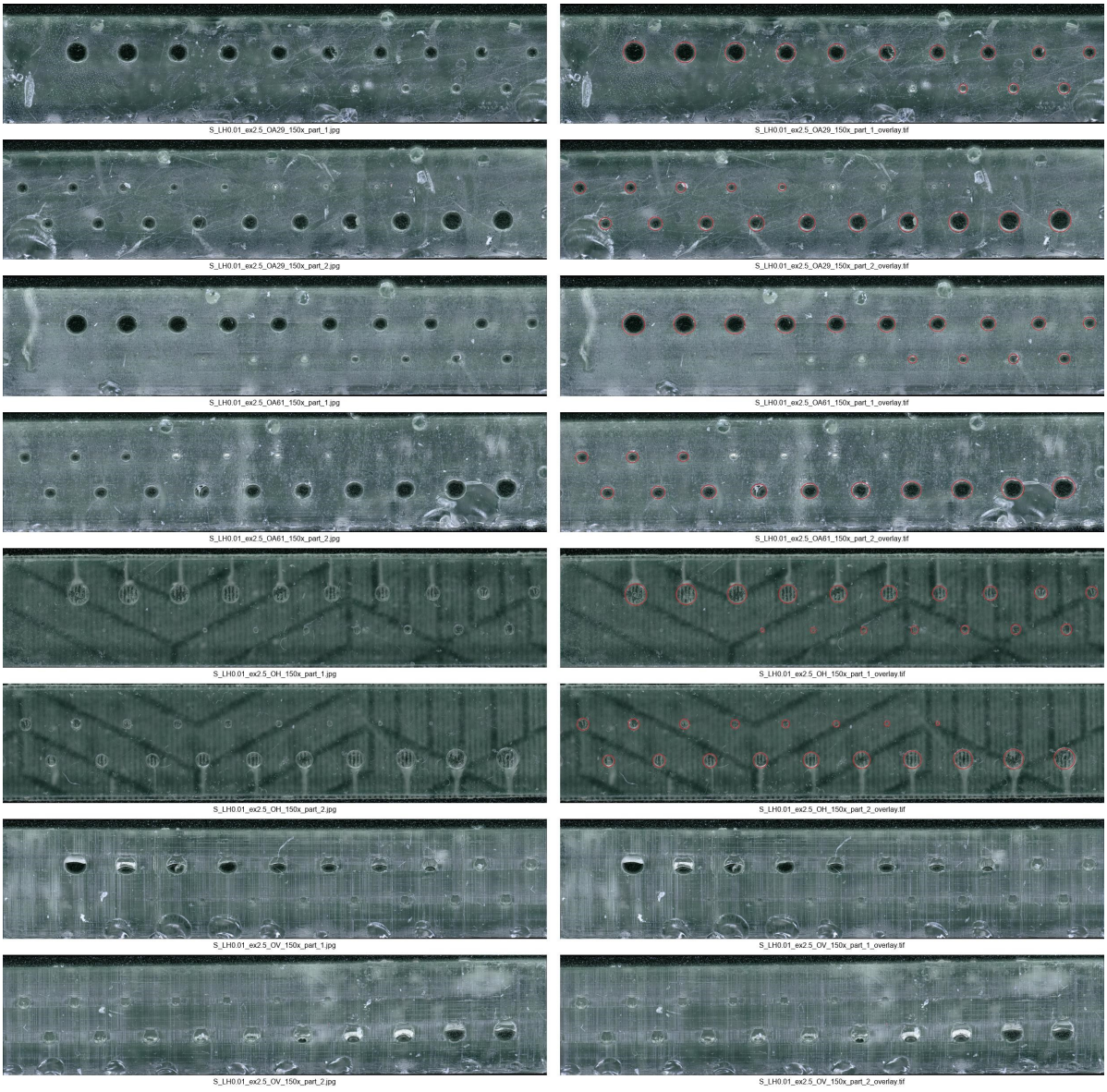

Figure H.1

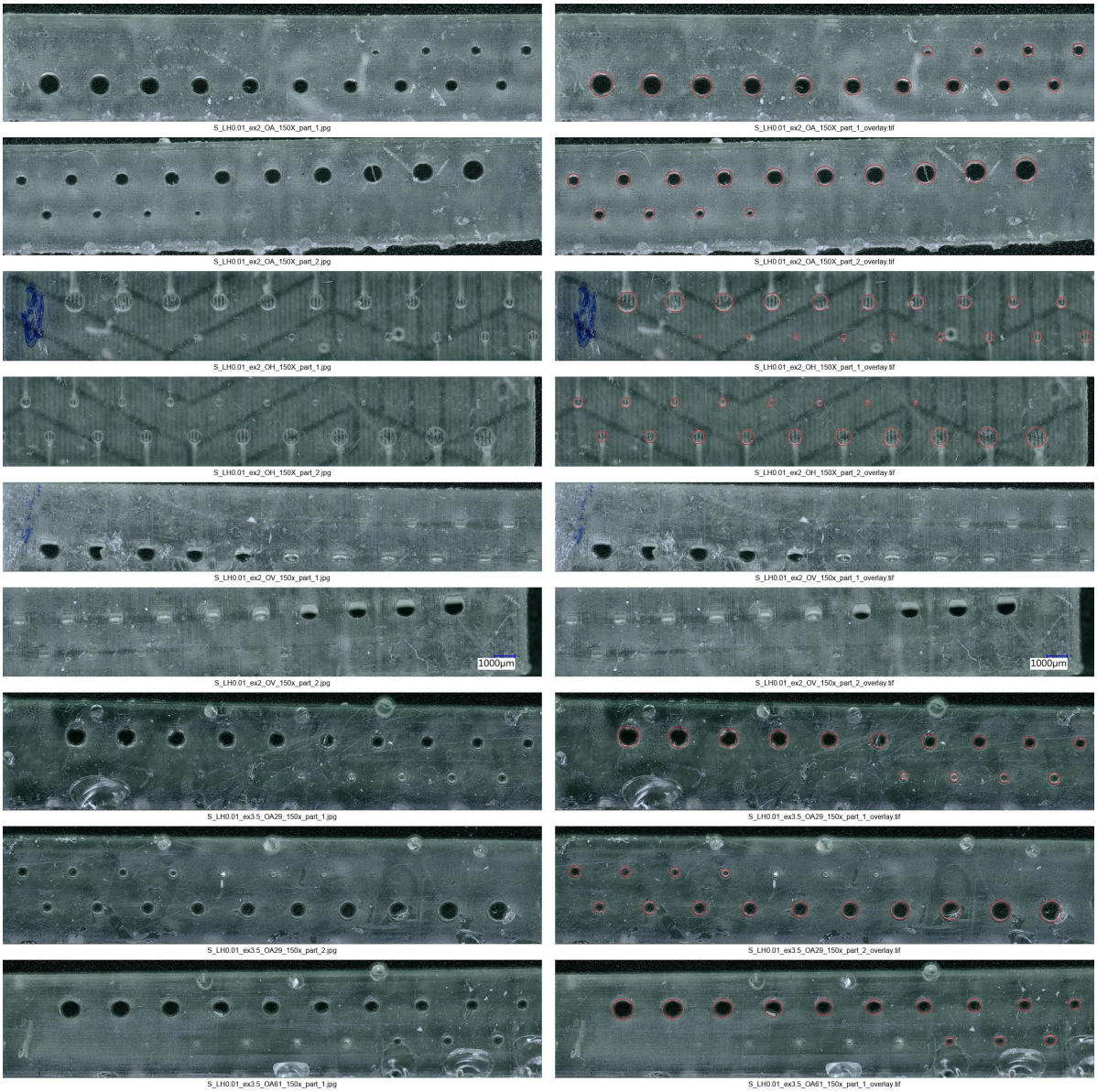
S_LH0.01_ex2_OA_150X_part_1.jpg
S_LH0.01_ex2_OA_150X_part_1_overlay.tif
S_LH0.01_ex2_OA_150X_part_2.jpg
S_LH0.01_ex2_OA_150X_part_2_overlay.tif
S_LH0.01_ex2_OH_150X_part_1.jpg
S_LH0.01_ex2_OH_150X_part_1_overlay.tif
S_LH0.01_ex2_OH_150X_part_2.jpg
S_LH0.01_ex2_OH_150X_part_2_overlay.tif
S_LH0.01_ex2_OV_150x_part_1.jpg
S_LH0.01_ex2_OV_150x_part_1_overlay.tif
1000µm
S_LH0.01_ex2_OV_150x_part_2.jpg
1000µm
S_LH0.01_ex2_OV_150x_part_2_overlay.tif
S_LH0.01_ex3.5_OA29_150x_part_1.jpg
S_LH0.01_ex3.5_OA29_150x_part_1_overlay.tif
S_LH0.01_ex3.5_OA29_150x_part_2.jpg
S_LH0.01_ex3.5_OA29_150x_part_2_overlay.tif
S_LH0.01_ex3.5_OA61_150x_part_1.jpg
S_LH0.01_ex3.5_OA61_150x_part_1_overlay.tif

Figure H.2

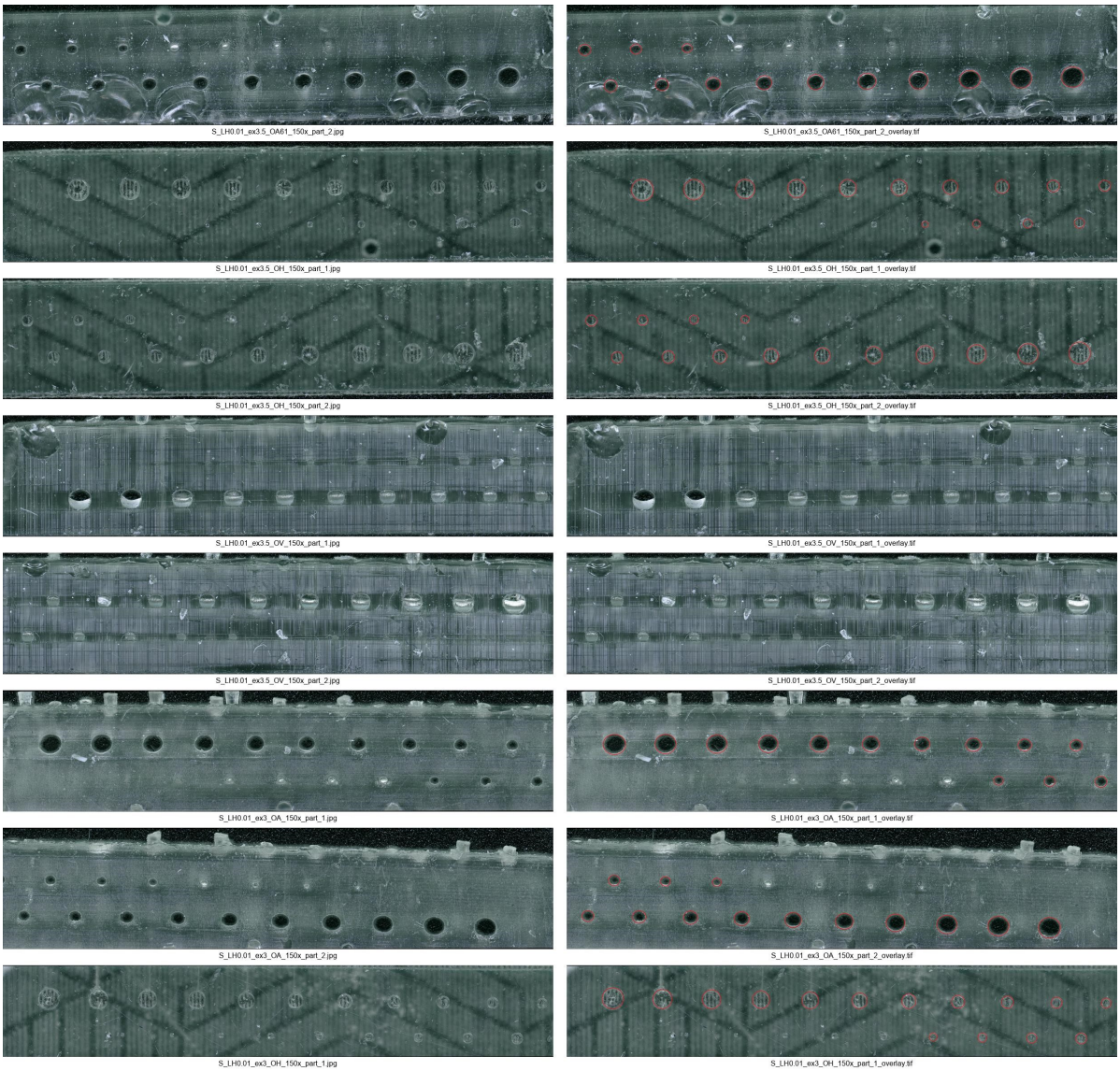
S_LH0.01_ex3.5_OA61_150x_part_2.jpg
S_LH0.01_ex3.5_OA61_150x_part_2_overlay.tif
S_LH0.01_ex3.5_OH_150x_part_1.jpg
S_LH0.01_ex3.5_OH_150x_part_1_overlay.tif
S_LH0.01_ex3.5_OH_150x_part_2.jpg
S_LH0.01_ex3.5_OH_150x_part_2_overlay.tif
S_LH0.01_ex3.5_OV_150x_part_1.jpg
S_LH0.01_ex3.5_OV_150x_part_1_overlay.tif
S_LH0.01_ex3.5_OV_150x_part_2.jpg
S_LH0.01_ex3.5_OV_150x_part_2_overlay.tif
S_LH0.01_ex3_OA_150x_part_1.jpg
S_LH0.01_ex3_OA_150x_part_1_overlay.tif
S_LH0.01_ex3_OA_150x_part_2.jpg
S_LH0.01_ex3_OA_150x_part_2_overlay.tif
S_LH0.01_ex3_OH_150x_part_1.jpg
S_LH0.01_ex3_OH_150x_part_1_overlay.tif

Figure H.3

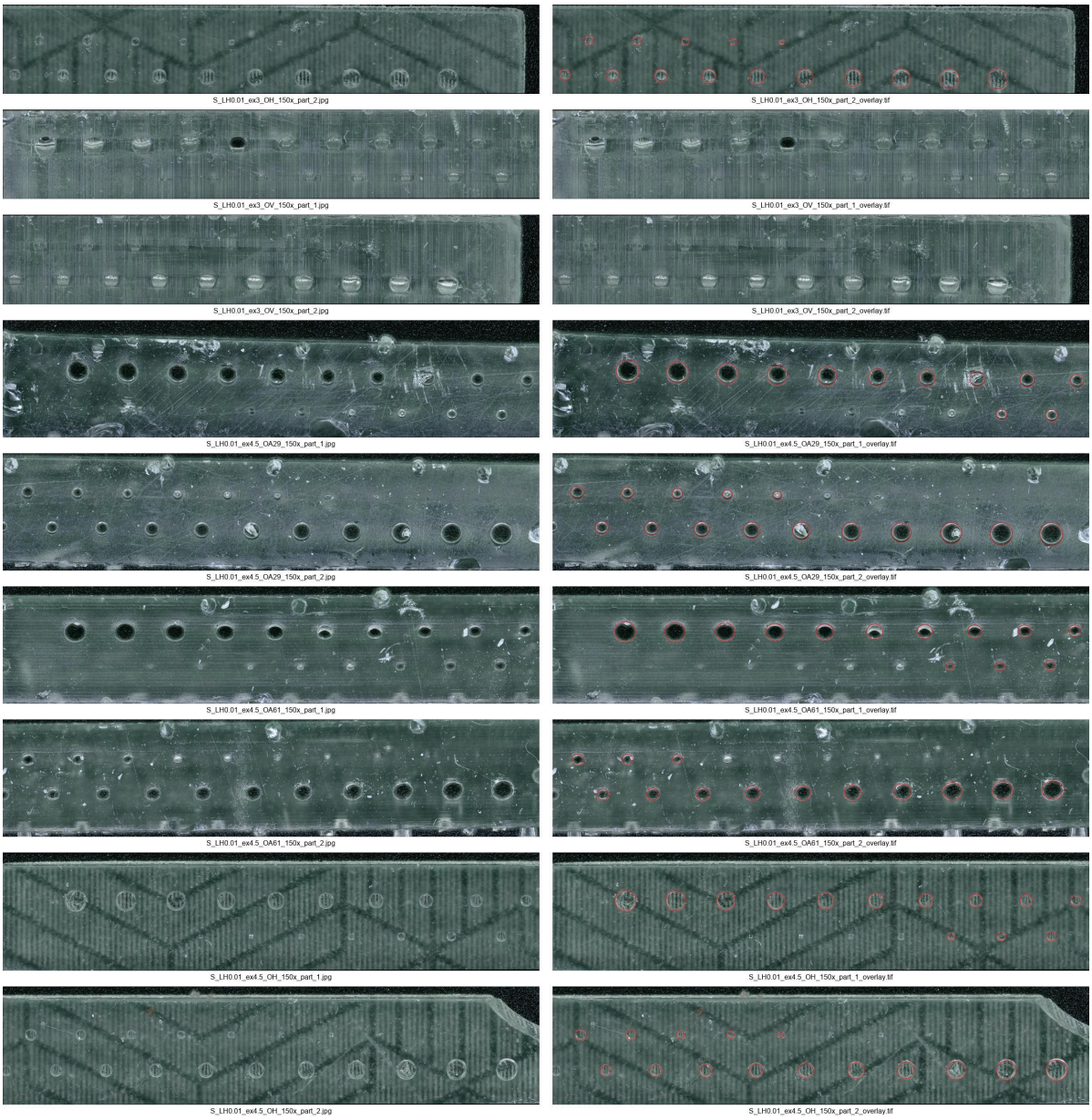
S_LH0.01_ex3_OH_150x_part_2.jpg
S_LH0.01_ex3_OH_150x_part_2_overlay.tif
S_LH0.01_ex3_OV_150x_part_1.jpg
S_LH0.01_ex3_OV_150x_part_1_overlay.tif
S_LH0.01_ex3_OV_150x_part_2.jpg
S_LH0.01_ex3_OV_150x_part_2_overlay.tif
S_LH0.01_ex4.5_OA29_150x_part_1.jpg
S_LH0.01_ex4.5_OA29_150x_part_1_overlay.tif
S_LH0.01_ex4.5_OA29_150x_part_2.jpg
S_LH0.01_ex4.5_OA29_150x_part_2_overlay.tif
S_LH0.01_ex4.5_OA61_150x_part_1.jpg
S_LH0.01_ex4.5_OA61_150x_part_1_overlay.tif
S_LH0.01_ex4.5_OA61_150x_part_2.jpg
S_LH0.01_ex4.5_OA61_150x_part_2_overlay.tif
S_LH0.01_ex4.5_OH_150x_part_1.jpg
S_LH0.01_ex4.5_OH_150x_part_1_overlay.tif
S_LH0.01_ex4.5_OH_150x_part_2.jpg
S_LH0.01_ex4.5_OH_150x_part_2_overlay.tif

Figure H.4

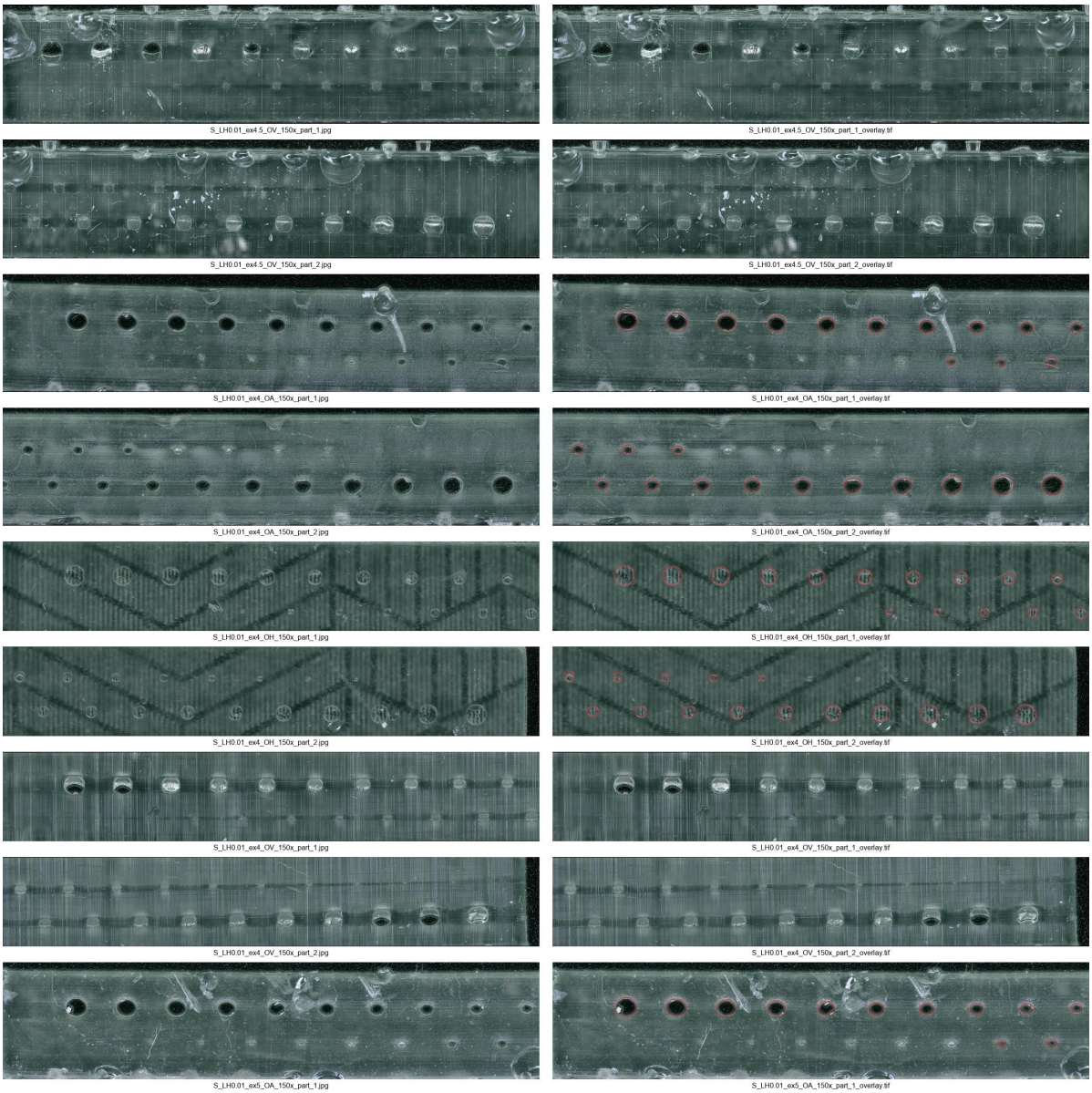
S_LH0.01_ex4.5_OV_150x_part_1.jpg
S_LH0.01_ex4.5_OV_150x_part_1_overlay.tif
S_LH0.01_ex4.5_OV_150x_part_2.jpg
S_LH0.01_ex4.5_OV_150x_part_2_overlay.tif
S_LH0.01_ex4_OA_150x_part_1.jpg
S_LH0.01_ex4_OA_150x_part_1_overlay.tif
S_LH0.01_ex4_OA_150x_part_2.jpg
S_LH0.01_ex4_OA_150x_part_2_overlay.tif
S_LH0.01_ex4_OH_150x_part_1.jpg
S_LH0.01_ex4_OH_150x_part_1_overlay.tif
S_LH0.01_ex4_OH_150x_part_2.jpg
S_LH0.01_ex4_OH_150x_part_2_overlay.tif
S_LH0.01_ex4_OV_150x_part_1.jpg
S_LH0.01_ex4_OV_150x_part_1_overlay.tif
S_LH0.01_ex4_OV_150x_part_2.jpg
S_LH0.01_ex4_OV_150x_part_2_overlay.tif
S_LH0.01_ex5_OA_150x_part_1.jpg
S_LH0.01_ex5_OA_150x_part_1_overlay.tif

Figure H.5

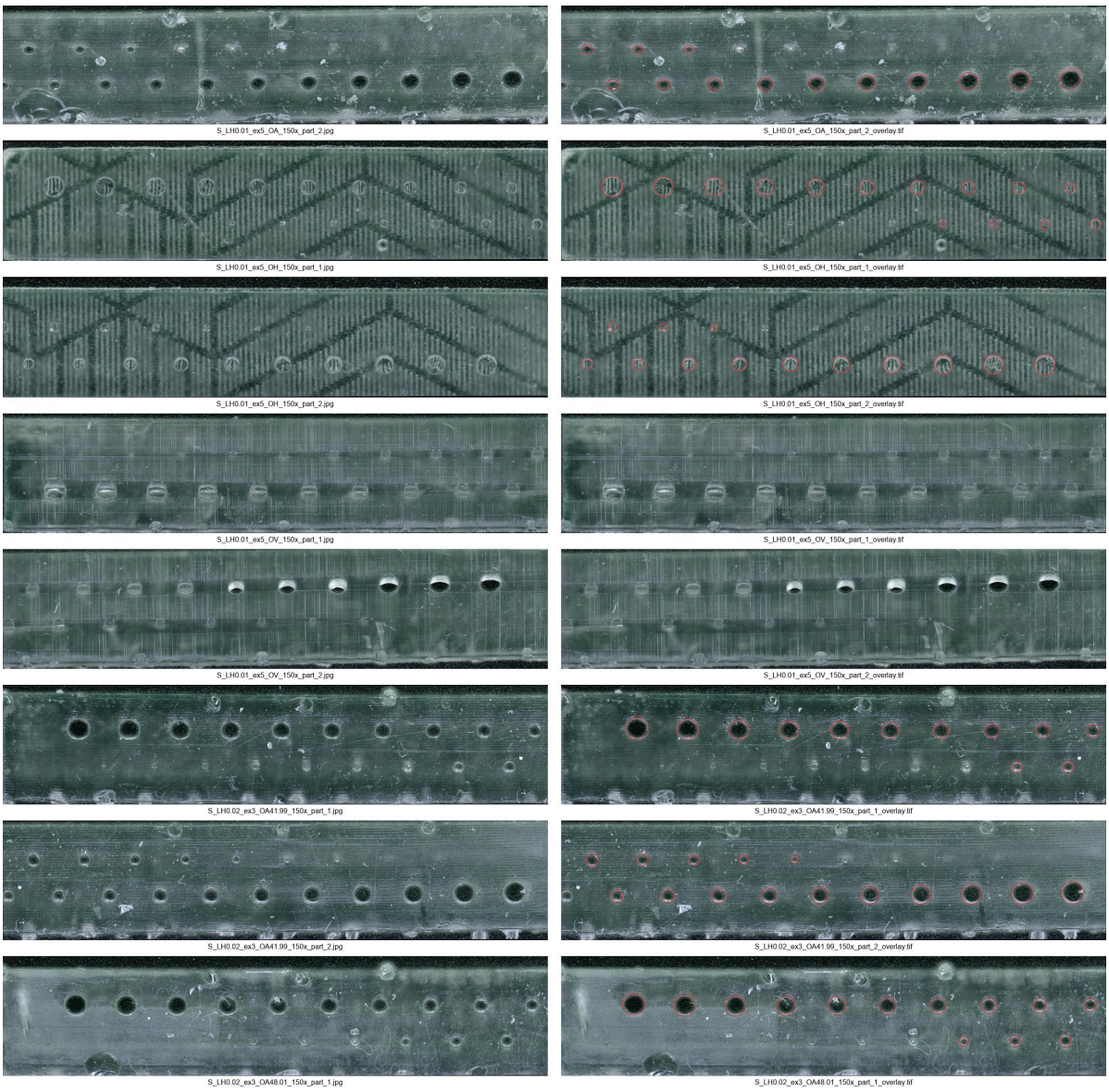
S_LH0.01_ex5_OA_150x_part_2.jpg
S_LH0.01_ex5_OA_150x_part_2_overlay.tif
S_LH0.01_ex5_OH_150x_part_1.jpg
S_LH0.01_ex5_OH_150x_part_1_overlay.tif
S_LH0.01_ex5_OH_150x_part_2.jpg
S_LH0.01_ex5_OH_150x_part_2_overlay.tif
S_LH0.01_ex5_OV_150x_part_1.jpg
S_LH0.01_ex5_OV_150x_part_1_overlay.tif
S_LH0.01_ex5_OV_150x_part_2.jpg
S_LH0.01_ex5_OV_150x_part_2_overlay.tif
S_LH0.02_ex3_OA41.99_150x_part_1.jpg
S_LH0.02_ex3_OA41.99_150x_part_1_overlay.tif
S_LH0.02_ex3_OA41.99_150x_part_2.jpg
S_LH0.02_ex3_OA41.99_150x_part_2_overlay.tif
S_LH0.02_ex3_OA48.01_150x_part_1.jpg
S_LH0.02_ex3_OA48.01_150x_part_1_overlay.tif

Figure H.6

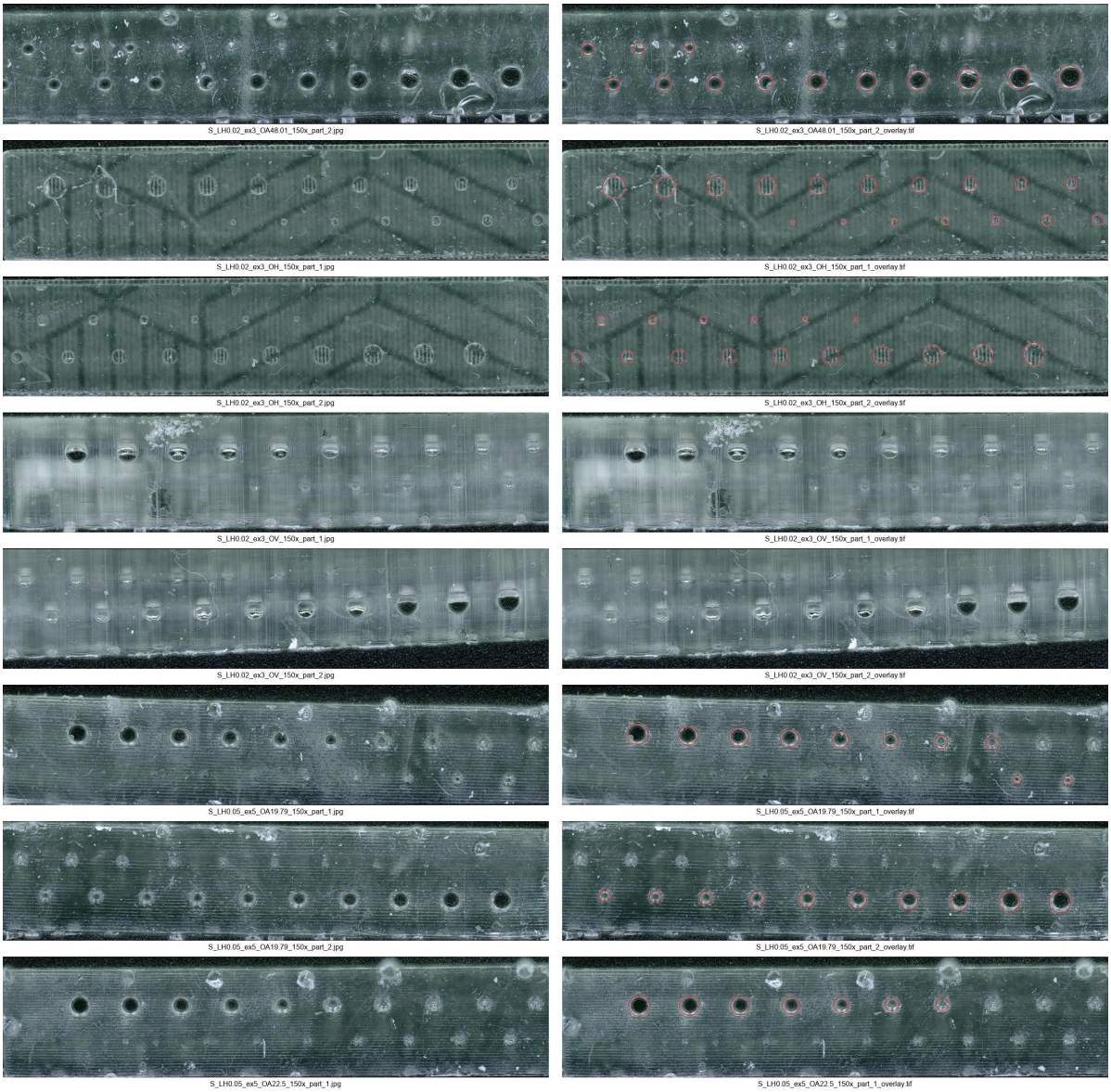
S_LH0.02_ex3_OA48.01_150x_part_2.jpg
S_LH0.02_ex3_OA48.01_150x_part_2_overlay.tif
S_LH0.02_ex3_OH_150x_part_1.jpg
S_LH0.02_ex3_OH_150x_part_1_overlay.tif
S_LH0.02_ex3_OH_150x_part_2.jpg
S_LH0.02_ex3_OH_150x_part_2_overlay.tif
S_LH0.02_ex3_OV_150x_part_1.jpg
S_LH0.02_ex3_OV_150x_part_1_overlay.tif
S_LH0.02_ex3_OV_150x_part_2.jpg
S_LH0.02_ex3_OV_150x_part_2_overlay.tif
S_LH0.05_ex5_OA19.79_150x_part_1.jpg
S_LH0.05_ex5_OA19.79_150x_part_1_overlay.tif
S_LH0.05_ex5_OA19.79_150x_part_2.jpg
S_LH0.05_ex5_OA19.79_150x_part_2_overlay.tif
S_LH0.05_ex5_OA22.5_150x_part_1.jpg
S_LH0.05_ex5_OA22.5_150x_part_1_overlay.tif

Figure H.7

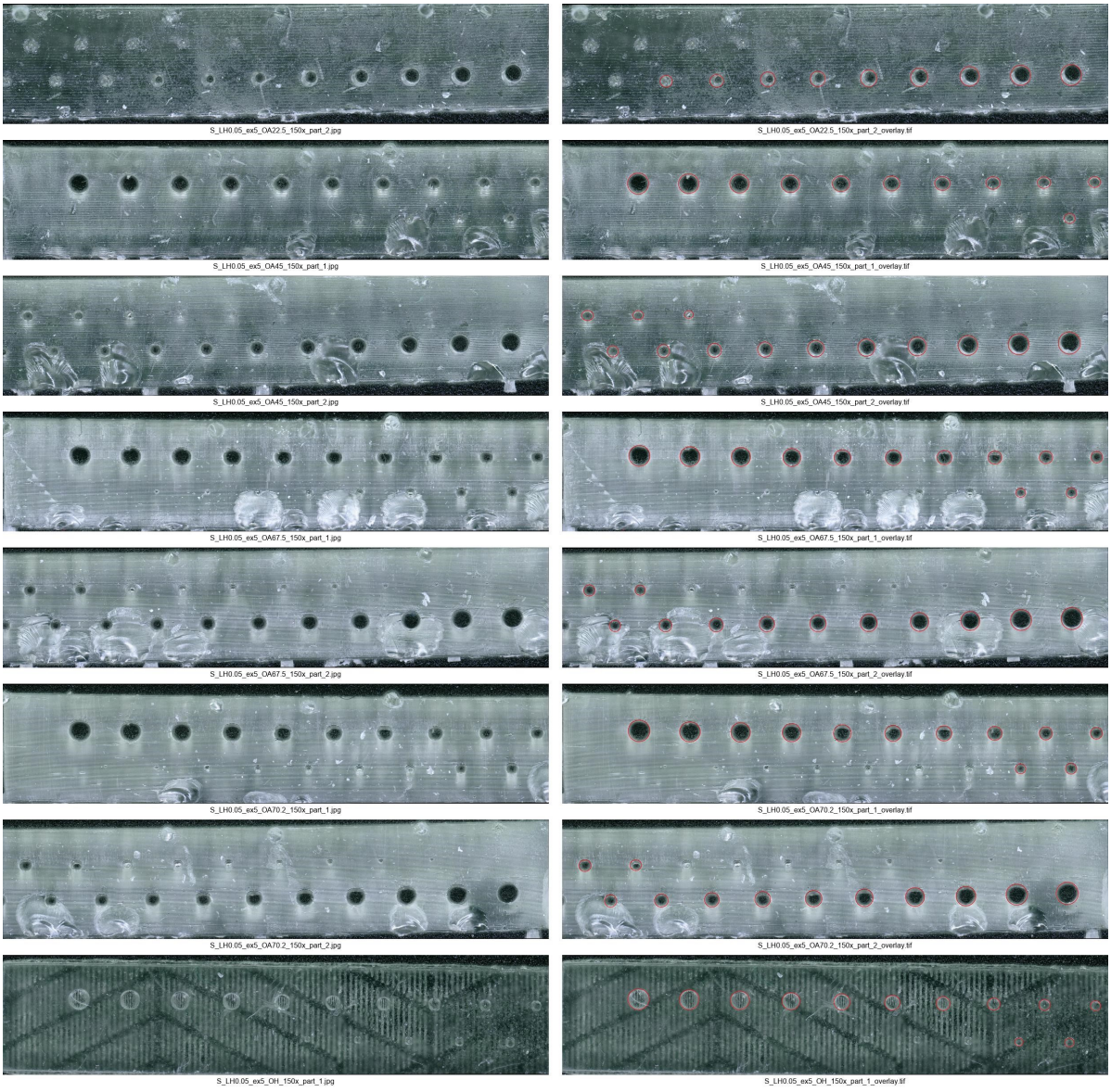
S_LH0.05_ex5_OA22.5_150x_part_2.jpg
S_LH0.05_ex5_OA22.5_150x_part_2_overlay.tif
S_LH0.05_ex5_OA45_150x_part_1.jpg
S_LH0.05_ex5_OA45_150x_part_1_overlay.tif
S_LH0.05_ex5_OA45_150x_part_2.jpg
S_LH0.05_ex5_OA45_150x_part_2_overlay.tif
S_LH0.05_ex5_OA67.5_150x_part_1.jpg
S_LH0.05_ex5_OA67.5_150x_part_1_overlay.tif
S_LH0.05_ex5_OA67.5_150x_part_2.jpg
S_LH0.05_ex5_OA67.5_150x_part_2_overlay.tif
S_LH0.05_ex5_OA70.2_150x_part_1.jpg
S_LH0.05_ex5_OA70.2_150x_part_1_overlay.tif
S_LH0.05_ex5_OA70.2_150x_part_2.jpg
S_LH0.05_ex5_OA70.2_150x_part_2_overlay.tif
S_LH0.05_ex5_OH_150x_part_1.jpg
S_LH0.05_ex5_OH_150x_part_1_overlay.tif

Figure H.8

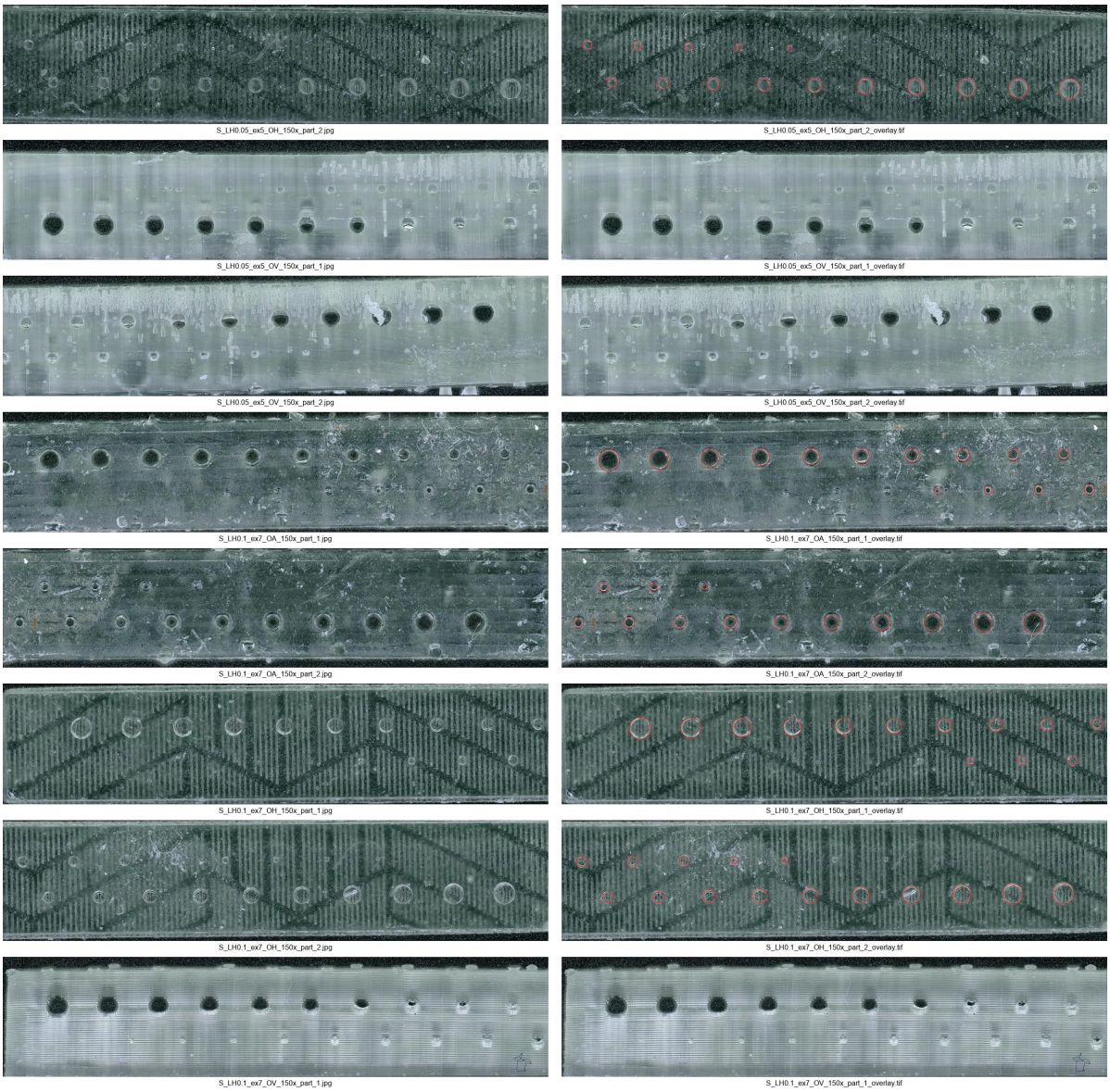

Figure H.9

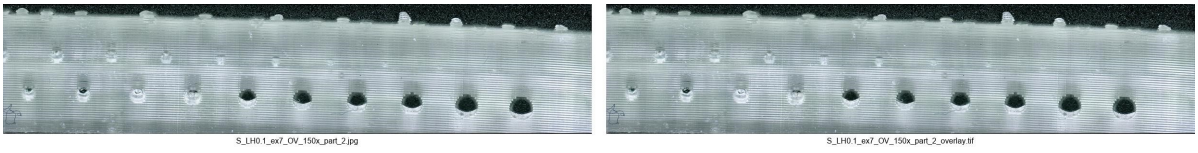

Figure H.10

Print Settings of Included Samples

Table I.1: A table of the variable print settings per sample, the orientation is determined as degrees from orthogonal to the buildplate of the sample, or the angle of the channel with the build plate. [1]: angle in degrees with the angle of the channel adhering to the arctan rule indicated by *

ID	Angle[1], Y/N*	Layer Height (mm)	Exposure Time (s)
0.01_OA29_2.5_1.0	60.95	0.01	2.5
0.01_OA29_2.5_2.0	60.95	0.01	2.5
0.01_OA29_3.5_1.0	60.95	0.01	3.5
0.01_OA29_3.5_2.0	60.95	0.01	3.5
0.01_OA29_4.5_1.0	60.95	0.01	4.5
0.01_OA29_4.5_2.0	60.95	0.01	4.5
0.01_OA61_2.5_1.0	29.05*	0.01	2.5
0.01_OA61_2.5_2.0	29.05*	0.01	2.5
0.01_OA61_3.5_1.0	29.05*	0.01	3.5
0.01_OA61_3.5_2.0	29.05*	0.01	3.5
0.01_OA61_4.5_1.0	29.05*	0.01	4.5
0.01_OA61_4.5_2.0	29.05*	0.01	4.5
0.01_OA_2_1.0	29.05*	0.01	2
0.01_OA_2_2.0	29.05*	0.01	2
0.01_OA_3_1.0	29.05*	0.01	3
0.01_OA_3_2.0	29.05*	0.01	3
0.01_OA_4_1.0	29.05*	0.01	4
0.01_OA_4_2.0	29.05*	0.01	4
0.01_OA_5_1.0	29.05*	0.01	5
0.01_OA_5_2.0	29.05*	0.01	5
0.01_OH_2.5_1.0	90	0.01	2.5
0.01_OH_2.5_2.0	90	0.01	2.5
0.01_OH_2_1.0	90	0.01	2
0.01_OH_2_2.0	90	0.01	2
0.01_OH_3.5_1.0	90	0.01	3.5
0.01_OH_3.5_2.0	90	0.01	3.5
0.01_OH_3_1.0	90	0.01	3
0.01_OH_3_2.0	90	0.01	3
0.01_OH_4.5_1.0	90	0.01	4.5
0.01_OH_4.5_2.0	90	0.01	4.5
0.01_OH_4_1.0	90	0.01	4

ID	Angle[1], Y/N*	Layer Height (mm)	Exposure Time (s)
0.01_OH_4_2.0	90	0.01	4
0.01_OH_5_1.0	90	0.01	5
0.01_OH_5_2.0	90	0.01	5
0.02_OA41.99_3_1.0	48.01*	0.02	3
0.02_OA41.99_3_2.0	48.01*	0.02	3
0.02_OA48.01_3_1.0	41.99	0.02	3
0.02_OA48.01_3_2.0	41.99	0.02	3
0.02_OH_3_1.0	90	0.02	3
0.02_OH_3_2.0	90	0.02	3
0.05_OA19.79_5_1.0	70.2*	0.05	5
0.05_OA19.79_5_2.0	70.2*	0.05	5
0.05_OA22.5_5_1.0	67.5	0.05	5
0.05_OA22.5_5_2.0	67.5	0.05	5
0.05_OA45_5_1.0	45	0.05	5
0.05_OA45_5_2.0	45	0.05	5
0.05_OA67.5_5_1.0	22.5	0.05	5
0.05_OA67.5_5_2.0	22.5	0.05	5
0.05_OA70.2_5_1.0	19.79	0.05	5
0.05_OA70.2_5_2.0	19.79	0.05	5
0.05_OH_5_1.0	90	0.05	5
0.05_OH_5_2.0	90	0.05	5
0.1_OA_7_1.0	79.8*	0.10	7
0.1_OA_7_2.0	79.8*	0.10	7
0.1_OH_7_1.0	90	0.10	7
0.1_OH_7_2.0	90	0.10	7

J

Error Estimation

Printer Error
The difference between the two lines of ovals is investigated. A difference in the number of open pores between the two lines was observed in 30 of 38 samples (the original 28 angled and orthogonal to the build plate samples including the parallel to the build plate oriented samples) as seen in Appendix G. This suggests that part of the error can be attributed to the printing process. The number of pairs of pores of similar intended size in the same sample is 292, with 25 samples having a different number of open pores for the 28 samples included in the analysis with fitted ovals (totaling the 609 open pores). The measured size of these pores can be compared to the intra-operator error. The normalized error in the area was compared with the intended area between the intra-sample equivalent channel lines. A Bland-Altman plot to visualize the agreement in the measurements is presented in Figure J.2. The Bland-Altman illustrates a mean difference of **-0.0043 mm**^{2} in the area for pores of the same intended diameter. The difference in roundness is **0.0002** (unitless). No systemic difference between the lines was expected, and this result may be caused by outliers and the use of a relatively large dataset. The variability in the area can be seen to decrease for smaller cross-sectional area channels, but may be larger proportionally. The absolute normalized relative error for the area and roundness for every intended pore size is exhibited in Appendix K Table K.1 and for every sample with differing printer settings in Table K.2. The absolute normalized relative error of the area is **4.8% (4.3%, 5.3%)**. The absolute normalized relative error of the roundness is **0.115% (0.094%, 0.136%)**.

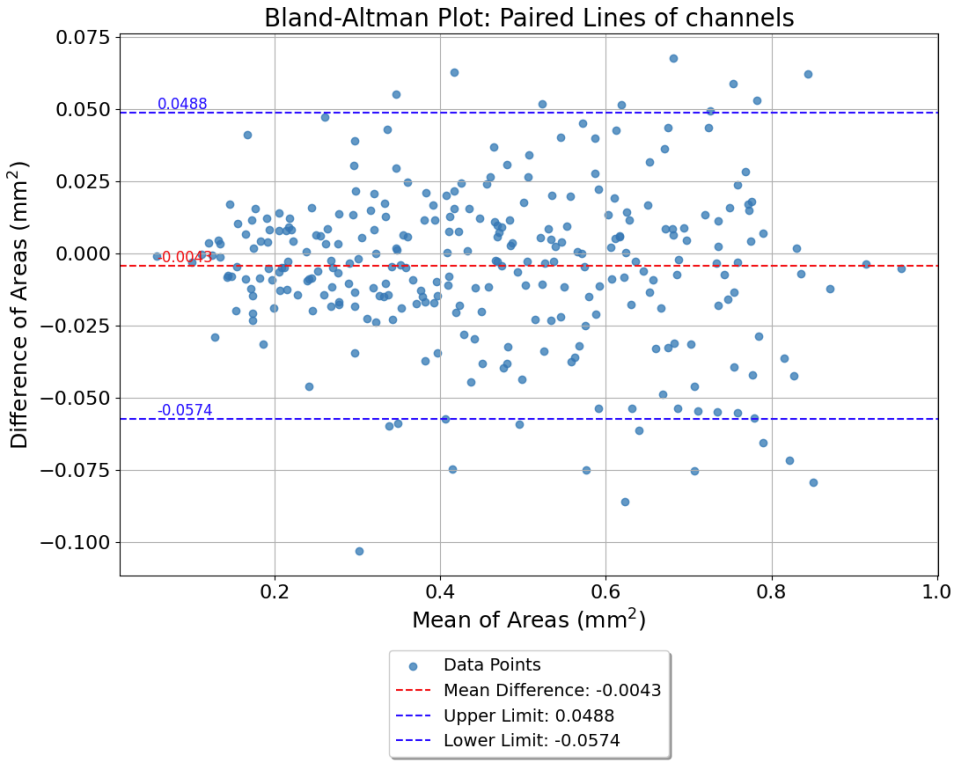

Figure J.1: A Bland-Altman plot of the agreement of the Area between pores in the same print (292 differences). The difference of the means of both poreschannels is visualized on the y axis, and the mean Area on the x axis.

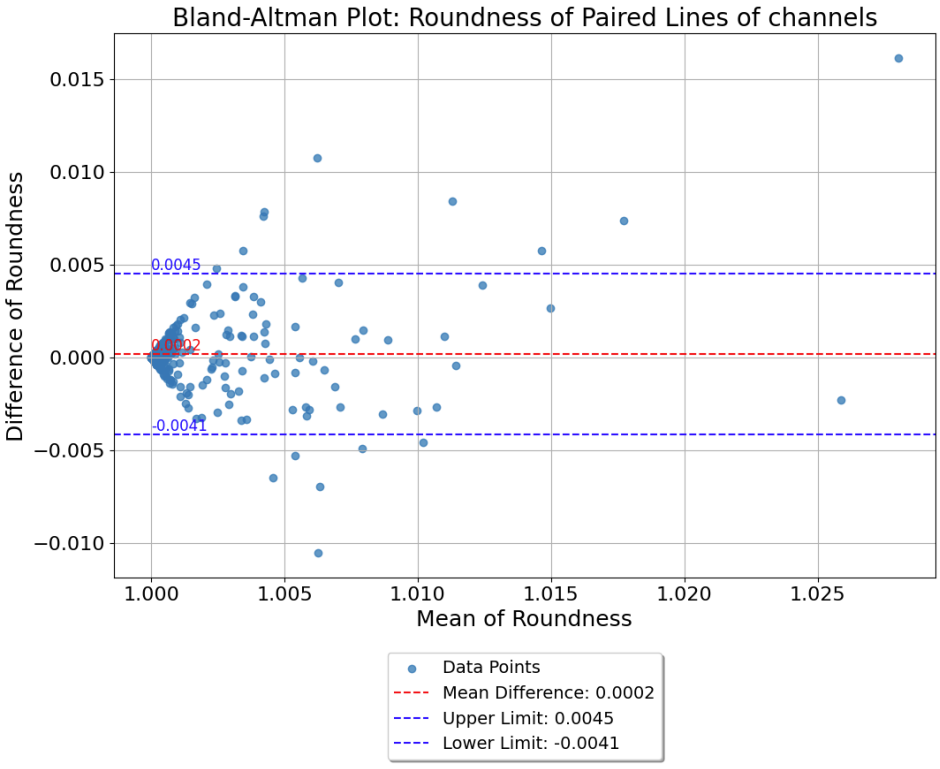

Figure J.2: A Bland-Altman plot of the agreement of the Roundness between pores in the same print (292 differences). The difference of the means of both pores is visualized on the y axis, and the mean Area on the x axis.

Intra-operator Error
Both researchers manually applied ovals to 4 sample images twice, representing 2 complete samples containing angled and orthogonal pores. The relative difference in the area mean is illustrative of the variance in measurements found by one researcher. The relative error to the intended area shows how large the average error from the intended area was for that researcher. Both researchers showed similar variations relative to their own measurements (1.9%, 95% CI: 1.5% - 2.3% versus 2.0%, 95% CI: 1.4% - 2.5%) and versus the intended area (4.7%, 95% CI: 3.8% - 5.6% versus 3.6%, 95% CI: 2.8% - 4.3%) as is shown in Table K.3. The overall absolute intra-operator error relative to their own measurements is **2% (95% CI: 1.6% - 2.3%)**, and relative to the intended area is **4.1% (95% CI: 3.6% - 4.7%)**. This is an indication that the pore sizes differ from the intended area in addition to there being an intra-operator error, because the error for both researchers to their own measurements is smaller than the error to the intended area. As a result it is likely that the value being measured by the operators varies slightly from the intended area. A difference is observed in the error relative to the intended area between the orientations (3% for orthogonal pairs, 95% CI: 2.5% - 3.6% versus 5.4% for angled pairs, 95% CI: 4.4% - 6.4%). This illustrates increased variation in measurements done by a single operator. No such difference was found between researchers in the roundness for the orientations. The overall absolute intra-operator error relative to their own measurements for the roundness is **0.030% (0.024%, 0.037%)**, and relative to the intended roundness is **0.026% (0.020%, 0.033%)**.

A Bland-Altman plot to visualize the agreement in the measurements of the area is presented in Figure J.3. The Bland-Altman illustrates a mean difference of **0.0011 mm**^{2} in the area for consecutive measurements by the same operator. A Bland-Altman plot to visualize the agreement in the measurements of the roundness is presented in Figure J.4. The difference in roundness is **0.0001** (unitless).

In the Bland-Altman plot for the roundness, average values lower than 1 can be observed. This is theoretically impossible. It is likely the result of the acquisition of the roudness values in ImageJ, as the pixellation introduces a measurment error that has been observed to cause roundness values below 1. This Measurement error is dependent on the size of the intended object and can vary for circles between absolute values of 0.1% - 0.00001% for the area and 0.8% - 8% for the perimeter according to a test performed by Takashimizu *et al.* [114]. A decrease in the perimeter due to the measurement error introduced by ImageJ might cause roundness values to be below 1 for pores that approximate perfect roundness when using the equation to calculate the roundness as introduced in Section 3.8.1.

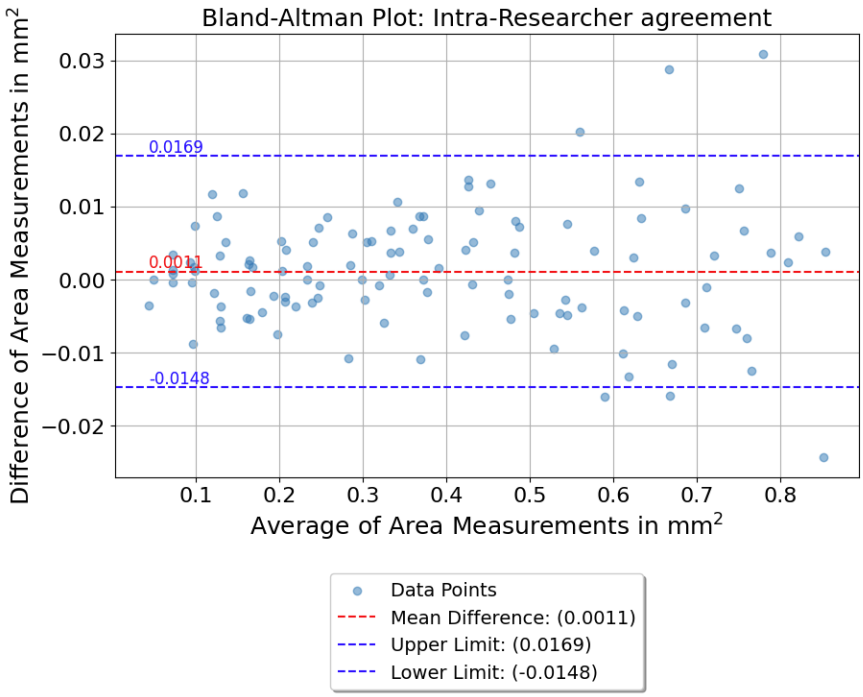

Figure J.3: A Bland-Altman plot of the intraoperator error for the Area (116 differences). The difference of the means within both operators is visualized on the y axis, and the mean Area on the x axis.

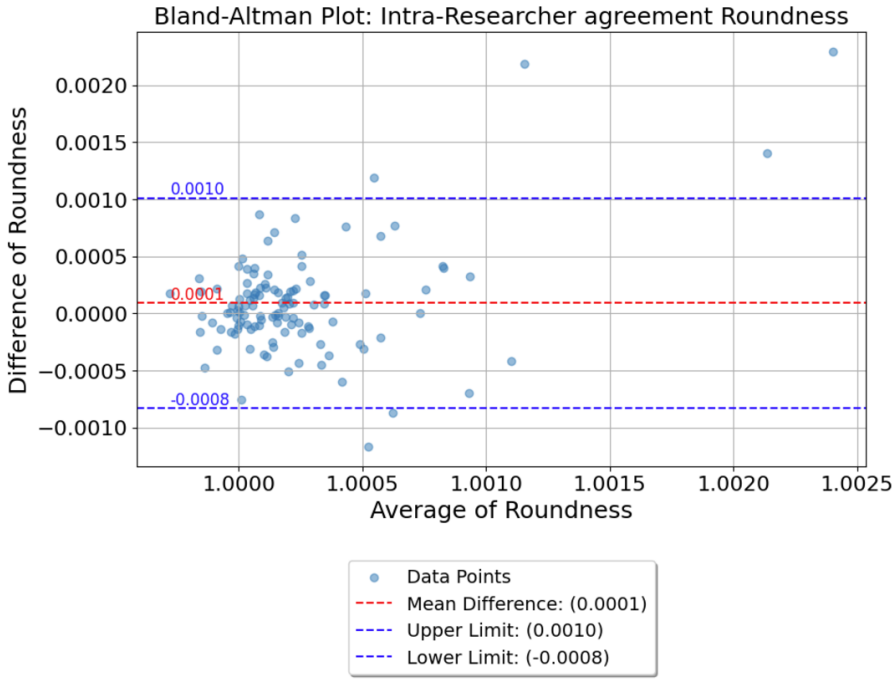

Figure J.4: A Bland-Altman plot of the intraoperator error for theRoundness (116 differences). The difference of the means within both operators is visualized on the y axis, and the mean Area on the x axis.

Inter-operator Error

The Inter-operator error for the area was determined using the approach as described in Section 3.8.1. The averages of the two values sampled for the intra-operator test were taken for both researchers. These means were subtracted and their absolute value was divided by their respective average to obtain a normalized mean difference. The result was 58 values for normalized mean differences. The overall inter-operator difference for the area amounted to **3% (95% CI: 2.3% - 3.8%)** as can be seen in Table K.6. The overall absolute relative difference for the roundness was **0.028% (0.017%, 0.039%)** . A difference was found between the researchers in the absolute relative error of the area of angled and orthogonally oriented pores. The difference was smaller for the orthogonally printed pores (1.9%, 95% CI: 1.1% - 2.8%), compared to the angled pores (4.3%, 95% CI: 3.1% - 5.5%).

A Bland-Altman test was done to visualize the agreement and to check for consistent bias as seen in Figures J.5 and J.6. The Bland-Altman illustrates a mean difference of **-0.0043 mm**^{2} in the area for consecutive measurements by the same operator. The difference in roundness is **-0.00005** (unitless). Average roundness values below 1 were again likely the consequence of measurement error for the perimeter caused by ImageJ.

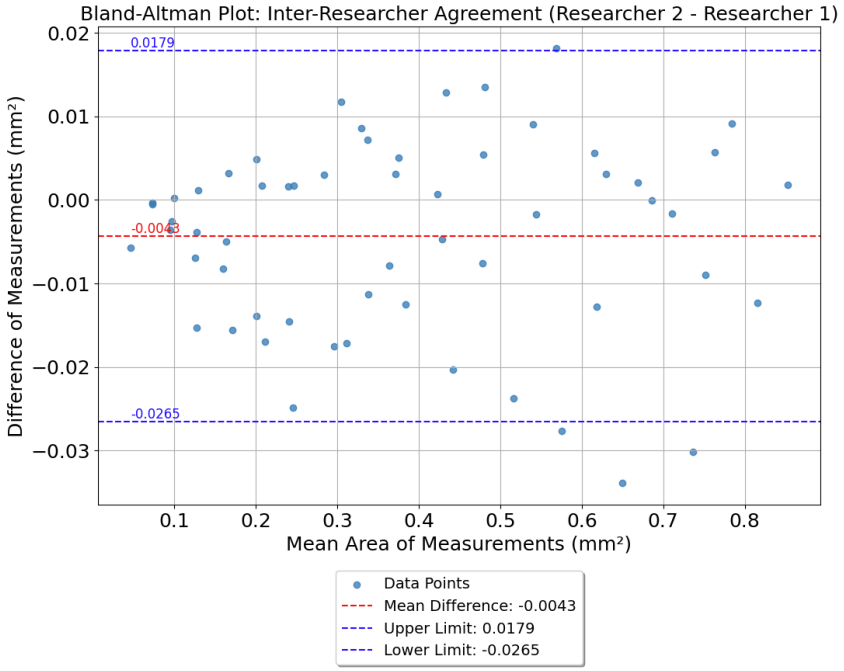

Figure J.5: A Bland-Altman plot of the interoperator error (58 differences). The difference of the means between both operators is visualized on the y axis, and the mean Area on the x axis.

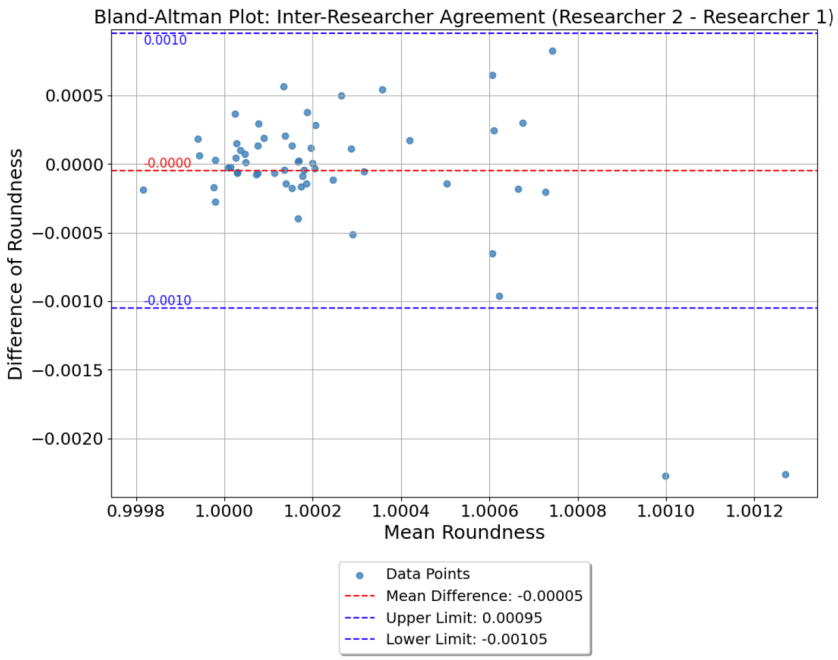

Figure J.6: A Bland-Altman plot of the interoperator error for the roundness (58 differences). The difference of the means between both operators is visualized on the y axis, and the mean Area on the x axis.

K

Supplement to Error Estimation

K.1. Per intended size and sample

Table K.1: Absolute normalized relative error by channel Nr for the area and roundness. The number denotes the diameter, with 1 being 1 mm in diameter and consequent numbers decreasing with 50 µm per step.

Nr	$\lvert\Delta A_{\mathbf{rel}}\rvert$ (95% CI)	$\lvert\Delta R_{\mathbf{rel}}\rvert$ (95% CI)	Count
1.0	0.040 (0.028, 0.052)	0.00101 (0.00019, 0.00183)	28
2.0	0.042 (0.028, 0.056)	0.00044 (0.00005, 0.00082)	28
3.0	0.033 (0.021, 0.045)	0.00090 (0.00035, 0.00145)	28
4.0	0.045 (0.032, 0.058)	0.00102 (0.00051, 0.00152)	28
5.0	0.046 (0.030, 0.063)	0.00090 (0.00030, 0.00150)	28
6.0	0.049 (0.031, 0.067)	0.00096 (0.00056, 0.00135)	27
7.0	0.059 (0.029, 0.088)	0.00140 (0.00062, 0.00219)	25
8.0	0.050 (0.035, 0.065)	0.00111 (0.00059, 0.00163	23
9.0	0.054 (0.039, 0.068)	0.00154 (0.00034, 0.00273)	20
10.0	0.064 (0.031, 0.097)	0.00148 (0.00036, 0.00260)	19
11.0	0.051 (0.034, 0.068)	0.00196 (0.00028, 0.00364)	19
12.0	0.053 (0.033, 0.073)	0.00197 (0.00076, 0.00317)	15
13.0	0.077 (-0.088, 0.241)	0.00092 (-0.00129, 0.00312)	4

Table K.2: Absolute normalized relative error of the area and roundness by sample ID

Base ID	$\lvert\Delta A_{\mathbf{rel}}\rvert$ **(95% CI)**	$\lvert\Delta R_{\mathbf{rel}}\rvert$ **(95% CI)**	**Count**
0.01_OA29_2.5	0.064 (0.045, 0.083)	0.00038 (-0.00009, 0.00086)	13
0.01_OA29_3.5	0.061 (0.027, 0.095)	0.00116 (0.00055, 0.00177)	13
0.01_OA29_4.5	0.045 (0.021, 0.069)	0.00039 (0.00011, 0.00067)	12
0.01_OA61_2.5	0.029 (0.017, 0.040)	0.00173 (0.00037, 0.00308)	12
0.01_OA61_3.5	0.048 (0.017, 0.079)	0.00183 (0.00067, 0.00299)	12
0.01_OA61_4.5	0.044 (0.031, 0.056)	0.00321 (0.00134, 0.00508)	12
0.01_OA_2	0.028 (0.013, 0.043)	0.00033 (0.00022, 0.00044)	13
0.01_OA_3	0.043 (0.021, 0.064)	0.00200 (0.00115, 0.00285)	12
0.01_OA_4	0.032 (0.017, 0.046)	0.00237 (0.00146, 0.00328)	12
0.01_OA_5	0.042 (0.012, 0.071)	0.00451 (0.00179, 0.00722)	12
0.01_OH_2	0.040 (0.012, 0.069)	0.00071 (0.00011, 0.00130)	12
0.01_OH_2.5	0.051 (0.023, 0.080)	0.00019 (-0.00002, 0.00039)	8
0.01_OH_3	0.035 (0.007, 0.062)	0.00012 (0.00002, 0.00022)	7
0.01_OH_3.5	0.017 (-0.0004, 0.034)	0.00011 (-0.00005, 0.00027)	6
0.01_OH_4	0.008 (-0.0002, 0.016)	0.00007 (0.00001, 0.00013)	6
0.01_OH_4.5	0.034 (-0.011, 0.079)	0.00009 (-0.00010, 0.00027)	5
0.01_OH_5	0.029 (0.013, 0.046)	0.00030 (0.00009, 0.00051)	8
0.02_OA41.99_3	0.025 (0.010, 0.040)	0.00084 (0.00054, 0.00113)	12
0.02_OA48.01_3	0.051 (0.033, 0.068)	0.00019 (0.00009, 0.00029)	12
0.02_OH_3	0.040 (0.020, 0.059)	0.00034 (0.00001, 0.00067)	9
0.05_OA19.79_5	0.080 (0.038, 0.123)	0.00107 (0.00013, 0.00200)	8
0.05_OA22.5_5	0.161 (0.076, 0.245)	0.00072 (-0.00006, 0.00150)	7
0.05_OA45_5	0.072 (0.053, 0.091)	0.00387 (0.00165, 0.00610)	11
0.05_OA67.5_5	0.055 (0.032, 0.078)	0.00081 (0.00018, 0.00144)	11
0.05_OA70.2_5	0.043 (0.028, 0.058)	0.00060 (0.00024, 0.00096)	11
0.05_OH_5	0.047 (0.029, 0.064)	0.00040 (-0.00001, 0.00080)	11
0.1_OA_7	0.095 (0.050, 0.140)	0.00050 (0.00016, 0.00084)	13
0.1_OH_7	0.031 (0.019, 0.043)	0.00048 (0.00011, 0.00085)	12
Total	0.048 (0.043, 0.053)	0.00115 (0.00094, 0.00136)	292

K.2. Intra-operator Error

Table K.3: Table of the absolute Intra-operator error relative to eachother ($|\Delta A_{\text{rel}}|$) and relative to the intended area ($|\Delta A_{\text{intended}}|$).

Pair	$\lvert\Delta A_{\mathbf{rel}}\rvert$ **(95% CI)**	$\lvert\Delta A_{\mathbf{intended}}\rvert$ **(95% CI)**
Pair 1 (Researcher 1)	0.017 (0.0114, 0.0216)	0.033 (0.0224, 0.0432)
Pair 2 (Researcher 2)	0.015 (0.0097, 0.0196)	0.035 (0.0257, 0.0436)
Pair 3 (Researcher 1)	0.019 (0.0107, 0.0283)	0.025 (0.0165, 0.0338)
Pair 4 (Researcher 2)	0.031 (0.0163, 0.0463)	0.028 (0.0110, 0.0454)
Pair 5 (Researcher 1)	0.022 (0.0148, 0.0290)	0.061 (0.0411, 0.0815)
Pair 6 (Researcher 2)	0.017 (0.0019, 0.0325)	0.019 (0.0114, 0.0265)
Pair 7 (Researcher 1)	0.019 (0.0056, 0.0331)	0.074 (0.0524, 0.0952)
Pair 8 (Researcher 2)	0.015 (0.0089, 0.0202)	0.061 (0.0426, 0.0789)
Researcher 1	0.019 (0.0150, 0.0234)	0.047 (0.0382, 0.0558)
Researcher 2	0.020 (0.0143, 0.0253)	0.036 (0.0281, 0.0432)
Orthogonal Pairs	0.021 (0.0159, 0.0253)	0.030 (0.0245, 0.0356)
Angled Pairs	0.018 (0.0131, 0.0233)	0.054 (0.0444, 0.0640)
Overall	0.020 (0.0161, 0.0229)	0.041 (0.0355, 0.0471)

Table K.4: Table of the absolute Intra-operator error relative to eachother ($|\Delta R_{\text{rel}}|$) and relative to the intended roundness ($|\Delta R_{\text{intended}}|$).

Pair	$\lvert\Delta R_{\textbf{rel}}\rvert$ **(95% CI)**	$\lvert\Delta R_{\textbf{intended}}\rvert$ **(95% CI)**
Pair 1 (Researcher 1)	0.00028 (0.00012, 0.00043)	0.00015 (0.00006, 0.00023)
Pair 2 (Researcher 2)	0.00023 (0.00009, 0.00037)	0.00029 (0.00014, 0.00043)
Pair 3 (Researcher 1)	0.00030 (0.00012, 0.00049)	0.00034 (0.00006, 0.00062)
Pair 4 (Researcher 2)	0.00034 (0.00018, 0.00051)	0.00022 (0.00008, 0.00036)
Pair 5 (Researcher 1)	0.00036 (-0.00000, 0.00073)	0.00032 (-0.00007, 0.00070)
Pair 6 (Researcher 2)	0.00029 (-0.00006, 0.00064)	0.00022 (0.00004, 0.00040)
Pair 7 (Researcher 1)	0.00034 (0.00017, 0.00051)	0.00036 (0.00016, 0.00056)
Pair 8 (Researcher 2)	0.00028 (0.00014, 0.00042)	0.00022 (0.00012, 0.00032)
Researcher 1	0.00032 (0.00022, 0.00042)	0.00029 (0.00017, 0.00041)
Researcher 2	0.00029 (0.00020, 0.00038)	0.00024 (0.00017, 0.00030)
Orthogonal Pairs	0.00029 (0.00022, 0.00037)	0.00025 (0.00016, 0.00033)
Angled Pairs	0.00032 (0.00020, 0.00044)	0.00028 (0.00017, 0.00039)
Overall	0.00030 (0.00024, 0.00037)	0.00026 (0.00020, 0.00033)

K.3. Inter-operator Error

Table K.5: Mean Relative Difference for the roundness with Confidence Intervals as the inter-operator error

Comparison	$\lvert\Delta R_{\textbf{rel}}\rvert$ **(95% CI)**	$\Delta R_{\textbf{rel}}$ **(95% CI)**
Pair 1	0.00019 (0.00009, 0.00028)	0.00013 (0.00001, 0.00025)
Pair 2	0.00029 (-0.00000, 0.00058)	-0.00011 (-0.00044, 0.00022)
Pair 3	0.00038 (0.00001, 0.00074)	-0.00014 (-0.00057, 0.00028)
Pair 4	0.00028 (0.00012, 0.00045)	-0.00008 (-0.00032, 0.00015)
Orthogonal Pairs	0.00024 (0.00009, 0.00039)	0.00001 (-0.00017, 0.00018)
Angled Pairs	0.00033 (0.00015, 0.00051)	-0.00011 (-0.00033, 0.00011)
Overall	0.00028 (0.00017, 0.00039)	-0.00005 (-0.00018, 0.00009)

Table K.6: Normalized mean difference for the area as the inter-operator error.

Comparison	$\lvert\Delta A_{\textbf{rel}}\rvert$ **(95% CI)**	$\Delta A_{\textbf{rel}}$ **(95% CI)**
Pair 1	0.011 (0.0076, 0.0153)	0.0053 (-0.0017, 0.0122)
Pair 2	0.027 (0.0112, 0.0426)	0.0003 (-0.0212, 0.0219)
Pair 3	0.059 (0.0406, 0.0773)	-0.0589 (-0.0773, -0.0406)
Pair 4	0.028 (0.0142, 0.0417)	-0.0266 (-0.0413, -0.0118)
Orthogonal Pairs	0.019 (0.0111, 0.0278)	0.0027 (-0.0083, 0.0137)
Angled Pairs	0.043 (0.0306, 0.0551)	-0.0421 (-0.0548, -0.0295)
Overall	0.030 (0.0227, 0.0380)	-0.0182 (-0.0282, -0.0082)

Samples per Test

Table L.1: Samples included for every Error, Area, and Roundness Analysis. Every sample includes 2 lines of channels ranging from 1 mm to 50 µm

Exposure Angled	Layer Height Angled	Angles vs Horizontal	Arctan Rule vs Inverse	Angle Test
LH_0.01_ex2_OA	LH_0.01_ex2.5_OA29	LH_0.01_ex2_OH	LH_0.01_ex2.5_OA29	LH_0.05_ex5_OH
LH_0.01_ex2.5_OA29	LH_0.01_ex2.5_OA61	LH_0.01_ex2_OA	LH_0.01_ex2.5_OA61	LH_0.05_ex5_OA19.79
LH_0.01_ex2.5_OA61	LH_0.1_ex7_OA	LH_0.01_ex2.5_OH	LH_0.01_ex3.5_OA29	LH_0.05_ex5_OA22.5
LH_0.01_ex3.5_OA29	LH_0.02_ex3_OA42	LH_0.01_ex2.5_OA29	LH_0.01_ex3.5_OA61	LH_0.05_ex5_OA45
LH_0.01_ex3.5_OA61	LH_0.02_ex3_OA48	LH_0.01_ex2.5_OA61	LH_0.05_ex5_OA19.79	LH_0.05_ex5_OA67.5
LH_0.01_ex4_OA	LH_0.05_ex5_OA19.79	LH_0.01_ex3_OH	LH_0.05_ex5_OA70.2	LH_0.05_ex5_OA70.2
LH_0.01_ex4.5_OA29	LH_0.05_ex5_OA70.2	LH_0.01_ex3_OA	LH_0.02_ex3_OA42	LH_0.05_ex5_OV
LH_0.01_ex4.5_OA61		LH_0.01_ex3.5_OH	LH_0.02_ex3_OA48	
LH_0.01_ex5_OA		LH_0.01_ex3.5_OA29	LH_0.01_ex4.5_OA29	
		LH_0.01_ex3.5_OA61	LH_0.01_ex4.5_OA61	
		LH_0.01_ex4_OH		
		LH_0.01_ex4_OA		
		LH_0.01_ex4.5_OH		
		LH_0.01_ex4.5_OA29		
		LH_0.01_ex4.5_OA61		
		LH_0.01_ex5_OH		
		LH_0.01_ex5_OA		
		LH_0.1_ex7_OH		
		LH_0.1_ex7_OA		
		LH_0.02_ex3_OH		
		LH_0.02_ex3_OA42		
		LH_0.02_ex3_OA48		
		LH_0.05_ex5_OH		
		LH_0.05_ex5_OA19.79		
		LH_0.05_ex5_OA70.2		

M

Grouping of Pore Roundness and Error

The average values of the roundness and the normalized error of the intended area per intended pore size grouped for the intended diameter can be seen in Table M.1. The Kruskal-Wallis test for the normalized error of the area showed no statistical difference for a threshold of p = 0.05 (Statistic: 14.71502, p-value=0.32548). The roundness did show a statistically significant difference (Statistic: 25.78028, p-value = 0.01819). A follow-up Dunn's test to identify this difference no longer was able to identify this difference, likely due to stringent multiple testing correction (Bonferroni), as seen in Appendix O.

A decrease in roundness with decreasing pore size is plausible, as pixelation effects become more pronounced at a smaller size. Furthermore, smaller pores are affected to a larger extent by excess polymerized resin, since the normalized cumulative dose represents a larger proportion of the total channel volume in angled samples. This trend does not necessarily hold for orthogonal channels. As a result of the underlying printing mechanism and the Kruskal-Wallis test of the roundness, it cannot be ruled out that smaller diameter channels are comparatively less round and may exhibit increased deviation from the intended area. Furthermore, this test considered all pores. A bias may exist that open pores at smaller intended diameter were already printed using more optimized settings. Smaller pores printed at similar layer height, exposure time, and orientation, may exhibit increased error from the area and decreased roundness.

Table M.1: Summary of Roundness and Normalized Error Area by Intended pore diameter with the number of pores measured.

Ø (mm)	Roundness (Mean and 95% CI)	Normalized Error Area (Mean and 95% CI)	Count
1	1.00104 (1.00046, 1.00162)	0.00039 (-0.02017, 0.02095)	56
0.95	1.00116 (1.00048, 1.00183)	-0.01002 (-0.03321, 0.01318)	56
0.9	1.0013 (1.00066, 1.00194)	-0.01685 (-0.04094, 0.00725)	56
0.85	1.0014 (1.0007, 1.0021)	-0.02206 (-0.04819, 0.00406)	56
0.8	1.00165 (1.00087, 1.00244)	-0.02565 (-0.05407, 0.00276)	56
0.75	1.00155 (1.00072, 1.00238)	-0.0378 (-0.06749, -0.0081)	55
0.7	1.00167 (1.00085, 1.0025)	-0.03875 (-0.07245, -0.00505)	51
0.65	1.00176 (1.00096, 1.00256)	-0.0299 (-0.06592, 0.00612)	47
0.6	1.00233 (1.00111, 1.00355)	-0.03484 (-0.07646, 0.00677)	43
0.55	1.00207 (1.00073, 1.0034)	-0.04356 (-0.09298, 0.00586)	40
0.5	1.00315 (1.00106, 1.00524)	-0.04681 (-0.10452, 0.0109)	39
0.45	1.00406 (1.00171, 1.00641)	-0.06218 (-0.13184, 0.00748)	33
0.4	1.00266 (1.00111, 1.00421)	-0.04342 (-0.17067, 0.08384)	17
0.35	1.00118 (0.99826, 1.0041)	0.0925 (-0.16608, 0.35109)	4
Overall	1.00182 (1.00154, 1.00211)	-0.02808 (-0.03818, -0.01798)	609

N

Orientation Test Expanded

To assess the effect of the orientation on the pores, the normalized error to the intended area of the measured area and the roundness were grouped according to their orientation (angled versus orthogonal) and compared. The results can be seen in Table N.1. The mean normalized error of angled samples did not significantly differ from 0, meaning that angled pores might have printed accurately on average. A Shapiro-Wilks analysis for the roundness and the normalized error of the area of the pores was done to see if the groups were normally distributed. Based on the result of the Shapiro-Wilks test, a Mann-whitney U test was consequently done to assess if the groups differed significantly in roundness or normalized error of the area. Both groups significantly differed from each other (Roundness U statistic: 54598.0 p-value <0.0001, normalized error of the area U statistic: 47792.0 p-value <0.0001) as can be seen in Appendix O. The normalized error from the intended area can therefore be assumed to be smaller for the angled pores compared to the orthogonally printed pores. The roundness, however, is smaller and therefore closer to being circular for the orthogonal pores. This is expected, as orthogonal samples are not impacted by overcuring of resin in the channels.

Additionally, it is tested if the angle itself makes a difference. This has been done in two ways.

Table N.1: Summary of roundness and normalized error of the area by orientation ”angle” versus ”Orthogonal pores”

Orientation	Roundness (Mean and 95% CI)	Normalized Error Area (Mean and 95% CI)
Angle	1.00245 (1.00206, 1.00283)	-0.01195 (-0.02499, 0.00109)
Orthogonal	1.00028 (1.00018, 1.00038)	-0.06808 (-0.08009, -0.05607)
Combined	1.00182 (1.00154, 1.00211)	-0.02808 (-0.03818, -0.01798)

An angle test was done to compare the effects of multiple angles as described in the main text. Furthermore the hypothesized optimal angle adhering to the arctan rule for the channels was compared to 90° - arctan rule which is theorized to be optimal for printing the flat surface samples to see if there was a significantly influence of the normalized error of the area or of the roundness. A Mann-Whitney U test shows a significant difference in the roundness and normalized error of the area between the two groups (Roundness Statistic: 12916, p-value = <0.0001, Normalized error of the Area Statistic: 3501, p-value <0.0001). Table N.2 shows that channels adhering to the arctan rule are both less round and smaller relative to the intended area compared to a random other angle.

Table N.2: Summary of roundness and normalized error of the area for the optimal versus the suboptimal angle

Group	Roundness (Mean and 95% CI)	Normalized Error Area (Mean and 95% CI)
arctan	1.00254 (1.00212, 1.00296)	-0.018 (-0.03282, -0.00319)
90 - arctan	1.00037 (1.00024, 1.0005)	0.07952 (0.06296, 0.09607)

O Statistics

O.1. Shapiro-Wilk and Kruskall-Wallis for channel size

Table O.1: Shapiro-Wilk test for normality for roundness by Nr of the pore. Nr 1 stands for a pore of size 1 mm in diameter, decreasing by 50 µm for increasing number.

Nr	Statistic	p-value
1.0	0.55546	< 0.00001
2.0	0.53820	< 0.00001
3.0	0.62455	< 0.00001
4.0	0.60619	< 0.00001
5.0	0.64757	< 0.00001
6.0	0.56206	< 0.00001
7.0	0.62397	< 0.00001
8.0	0.69781	< 0.00001
9.0	0.65451	< 0.00001
10.0	0.55594	< 0.00001
11.0	0.48130	< 0.00001
12.0	0.67634	< 0.00001
13.0	0.83422	0.00622
14.0	0.71636	0.01771

Table O.2: Results of Kruskal-Wallis test for the roundness for making sure area is not influential on the roundness

Test	Statistic	p-value
Kruskal-Wallis Test	25.78028	0.01819

Table O.3: Dunn's test as a post-hoc analysis for the roundness related to smaller areas with Bonferroni correction.

Nr	1.0	2.0	3.0	4.0	5.0	6.0	7.0	8.0	9.0	10.0	11.0	12.0	13.0
1.0	1.00	1.00	1.00	1.00	1.00	1.00	1.00	1.00	1.00	1.00	0.169	1.00	0.944
2.0	1.00	1.00	1.00	1.00	1.00	1.00	1.00	1.00	1.00	1.00	0.060	1.00	0.487
3.0	1.00	1.00	1.00	1.00	1.00	1.00	1.00	1.00	1.00	1.00	0.112	1.00	0.725
4.0	1.00	1.00	1.00	1.00	1.00	1.00	1.00	1.00	1.00	1.00	1.000	1.00	1.000
5.0	1.00	1.00	1.00	1.00	1.00	1.00	1.00	1.00	1.00	1.00	1.000	1.00	1.000
6.0	1.00	1.00	1.00	1.00	1.00	1.00	1.00	1.00	1.00	1.00	1.000	1.00	1.000
7.0	1.00	1.00	1.00	1.00	1.00	1.00	1.00	1.00	1.00	1.00	1.000	1.00	1.000
8.0	1.00	1.00	1.00	1.00	1.00	1.00	1.00	1.00	1.00	1.00	1.000	1.00	1.000
9.0	1.00	1.00	1.00	1.00	1.00	1.00	1.00	1.00	1.00	1.00	1.000	1.00	1.000
10.0	1.00	1.00	1.00	1.00	1.00	1.00	1.00	1.00	1.00	1.00	1.000	1.00	1.000
11.0	0.169	0.060	0.112	1.00	1.00	1.00	1.00	1.00	1.00	1.00	1.000	1.00	1.000
12.0	1.00	1.00	1.00	1.00	1.00	1.00	1.00	1.00	1.00	1.00	1.000	1.00	1.000
13.0	0.944	0.487	0.725	1.00	1.00	1.00	1.00	1.00	1.00	1.00	1.000	1.00	1.000
14.0	1.00	1.00	1.00	1.00	1.00	1.00	1.00	1.00	1.00	1.00	1.000	1.00	1.000

Table O.4: Shapiro-Wilk test for normality by Nr for the normalized error to the area. Nr 1 stands for a pore of size 1 mm in diameter, decreasing by 50 µm for increasing number.

Nr	Statistic	p-value
1.0	0.92128	0.00134
2.0	0.94696	0.01558
3.0	0.93506	0.00480
4.0	0.94755	0.01655
5.0	0.94662	0.01505
6.0	0.95939	0.06067
7.0	0.97552	0.36915
8.0	0.97992	0.58911
9.0	0.98060	0.67094
10.0	0.98291	0.79545
11.0	0.96346	0.23219
12.0	0.95623	0.20177
13.0	0.94556	0.39022
14.0	0.94132	0.66237

Table O.5: Results of Kruskal-Wallis test for the normalized error to the intended area.

Test	Statistic	p-value
Kruskal-Wallis Test	14.71502	0.32548

O.2. Shapiro-Wilk and Mann-Whitney tests for the angles

Table O.6: Shapiro-Wilk Test for normality of the angled and orthogonal groups for the roundness and normalized error of the area.

Test	Statistic	p-value
Shapiro-Wilk for Angled group (Roundness)	0.6391	3.27×10^{-29}
Shapiro-Wilk for Orthogonal group (Roundness)	0.4953	3.61×10^{-22}
Shapiro-Wilk for Angled group (NEA)	0.9826	4.59×10^{-5}
Shapiro-Wilk for Orthogonal group (NEA)	0.9356	4.68×10^{-7}

Table O.7: Mann-Whitney U test results of orthogonal channels versus all angled channels.

Comparison	U-Statistic	p-value	Interpretation
Angled vs Orthogonal (Roundness)	54598.0	2.68×10^{-17}	p = 2.679 $\times^{-17}$
Angled vs Orthogonal (NEA)	47792.0	5.85×10^{-7}	p = $\times$5.855 $\times^{-7}$

Table O.8: Shapiro-Wilk test results for roundness and normalized error of the area of the arctan versus 90-arctan rule oriented samples. Arctan angle refers to the angle of the channel as measured from the build plate.

Group	Shapiro-Wilk p (Roundness)	Shapiro-Wilk p (Error Area)
arctan	p = 2.270394 $\times^{-08}$	p = 0.00045
90 - arctan	p = 1.080837 $\times^{-15}$	p = 0.00418

Table O.9: Mann-Whitney U test results for roundness and normalized error of the area of the arctan versus 90-arctan rule oriented samples.

Test	U Statistic	p Value
Mann-Whitney U for Roundness	12916.00000	8.79285×10^{-22}
Mann-Whitney U for Normalized Error Area	3501.00000	3.33265×10^{-13}

P

Measurement of Printed Channels

Figures P.2 and P.3 show the geometry of a small circular and square cross-section channel used to check the microfluidic setup and to test the suitability for micro optical coherence tomography as illustrated in Figure P.1. The transparency is sufficient to inspect the internal channel, which is not impacted by the coating. The micro optical coherence tomography was used to measure the internal diameter of the channel, which matched that of the measurement using the digital microscope.

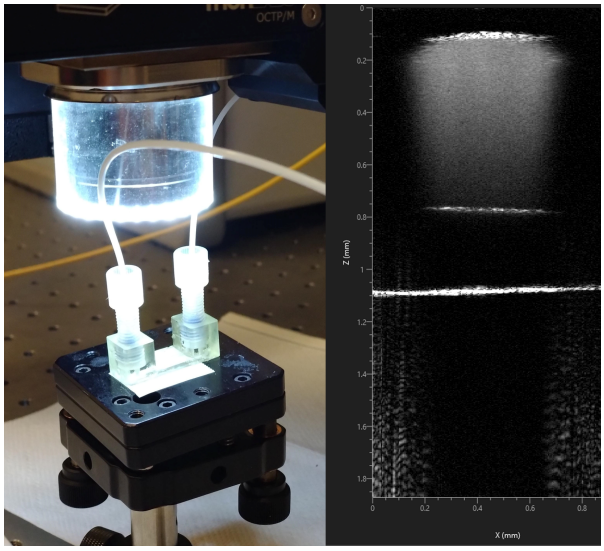

Figure P.1: A sample device showcasing the transparency being sufficient for micro optical coherence tomography

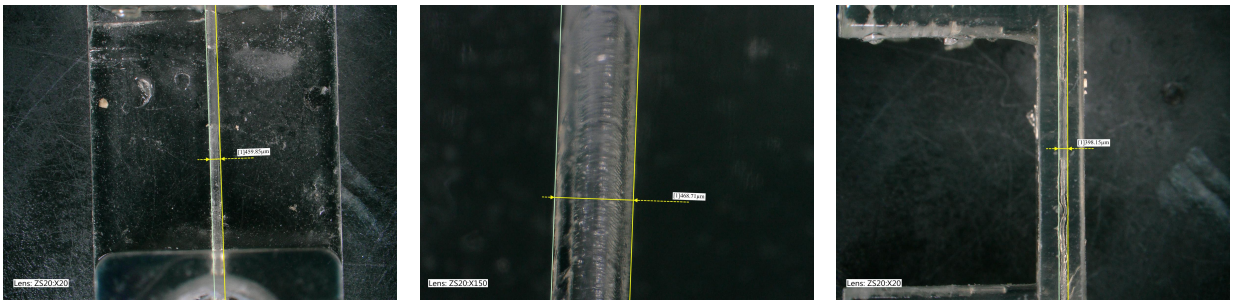

(a) (b) (c)

Figure P.2: (a) Circular cross-sectional test device with an intended diameter of 500 µm as seen from the top, the diameter of the channel measures to be approximately 460 µm. (b) The transparency allows for visual inspection of the inside of the channel, which was not impacted by the application of the acryllic varnish. (c) The side view of the device, measures to be around 400 µm in diameter.

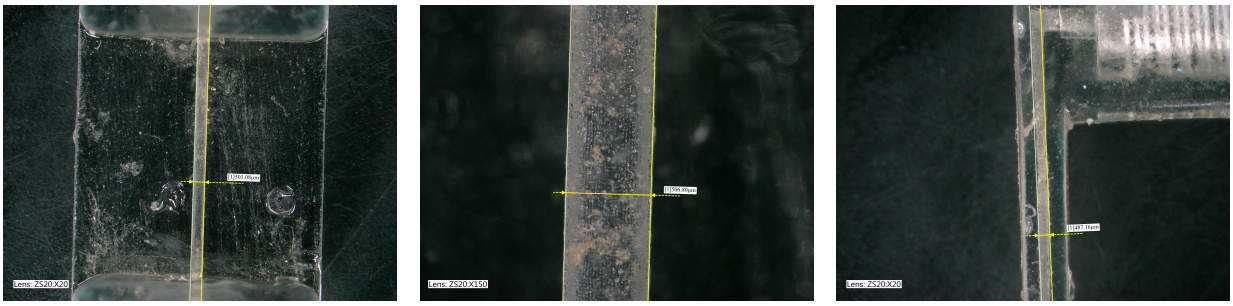

(a) (b) (c)

Figure P.3: (a) Square cross-sectional test device as seen from the top, the diameter of the channel measures to be approximately 500 µm. (b) The transparency allows for visual inspection of the inside of the channel, which was not impacted by the application of the acryllic varnish. (c) The side view of the device, measures to be around 487 µm in diameter.

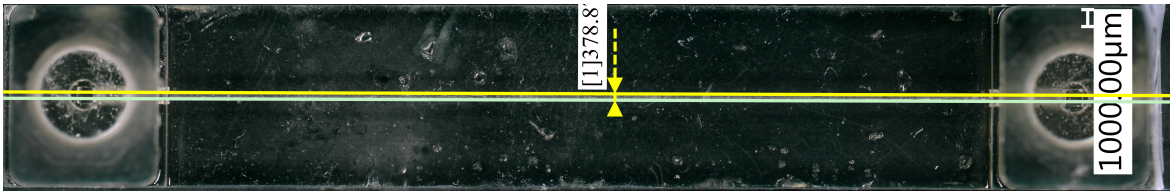

(a)

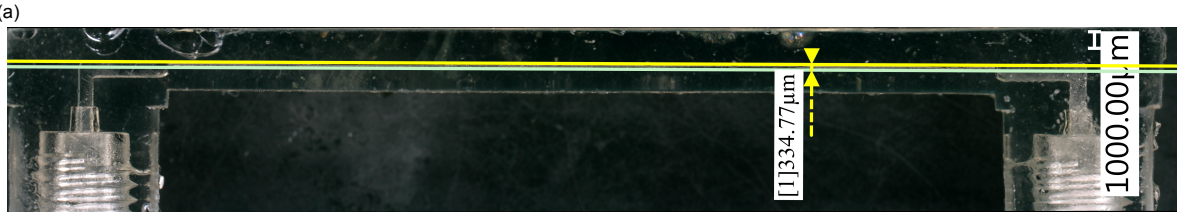

(b)

Figure P.4: Devices printed at 10 µm layer height and 2.5 s exposure time intended to be 400 µm in diameter. (a) Top view of 380 µm in diameter channel. (b) Side view of 330 µm in diameter channel.

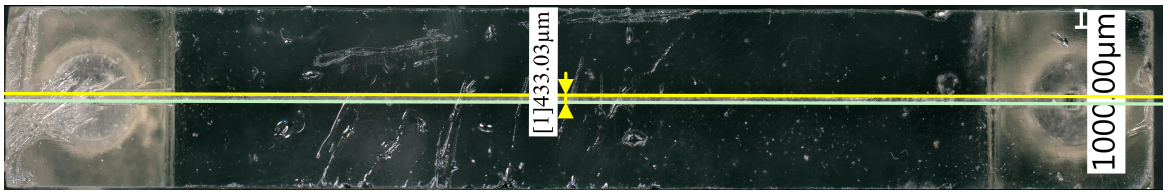

(a)

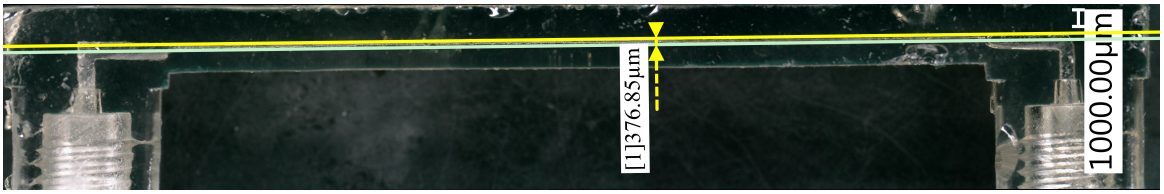

(b)

Figure P.5: Devices printed at 10 µm layer height and 2.5 s exposure time intended to be 450 µm in diameter. (a) Top view of 433 µm in diameter channel. (b) Side view of 377 µm in diameter channel.

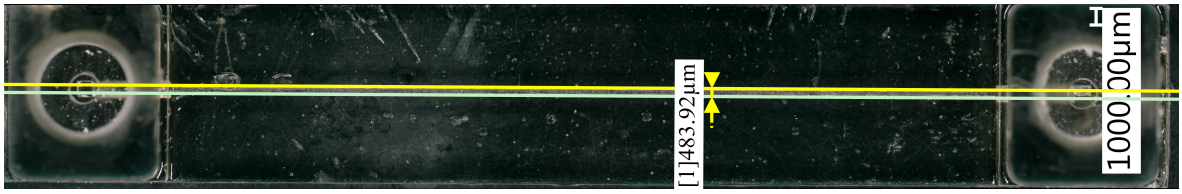

(a)

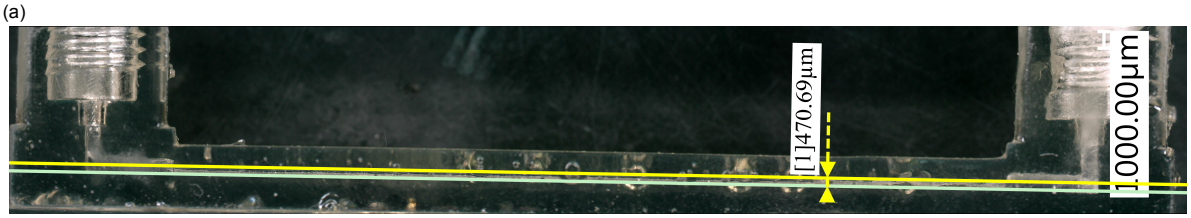

(b)

Figure P.6: Devices printed at 10 µm layer height and 2.5 s exposure time intended to be 500 µm in diameter. (a) Top view of 483 µm in diameter channel. (b) Side view of 471 µm in diameter channel.

Q

Flow Test Results

Underneath is the data used for Figures 4.19 and 4.20.

Table Q.1: Comparison of flow rate and pressure drop for the Experimental, Axisymmetric computational, and Analytical models of the control test setup.

Flow Rate (µl/min)	Pressure Drop (mbar)
Experimental results	
1211.696	30.3364
3594.281	78.3054
5787.781	129.748
10412.273	263.138
Computational model	
1199.054	28.3968
3560.864	85.1268
5727.788	138.072
10419.450	255.581
Analytical model	
1211.696	30.1687
3594.281	89.4606
5787.781	142.306
10412.273	259.172

Table Q.2: Pressure drop comparison for the Experimental, Axisymmetric computational, and Analytical models of the microfluidic channel.

Flow Rate (µl/min)	Pressure Drop (mbar)
Experimental results	
354.939	21.677
787.918	41.595
2474.140	120.284
4084.509	200.738
7659.299	412.572
Computational model	
354.858	11.082
787.689	24.677
2472.645	78.345
4081.328	130.429
7652.075	248.553
Analytical model	
354.939	11.631
787.918	25.820
2474.140	81.078
4084.509	133.851
7659.299	250.998

R

Estimating the True Channel Size

R.1. Expected Channel Size

Using the calculations in Sections 2.6 and 4.1.1 the mathematical model developed by Gong *et al.* [86] was adjusted for calculating the effect of exposure time, orientation, and layer height on overexposure in a circular cross-sectional channel. The Python code used for the model is given for reference in Appendix S. This model is an indication of the impact on overcuring with limitations. For instance, it only calculates the impact of overcuring at the midline of the circle before overlaying the overcured region on the circle. In reality, the sides will experience a slightly larger amount of overcuring due to an increased number of layers added at that pixel location relative to the midline, where the channel is widest.

This model showed a channel of 450 µm to be approximately 280 µm in the minor axis and 414 µm for the major axis. The shape approximates a pointed ellipse. This shape results from the overcuring process. The parameters used in the constructed model were: an angle of 60.95 degrees, an exposure time of 2.5 s, a layer height of 10 µm, a device thickness of 4 mm, and a starting position in the device at 2.275 mm depth. The thickness and starting point are relevant for calculating the number of layers printed on top of the channel causing overcuring inside. An illustration of the cross-sectional shape as approximated using the mathematical model is provided in Figure R.1.

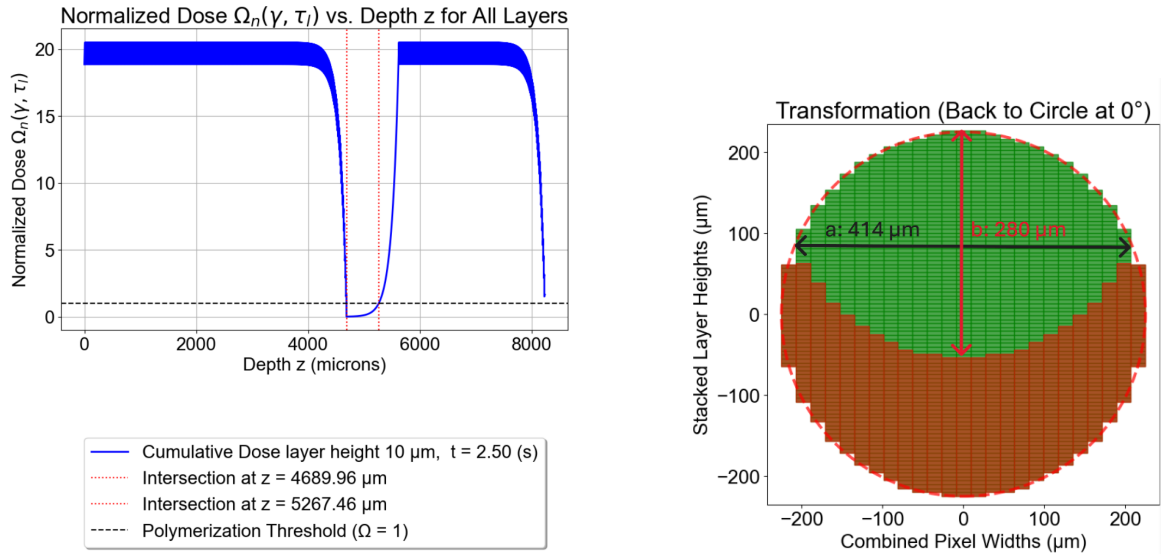

(a) (b)

Figure R.1: (a) The normalized dose for the depth of the 450 µm diameter microfluidic channel. The channel is angled at 60.95 degrees. The intersections show where the normalized dose is larger than 1, meaning which regions will in theory have been able to polymerize. The diameter of the angled channel is 577.5 (the distance between the intersections). (b) An approximation for illustrative purposes of the cross-section of the channel when normalized for the angle. The major axis a is approximately 414 µm, and the minor axis b is approximately 280 µm. In red the overcured area is approximated and visualized.

R.2. Calculating the Resistance

Equation R.1 from Christov [118] can be used for calculating the hydraulic resistance for an elliptical shape, which more closely reflects the expected true shape according to the mathematical model:

$$R = \frac{4}{\pi}\eta L \frac{1 + \left(\frac{b}{a}\right)^2}{\left(\frac{b}{a}\right)^3} \frac{1}{a^4} \tag{R.1}$$

where: R is the hydraulic resistance, η is the dynamic viscosity, L is the channel length, a is the semi-major axis, and b is the semi-minor axis. A hydraulic resistance of $3.02 \cdot 10^{11}$ Pa·s/m^3 was analytically calculated using the calculated minor and major axis and the equation for the resistance of an elliptical shape. This more closely approximates the value found experimentally of $3.19 \cdot 10^{11}$ Pa·s/m^3, but still seemingly underestimates the resistance. The measured dimensions as seen in Section 4.3.2 can similarly be used to calculate the hydraulic resistance. The channel was observed to be 433 µm in diameter from the top view and approximately 377 µm from the side view using the approach described in Section 4.4.1. These measurements translate to a resistance of $2.24 \cdot 10^{11}$ Pa·s/m^3 using the same equation for an elliptical cross-sectional shape, which is smaller than the experimentally observed resistance. The observed variations in channel diameter as illustrated in Figure 4.17 may increase the resistance.
Finally, the Hagen-Poisseuille calculations in Section 3.9.1 can be used to calculate the expected diameter of a circular channel for the measured resistance. This would be approximately 330 µm in diameter, a 120 µm diameter decrease from intended.

We can therefore conclude that the channel is smaller than intended. Both the measurements and calculated dimensions imply an elliptical cross-sectional shape for the channel. The measurements done may not have accurately described the channel dimensions. Furthermore, the calculations prove to most closely approximate the printed channel size, especially considering the approximated elliptical cross-sectional shape may still not accurately capture the pointed elliptical cross-sectional shape that is expected from the calculation.

S

Python Code

This Python [116] code was used to assess and visualize the true size of the channel as explained in Appendix R. It makes use of the equations provided by Gong *et al.* [86] based on the Lambert-Beer law to approximate the depth of the channel when accounted for overcuring of photopolymer resin in the channel. The code is provided for transparency into the adaptation of the equations. It was validated using the parameters in their study (ζ_l: 0.69, τ_l: 2.0, z_l: 50) and using Figure 8a and 8b.

The code supplements the mathematical approach by adding angling of the channel and visualizing the effect on the cross-sectional shape of the cylindrical channel using MSLA and pixels. This code was used in an altered form but using a similar approach to generate Figures 4.1, 4.3, 4.4, 4.5, and 4.6 in Section 4.1.1 and Figure R.1 in Appendix R.

Several assumptions and limitations apply. First, it assumes uniform light exposure across each pixel. Second, it relies on the validity of the optical model for resin formulation as proposed in the referenced study. A key limitation is that overcure depth was only calculated along the channel's midline, where it is minimal due to the reduced number of subsequently printed layers. The code does attempt to incorporate the limitation in the constant layer height in reaching the desired diameter.

```
#Required packages
import math
import numpy as np
import matplotlib.pyplot as plt
from matplotlib import rc
from matplotlib.patches import Rectangle, Ellipse
from collections import defaultdict

#Set plot font
rc('font', **{'family': 'sans-serif', 'sans-serif': ['Arial']})
plt.rcParams['font.size'] = 20
Afont = {'fontname': 'Arial'}

#Main input variables for the channel
Ang =  60.95  #Channel angle in degrees
diam = 450  #Channel diameter in micrometer
pix = 18  #Pixel width in micrometer
LH = 10  #Layer height in micrometer
thickness_device = 4000  #Thickness of the surrounding walls of the channel in micrometer
Position_channel = 2275  #Starting depth of channel in micrometer
t = 2.5  #Exposure time for each layer in seconds 1.525 for polymerization front, 1.65753
    for back at 10 um

#Given printer parameters
```

```
I0 = 4.0  #Initial irradiance at z = 0 (mW/cm^2)
ha = 120  #Penetration depth in micrometers
zl = LH  #Layer thickness in micrometers
Ec = 6.1  #Critical dose in mJ/cm^2

#Apply angle to channel, device, and starting position
dis = None
thick = None
pos = None

def draw_channel(angle_degrees, distance):
    global dis
    angle_radians = math.radians(angle_degrees)
    mid_x = 0
    mid_y1 = mid_x * math.tan(angle_radians)
    mid_y2 = mid_y1 + (distance / math.cos(angle_radians))
    dis = mid_y2


def draw_device(angle_degrees, distance):
    global thick
    angle_radians = math.radians(angle_degrees)
    mid_x = 0
    mid_y1 = mid_x * math.tan(angle_radians)
    mid_y2 = mid_y1 + (distance / math.cos(angle_radians))
    thick = mid_y2

def draw_position_channel(angle_degrees, distance):
    global pos
    angle_radians = math.radians(angle_degrees)
    mid_x = 0
    mid_y1 = mid_x * math.tan(angle_radians)
    mid_y2 = mid_y1 + (distance / math.cos(angle_radians))
    pos = mid_y2

draw_channel(angle_degrees=Ang, distance=diam)
draw_device(angle_degrees=Ang, distance=thickness_device)
draw_position_channel(angle_degrees=Ang, distance=Position_channel)

#Channel dimensions as intended and after discretizing for layer height and applying the
    angle
nzl = round(dis / zl)  #Number of layers for the channel using angled distance
N = round(thick / LH)  #Number of layers needed for the device thickness
start = round(pos / LH)  #Number oflayers before the channel starts
print(f"Layers for the channel: {nzl}")
print(f"Diameter of channel at {Ang} degrees: {dis:.2f}")  #Measured diameter after angling
print(f"Printer intended channel size: {nzl * zl}")  #Different from perfect due to angling
    changing the diameter and approximation using LH
print(f"Thickness of device at {Ang} degrees: {thick:.2f}")
print(f"Layers for device at {Ang} degrees: {N}")
print(f"Printer intended device size: {N * zl}")  #Different from perfect due to angling
    changing the diameter
print(f"Start of channel in device at {Ang} degrees: {pos:.2f}")
print(f"Start of channel in device at {Ang} degrees at layer number: {start:.2f}")

#Calculating the curing depth and normalized dose of the initial layer
channel_list = list(range(start, start + nzl))  #Position of channel
alpha = 1 / ha
Tc = Ec / I0
Dz = I0 * np.exp(-zl / ha) * t  #Penetration depth
Emax = I0 * t  #tp
Cd = ha * np.log(Emax / Ec)
print(f" The curing depth {Cd:.2f}")
zp = ha * np.log((t) / Tc)
print(f" The curing depth {zp:.2f}, should be similar to previous")
zeta_l = zl / ha  #Normalized layer thickness
tau_l = t / Tc  #Normalized layer exposure time
normDose = (t / Tc) * (np.exp(-zl / ha))
unitlessnormdose = tau_l * np.exp(- zeta_l)
omega_back = tau_l * np.exp(-zeta_l)  #Normalized dose at the back of each layer
omega_front = tau_l  #Normalized dose at the front of each layer
```

```
print(f"Cumulative dose at the back of the first layer (should be at least 1): {omega_back:.2f}")
print(f"Cumulative dose at the front of the first layer (preferably close to the value for the back): {omega_front:.2f}")

#Function for normalized dose within layer
def normalized_dose(gamma, n, tau_l, zeta_l):
    return tau_l * np.exp(-((n + 1) - gamma) * zeta_l)


z_values_full = np.linspace(0, (N) * zl, N * 100)  #Full depth range from 0 to total thickness
cumulative_dose = np.zeros_like(z_values_full)

#Plotting the normalized dose for each layer
plt.figure(figsize=(10, 6))
zeta_l = zl / ha  #Normalized layer thickness
tau_l = t / Tc  #Normalized layer exposure time
z_values_full = np.linspace(0, (N) * zl, N * 100)  #Full depth range from 0 to total thickness
cumulative_dose = np.zeros_like(z_values_full)
for n in range(N):
    if n not in channel_list:
        z_values = np.linspace(0, (n + 1) * zl, N * 100)
        gamma_values = z_values / zl
        dose_values = normalized_dose(gamma_values, n, tau_l, zeta_l)
        mask = (z_values_full >= 0 * zl) & (z_values_full <= (n + 1) * zl)
        cumulative_dose[mask] += normalized_dose(z_values_full[mask] / zl, n, tau_l, zeta_l)
    else:
        pass  #If n is in channel_list; no printed layer

#Plot the cumulative normalized dose as a new line
plt.plot(z_values_full, cumulative_dose, color='blue', linestyle='-', linewidth=2,
         label=f'Cumulative Dose layer height 10 µm,  t = {t:.2f} (s)')

#Find intersection with normalized dose of 1 to see the where no polymerization occurs
intersection_indices = np.where(np.diff(np.sign(cumulative_dose - 1)))[0]
intersection_depths = z_values_full[intersection_indices]
for depth in intersection_depths:
    plt.axvline(x=depth, color='red', linestyle='dotted', label=f'Intersection at z = {depth:.2f} µm')

#Reverse the angling of the printed layers to find the expected channel diameter
def measure_perpendicular_distance(angle_degrees, angled_distance):
    angle_radians = math.radians(angle_degrees)
    perpendicular_distance = angled_distance * math.cos(angle_radians)
    return perpendicular_distance

#Find the printed channel size and overcuring depth
Final = intersection_depths[1] - intersection_depths[0]
Excess = dis - Final  #Error as calculated from the intended diameter
Final_norm = measure_perpendicular_distance(Ang, Final)
Excess_norm = measure_perpendicular_distance(Ang, Excess)
Excess_2 = round(dis / zl) * zl - Final  #Error as calculated from printer input instead of intended (different due to layer discretization)
print(f" The printed channel diam at {Ang} degrees cross-section: {Final:.2f}, with a difference from the intended size of {Excess:.2f}")
print(f" The printed channel diam at {Ang} degrees cross-section: {Final:.2f}, with an overcure of the layered size of {Excess_2:.2f}")
print(f" The printed channel diam at parallel cross-section: {Final_norm:.2f}, with an overcure of {Excess_norm:.2f}")
plt.axhline(y=1, color='k', linestyle='--', label='Polymerization Threshold Ω( = 1)')
plt.xlabel('Depth z (microns)')
plt.ylabel(r'Normalized Dose $\Omega_n(\gamma, \tau_l)$')
plt.title(r'Normalized Dose $\Omega_n(\gamma, \tau_l)$' "f'vs. Depth z for All Layers ')
plt.legend(loc='lower center', bbox_to_anchor=(0.5, -0.75),
           ncol=1, fancybox=True, shadow=True)
plt.grid(True)
plt.show()

#Compare the angled print to the horizontal print cross-sectionally
```

```python
def draw_circle_and_ellipse_with_rectangles(radius, rect_width, rect_height, angle_degrees):
    x_min, x_max = -radius, radius
    y_min, y_max = -radius, radius

    #Fill the cross-section of the horizontal channel with pixel width * layer height
    circle_rectangles = []
    y = y_min
    while y <= y_max:
        x = x_min
        while x <= x_max:
            if math.sqrt((x + 0.5 * rect_width) ** 2 + (y + 0.5 * rect_height) ** 2) <= radius:
                circle_rectangles.append((x, y))
            x += rect_width
        y += rect_height

    plt.figure(figsize=(16, 8))

    #Plot the circle cross-section
    plt.subplot(1, 2, 1)
    for x, y in circle_rectangles:
        rectangle = plt.Rectangle((x, y), rect_width, rect_height, color="blue", alpha=0.7, linewidth=3)
        plt.gca().add_patch(rectangle)

    circle = plt.Circle((0, 0), radius, color="red", fill=False, linestyle="--", label="Circle boundary", linewidth=3,
                        alpha=0.7)
    plt.gca().add_patch(circle)
    plt.xlim(x_min - rect_width, x_max + rect_width)
    plt.ylim(y_min - rect_height, y_max + rect_height)
    plt.gca().set_aspect('equal', adjustable='box')
    plt.title(f"Parallel (layer height: {rect_height} µm, r: {radius} µm)")
    plt.xlabel("Combined Pixel Widths (µm)")
    plt.ylabel("Stacked Layer Heights (µm)")
    plt.legend(loc='lower center', bbox_to_anchor=(0.5, -0.3),
               ncol=1, fancybox=True, shadow=True)
    angle_radians = math.radians(angle_degrees)
    minor_axis = radius / math.cos(angle_radians)  # Reduced axis due to tilt

    #Fill the cross-section of the angled channel with pixel width * layer height
    ellipse_rectangles = []

    y = -minor_axis
    while y <= minor_axis:
        x = x_min
        while x <= x_max:
            x_center = x + 0.5 * rect_width
            y_center = y + 0.5 * rect_height
            if ((x_center ** 2) / (radius ** 2)) + ((y_center ** 2) / (minor_axis ** 2)) <= 1:
                ellipse_rectangles.append((x, y))

            x += rect_width
        y += rect_height

    #Plot the ellipse cross-section
    plt.subplot(1, 2, 2)
    for x, y in ellipse_rectangles:
        rectangle = plt.Rectangle((x, y), rect_width, rect_height, color="blue", alpha=0.7)
        plt.gca().add_patch(rectangle)

    ellipse = Ellipse((0, 0), 2 * radius, 2 * minor_axis, color="red", fill=False, linestyle="--",
                      label="Ellipse boundary", linewidth=3, alpha=0.7)
    plt.gca().add_patch(ellipse)
    plt.xlim(x_min - rect_width - 600, x_max + rect_width + 600)
    plt.ylim(-minor_axis - rect_height, minor_axis + rect_height)
    plt.gca().set_aspect('equal', adjustable='box')
    plt.title(f"Angled (Angle: {angle_degrees}°, layer height: {rect_height} µm, r: {radius} µm)")
```

```
    plt.xlabel("Combined Pixel Widths (µm)")
    plt.ylabel("Stacked Layer Heights (µm)")
    plt.legend(loc='lower center', bbox_to_anchor=(0.5, -0.3),
               ncol=1, fancybox=True, shadow=True)
    plt.tight_layout()
    plt.show()


draw_circle_and_ellipse_with_rectangles(radius=diam / 2, rect_width=pix, rect_height=LH,
    angle_degrees=Ang)

#Compare tthe angled channel to the end product when looking through it horizontally after
    printing at an angle
#Repeat the process adding the calculated overcured resin at the diameter
#Overcure at sides are underestimated because they lie deeper but the overcure is only added
    using this approach
#It is assumed that the exposure at a pixel is uniform and equally distributed
def draw_circle_and_ellipse_with_rectangles_and_curing(radius, rect_width, rect_height,
    angle_degrees, overlay_height):
    angle_radians = math.radians(angle_degrees)
    minor_axis = radius / math.cos(angle_radians)
    ellipse_rectangles = []
    transformed_rectangles = []

    #Fill ellipse with pixel width * layer height
    y = -minor_axis
    while y <= minor_axis:
        x = -radius
        while x <= radius:
            x_center = x + 0.5 * rect_width
            y_center = y + 0.5 * rect_height

            if ((x_center ** 2) / (radius ** 2)) + ((y_center ** 2) / (minor_axis ** 2)) <=
                1:
                ellipse_rectangles.append((x, y))
                transformed_x = x
                transformed_y = y * math.cos(angle_radians)
                transformed_rectangles.append((transformed_x, transformed_y))

            x += rect_width
        y += rect_height

    stacks = defaultdict(list)
    transformed_stacks = defaultdict(list)
    for x, y in ellipse_rectangles:
        stacks[x].append(y)
    for x, y in transformed_rectangles:
        transformed_stacks[x].append(y)

    #Plot the ellipse and rectangles
    fig, axes = plt.subplots(1, 2, figsize=(16, 8))
    ax1, ax2 = axes

    p = -1
    for x, y_values in stacks.items():
        min_y = min(y_values)
        overlay_limit = min_y + overlay_height  #Overlay starts at the bottom and extends
            freely
        p += 1
        for y in y_values:
            color = "green"
            if y < overlay_limit:
                color = "green"
            rect = Rectangle((x, y), rect_width, rect_height, color=color, alpha=0.7)
            ax1.add_patch(rect)
        overlay_rect = Rectangle((x, min_y), rect_width, min(overlay_height, max(y_values) -
            min_y + rect_height),
                                 color="red", alpha=0.5)  #Min(overlay_height, max(y_values)
                                     - min_y)
        ax1.add_patch(overlay_rect)

```

```
    ellipse = Ellipse((0, 0), 2 * radius, 2 * minor_axis, color="red", fill=False, linestyle="--", linewidth=3,
                      alpha=0.7)
    ax1.add_patch(ellipse)
    ax1.set_xlim(-radius - rect_width - 300, radius + rect_width + 300)
    ax1.set_ylim(-minor_axis - rect_height, minor_axis + rect_height)
    ax1.set_aspect('equal', adjustable='box')
    ax1.set_title(f"Ellipse Approximation (Angle: {angle_degrees}°)")
    ax1.set_xlabel("Combined Pixel Widths (µm)")
    ax1.set_ylabel("Stacked Layer Heights (µm)")

    #Again fill the ellipse but correcting for the angle to visualize final channel
    sd = 0
    for x, y_values in transformed_stacks.items():
        min_y = min(y_values)
        overlay_limit = min_y + overlay_height * math.cos(angle_radians)
        for y in y_values:
            color = "green"
            if y <= overlay_limit:
                color = "green"
            rect = Rectangle((x, y), rect_width, rect_height * math.cos(angle_radians), color=color, alpha=0.7)
            ax2.add_patch(rect)
        overlay_rect = Rectangle((x, min_y), rect_width, min(overlay_height * math.cos(angle_radians),
                                                             max(y_values) - min_y + rect_height * math.cos(
                                                                 angle_radians)),
                                 color="red", alpha=0.5)
        if min(overlay_height * math.cos(angle_radians),
               max(y_values) - min_y + rect_height * math.cos(angle_radians)) < overlay_height * math.cos(
                angle_radians):
            sd += rect_width
        ax2.add_patch(overlay_rect)

    circle = Ellipse((0, 0), 2 * radius, 2 * radius, color="red", fill=False, linestyle="--", linewidth=3, alpha=0.7)
    ax2.add_patch(circle)
    ax2.set_xlim(-radius - rect_width, radius + rect_width)
    ax2.set_ylim(-radius - rect_height, radius + rect_height)
    ax2.set_aspect('equal', adjustable='box')
    ax2.set_title("Transformation (Back to Circle at 0°)")
    ax2.set_xlabel("Combined Pixel Widths (µm)")
    ax2.set_ylabel("Stacked Layer Heights (µm)")
    plt.show()

    #Check whether the sides of the channel are closed and the channel width as opposed to height
    check = []
    print(f"{sd}")
    print(f"Total stacks in x-direction: {len(stacks)}, Max width after deducting clogged sides: {len(stacks) * rect_width - sd}")
    for x, y_values in stacks.items():
        if len(y_values) == nzl:
            check.append(1)
        if len(y_values) > nzl:
            check.append(2)

    if len(check) >= 1:
        if 2 not in check:
            print("Succes, the maximum number of layers is similar to the maximum number calculated previously.")



draw_circle_and_ellipse_with_rectangles_and_curing(radius=diam / 2, rect_width=pix, rect_height=LH, angle_degrees=Ang,
                                                   overlay_height=Excess_2)


```

```
#draw a side view of the angled channel in the device thickness for visualization purposes
def draw_channel_within_device(angle_degrees, device_thickness, channel_diameter, channel_start_pos):
    angle_radians = math.radians(angle_degrees)
    x = np.linspace(-500, 500, 10)

    #Define device top and bottom
    y_device_bottom = x * math.tan(angle_radians)
    y_device_top = y_device_bottom + (device_thickness / math.cos(angle_radians))

    #Place the channel within device
    y_channel_bottom = y_device_bottom + (channel_start_pos / math.cos(angle_radians))
    y_channel_top = y_channel_bottom + (channel_diameter / math.cos(angle_radians))

    plt.figure(figsize=(10, 8))
    plt.axhline(-(thickness_device/math.cos(angle_radians)+(500 / math.cos(angle_radians)) + 500), color="blue", linestyle="-", label="LCD UV light source", linewidth=8)

    #Plot the device top and bottom
    plt.plot(x, -y_device_bottom, color="grey", linewidth=4, label="Device Bottom")
    plt.plot(x, -y_device_top, color="black", linewidth=4, label="Device Top")

    #Plot the channel top and bottom
    plt.plot(x, -y_channel_bottom, color="red", linewidth=4, label="Channel Bottom")
    plt.plot(x, -y_channel_top, color="orange", linewidth=4, label="Channel Top")

    #Vertical measure line for channel
    mid_x = 0
    mid_y1 = mid_x * math.tan(angle_radians) + (channel_start_pos / math.cos(angle_radians))
    mid_y2 = mid_y1 + (channel_diameter / math.cos(angle_radians))
    plt.plot([-mid_x, -mid_x], [-mid_y1, -mid_y2], color="purple", linestyle="--",
             label=f"Channel Height: {mid_y2 - mid_y1:.2f} µm", linewidth=3)

    plt.text(-mid_x + 150, -((mid_y2 + mid_y1) / 2),
             f"Channel size: {mid_y2 - mid_y1:.2f} µm, and {channel_diameter} µm \n real: {nzl * LH} µm and {nzl * LH * math.cos(angle_radians):.2f} µm", rotation=0, va='center', fontsize=10)

    #More geometry
    y_dev_bot = mid_x * math.tan(angle_radians)
    y_dev_top = y_dev_bot + (device_thickness / math.cos(angle_radians))
    y_chan_bot = y_dev_bot + (channel_start_pos / math.cos(angle_radians))
    y_chan_top = y_chan_bot + (channel_diameter / math.cos(angle_radians))

    #Plot distance top to channel
    plt.plot([-mid_x + 20, -mid_x + 20], [-y_chan_top, -y_dev_top], color="green", linestyle="--",
             linewidth=2)
    plt.text(-mid_x + 150, -((y_chan_top + y_dev_top) / 2),
             f"Top Gap: {(y_dev_top - y_chan_top):.2f} µm, and {device_thickness-channel_diameter-channel_start_pos} µm \n real: {(N - nzl - start) * LH} µm and {((N - nzl - start) * LH) * math.cos(angle_radians):.2f} µm", rotation=0, va='center', fontsize=10)

    #Plot distance bottom to channel
    plt.plot([-mid_x - 20, -mid_x - 20], [-y_dev_bot, -y_chan_bot], color="blue", linestyle="--",
             linewidth=2)
    plt.text(-mid_x + 150, -((y_chan_bot + y_dev_bot) / 2),
             f"Bottom Gap: {(y_chan_bot - y_dev_bot):.2f}, and {channel_start_pos} µm \n real: {(start)* LH} µm  and {(start)* LH * math.cos(angle_radians):.2f} µm", rotation=0, va='center', fontsize=10)

    plt.gca().set_aspect('equal', adjustable='box')
    plt.xlim(-1000, 1000)
    plt.ylim(-(thickness_device/math.cos(angle_radians)+(500 / math.cos(angle_radians)) + 500), 500 / math.cos(angle_radians))
    plt.title(f"Angled Channel Inside Device at {angle_degrees}° \n This is a visualization PRE-printing excluding overcuring. \n Stacking layers are an approximation of \n the intended channel diameter and alter the size", fontsize=18)
    plt.axis('off')
```

```
    plt.legend(loc='lower center', bbox_to_anchor=(-1, 0), ncol=1, fontsize = 10)
    plt.show()

draw_channel_within_device(angle_degrees=Ang,
                           device_thickness=thickness_device,
                           channel_diameter=diam,
                           channel_start_pos=Position_channel)
```

Listing S.1: Full Python script for angled channel simulation. This code is partly generated and cleaned using ChatGPT-4o (OpenAI [208]) and validated against Gong *et al.* [86]. The output is the normalized dose of the channel representing the overcure of the entered channel diameter, data on the channel dimensions and deviation from the intended size, a cross-sectional view of the channel using the pixel width and layer height at the intended angle versus the horizontal approach, and a cross-sectional view with an overlay of the overcured resin depth as calculated at the diameter of the channel as printed at an angle and when viewing the cross-section orthogonally.

Bibliography

[1] R. F. R. Ursem *et al.*, “Worth your sweat: Wearable microfluidic flow rate sensors for meaningful sweat analytics,” *Lab on a chip*, vol. 25, no. 5, pp. 1296–1315, 2025. DOI: https://doi.org/10.1039/d4lc00927d. [Online]. Available: https://pubmed.ncbi.nlm.nih.gov/39878525/.

[2] W. B. Lo *et al.*, “The circle before willis: A historical account of the intracranial anastomosis,” *Neurosurgery*, vol. 66, no. 1, 7–18, discussion 17–8, 2010, ISSN: 1524-4040 (Electronic). DOI: 10.1227/01.NEU.0000362002.63241.A5. [Online]. Available: https://www.ncbi.nlm.nih.gov/pubmed/19935436.

[3] Z. Vrselja *et al.*, “Function of circle of willis,” *J Cereb Blood Flow Metab*, vol. 34, no. 4, pp. 578–84, 2014, ISSN: 1559-7016 (Electronic). DOI: 10.1038/jcbfm.2014.7. [Online]. Available: https://www.ncbi.nlm.nih.gov/pubmed/24473483.

[4] R. S. Shah *et al.*, “Cerebral vascular anatomy and physiology,” *Surgery (Oxford)*, vol. 39, no. 8, pp. 463–469, Aug. 2021. DOI: https://doi.org/10.1016/j.mpsur.2021.06.006.

[5] A. Singh *et al.*, “Small-vessel disease in the brain,” *American Heart Journal Plus: Cardiology Research and Practice*, vol. 27, p. 100 277, 2023, ISSN: 2666-6022. DOI: https://doi.org/10.1016/j.ahjo.2023.100277. [Online]. Available: https://www.sciencedirect.com/science/article/pii/S2666602223000290.

[6] J. A. Feekes *et al.*, “Tertiary microvascular territories define lacunar infarcts in the basal ganglia,” *Ann Neurol*, vol. 58, no. 1, pp. 18–30, 2005, ISSN: 0364-5134 (Print) 0364-5134 (Linking). DOI: 10.1002/ana.20505. [Online]. Available: https://www.ncbi.nlm.nih.gov/pubmed/15900563.

[7] V. Vogels *et al.*, “Deep cerebral perforators: Anatomical distribution and clinical symptoms: An overview,” *Stroke*, vol. 52, no. 10, e660–e674, 2021, ISSN: 1524-4628 (Electronic). DOI: 10.1161/STROKEAHA.120.034096. [Online]. Available: https://www.ncbi.nlm.nih.gov/pubmed/34311568.

[8] S. H. Ha *et al.*, “Factors associated with two different stroke mechanisms in perforator infarctions regarding the shape of arteries,” *Sci Rep*, vol. 12, no. 1, p. 16 752, 2022, ISSN: 2045-2322 (Electronic). DOI: 10.1038/s41598-022-21329-7. [Online]. Available: https://www.ncbi.nlm.nih.gov/pubmed/36202949.

[9] S. Marinkovic *et al.*, “Anatomic and clinical correlations of the lenticulostriate arteries,” *Clin Anat*, vol. 14, no. 3, pp. 190–5, 2001, ISSN: 0897-3806 (Linking). DOI: 10.1002/ca.1032. [Online]. Available: https://www.ncbi.nlm.nih.gov/pubmed/11301466.

[10] Y.-C. Chen *et al.*, “Correlation between the number of lenticulostriate arteries and imaging of cerebral small vessel disease,” *Frontiers in Neurology*, vol. 10, Aug. 2019. DOI: https://doi.org/10.3389/fneur.2019.00882.

[11] F. Umansky *et al.*, “The perforating branches of the middle cerebral artery. a microanatomical study,” *J Neurosurg*, vol. 62, no. 2, pp. 261–8, 1985, ISSN: 0022-3085 (Linking). DOI: 10.3171/jns.1985.62.2.0261. [Online]. Available: https://www.ncbi.nlm.nih.gov/pubmed/3968566.

[12] J. Li *et al.*, “Association of morphology of lenticulostriate arteries and proximal plaque characteristics with single subcortical infarction: A whole□brain high□resolution vessel wall imaging study,” *Journal of the American Heart Association*, vol. 13, no. 10, May 2024. DOI: https://doi.org/10.1161/jaha.123.032856.

[13] M. Kizhisseri *et al.*, “An analytical method informed by clinical imaging data for estimating outlet boundary conditions in computational fluid dynamics analysis of carotid artery blood flow,” *Sci Rep*, vol. 13, no. 1, p. 14 973, 2023, ISSN: 2045-2322 (Electronic). DOI: 10.1038/s41598-023-42004-5. [Online]. Available: https://www.ncbi.nlm.nih.gov/pubmed/37696859.

[14] L. Pantoni, “Cerebral small vessel disease: From pathogenesis and clinical characteristics to therapeutic challenges,” *The Lancet Neurology*, vol. 9, no. 7, pp. 689–701, 2010, ISSN: 1474-4422. DOI: https://doi.org/10.1016/S1474-4422(10)70104-6. [Online]. Available: https://www.sciencedirect.com/science/article/pii/S1474442210701046.

[15] J. M. Wardlaw *et al.*, “Neuroimaging standards for research into small vessel disease and its contribution to ageing and neurodegeneration,” *Lancet Neurol*, vol. 12, no. 8, pp. 822–38, 2013, ISSN: 1474-4422 (Print) 1474-4422. DOI: 10.1016/s1474-4422(13)70124-8. [Online]. Available: https://www.ncbi.nlm.nih.gov/pubmed/23867200.

[16] J. Chojdak-Łukasiewicz *et al.*, “Cerebral small vessel disease: A review,” *Adv Clin Exp Med*, vol. 30, no. 3, pp. 349–356, 2021, ISSN: 1899-5276 (Print) 1899-5276. DOI: 10.17219/acem/131216.

[17] M. A. Alioglu *et al.*, “3d embedded printing of microfluidic devices using a functional silicone composite support bath,” *Additive Manufacturing*, vol. 70, p. 103 566, 2023, ISSN: 22148604. DOI: 10.1016/j.addma.2023.103566. [Online]. Available: https://www.sciencedirect.com/science/article/pii/S2214860423001793.

[18] Y. S. Park *et al.*, “Mri assessment of cerebral small vessel disease in patients with spontaneous intracerebral hemorrhage,” *Yonsei Med J*, vol. 60, no. 8, pp. 774–781, 2019, ISSN: 0513-5796 (Print) 0513-5796. DOI: 10.3349/ymj.2019.60.8.774. [Online]. Available: https://www.ncbi.nlm.nih.gov/pubmed/31347333.

[19] A. S. Das *et al.*, “Asymptomatic cerebral small vessel disease: Insights from population-based studies,” *J Stroke*, vol. 21, no. 2, pp. 121–138, 2019, ISSN: 2287-6391 (Print) 2287-6391. DOI: 10.5853/jos.2018.03608. [Online]. Available: https://www.ncbi.nlm.nih.gov/pubmed/30991799.

[20] P. L. Kolominsky-Rabas *et al.*, “Epidemiology of ischemic stroke subtypes according to toast criteria: Incidence, recurrence, and long-term survival in ischemic stroke subtypes: A population-based study,” *Stroke*, vol. 32, no. 12, pp. 2735–40, 2001, ISSN: 1524-4628 (Electronic) 0039-2499 (Linking). DOI: 10.1161/hs1201.100209. [Online]. Available: https://www.ncbi.nlm.nih.gov/pubmed/11739965.

[21] Y. Shi *et al.*, “Cerebral blood flow in small vessel disease: A systematic review and meta-analysis,” *J Cereb Blood Flow Metab*, vol. 36, no. 10, pp. 1653–1667, 2016, ISSN: 1559-7016 (Electronic) 0271-678X (Print) 0271-678X (Linking). DOI: 10.1177/0271678X16662891. [Online]. Available: https://www.ncbi.nlm.nih.gov/pubmed/27496552.

[22] M. A. Gimbrone *et al.*, “The critical role of mechanical forces in blood vessel development, physiology and pathology,” *Journal of Vascular Surgery*, vol. 29, no. 6, pp. 1104–1151, 1999, ISSN: 0741-5214. DOI: https://doi.org/10.1016/S0741-5214(99)70252-1. [Online]. Available: https://www.sciencedirect.com/science/article/pii/S0741521499702521.

[23] F. Syed *et al.*, “Modeling dynamics of the cardiovascular system using fluid-structure interaction methods,” *Biology (Basel)*, vol. 12, no. 7, 2023, ISSN: 2079-7737. DOI: 10.3390/biology12071026.

[24] D. Pavlin-Premrl *et al.*, “Computational fluid dynamics in intracranial atherosclerosis - lessons from cardiology: A review of cfd in intracranial atherosclerosis,” *J Stroke Cerebrovasc Dis*, vol. 30, no. 10, p. 106 009, 2021, ISSN: 1532-8511 (Electronic). DOI: \url{10.1016/j.jstrokecerebrovasdis.2021.106009}. [Online]. Available: https://www.ncbi.nlm.nih.gov/pubmed/34343837.

[25] M. Colombo *et al.*, “Integrative modeling of hemodynamic changes and perfusion impairment in coronary microvascular disease,” *Front Bioeng Biotechnol*, vol. 11, p. 1 204 178, 2023, ISSN: 2296-4185 (Print) 2296-4185 (Electronic) 2296-4185 (Linking). DOI: 10.3389/fbioe.2023.1204178. [Online]. Available: https://www.ncbi.nlm.nih.gov/pubmed/37564992.

[26] Georgia Institute of Technology, *Microfluidic device with artificial arteries measures drugs’ influence on blood clotting*, Mar. 2014. [Online]. Available: https://medicalxpress.com/news/2014-03-microfluidic-device-artificial-arteries-drugs.html.

[27] S. Wang *et al.*, “Pipe phantoms with applications in molecular imaging and system characterization,” *IEEE Trans Ultrason Ferroelectr Freq Control*, vol. 64, no. 1, pp. 39–52, 2017, ISSN: 1525-8955 (Electronic). DOI: 10.1109/TUFFC.2016.2626465. [Online]. Available: https://www.ncbi.nlm.nih.gov/pubmed/27845659.

[28] T. Mashiko *et al.*, “Development of three-dimensional hollow elastic model for cerebral aneurysm clipping simulation enabling rapid and low cost prototyping,” *World Neurosurg*, vol. 83, no. 3, pp. 351–61, 2015, ISSN: 1878-8769 (Electronic). DOI: 10.1016/j.wneu.2013.10.032. [Online]. Available: https://www.ncbi.nlm.nih.gov/pubmed/24141000.

[29] D. P. G. Nilsson *et al.*, “Patient-specific brain arteries molded as a flexible phantom model using 3d printed water-soluble resin,” *Sci Rep*, vol. 12, no. 1, p. 10 172, 2022, ISSN: 2045-2322 (Electronic) 2045-2322 (Linking). DOI: 10.1038/s41598-022-14279-7. [Online]. Available: https://www.ncbi.nlm.nih.gov/pubmed/35715506.

[30] S. Soloukey *et al.*, “Patient-specific vascular flow phantom for mri- and doppler ultrasound imaging,” *Ultrasound Med Biol*, 2024, ISSN: 1879-291X (Electronic). DOI: 10.1016/j.ultrasmedbio.2024.02.010. [Online]. Available: https://www.ncbi.nlm.nih.gov/pubmed/38471997.

[31] S. Esmaeili *et al.*, “An artificial blood vessel fabricated by 3d printing for pharmaceutical application,” *Nanomedicine Journal*, vol. 6, no. 3, pp. 183–194, 2019, ISSN: 2322-3049. DOI: 10.22038/nmj.2019.06.00005. [Online]. Available: https://nmj.mums.ac.ir/article_13183.html.

[32] P. A. Dayton *et al.*, “A preliminary evaluation of the effects of primary and secondary radiation forces on acoustic contrast agents,” *IEEE Transactions on Ultrasonics, Ferroelectrics and Frequency Control*, vol. 44, no. 6, pp. 1264–1277, 1997, ISSN: 0885-3010. DOI: 10.1109/58.656630.

[33] B. K. Bharadvaj *et al.*, “Steady flow in a model of the human carotid bifurcation. part i–flow visualization,” *J Biomech*, vol. 15, no. 5, pp. 349–62, 1982, ISSN: 0021-9290 (Linking). DOI: 10.1016/0021-9290(82)90057-4. [Online]. Available: https://www.ncbi.nlm.nih.gov/pubmed/7118950.

[34] D. R. Myers *et al.*, “Vascularized microfluidics and their untapped potential for discovery in diseases of the microvasculature,” *Annu Rev Biomed Eng*, vol. 23, pp. 407–432, 2021, ISSN: 1545-4274 (Electronic). DOI: 10.1146/annurev-bioeng-091520-025358. [Online]. Available: https://www.ncbi.nlm.nih.gov/pubmed/33863238.

[35] S. M. Scott *et al.*, “Fabrication methods for microfluidic devices: An overview,” *Micromachines (Basel)*, vol. 12, no. 3, 2021, ISSN: 2072-666X (Print) 2072-666X (Electronic) 2072-666X (Linking). DOI: 10.3390/mi12030319. [Online]. Available: https://www.ncbi.nlm.nih.gov/pubmed/33803689%20https://mdpi-res.com/d_attachment/micromachines/micromachines-12-00319/article_deploy/micromachines-12-00319.pdf?version=1616094428.

[36] Y. Xia *et al.*, “Soft lithography,” *Angew Chem Int Ed Engl*, vol. 37, no. 5, pp. 550–575, 1998, ISSN: 1521-3773 (Electronic) 1433-7851 (Linking). DOI: 10.1002/(SICI)1521-3773(19980316)37:5<550::AID-ANIE550>3.0.CO;2-G. [Online]. Available: https://www.ncbi.nlm.nih.gov/pubmed/29711088.

[37] D. B. Weibel *et al.*, “Microfabrication meets microbiology,” *Nat Rev Microbiol*, vol. 5, no. 3, pp. 209–18, 2007, ISSN: 1740-1534 (Electronic) 1740-1526 (Linking). DOI: 10.1038/nrmicro1616. [Online]. Available: https://www.ncbi.nlm.nih.gov/pubmed/17304250.

[38] A. Aazmi *et al.*, “Engineered vasculature for organ-on-a-chip systems,” *Engineering*, vol. 9, pp. 131–147, 2022, ISSN: 2095-8099. DOI: 10.1016/j.eng.2021.06.020. [Online]. Available: https://www.sciencedirect.com/science/article/pii/S2095809921003337.

[39] E. Gal-Or *et al.*, “Chemical analysis using 3d printed glass microfluidics,” *Analytical Methods*, vol. 11, no. 13, pp. 1802–1810, 2019, ISSN: 1759-9660 1759-9679. DOI: 10.1039/c8ay01934g. [Online]. Available: http://dx.doi.org/10.1039/C8AY01934G.

[40] W. J. Polacheck *et al.*, “Microfabricated blood vessels for modeling the vascular transport barrier,” *Nat Protoc*, vol. 14, no. 5, pp. 1425–1454, 2019, ISSN: 1750-2799 (Electronic) 1754-2189 (Print) 1750-2799 (Linking). DOI: 10.1038/s41596-019-0144-8. [Online]. Available: https://www.ncbi.nlm.nih.gov/pubmed/30953042.

[41] M. E. Miali *et al.*, “Leaf-inspired authentically complex microvascular networks for deciphering biological transport process,” *ACS Appl Mater Interfaces*, vol. 11, no. 35, pp. 31 627–31 637, 2019, ISSN: 1944-8252 (Electronic) 1944-8244 (Linking). DOI: 10.1021/acsami.9b09453. [Online]. Available: https://www.ncbi.nlm.nih.gov/pubmed/31412200.

[42] H. L. Ma *et al.*, “Rapid fabrication of microfluidic devices for biological mimicking: A survey of materials and biocompatibility,” vol. 12, no. 3, 2021. DOI: 10.3390/mi12030346.

[43] J. Bae *et al.*, “Fabricating and laminating films with through-holes and engraved / protruding structures for 3d micro / nanofluidic platforms,” *Small Methods*, vol. 7, no. 9, e2300211, 2023, ISSN: 2366-9608 (Electronic) 2366-9608 (Linking). DOI: 10.1002/smtd.202300211. [Online]. Available: https://www.ncbi.nlm.nih.gov/pubmed/37246254.

[44] P. M. Cogswell *et al.*, “Intracranial vasculature 3d printing: Review of techniques and manufacturing processes to inform clinical practice,” *3D Print Med*, vol. 6, no. 1, p. 18, 2020, ISSN: 2365-6271 (Electronic). DOI: 10.1186/s41205-020-00071-8. [Online]. Available: https://www.ncbi.nlm.nih.gov/pubmed/32761490.

[45] C. G. Khan Malek, “Laser processing for bio-microfluidics applications (part i),” *Anal Bioanal Chem*, vol. 385, no. 8, pp. 1351–61, 2006, ISSN: 1618-2642 (Print) 1618-2642 (Linking). DOI: 10.1007/s00216-006-0514-2. [Online]. Available: https://www.ncbi.nlm.nih.gov/pubmed/16773304.

[46] C. G. Khan Malek, “Laser processing for bio-microfluidics applications (part ii),” *Anal Bioanal Chem*, vol. 385, no. 8, pp. 1362–9, 2006, ISSN: 1618-2642 (Print) 1618-2642 (Linking). DOI: 10.1007/s00216-006-0517-z. [Online]. Available: https://www.ncbi.nlm.nih.gov/pubmed/16773302.

[47] R. Su *et al.*, “3d printed microfluidics: Advances in strategies, integration, and applications,” *Lab Chip*, vol. 23, no. 5, pp. 1279–1299, 2023, ISSN: 1473-0189 (Electronic) 1473-0189 (Linking). DOI: 10.1039/d2lc01177h. [Online]. Available: https://www.ncbi.nlm.nih.gov/pubmed/36779387.

[48] I. Gibson *et al.*, *Additive Manufacturing Technologies: 3D Printing, Rapid Prototyping, and Direct Digital Manufacturing*. Springer New York, 2014, ISBN: 9781493921133. [Online]. Available: https://books.google.nl/books?id=OPGbBQAAQBAJ.

[49] J. M. Lee *et al.*, “3d bioprinting processes: A perspective on classification and terminology,” *Int J Bioprint*, vol. 4, no. 2, p. 151, 2018, ISSN: 2424-8002 (Electronic). DOI: 10.18063/IJB.v4i2.151. [Online]. Available: https://www.ncbi.nlm.nih.gov/pubmed/33102923.

[50] J. Collingwood *et al.*, “High-speed 3d printing for microfluidics: Opportunities and challenges,” *Materials Today: Proceedings*, 2023, ISSN: 22147853. DOI: 10.1016/j.matpr.2023.05.683. [Online]. Available: https://www.sciencedirect.com/science/article/pii/S2214785323033254.

[51] A. K. Au *et al.*, “3d-printed microfluidics,” *Angew Chem Int Ed Engl*, vol. 55, no. 12, pp. 3862–81, 2016, ISSN: 1521-3773 (Electronic) 1433-7851 (Print) 1433-7851 (Linking). DOI: 10.1002/anie.201504382. [Online]. Available: https://www.ncbi.nlm.nih.gov/pubmed/26854878.

[52] P. Prabhakar *et al.*, “3d-printed microfluidics and potential biomedical applications,” *Frontiers in Nanotechnology*, vol. 3, 2021, ISSN: 2673-3013. DOI: 10.3389/fnano.2021.609355. [Online]. Available: https://www.frontiersin.org/articles/10.3389/fnano.2021.609355/full.

[53] O.-o. O. Akeredolu, “Circular channel fabrication in microfluidic devices,” *Elveflow*, Sep. 2020. [Online]. Available: https://www.elveflow.com/microfluidic-reviews/soft-lithography-microfabrication/circular-channel-fabrication-in-microfluidic-devices/.

[54] J. M. Otton *et al.*, “3d printing from cardiovascular ct: A practical guide and review,” *Cardiovasc Diagn Ther*, vol. 7, no. 5, pp. 507–526, 2017, ISSN: 2223-3660 (Electronic). DOI: 10.21037/cdt.2017.01.12. [Online]. Available: https://www.ncbi.nlm.nih.gov/pubmed/29255693.

[55] D. R. Serrano *et al.*, “3d printing technologies in personalized medicine, nanomedicines, and biopharmaceuticals,” *Pharmaceutics*, vol. 15, no. 2, 2023, ISSN: 1999-4923 (Electronic). DOI: 10.3390/pharmaceutics15020313. [Online]. Available: https://www.ncbi.nlm.nih.gov/pubmed/36839636.

[56] 2014. [Online]. Available: https://umcgresearch.org/w/3d-lab.

[57] E. MC, *Emi – experimental medical instrumentation - core facility - erasmus mc*, 2021. [Online]. Available: https://www.erasmusmc.nl/en/research/core-facilities/emi#41d1d850-8829-435c-95df-bba936de8d9b.

[58] V. Kizilgoz *et al.*, “Evaluation of circle of willis variants using magnetic resonance angiography,” *Sci Rep*, vol. 12, no. 1, p. 17 611, 2022, ISSN: 2045-2322 (Electronic). DOI: 10.1038/s41598-022-21833-w. [Online]. Available: https://www.ncbi.nlm.nih.gov/pubmed/36266391.

[59] H. van den Brink *et al.*, “Advanced mri in cerebral small vessel disease,” *Int J Stroke*, vol. 18, no. 1, pp. 28–35, 2023, ISSN: 1747-4949 (Electronic). DOI: 10.1177/17474930221091879. [Online]. Available: https://www.ncbi.nlm.nih.gov/pubmed/35311609.

[60] L. Wei *et al.*, “Automatic 3d segmentation and quantification of lenticulostriate arteries from high-resolution 7 tesla mra images,” *IEEE Trans Image Process*, vol. 25, no. 1, pp. 400–13, 2016, ISSN: 1941-0042 (Electronic). DOI: 10.1109/TIP.2015.2499085. [Online]. Available: https://www.ncbi.nlm.nih.gov/pubmed/26571526.

[61] S. Bollmann *et al.*, “Imaging of the pial arterial vasculature of the human brain in vivo using high-resolution 7t time-of-flight angiography,” *Elife*, vol. 11, e71186, 2022, ISSN: 2050-084X (Electronic). DOI: 10.7554/eLife.71186. [Online]. Available: https://www.ncbi.nlm.nih.gov/pubmed/35486089.

[62] Z. Li *et al.*, “Quantitative modeling of lenticulostriate arteries on 7-t tof-mra for cerebral small vessel disease,” *European Radiology Experimental*, vol. 8, no. 1, Nov. 2024. DOI: https://doi.org/10.1186/s41747-024-00512-7.

[63] [Online]. Available: https://formlabs.com/blog/form-3-form-2-3d-printer-comparison/.

[64] [Online]. Available: https://formlabs.com/blog/biomed-flex-80a-resin-biomed-elastic-50a-resin-flexible-biocompatible-3d-printing-materials/.

[65] A. S. Reddy *et al.*, “Construction of a comprehensive endovascular test bed for research and device development in mechanical thrombectomy in stroke,” *J Neurosurg*, vol. 134, no. 3, pp. 1190–1197, 2020, ISSN: 1933-0693 (Electronic) 0022-3085 (Linking). DOI: 10.3171/2020.1.JNS192732. [Online]. Available: https://www.ncbi.nlm.nih.gov/pubmed/32244204.

[66] M. Carlsohn *et al.*, *3D real-time visualization of blood flow in cerebral aneurysms by light field particle image velocimetry*. 2016, p. 989 703. DOI: 10.1117/12.2220417.

[67] J. R. Anderson *et al.*, “Three-dimensional printing of anatomically accurate, patient specific intracranial aneurysm models,” *J Neurointerv Surg*, vol. 8, no. 5, pp. 517–20, 2016, ISSN: 1759-8486 (Electronic). DOI: 10.1136/neurintsurg-2015-011686. [Online]. Available: https://www.ncbi.nlm.nih.gov/pubmed/25862767.

[68] H. Yu *et al.*, “An in-vitro flow study using an artificial circle of willis model for validation of an existing one-dimensional numerical model,” *Ann Biomed Eng*, vol. 47, no. 4, pp. 1023–1037, 2019, ISSN: 1573-9686 (Electronic) 0090-6964 (Print) 0090-6964 (Linking). DOI: 10.1007/s10439-019-02211-6. [Online]. Available: https://www.ncbi.nlm.nih.gov/pubmed/30673955.

[69] F. J. Joseph *et al.*, “Neurosurgical simulator for training aneurysm microsurgery-a user suitability study involving neurosurgeons and residents,” *Acta Neurochir (Wien)*, vol. 162, no. 10, pp. 2313–2321, 2020, ISSN: 0942-0940 (Electronic) 0001-6268 (Print) 0001-6268 (Linking). DOI: 10.1007/s00701-020-04522-3. [Online]. Available: https://www.ncbi.nlm.nih.gov/pubmed/32780255.

[70] G. Gonzalez *et al.*, “Current and emerging trends in polymeric 3d printed microfluidic devices,” *Additive Manufacturing*, vol. 55, p. 102 867, 2022, ISSN: 2214-8604. DOI: ARTN10286710.1016/j.addma.2022.102867. [Online]. Available: https://www.sciencedirect.com/science/article/pii/S2214860422002664.

[71] M. J. Beauchamp *et al.*, “Moving from millifluidic to truly microfluidic sub-100-mum cross-section 3d printed devices,” *Anal Bioanal Chem*, vol. 409, no. 18, pp. 4311–4319, 2017, ISSN: 1618-2650 (Electronic). DOI: 10.1007/s00216-017-0398-3. [Online]. Available: https://www.ncbi.nlm.nih.gov/pubmed/28612085.

[72] A. D. Castiaux *et al.*, “Polyjet 3d-printed enclosed microfluidic channels without photocurable supports,” *Anal Chem*, vol. 91, no. 10, pp. 6910–6917, 2019, ISSN: 1520-6882 (Electronic). DOI: 10.1021/acs.analchem.9b01302. [Online]. Available: https://www.ncbi.nlm.nih.gov/pubmed/31035747.

[73] M. D. Nelson *et al.*, “Flexible, transparent, sub-100 µm microfluidic channels with fused deposition modeling 3d-printed thermoplastic polyurethane,” *Journal of Micromechanics and Microengineering*, vol. 29, no. 9, p. 095 010, 2019, ISSN: 0960-1317. DOI: 10.1088/1361-6439/ab2f26. [Online]. Available: https://dx.doi.org/10.1088/1361-6439/ab2f26.

[74] S. C. Ligon *et al.*, “Polymers for 3d printing and customized additive manufacturing,” *Chem Rev*, vol. 117, no. 15, pp. 10 212–10 290, 2017, ISSN: 1520-6890 (Electronic). DOI: 10.1021/acs.chemrev.7b00074. [Online]. Available: https://www.ncbi.nlm.nih.gov/pubmed/28756658.

[75] V. Mehta *et al.*, “3d printed microfluidic devices: A review focused on four fundamental manufacturing approaches and implications on the field of healthcare,” ISSN: 2.

[76] N. Bhattacharjee *et al.*, “The upcoming 3d-printing revolution in microfluidics,” *Lab Chip*, vol. 16, no. 10, pp. 1720–42, 2016, ISSN: 1473-0189 (Electronic). DOI: 10.1039/c6lc00163g. [Online]. Available: https://www.ncbi.nlm.nih.gov/pubmed/27101171.

[77] M. Salmi, “Additive manufacturing processes in medical applications,” *Materials (Basel)*, vol. 14, no. 1, p. 191, 2021, ISSN: 1996-1944 (Electronic). DOI: 10.3390/ma14010191. [Online]. Available: https://www.ncbi.nlm.nih.gov/pubmed/33401601.

[78] L. Chen *et al.*, “Millifluidics, microfluidics, and nanofluidics: Manipulating fluids at varying length scales,” *Materials Today Nano*, vol. 16, p. 100 136, 2021, ISSN: 25888420. DOI: 10.1016/j.mtnano.2021.100136. [Online]. Available: https://www.sciencedirect.com/science/article/pii/S2588842021000286.

[79] L.-Y. Zhou *et al.*, “A review of 3d printing technologies for soft polymer materials,” *Advanced Functional Materials*, vol. 30, no. 28, p. 2 000 187, 2020, ISSN: 1616-301X 1616-3028. DOI: 10.1002/adfm.202000187. [Online]. Available: https://doi.org/10.1002/adfm.202000187.

[80] S. Y. Hann *et al.*, “Recent advances in 3d printing: Vascular network for tissue and organ regeneration,” *Transl Res*, vol. 211, pp. 46–63, 2019, ISSN: 1878-1810 (Electronic). DOI: 10.1016/j.trsl.2019.04.002. [Online]. Available: https://www.ncbi.nlm.nih.gov/pubmed/31004563.

[81] R. F. Quero *et al.*, “Using multi-material fused deposition modeling (fdm) for one-step 3d printing of microfluidic capillary electrophoresis with integrated electrodes for capacitively coupled contactless conductivity detection,” *Sensors and Actuators B: Chemical*, vol. 365, p. 131 959, 2022, ISSN: 09254005. DOI: 10.1016/j.snb.2022.131959. [Online]. Available: https://www.sciencedirect.com/science/article/pii/S0925400522006013.

[82] K. Griffin *et al.*, “3d printed microfluidics for bioanalysis: A review of recent advancements and applications,” *TrAC Trends in Analytical Chemistry*, vol. 158, p. 116 892, 2023, ISSN: 01659936. DOI: 10.1016/j.trac.2022.116892. [Online]. Available: https://www.sciencedirect.com/science/article/pii/S0165993622003752.

[83] N. P. Macdonald *et al.*, “Comparing microfluidic performance of three-dimensional (3d) printing platforms,” *Anal Chem*, vol. 89, no. 7, pp. 3858–3866, 2017, ISSN: 1520-6882 (Electronic) 0003-2700 (Linking). DOI: 10.1021/acs.analchem.7b00136. [Online]. Available: https://www.ncbi.nlm.nih.gov/pubmed/28281349.

[84] J. M. Lee *et al.*, “Characterization and evaluation of 3d printed microfluidic chip for cell processing,” *Microfluidics and Nanofluidics*, vol. 20, no. 1, p. 5, 2016, ISSN: 1613-4982. DOI: 10.1007/s10404-015-1688-8. [Online]. Available: https://doi.org/10.1007/s10404-015-1688-8.

[85] K. M. Leong *et al.*, “Democratizing access to microfluidics: Rapid prototyping of open microchannels with low-cost lcd 3d printers,” Sep. 2023. DOI: https://doi.org/10.1101/2023.09.26.558021.

[86] H. Gong *et al.*, “Optical approach to resin formulation for 3d printed microfluidics,” *RSC Adv*, vol. 5, no. 129, pp. 106 621–106 632, 2015, ISSN: 2046-2069 (Electronic). DOI: 10.1039/C5RA23855B. [Online]. Available: https://www.ncbi.nlm.nih.gov/pubmed/26744624.

[87] A. Al Rashid *et al.*, “Vat photopolymerization of polymers and polymer composites: Processes and applications,” *Additive Manufacturing*, vol. 47, p. 102 279, 2021, ISSN: 22148604. DOI: 10.1016/j.addma.2021.102279. [Online]. Available: https://www.sciencedirect.com/science/article/pii/S2214860421004395.

[88] M. Pagac *et al.*, *A review of vat photopolymerization technology: Materials, applications, challenges, and future trends of 3d printing*, Electronic Article, 2021. DOI: 10.3390/polym13040598.

[89] G. Vladić *et al.*, “Vat photopolymerization,” in *Polymers for 3D Printing*, J. Izdebska-Podsiadły, Ed. William Andrew Publishing, 2022, pp. 65–74, ISBN: 9780128183113. DOI: 10.1016/b978-0-12-818311-3.00018-5. [Online]. Available: https://www.sciencedirect.com/science/article/pii/B9780128183113000185.

[90] W. Zrafi *et al.*, “Topographic variability of the normal circle of willis anatomy on a paediatric population,” *Brain Communications*, vol. 3, no. 2, Apr. 2021. DOI: https://doi.org/10.1093/braincomms/fcab055. [Online]. Available: https://pmc.ncbi.nlm.nih.gov/articles/PMC8204365/#sup1.

[91] A. Amini *et al.*, “Recent developments in digital light processing 3d-printing techniques for microfluidic analytical devices,” *Journal of Chromatography A*, vol. 1692, p. 463 842, Mar. 2023. DOI: https://doi.org/10.1016/j.chroma.2023.463842. [Online]. Available: https://www.sciencedirect.com/science/article/pii/S0021967323000705.

[92] L. Schittecatte *et al.*, “From resin formulation and process parameters to the final mechanical properties of 3d printed acrylate materials,” *MRS Communications*, vol. 13, no. 3, pp. 357–377, Apr. 2023. DOI: https://doi.org/10.1557/s43579-023-00352-3.

[93] P. Jacobs *et al.*, *Rapid Prototyping & Manufacturing: Fundamentals of Stereolithography*. Society of Manufacturing Engineers, 1992, ISBN: 9780872634251. [Online]. Available: https://books.google.nl/books?id=HvcN0w1VyxwC.

[94] B. Heidt *et al.*, “The liberalization of microfluidics: Form 2 benchtop 3d printing as an affordable alternative to established manufacturing methods,” *physica status solidi (a)*, vol. 217, no. 13, Mar. 2020. DOI: https://doi.org/10.1002/pssa.201900935.

[95] I. Cotabarren *et al.*, “An assessment of the dimensional accuracy and geometry-resolution limit of desktop stereolithography using response surface methodology,” *Rapid Prototyping Journal*, vol. 25, no. 7, pp. 1169–1186, 2019, ISSN: 1355-2546. DOI: 10.1108/Rpj-03-2019-0060. [Online]. Available: https://www.emerald.com/insight/content/doi/10.1108/rpj-03-2019-0060/full/html.

[96] D. D. Rubayo *et al.*, “Influences of build angle on the accuracy, printing time, and material consumption of additively manufactured surgical templates,” *The Journal of Prosthetic Dentistry*, vol. 126, no. 5, pp. 658–663, Nov. 2021. DOI: 10.1016/j.prosdent.2020.09.012.

[97] C. Espinar *et al.*, “The influence of printing angle on color and translucency of 3d printed resins for dental restorations,” *Dental Materials*, vol. 39, no. 4, pp. 410–417, Apr. 2023. DOI: 10.1016/j.dental.2023.03.011.

[98] I. Ahmed *et al.*, “Multi-resin masked stereolithography (msla) 3d printing for rapid and inexpensive prototyping of microfluidic chips with integrated functional components,” *Biosensors (Basel)*, vol. 12, no. 8, p. 652, 2022, ISSN: 2079-6374 (Electronic). DOI: 10.3390/bios12080652. [Online]. Available: https://www.ncbi.nlm.nih.gov/pubmed/36005047.

[99] Y. Xu *et al.*, “In-situ transfer vat photopolymerization for transparent microfluidic device fabrication,” *Nature Communications*, vol. 13, no. 1, p. 918, Feb. 2022. DOI: https://doi.org/10.1038/s41467-022-28579-z. [Online]. Available: https://www.nature.com/articles/s41467-022-28579-z.

[100] B. A. Ariana *et al.*, “Controlled compliancy of 3d printed vascular patient specific phantoms,” in *Proc.SPIE*, vol. 10954, p. 109540C. DOI: 10.1117/12.2512528. [Online]. Available: https://doi.org/10.1117/12.2512528.

[101] C. Guttridge *et al.*, “Biocompatible 3d printing resins for medical applications: A review of marketed intended use, biocompatibility certification, and post-processing guidance,” *Annals of 3D Printed Medicine*, vol. 5, p. 100 044, 2022, ISSN: 26669641. DOI: 10.1016/j.stlm.2021.100044. [Online]. Available: https://www.sciencedirect.com/science/article/pii/S2666964121000394.

[102] S. Kress *et al.*, “3d printing of cell culture devices: Assessment and prevention of the cytotoxicity of photopolymers for stereolithography,” *Materials (Basel)*, vol. 13, no. 13, 2020, ISSN: 1996-1944 (Electronic). DOI: 10.3390/ma13133011. [Online]. Available: https://www.ncbi.nlm.nih.gov/pubmed/32640644.

[103] C. Cavaniol *et al.*, “Flowmetering for microfluidics,” *Lab Chip*, vol. 22, no. 19, pp. 3603–3617, 2022, ISSN: 1473-0189 (Electronic). DOI: 10.1039/d2lc00188h. [Online]. Available: https://www.ncbi.nlm.nih.gov/pubmed/35770690.

[104] C. Roloff *et al.*, “Comparison of intracranial aneurysm flow quantification techniques: Standard piv vs stereoscopic piv vs tomographic piv vs phase-contrast mri vs cfd,” *J Neurointerv Surg*, vol. 11, no. 3, pp. 275–282, 2019, ISSN: 1759-8486 (Electronic). DOI: 10.1136/neurintsurg-2018-013921. [Online]. Available: https://www.ncbi.nlm.nih.gov/pubmed/30061369.

[105] J. Stahl *et al.*, “Fabrication of flexible intracranial aneurysm models using stereolithography 3d printing,” *Current Directions in Biomedical Engineering*, vol. 9, no. 1, pp. 395–398, 2023, ISSN: 2364-5504. DOI: 10.1515/cdbme-2023-1099.

[106] Liqcreate, *Liqcreate Bio-Med Clear*. [Online]. Available: https://www.liqcreate.com/downloads/tds/TDS%20Liqcreate%20Bio-Med%20Clear%20%5BV3%2027-11-2023%5D.pdf.

[107] ELEGOO, *Elegoo mars 4 - 9k user-friendly desktop resin 3d printer*, 2025. [Online]. Available: https://eu.elegoo.com/en-fr/products/elegoo-mars-4-msla-resin-3d-printer-with-9k-mono-lcd.

[108] Liqcreate, *Biocompatible 3d-printing resin - liqcreate bio-med clear*, 2021. [Online]. Available: https://www.liqcreate.com/product/bio-med-clear-biocompatible-resin/.

[109] D. Systèmes, *Welcome to solidworks 2023 - 2023 - what’s new in solidworks*, 2023. [Online]. Available: https://help.solidworks.com/2023/english/WhatsNew/c_wn2023_welcome.htm.

[110] Lychee, *Lychee*, 2024. [Online]. Available: https://mango3d.io/changelogs/lychee-slicer-version-6-2-0.

[111] K. CORPORATION, *Digitale microscoop vhx-6000-reeks geavanceerde waarneming met uitstekende bruikbaarheid | keyence international belgium(nederlands)*, 2025. [Online]. Available: https://www.keyence.eu/nlnl/ss/products/microscope/vhx-6000/.

[112] J. Schindelin *et al.*, "Fiji: An open-source platform for biological-image analysis," *Nature Methods*, vol. 9, no. 7, pp. 676–82, 2012. DOI: https://doi.org/10.1038/nmeth.2019.

[113] Fluigent, *Smart microfluidics - fluigent*. [Online]. Available: https://www.fluigent.com/.

[114] Y. Takashimizu *et al.*, "New parameter of roundness r: Circularity corrected by aspect ratio," *Progress in Earth and Planetary Science*, vol. 3, no. 1, Jan. 2016. DOI: https://doi.org/10.1186/s40645-015-0078-x.

[115] S. B. Greenberg *et al.*, "Normal pulmonary artery and branch pulmonary artery sizes in children," *The International Journal of Cardiovascular Imaging*, vol. 34, no. 6, pp. 967–974, Jan. 2018. DOI: https://doi.org/10.1007/s10554-018-1303-7.

[116] G. Van Rossum *et al.*, *Python 3 Reference Manual*. Scotts Valley, CA: CreateSpace, 2009, ISBN: 1441412697.

[117] J. D. Hunter, "Matplotlib: A 2d graphics environment," *Computing in Science & Engineering*, vol. 9, no. 3, pp. 90–95, 2007. DOI: 10.1109/MCSE.2007.55.

[118] I. Christov, "Soft hydraulics: From newtonian to complex fluid flows through compliant conduits," *Journal of Physics: Condensed Matter*, vol. 34, no. 6, pp. 063 001–063 001, Nov. 2021. DOI: https://doi.org/10.1088/1361-648x/ac327d.

[119] COMSOL, *Comsol multiphysics® simulation software*, 2024. [Online]. Available: https://www.comsol.com/product-download/6.2.

[120] H. Gong *et al.*, "Custom 3d printer and resin for 18 μm × 20 μm microfluidic flow channels," *Lab on a Chip*, vol. 17, no. 17, pp. 2899–2909, 2017. DOI: https://doi.org/10.1039/c7lc00644f. [Online]. Available: https://pubs.rsc.org/en/content/articlelanding/2017/lc/c7lc00644f/unauth#!divAbstract.

[121] P. D. Morris *et al.*, "A novel method for measuring absolute coronary blood flow and microvascular resistance in patients with ischaemic heart disease," *Cardiovascular research*, vol. 117, no. 6, pp. 1567–1577, Jul. 2020. DOI: https://doi.org/10.1093/cvr/cvaa220.

[122] K. Kahveci *et al.*, "A numerical model of pulsatile blood flow in compliant arteries of a truncated vascular system," *International Communications in Heat and Mass Transfer*, vol. 67, pp. 51–58, Oct. 2015. DOI: https://doi.org/10.1016/j.icheatmasstransfer.2015.06.010.

[123] Y. Zhang *et al.*, "Open-source interactive design platform for 3d-printed microfluidic devices," *Communications Engineering*, vol. 3, no. 1, May 2024. DOI: https://doi.org/10.1038/s44172-024-00217-0.

[124] H. Shafique *et al.*, "High-resolution low-cost lcd 3d printing for microfluidic and organ-on-a-chip devices," *Lab on a chip*, Jan. 2024. DOI: https://doi.org/10.1039/d3lc01125a.

[125] A. V. Nielsen *et al.*, "3d printed microfluidics," *Annual Review of Analytical Chemistry*, vol. 13, no. 1, pp. 45–65, Jun. 2020. DOI: https://doi.org/10.1146/annurev-anchem-091619-102649.

[126] Nov. 2024. [Online]. Available: https://cadworks3d.com/3dprinters/.

[127] D. Wu *et al.*, "Mechanics of shape distortion of dlp 3d printed structures during uv post-curing," *Soft Matter*, vol. 15, no. 30, pp. 6151–6159, Jan. 2019. DOI: https://doi.org/10.1039/c9sm00725c.

[128] X. Wang *et al.*, "High-precision digital light processing (dlp) printing of microstructures for microfluidics applications based on a machine learning approach," *Virtual and physical prototyping*, vol. 19, no. 1, Feb. 2024. DOI: https://doi.org/10.1080/17452759.2024.2318774.

[129] Z. Luo *et al.*, “Digital light processing 3d printing for microfluidic chips with enhanced resolution via dosing- and zoning-controlled vat photopolymerization,” *Microsystems Nanoengineering*, vol. 9, no. 1, pp. 1–13, Aug. 2023. DOI: https://doi.org/10.1038/s41378-023-00542-y. [Online]. Available: https://www.nature.com/articles/s41378-023-00542-y.

[130] B. Orzeł *et al.*, “Comparison of 3d printout quality from fdm and msla technology in unit production,” *Symmetry*, vol. 14, no. 5, p. 910, Apr. 2022. DOI: https://doi.org/10.3390/sym14050910.

[131] A. Grymak *et al.*, “Effect of various printing parameters on the accuracy (trueness and precision) of 3d-printed partial denture framework,” *Journal of the Mechanical Behavior of Biomedical Materials*, vol. 140, p. 105 688, Apr. 2023. DOI: https://doi.org/10.1016/j.jmbbm.2023.105688.

[132] Z. Yu *et al.*, “High-accuracy dlp 3d printing of closed microfluidic channels based on a mask option strategy,” *The International Journal of Advanced Manufacturing Technology*, vol. 127, no. 7-8, pp. 4001–4012, Jun. 2023. DOI: https://doi.org/10.1007/s00170-023-11769-4.

[133] B. Dhanunjayarao *et al.*, “Assessment of dimensional accuracy of 3d printed part using resin 3d printing technique,” *Materials Today: Proceedings*, Mar. 2022. DOI: https://doi.org/10.1016/j.matpr.2022.03.148.

[134] N. D. Borra *et al.*, “Parametric optimization for dimensional correctness of 3d printed part using masked stereolithography: Taguchi method,” *Rapid Prototyping Journal*, Jul. 2022. DOI: https://doi.org/10.1108/rpj-03-2022-0080.

[135] M. Štaffová *et al.*, “3d printing and post-curing optimization of photopolymerized structures: Basic concepts and effective tools for improved thermomechanical properties,” *Polymer Testing*, vol. 108, p. 107 499, Apr. 2022. DOI: https://doi.org/10.1016/j.polymertesting.2022.107499.

[136] R. Gao *et al.*, “Artificial blood vessel frameworks from 3d printing-based super-assembly as in vitro models for early diagnosis of intracranial aneurysms,” *Chemistry of Materials*, vol. 32, no. 7, pp. 3188–3198, 2020, doi: 10.1021/acs.chemmater.0c00208, ISSN: 0897-4756 1520-5002. DOI: 10.1021/acs.chemmater.0c00208. [Online]. Available: https://doi.org/10.1021/acs.chemmater.0c00208.

[137] N. Kaneko *et al.*, “In vitro modeling of human brain arteriovenous malformation for endovascular simulation and flow analysis,” *World Neurosurg*, vol. 141, e873–e879, 2020, ISSN: 1878-8769 (Electronic). DOI: 10.1016/j.wneu.2020.06.084. [Online]. Available: https://www.ncbi.nlm.nih.gov/pubmed/32565379.

[138] E. Paccione *et al.*, “Challenges in hemodynamics assessment in complex neurovascular geometries using computational fluid dynamics and benchtop flow simulation in 3d printed patient specific phantoms,” *Proc SPIE Int Soc Opt Eng*, vol. 11600, 2021, ISSN: 0277-786X (Print) 1996-756X (Electronic) 0277-786X (Linking). DOI: 10.1117/12.2582169. [Online]. Available: https://www.ncbi.nlm.nih.gov/pubmed/33814673.

[139] T. A. Kaufmann *et al.*, “Flow distribution during cardiopulmonary bypass in dependency on the outflow cannula positioning,” *Artif Organs*, vol. 33, no. 11, pp. 988–92, 2009, ISSN: 1525-1594 (Electronic) 0160-564X (Linking). DOI: 10.1111/j.1525-1594.2009.00938.x. [Online]. Available: https://www.ncbi.nlm.nih.gov/pubmed/20021472.

[140] M. J. Page *et al.*, “Prisma 2020 explanation and elaboration: Updated guidance and exemplars for reporting systematic reviews,” *Bmj*, vol. 372, n160, 2021, ISSN: 1756-1833. DOI: 10.1136/bmj.n160. [Online]. Available: http://www.bmj.com/content/372/bmj.n160.abstract.

[141] M. S. Pravdivtseva *et al.*, “3d-printed, patient-specific intracranial aneurysm models: From clinical data to flow experiments with endovascular devices,” *Med Phys*, vol. 48, no. 4, pp. 1469–1484, 2021, ISSN: 2473-4209 (Electronic) 0094-2405 (Linking). DOI: 10.1002/mp.14714. [Online]. Available: https://www.ncbi.nlm.nih.gov/pubmed/33428778.

[142] X. Tian *et al.*, “A transparent vessel-on-a-chip device for hemodynamic analysis and early diagnosis of intracranial aneurysms by cfd and pc-mri,” *ACS Sens*, vol. 5, no. 12, pp. 4064–4071, 2020, ISSN: 2379-3694 (Electronic) 2379-3694 (Linking). DOI: 10.1021/acssensors.0c02164. [Online]. Available: https://www.ncbi.nlm.nih.gov/pubmed/33289559.

[143] B. J. Kim *et al.*, “Post-stenotic recirculating flow may cause hemodynamic perforator infarction,” *J Stroke*, vol. 18, no. 1, pp. 66–72, 2016, ISSN: 2287-6391 (Print) 2287-6405 (Electronic) 2287-6391 (Linking). DOI: 10.5853/jos.2015.01445. [Online]. Available: https://www.ncbi.nlm.nih.gov/pubmed/26687122.

[144] K. L. Falk *et al.*, “Optimizing the quality of 4d-dsa temporal information,” *AJNR Am J Neuroradiol*, vol. 40, no. 12, pp. 2124–2129, 2019, ISSN: 1936-959X (Electronic) 0195-6108 (Print) 0195-6108 (Linking). DOI: 10.3174/ajnr.A6290. [Online]. Available: https://www.ncbi.nlm.nih.gov/pubmed/31672837.

[145] G. Shaughnessy *et al.*, “Measuring blood velocity using 4d-dsa: A feasibility study,” *Med Phys*, vol. 45, no. 10, pp. 4510–4518, 2018, ISSN: 2473-4209 (Electronic). DOI: 10.1002/mp.13120. [Online]. Available: https://www.ncbi.nlm.nih.gov/pubmed/30102773.

[146] K. N. Sommer *et al.*, “Use of patient specific 3d printed neurovascular phantoms to simulate mechanical thrombectomy,” *3D Print Med*, vol. 7, no. 1, p. 32, 2021, ISSN: 2365-6271 (Electronic) 2365-6271 (Linking). DOI: 10.1186/s41205-021-00122-8. [Online]. Available: https://www.ncbi.nlm.nih.gov/pubmed/34568987.

[147] M. R. Levitt *et al.*, “Genetic correlates of wall shear stress in a patient-specific 3d-printed cerebral aneurysm model,” *J Neurointerv Surg*, vol. 11, no. 10, pp. 999–1003, 2019, ISSN: 1759-8486 (Electronic) 1759-8478 (Print) 1759-8478 (Linking). DOI: 10.1136/neurintsurg-2018-014669. [Online]. Available: https://www.ncbi.nlm.nih.gov/pubmed/30979845.

[148] V. K. Chivukula *et al.*, “Reconstructing patient-specific cerebral aneurysm vasculature for in vitro investigations and treatment efficacy assessments,” *J Clin Neurosci*, vol. 61, pp. 153–159, 2019, ISSN: 1532-2653 (Electronic) 0967-5868 (Print) 0967-5868 (Linking). DOI: 10.1016/j.jocn.2018.10.103. [Online]. Available: https://www.ncbi.nlm.nih.gov/pubmed/30470652.

[149] H. Li *et al.*, “An experimental study and finite element modeling of head and neck cooling for brain hypothermia,” *J Therm Biol*, vol. 71, pp. 99–111, 2018, ISSN: 0306-4565 (Print) 0306-4565 (Linking). DOI: 10.1016/j.jtherbio.2017.10.022. [Online]. Available: https://www.ncbi.nlm.nih.gov/pubmed/29301706.

[150] C. K. Ho *et al.*, “Wall-less flow phantoms with tortuous vascular geometries: Design principles and a patient-specific model fabrication example,” *IEEE Trans Ultrason Ferroelectr Freq Control*, vol. 64, no. 1, pp. 25–38, 2017, ISSN: 1525-8955 (Electronic) 0885-3010 (Linking). DOI: 10.1109/TUFFC.2016.2636129. [Online]. Available: https://www.ncbi.nlm.nih.gov/pubmed/27959808.

[151] J. Seong *et al.*, “Hemodynamic effects of long-term morphological changes in the human carotid sinus,” *J Biomech*, vol. 48, no. 6, pp. 956–62, 2015, ISSN: 1873-2380 (Electronic) 0021-9290 (Print) 0021-9290 (Linking). DOI: 10.1016/j.jbiomech.2015.02.009. [Online]. Available: https://www.ncbi.nlm.nih.gov/pubmed/25702250.

[152] J. Sherman *et al.*, “Investigation of new flow modifying endovascular image-guided interventional (eigi) techniques in patient-specific aneurysm phantoms (psaps) using optical imaging,” *Proc SPIE Int Soc Opt Eng*, vol. 6918, p. 69181v, 2008, ISSN: 0277-786X (Print) 1996-756X (Electronic) 0277-786X (Linking). DOI: 10.1117/12.772583. [Online]. Available: https://www.ncbi.nlm.nih.gov/pubmed/18946513.

[153] A. Souza *et al.*, “Flow visualizations in a pdms cerebral aneurysm biomodel,” in *Innovations in Mechanical Engineering II*, J. Machado *et al.*, Eds., Springer International Publishing, pp. 209–215, ISBN: 978-3-031-09382-1.

[154] H. Yi *et al.*, “Developing an in vitro validated 3d in silico internal carotid artery sidewall aneurysm model,” *Front Physiol*, vol. 13, p. 1 024 590, 2022, ISSN: 1664-042X (Electronic). DOI: 10.3389/fphys.2022.1024590. [Online]. Available: https://www.ncbi.nlm.nih.gov/pubmed/36605897.

[155] Y. Deene *et al.*, “A multi-modality medical imaging head and neck phantom: Part 1. design and fabrication,” *Phys Med*, vol. 96, pp. 166–178, 2022, ISSN: 1724-191X (Electronic). DOI: 10.1016/j.ejmp.2022.02.010. [Online]. Available: https://www.ncbi.nlm.nih.gov/pubmed/35190265.

[156] S. V. S. Nagesh *et al.*, “Use of 1000fps high speed x-ray angiography (hsangio) to quantify differences in flow diversion effects of three stents with different coverage densities in a cerebral aneurysm invitro model,” *Proc SPIE Int Soc Opt Eng*, vol. 12031, 2022, ISSN: 1996-756X (Electronic). DOI: 10.1117/12.2611754. [Online]. Available: https://www.ncbi.nlm.nih.gov/pubmed/35982767.

[157] M. Encarnacion Ramirez, “Cerebrovascular aneurysm clipping training models with pulsatile blood flow,” *Russian journal of neurosurgery*, vol. 23, no. 2, pp. 128–133, Jun. 2021. DOI: 10.17650/1683-3295-2021-23-2-128-133.

[158] K. N. Sommer *et al.*, “Evaluation of challenges and limitations of mechanical thrombectomy using 3d printed neurovascular phantoms,” *Proc SPIE Int Soc Opt Eng*, vol. 11601, 2021, ISSN: 1996-756X (Electronic). DOI: 10.1117/12.2580962. [Online]. Available: https://www.ncbi.nlm.nih.gov/pubmed/34334874.

[159] L. K. Jang *et al.*, “Three-dimensional bioprinting of aneurysm-bearing tissue structure for endovascular deployment of embolization coils,” *Biofabrication*, vol. 13, no. 1, p. 015 006, 2020, ISSN: 1758-5090 (Electronic). DOI: 10.1088/1758-5090/abbb9b. [Online]. Available: https://www.ncbi.nlm.nih.gov/pubmed/32977323.

[160] M. S. Lauren *et al.*, “Initial assessment of neuro pressure gradients in carotid stenosis using 3d printed patient-specific phantoms,” in *Proc.SPIE*, vol. 10953, p. 1 095 314. DOI: 10.1117/12.2510279. [Online]. Available: https://doi.org/10.1117/12.2510279.

[161] Y. Liu *et al.*, “Fabrication of cerebral aneurysm simulator with a desktop 3d printer,” *Sci Rep*, vol. 7, no. 1, p. 44 301, 2017, ISSN: 2045-2322 (Electronic). DOI: 10.1038/srep44301. [Online]. Available: https://www.ncbi.nlm.nih.gov/pubmed/28513626.

[162] W. D. Clark *et al.*, “Comparison between bench-top and computational modelling of cerebral thromboembolism in ventricular assist device circulation,” *Cardiovasc Eng Technol*, vol. 6, no. 3, pp. 242–55, 2015, ISSN: 1869-4098 (Electronic). DOI: 10.1007/s13239-015-0230-1. [Online]. Available: https://www.ncbi.nlm.nih.gov/pubmed/26577358.

[163] G. Y. Zhu *et al.*, “Experimental investigation of blood flow in the vertebral artery bifurcation,” in *6th World Congress of Biomechanics (WCB 2010). August 1-6, 2010 Singapore*, C. T. Lim *et al.*, Eds., Springer Berlin Heidelberg, pp. 1346–1349, ISBN: 978-3-642-14515-5.

[164] A. Kamoda *et al.*, “Biomedical engineering analysis of the rupture risk of cerebral aneurysms: Flow comparison of three small pre-ruptured versus six large unruptured cases,” in *13th International Conference on Biomedical Engineering*, C. T. Lim *et al.*, Eds., Springer Berlin Heidelberg, pp. 1600–1603, ISBN: 978-3-540-92841-6.

[165] MW Studio, *Envisiontec micro plus hires | gvuk design*, Aug. 2021. [Online]. Available: https://www.gvukdesign.co.uk/3d-printers/envisiontec-micro-plus-hires/.

[166] Ziff Davis company, *Original prusa sl1*, 2021. [Online]. Available: https://www.pcmag.com/reviews/original-prusa-sl1.

[167] FormLabs, *Form 4 vs. form 3/+*, 2025. [Online]. Available: https://formlabs.com/compare/form-4-vs-form-3/.

[168] 3D JAKE, *Photon m3 premium*, 2023. [Online]. Available: https://www.3djake.nl/anycubic-3d-printers-accessoires/photon-m3-premium.

[169] Liqcreate, *Biomed clear resin*, 2025. [Online]. Available: https://formlabs.com/store/materials/biomed-clear-resin/.

[170] Formlabs, *Dental lt clear v2 resin*, 2025. [Online]. Available: https://formlabs.com/eu/store/materials/dental-lt-clear-resin-v2/.

[171] L. Turnage, *Loctite med413 < loctite additive manufacturing*, Jul. 2024. [Online]. Available: https://www.loctiteam.com/med413-biocompatible/.

[172] 3D Systems, *Accura clearvue (sla)*, Jun. 2016. [Online]. Available: https://www.3dsystems.com/materials/accura-clearvue.

[173] 3Dresyns, *Biotough 3dresyns*, 2025. [Online]. Available: https://www.3dresyns.com/collections/biotough-3dresyns.

[174] 3Dresyns, *Microfluidic 3dresyn mf rlv1 clear rigid with low viscosity*. [Online]. Available: https://www.3dresyns.com/products/microfluidic-3dresyn-mf-rlv1-clear-rigid-with-low-viscosity-for-sla-dlp-lcd-printers.

[175] B9Creations, *Translucent red biocompatible 3d printing resin*, 2025. [Online]. Available: https://shop.b9c.com/biores-red.

[176] 3D Systems, *Nextdent ortho flex*. [Online]. Available: https://nextdent.com/products/nextdent-ortho-flex/.

[177] 3D Systems, *Nextdent ortho clear*, 2025. [Online]. Available: https://nextdent.com/products/ortho-clear/.

[178] Pro3dure, *Printodent® gr-18.2 ib | clear-transparent | 1 kg | d1001464*, 2024. [Online]. Available: https://www.pro3dure.com/en/printodent-gr-18.2-ib/D1001464.

[179] SprintRay, *Surgical guide 3 and idb 2 - now available in canada and europe*, Nov. 2023. [Online]. Available: https://sprintray.com/surgical-guide-3-and-idb-2-now-available-in-canada-and-europe/.

[180] Lumi industries, *Lumi industries*, Oct. 2022. [Online]. Available: https://www.lumindustries.com/3dresins/p3d-gr-10.

[181] L. Turnage, *Loctite 3d ind405 < loctite additive manufacturing*, Oct. 2023. [Online]. Available: https://www.loctiteam.com/ind405-high-elongation/.

[182] Harz Labs, *Catalog - harz labs*, 2020. [Online]. Available: https://harzlabs.com/products/materialy/dental-yellow-clear-pro.html.

[183] DSI, *Dsi 3d clear tray resin | dsi dental solutions*, 2023. [Online]. Available: https://www.dsisrael.com/post/dsi-3d-clear-tray-resin.

[184] Syntec shop, *Medicalprint® mould detax - syntecshop.com*, Aug. 2023. [Online]. Available: https://syntecshop.com/detax-medicalprint-clear-opaque-uv-378-388nm.

[185] 3DPrinters-Store, *Keystone resin - keyguide - clear - 5kg*, 2025. [Online]. Available: https://3dprinters-store.com/products/nexa3d-resin-keyguide-clear-5kg.

[186] 3DPrinters-Store, *Nexa3d resin - xmed412 - clear - 5kg*, 2025. [Online]. Available: https://3dprinters-store.com/products/nexa3d-xmed412-5kg.

[187] Syntec shop, *Freeprint® mould 3d (uv 405nm), multiple colours - syntecshop.com*, 2020. [Online]. Available: https://syntecshop.com/en/product/freeprint-mould-3d-uv-405nm-multiple-colours.

[188] Reizwerk Digitalagentur, *Dx ortho*, 2025. [Online]. Available: https://www.detax.com/dental/product/dx-ortho.

[189] Reizwerk Digitalagentur, *Dx splint 2.0*, 2025. [Online]. Available: https://www.detax.com/dental/product/dx-splint-20.

[190] 3D Systems, *Figure 4 med-amb 10 | 3d systems*, Aug. 2019. [Online]. Available: https://www.3dsystems.com/materials/figure-4-med-amb-10.

[191] formfutura, *Engineering lcd resin - flex 63a*, Mar. 2025. [Online]. Available: https://formfutura.com/product/engineering-lcd-series-flex-63a-resin/.

[192] 3D Systems, *Accura phoenix (sla) | 3d systems*, Jan. 2017. [Online]. Available: https://www.3dsystems.com/materials/accura-phoenix-sla.

[193] ApplyLabWork, *Design concept series: Msla modeling clear, for led/lcd printers*, 2025. [Online]. Available: https://applylabwork.com/design-concept-series-msla-modeling-clear-for-led-lcd-printers/.

[194] Liqcreate, *Liqcreate clear impact | clear transparent engineering resin*, May 2019. [Online]. Available: https://www.liqcreate.com/product/clear-impact/.

[195] 123-3d, *123-3d.nl - 3d-printers | kits | parts | filament*, 2025. [Online]. Available: https://www.123-3d.nl/eSun-eResin-PLA-resin-Transparant-1-kg-ERESIN-PLA-T-i7146-t43139.html?gad_source=1&gclid=Cj0KCQjw16O_BhDNARIsAC3i2GAcZ-Ufr3oTtLwRNCjxrE9VSfs9TpbHy_GYiYFF1O81yn3TiaHqdN4aArfZEALw_wcB.

[196] Resione, *G217 clear non-yellowing tough abs like 3d printer resin (1kg)*, 2020. [Online]. Available: https://www.resione.com/products/g217-clear-tough-abs-like-3d-printer-resin-1kg-1?srsltid=AfmBOoqvMZQjmwSVRc1SixdspnaJTKE5G4rw3ju6y_Bu657_A7m2qXKn.

[197] NOVA3d, *Nova3d ultra-clear resin for 3d printer*, 2025. [Online]. Available: https://nova3dp.com/products/nova3d-ultra-clear-resin-for-3d-printer.

[198] Sirayatech, *Siraya tech craft creative resin*, 2024. [Online]. Available: https://siraya.tech/products/craft-resin-by-siraya-tech.

[199] Piocreat, *Piocreat | high transparency resin*, 2021. [Online]. Available: %5Curl%7Bhttps://piocreat3d.myshopify.com/products/pionext-pc-clear-lcd-dlp-3d-printing-high-transparency-resin?srsltid=AfmBOor7RnITcTwVc_vz18dQkF93-_hNhKgeg5NFerQvSshYOTTnQmAg%7D.

[200] formfutura, *Engineering lcd resin - flex 82a*, Jan. 2025. [Online]. Available: https://formfutura.com/product/engineering-lcd-resin-flex-82a/.

[201] 3D Systems, *Accura sl 5530 (sla) | 3d systems*, Oct. 2016. [Online]. Available: https://www.3dsystems.com/materials/accura-sl-5530.

[202] 3D Systems, *Accura castpro (sla) | 3d systems*, Jun. 2016. [Online]. Available: https://www.3dsystems.com/materials/accura-castpro.

[203] 3D Systems, *Accura 60 (sla) | 3d systems*, Jun. 2016. [Online]. Available: https://www.3dsystems.com/materials/accura-60.

[204] 3D Systems, *Accura clearvue free (sl 7870) (sla) | 3d systems*, Jun. 2016. [Online]. Available: https://www.3dsystems.com/materials/accura-clearvue-free-sl-7870.

[205] Parallel Fluidics, Inc., *Parallel fluidics | hardware | 1/4-28 port*, Asset Port fitting, 2024. [Online]. Available: https://www.parallelfluidics.com/components/1-4-28-port.

[206] Dassault Systèmes, *My solidworks*, Asset for Luer connection, 2025. [Online]. Available: https://my.solidworks.com/asset/3dcc-746047.

[207] Dassault Systèmes, *3d contentcentral - free 3d cad models, 2d drawings, and supplier catalogs*, Asset Screw fitting, 2022. [Online]. Available: https://www.3dcontentcentral.com/download-model.aspx?catalogid=2565&id=607654.

[208] OpenAI, *Chatgpt-4o*, Accessed on March 30, 2025, 2025. [Online]. Available: https://chat.openai.com.